Ortho-substituent effects in NHC-catalysis

PETER QUINN

A thesis submitted for the degree of Doctor of Philosophy

Department of Chemistry

Durham University

2018

Contents

Statement of copyright

Abstract

N-Heterocyclic carbenes (NHCs) are extensively used in contemporary organocatalysis in diverse C-C bond forming reactions. Although successful, high catalyst loadings are typically required and chemoselectivity highly depends on catalyst type and structure. Catalysts are commonly selected by screening based approaches because it is not entirely clear how the structures of both the N-aryl ring and aldehyde substrate affect reactivity. In particular, *ortho*-substituents on both the NHC and aryl aldehyde have been found to display enhanced rate and equilibrium constants for deprotonation and hydroxyaryl adduct formation, however, the mechanistic reason is unclear.

Chapter 2 describes the synthesis, kinetic evaluation and structural analysis using X-ray crystallography and DFT calculations of a range of triazolium salts, which are precursors to triazolyl NHCs. The findings from this chapter suggest that large dihedral angles between the triazolium and N-aryl ring, which are found in *ortho*-substituted systems, lead to relatively fast proton transfer from the triazolium salts. This is attributed to a ground state destabilisation of the cationic starting material through reduced inter-ring conjugation.

Chapter 3 describes the kinetic studies aimed at investigating *ortho*-substituent effects on both the catalyst and aldehyde substrate on the intial hydroxyaryl adduct forming equilibrium. *Ortho*-substituted NHCs result in relatively fast rates and large equilibrium constants for hydroxyaryl adduct formation. This may be attributed to the relatively large dihedral angle between the triazolyl and N-aryl rings. Approach of the incoming electrophile requires the N-aryl ring to rotate out of plane of the triazolyl ring, which results in an energetic penalty for non-*ortho*-substituted NHCs. An *ortho*-alkoxy substituent on the aryl aldehyde have also been found to lead to enhanced rate and equilibrium constants for formation relative to unsubstitued aryl aldehyde. These findings are rationalised in terms of the formation of an increasingly optimal intramolecular H-bond in the transition state for hydroxyaryl adduct formation.

Chapter 4 describes the attempts to determine a pK_a for the conjugate acid of the Breslow intermediate based on the triazolyl scaffold. Methylated analogues were prepared and the kinetics of deprotonation by NMR and stopped flow UV-vis spectrophotometry are in agreement and suggest that a small proportion of O-methylated BI is observable in aqueous solution. Attempts were also made to reprotonate the BI to determine a pK_a value in aqueous solution.

Acknowledgements

I'd like to thank my supervisors Dr AnnMarie O'Donoghue and Dr David R. W. Hodgson for giving me the opportunity to carry out my PhD within their laboratories. I'd also like to thank RCUK for funding.

The department of chemistry has excellent technical staff, without whom the work in this thesis would not have been possible. Many thanks to the staff in the NMR service: Mrs Catherine Heffernan, Dr Raquel Bela-Vidal, Dr Juan Aguilar and Dr Alan Kenwright, for being very patient with me and my use of the NMR spectrometers and for my endless questions on NMR experiment and theory. Thanks also to the mass spectrometry service: Dr Jackie Mosely, Dr David Parker and Mr Peter Stokes and HPLC service: Dr Aileen Congreve and Mr Len Lauchlan. I would like to thank Dr Dmitry Yufit for obtaining the X-ray crystal structures and Dr Mark Fox for trouble shooting my early attempts at running DFT calculations.

Studying towards a PhD is as much about career development as it is about conducting research. I'd like to thank Dr Elizabeth Grayson and Dr Russell Taylor for many helpful discussions and direction in my professional development as a scientist.

Life in the lab and the department in general would not have been as enjoyable if it were not for the many people I've had the good fortune of working alongside: Oliver Maguire, David Wong Pascua, Jiayun Zhu, Dr Lami Nnamonu, Neshat Rozatian, Kevin Maduka, Mahdi Haghgoo, Stephen Rouse, Aisha Bismillah, Jay Wright, Xie Tianren, Melissa Walden, Edward Walter, Jonathan Purdie, Lottie Nicholson, David Tucker, Craig Fisher, Josh Walton, Marcus Lancashire, Alex Hampton, Darren Heeran, Etienne Lisse, Ben Murray, Niamh Ainsworth, Ryan Williams, Dan Sheppard and George Harrison. In particular, I had the good fortune of working alongside incredibly talented scientists who helped shape my ability to think as a scientist and for that I am eternally grateful to Oliver Maguire, Jiayun Zhu, Dr Lami Nnamonu and Neshat Rozatian for many helpful discussions on all areas of chemistry.

Football was a great release from the failed experiments (and also a good way to celebrate experiments that worked). I would like to thank all the members of Ustinov AFC and members of staff that I met playing football over the past three years. In particular, thanks to Folajimi, Daniel H., Asahi, Alex H., Eddy, Dzulfian, Boguslaw, Angus, Menno, Jeroen, Max B., Mike C., Tom H., Steve L. and Steve B.

I have been extremely lucky to have a very supportive family, who have always helped, encouraged and supported me. I would like to thank my parents and sister for their constant love, encouragement and support. Thanks also to Mary, who has always helped and encouraged Marianne, Erin and myself. Many thanks also to Almaz, Weini, Tsega, Sitel, Patrick, Will, Colleen, Mike, Rupert, Freddy, Shelagh, Tim and Olive.

My closest mates deserve a special mention: Adil, Alex, Seb, Rich, Gantz and Matt. I've always been able to catch up over a few beers and plenty of laughter, despite the fact that everyone lives all over the country.

Finally, I would like to thank Marianne, Erin and Henry for their love, patience and support throughout the entirety of my studies and to whom this thesis is dedicated.

To Marianne, Erin and Henry

Abbreviations

DBU	1,8-Diazabicyclo[5.4.0]undec-7-ene
Ad	Adamantyl
BI	Breslow intermediate
CD_3CN	Deuterated acetonitrile
DCl	Deuterium chloride
D_2O	Deuterium oxide
DO	Deuteroxide ion
DBAD	Di-tert-butyl azo-dicarboxylate
dr	Diastereomeric ratio
DCM	Dichloromethane
DMSO	Dimethyl sulphoxide
d	Doublet
ee	Enantiomeric excess
Eqn.	Equation
ESI	Electrospray ionisation
EtOH	Ethanol
GBC	General base catalysis
HPLC	High performance liquid chromatography
HCl	Hydrochloric acid
I	Ionic strength
LCMS	Liquid chromatography mass spectrometry
Mes	Mesityl (2,4,6-trimethylphenyl)
Me	Methyl
M	Mol dm^{-3}
NHC	N-heterocyclic carbene
ppm	Parts per million
Pr	Propyl
q	Quartet
quin	Quintet
ρ	Reaction constant
s	Second
s	Singlet (spectral)
SBC	Specific base catalysis
σ	Substituent constant
TMSDAM	Trimethylsilyl diazomethane
Boc	tert-Butyloxycarbonyl
THF	Tetrahydrofuran
UV	Ultraviolet
Vis	Visible

Chapter 1: Introduction

1.1 Introduction

Carbenes are compounds that contain a divalent carbon atom with two non-bonding electrons either paired (singlet state) or unpaired (triplet state). Such species were once thought to be reactive intermediates, but the isolation of phosphinosilylcarbene **1** by Bertrand[1] in 1988 and imidazol-2-ylidene **2**, the first stable N-heterocyclic carbene (NHC), by Arduengo[2] in 1991 (Figure 1) led to the development of many isolable heteroatom-substituted singlet carbenes. Such advances have led to a growing understanding of how electronic and steric effects influence the stability of carbenes.[3]

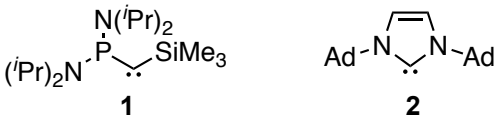

1 **2**

Figure 1: First isolated singlet carbenes.[1,2]

This chapter begins with a summary of the synthetic applications of NHCs in a range of umpolung reactions (via acyl anion and homoenolate intermediates), with examples of normal reactivity (via acyl azolium and enolate intermediates). This is followed by a discussion of the literature on the mechanistic work reported on the benzoin condensation, with questions posed which this thesis attempts to answer.

1.2 Organocatalysis

NHCs are now used extensively as nucleophilic organocatalysts for organic transformations.[4] The first NHC-catalysed reaction studied was the coupling of two benzaldehyde molecules to give benzoin. The synthesis of benzoin was discovered by Wöhler and Liebig in 1832 and was found to be catalysed by cyanide ions.[5] Lapworth proposed a mechanism for this transformation in 1903.[6] In 1943, Ukai demonstrated that catalytic quantities of thiazolium ions could promote the same reaction.[7] In 1958, using a H/D exchange experiment on thiamine pyrophosphates and related analogues, Breslow[8] proposed a mechanism for thiamine catalysed benzoin condensation, inspired by Lapworth's mechanism for cyanide catalysed benzoin condensation.[6] This mechanistic work set the foundation from which advances in NHC-catalysed organic transformations were made. This field has now expanded beyond the use of thiamine and related derivatives as precatalysts. There are also an increasing number of novel transformations which they are capable of catalysing.

Perhaps the most studied type of reaction catalysed by NHCs in the literature involves the use of "umpolung" reactivity, that is, reversal of polarity. Such catalysts are able to

convert an electrophilic carbon atom in a carbonyl group into a nucleophilic one. The key intermediate is the acyl anion equivalent, also known as the Breslow intermediate (BI). The electrophilic β carbon of an α, β-unsaturated carbonyl compound may also be converted into a nucleophilic "homoenolate". Normal reactivity of the substrate is also possible: acyl azoliums may be generated from α-haloaldehydes.

1.2.1 Acyl anion intermediates

The accepted mechanism for the formation of acyl anion equivalents first involves the *in situ* deprotonation of conjugate acid **3** with the aid of a base to give NHC **4**. Nucleophilic attack of carbene **4** at the electrophilic carbon of an aldehyde **5**, an a[1] synthon, gives **6.** Protonation of **6** gives hydroxyaryl adduct **7**. Deprotonation at C(α) gives the resonance stabilised enaminol-type BI **8**, now a d[1] synthon or acyl anion equivalent. Attack of this acyl anion intermediate at the electrophilic carbon of another aldehyde **9** gives **10**, which, after proton transfer to give **11** and ejection of the carbene **4** gives the benzoin product **12**. A catalytic cycle is shown in Scheme 1.

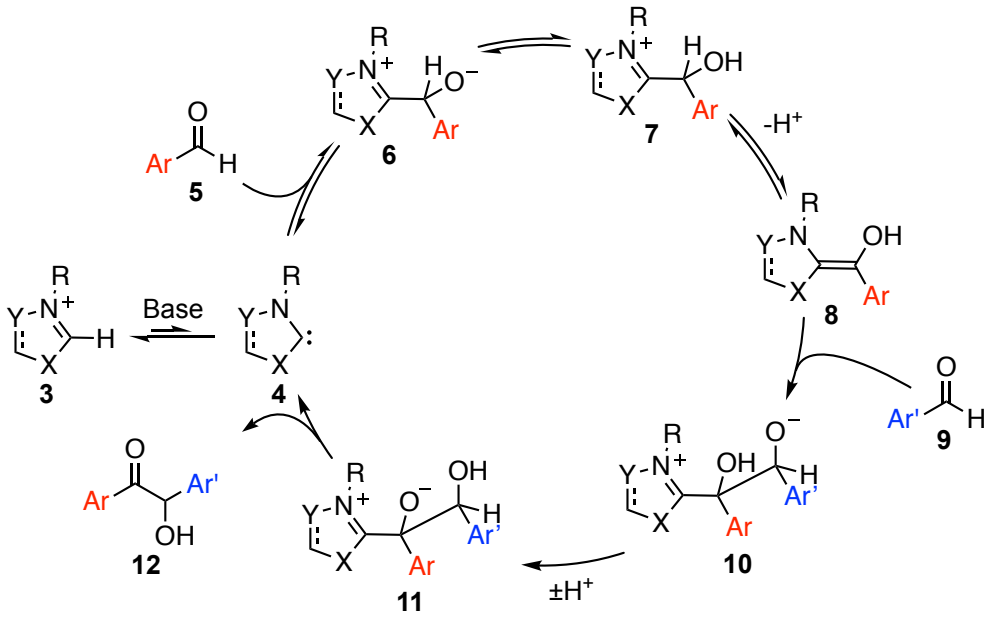

Scheme 1: Accepted model of the benzoin condensation proposed by Breslow.[8]

The result of this umpolung reactivity is a 2-hydroxyketone **12** with a stereogenic centre. A variety of different carbene catalysts have been used in asymmetric benzoin condensations, which have clear advantages over cyanide in terms of lower toxicity and having a structural framework that allows modification for asymmetric induction.

1.2.1.1 Benzoin condensation

The first asymmetric benzoin condensation was reported by Sheehan in 1966, catalysed by a chiral thiazolium ion with only 22% *ee*.[9] This was improved using the chiral thiazolium ion **13** (Figure 2) where an enantiomeric excess of 52% was obtained.[10] In 1996, Enders reported the use of triazolium **14** as a precatalyst that was capable of much better enantiomeric excesses (of up to 86%) than generally seen for reactions catalysed by thiazolylidenes.[11] Leeper reported the use of novel bicyclic thiazolium **15** in 1997 which gave *R*-benzoin with an enantiomeric excess of 21% and a yield of 50%.[12] A bicyclic system prevents the free rotation of the chiral group and therefore induces greater stereoselectivity. In 1998, Leeper reported the use of bicyclic triazolium precatalysts **16** and **17**, which gave 83% *ee* with a 38% yield, and 68% *ee* with an 11% yield, respectively.[13] Enders reported excellent enantioselectivity with chiral bicyclic triazolium ion precatalyst **18** in 2002, with 95% *ee*, but a poor yield was obtained (8%) for the dimerization of 4-methoxybenzaldehyde.[14] In 2009, Connon reported excellent enantioselectivity (99%) with chiral bicyclic triazolium ion **19** bearing an N-C_6F_5 substituent, but this was obtained in a poor yield of 29%.[15] In 2012, Ukaji and co-workers reported excellent enantioselectivity and yield with chiral bicyclic triazolium ion **20** bearing an N-pyridyl substituent.[16] The excellent enantioselectivity was proposed to be due to intramolecular H-bonding between the hydroxyl group and the pyridyl ring in the BI. Figure 2 highlights the structural diversity of the NHC precatalysts described above.

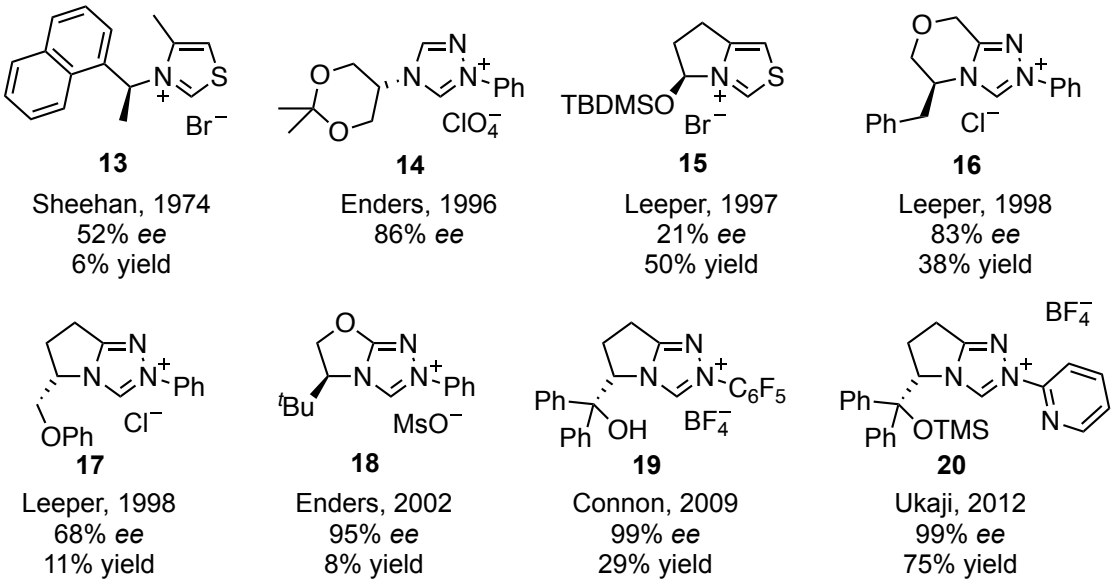

Figure 2: Selected chiral azolium salts for the benzoin condensation showing the improvement in yield and *ee* over the last 44 years.

1.2.1.2 Cross benzoin condensation

There have also been successful examples of chemo- and stereoselective aldehyde-aldehyde cross-acyloin reactions, which provide access to a wider range of products.

Connon and co-workers achieved chemoselective crossed aliphatic-aromatic acyloin condensations, where *ortho*-substituted aryl aldehydes **21** were key to the selectivity (Scheme 2).[17] The major products **24** arose from the attack of the NHC catalyst upon the aliphatic aldehyde **22**, followed by deprotonation and then attack of the BI **23** upon aryl aldehyde **21**. This is an interesting example since R_1 = Br worked very well, and the Br could also be either be removed by hydrogenation or used for further modification. The authors suggested that there is more than one factor affecting the chemoselectivity. Through a series of crossover experiments, the authors found (1) homodimerisation of aliphatic or *ortho*-substituted aryl aldehydes is slow, (2) aliphatic and *ortho*-substituted homodimers undergo retro acyloin either slowly or not at all, (3) unhindered aryl benzoins undergo retro-benzoin and (4) the major product from crossed acyloin reactions either undergo retro acyloin slowly or not at all.

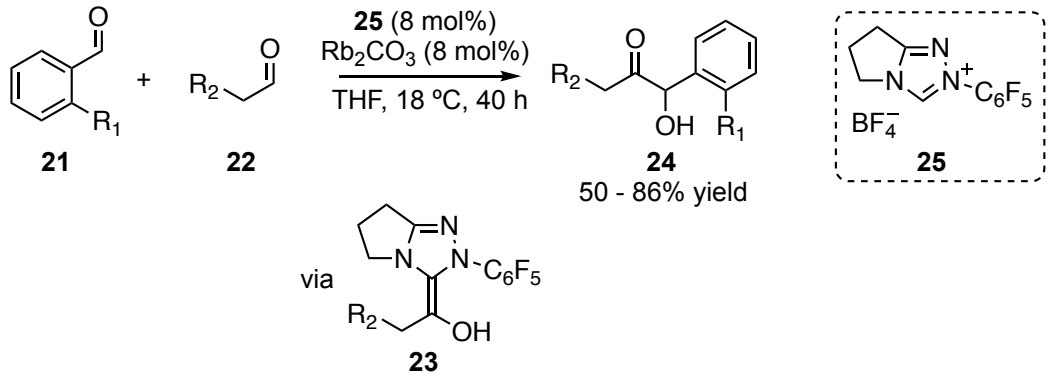

Scheme 2: Connon's chemoselective crossed aliphatic-aromatic acyloin condensation.[17]

Selective cross-benzoin condensations with aromatic aldehydes were achieved by Glorius and co-workers in 2011, using a sterically bulky N-2,6-diisopropylphenyl thiazolium salt **29** (Scheme 3).[18] These authors suggested the product outcome was due to the attack of the sterically hindered NHC at the less hindered non-*ortho*-substituted aryl aldehyde **26** and the resulting BI then attacks the *ortho*-chloro aryl aldehyde **27** based on electronics. However, no kinetic experiments were carried out to investigate the nucleophilicity of the NHC, the electrophilicity of the aryl aldehydes or what role the *ortho*-chloro substituent has in the observed chemoselectivity.

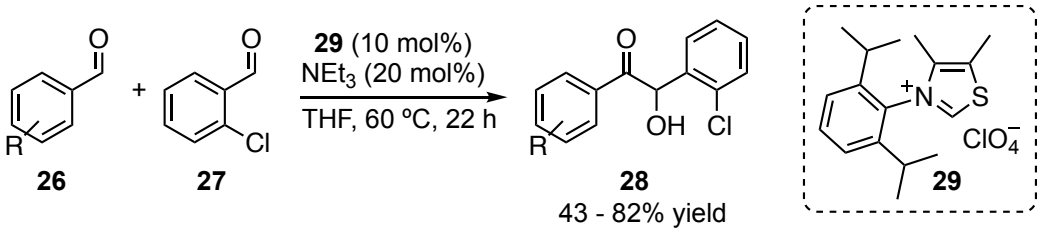

Scheme 3: Glorius' chemoselective crossed benzoin condensation.[18]

Yang also demonstrated that steric arguments may be used to explain the reversal in chemoselectivity in crossed aliphatic-aromatic acyloin condensations (Scheme 4).[19] Using a relatively unhindered thiazolium salt precatalyst **34** in THF, the predominant product **32** arose from the initial attack of the NHC on the electron withdrawing aryl aldehyde **30**. When a relatively sterically hindered triazolium precatalyst **35** in *m*-xylene was used, however, the major product **33** was derived from initial attack of the NHC at the less hindered aliphatic aldehyde **31**. The argument based on sterics of the two catalysts is flawed as different NHC scaffolds were used. It is not clear what the reason is for the reversal of selectivity.

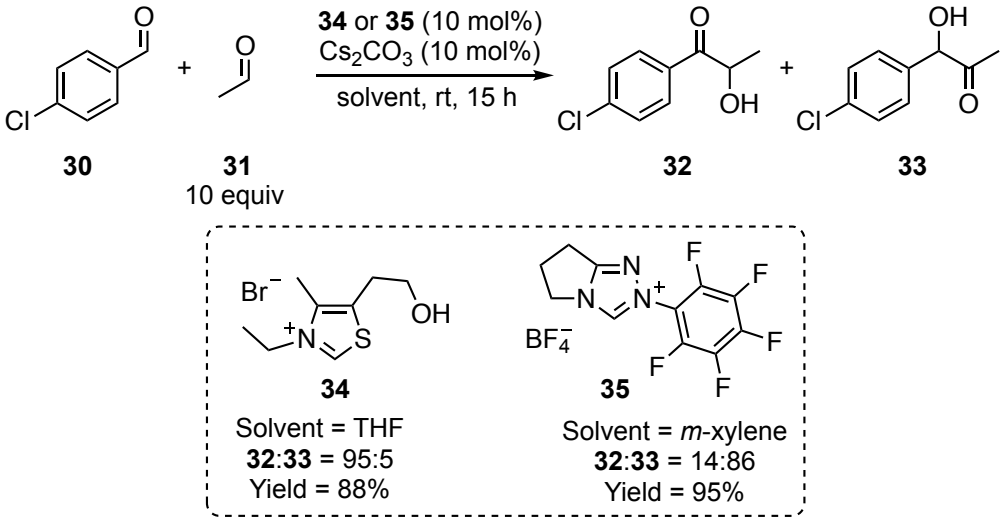

Scheme 4: Yang's chemoselectivity reversal in crossed aliphatic-aromatic acyloin condensation.[19]

In 2014, Yang and co-workers reported the chemoselective crossed aliphatic-aromatic acyloin condensation (Scheme 5).[20] The optimised conditions used 15 equivalents of the aliphatic aldehyde, which no doubt causes the favoured product to be that based on the initial attack of the NHC on the aliphatic aldehyde. These authors observed a change in chemoselectivity from the homo-dimerisation product **40** using catalysts **41**-**43**, to the crossed product **38** using catalyst **44.**

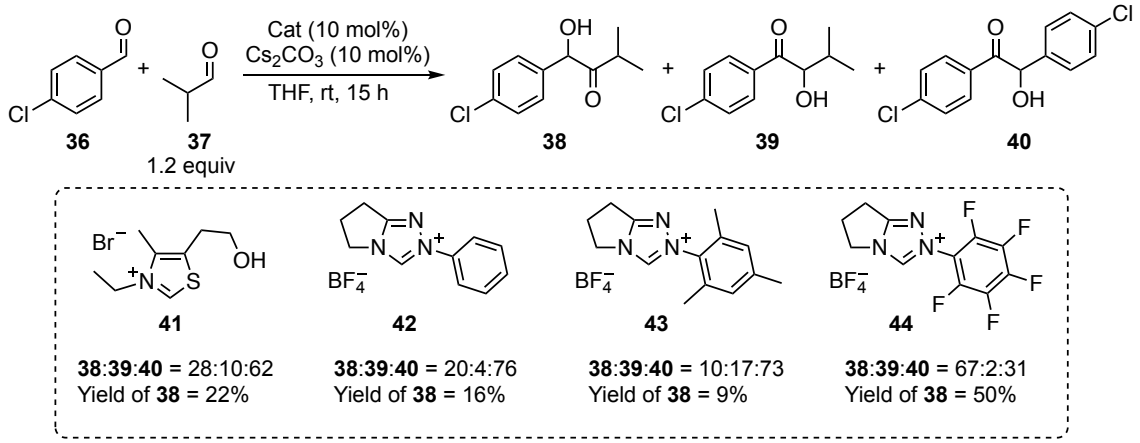

Scheme 5: Yang's chemoselective crosssed aliphatic-aromatic acyloin condensations, demonstrating a change in chemoselectivity when NHC are varied.[20]

Gravel and co-workers showed that the size of the fused ring in triazolyl-catalysed cross aliphatic-aromatic acyloin condensations can influence the observed chemoselectivity.[21] The selectivity for the crossed product shown in (Scheme 6) increases in the order **52** > **53** > **51**. From a series of crossover experiments, the authors suggested that the selectivity of the reaction is determined after the formation of the BI. Within the O'Donoghue research group, Zhu[22] has obtained X-ray crystal structures for 6- and 7-membered ring triazolium salts. It appears that the dihedral angle between the carbene lone pair and the C-H adjacent to N4 of the triazolium ring could have a significant steric effect on the approach of the aldehyde.

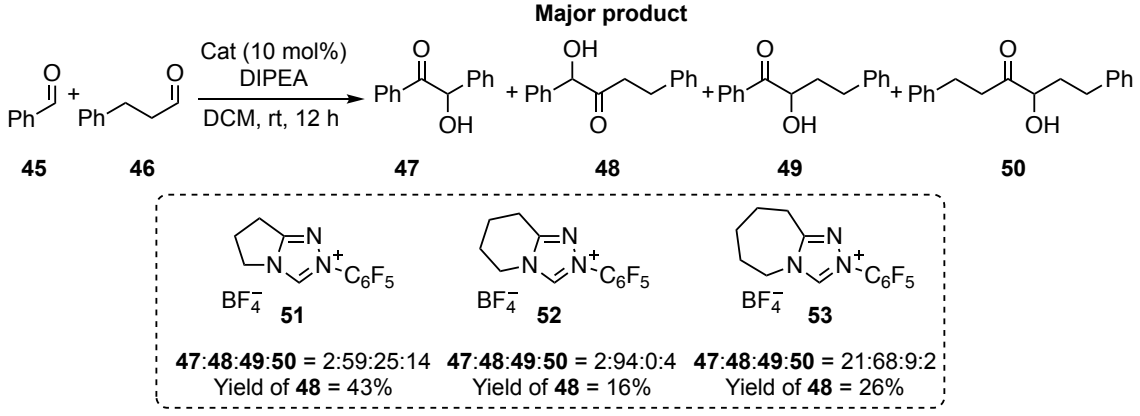

Scheme 6: Gravel's chemoselective crosssed aliphatic-aromatic acyloin condensation, demonstrating the influence of the bicyclic backbone on chemoselectivity.[21]

Using four thiamine diphosphate dependent enzymes, Müller and co-workers were able to chemo- and enantioselectively generate all four possible crossed-products in crossed aliphatic-aromatic acyloin condensations. Chemoselectivities up to 99% and ee's of up to 99% were achieved.[23] These chemoselective reactions are likely to benefit from the steric (and potentially electrostatic) properties of the enzyme active site.

Connon and co-workers recently reported a highly chemoselective intermolecular crossed benzoin condensation (Scheme 7).[24] These authors rationalised the product outcome based on the argument that the chemoselectivity is not determined by the initial adduct forming step[25] and that the BI derived from the *ortho*-bromobenzaldehyde **55** is too sterically bulky to act as a nucleophile. They proposed that the BI derived from benzaldehyde **54** would be a better nucleophile and attack would occur at the more electrophilic *ortho*-bromobenzaldehyde **55**. They also suggested that a slower retro-benzoin condensation associated with the major crossed product **56** may also explain the product outcome. However, no kinetic experiments were carried out to investigate the electrophilicities of the two aryl aldehydes **54** and **55**, the nucleophilicity of the NHC used compared to less sterically hindered N-aryl triazolium precatalysts, and the nucleophilicity of the resulting BIs.

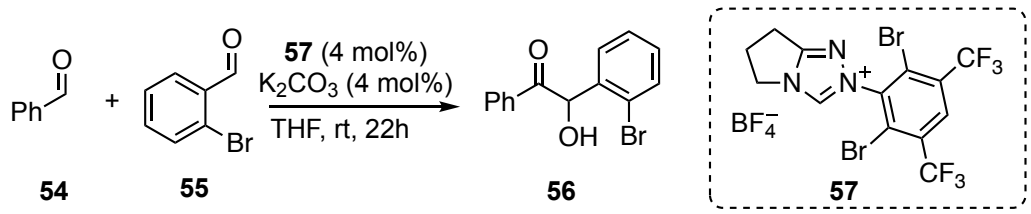

Scheme 7: Connon's chemoselective crosssed benzoin condensation, using a sterically bulky NHC precatalyst and *ortho*-bromobenzaldehyde as a directing group.

1.2.1.3 Stetter reaction

A variant of the benzoin condensation involving the nucleophilic attack of the Breslow intermediate on a Michael acceptor was first devised by Hermann Stetter, who in 1976 reported the application of thiazolylidenes for this transformation to give 1,4-dicarbonyl compounds.[26] The first intramolecular Stetter reaction, the cyclisation of salicylaldehyde derivative **58** to give chromanone **59**, catalysed by thiazolium precatalyst **60** was reported by Ciganek in 1995.[27] The reaction was rendered asymmetric in 1996 by Enders, using chiral triazolium precatalyst **61**.[28] The enantioselectivity was improved by Rovis in 2002, using chiral triazolium precatalysts **62** and **63** (Scheme 8).[29] This increase in enantiomeric excess may again be readily explained by the fact that the bicyclic system prevents rotation of the chiral substituent, inducing greater stereocontrol.

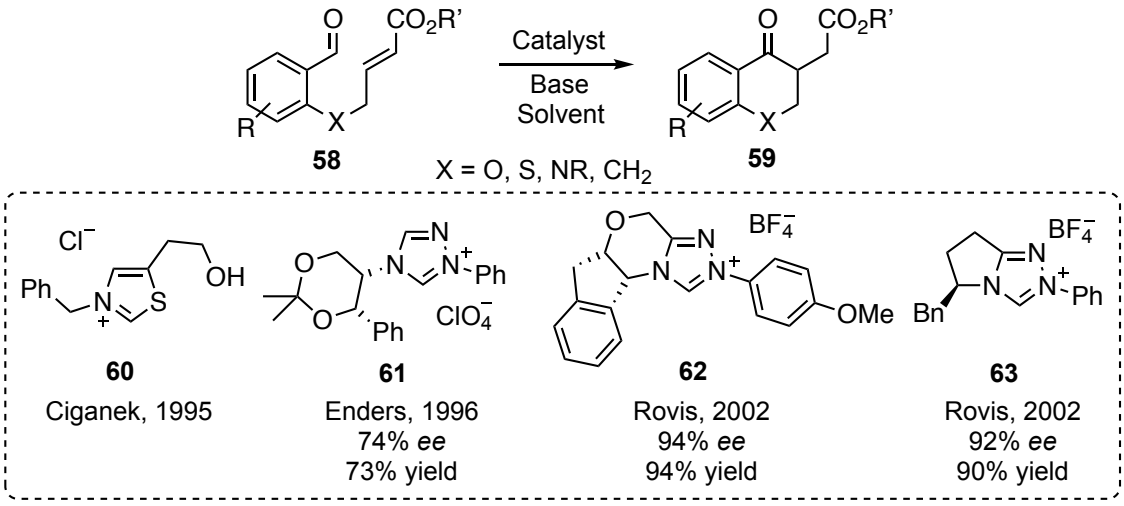

Scheme 8: Selected azolium precatalysts for enantioselective intramolecular Stetter reactions.

McErlean and co-workers reported the NHC-catalysed intramolecular vinylogous Stetter reaction which involves attack of the BI derived from initial attack at aldehyde **64** upon an α,β,γ,δ-unsaturated carbonyl compound to give a 1,6-dicarbonyl function **65** with a double bond (Scheme 9). This reaction was catalysed by triazolium precatalyst **66** and thiazolium precatalyst **67** in the presence of base, but failed in the presence of imidazolium precatalyst **68**.[30] These authors did not give potential mechanisitic reasons for this.

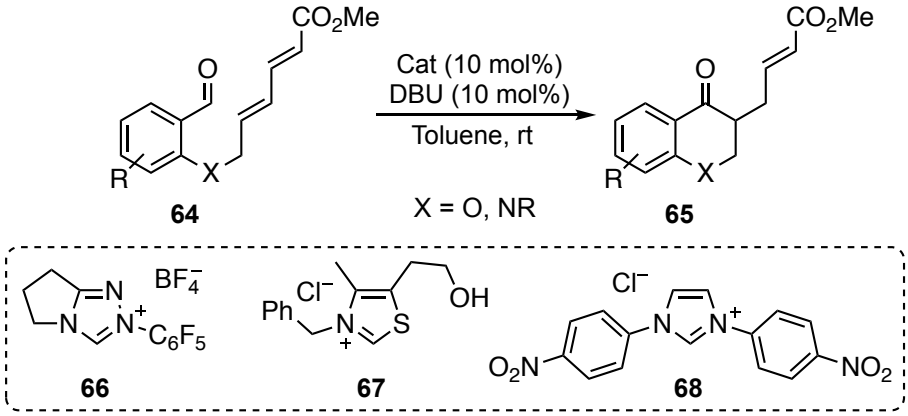

Scheme 9: McErlean's intramolecular vinylogous Stetter reaction.[30]

1.2.1.4 Hydroacylation of alkenes and alkynes

Hydroacylations of neutral alkenes and alkynes are also possible with acyl anion equivalents. In 2009, Glorius and co-workers reported the first NHC-catalysed intramolecular hydroacylation of unactivated alkenes **69** to yield a range of compounds **70** containing a 4º carbon in the presence of thiazolium precatalyst **71** (Scheme 10).[31] Prior to this, hydroacylation reactions were performed in the presence of transition metal complexes.[32]

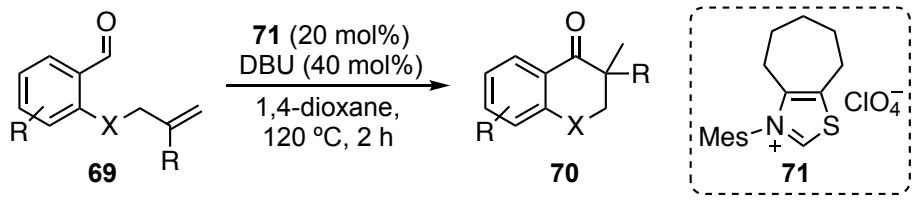

Scheme 10: Glorius' hydroacylation of tethered, unactivated alkenes.[31]

A highly enantioselective version of this reaction was reported two years later by the same group, with best *ee*s and yields obtained using triazolium precatalyst **77** (Scheme 11).[33] The triazolium precatalyst screening (**74** – **77**) seemed to suggest that electron donating *ortho*-disubstituted N-aryl triazoliums were favoured in terms of *ee* and yield, however no mechanistic explanation for this was given.

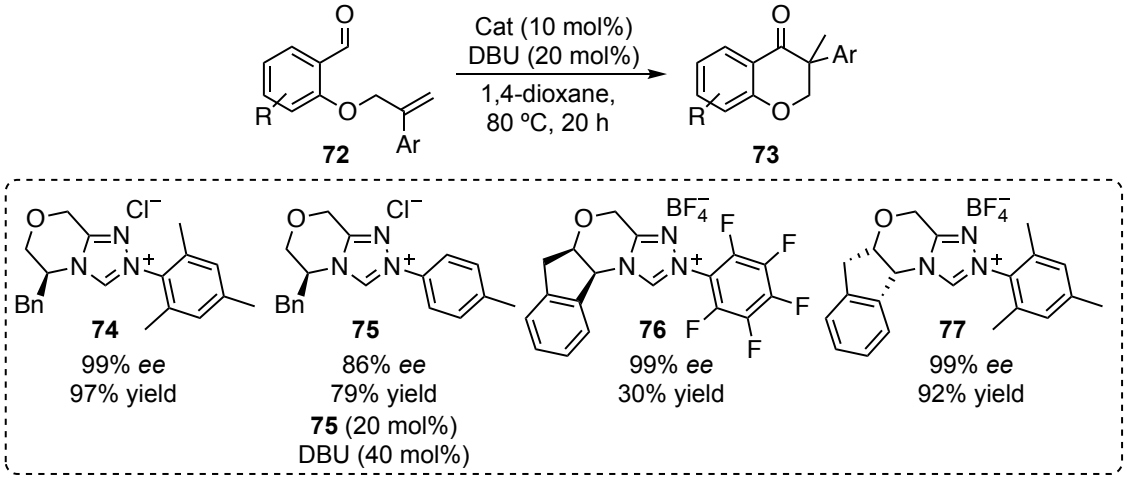

Scheme 11: Glorius' enantioselective hydroacylation of tethered, unactivated alkenes.[33]

Intramolecular hydroacylation of unactivated alkynes **78** was reported using thiazolium precatalyst **80** (Scheme 12) to give products **79** with an exocyclic alkene.[34] Again, a sterically hindered N-mesityl substituted precatalyst **80** was used. No other NHCs were trialled and therefore the mechanistic reason for the success of this reaction is unclear.

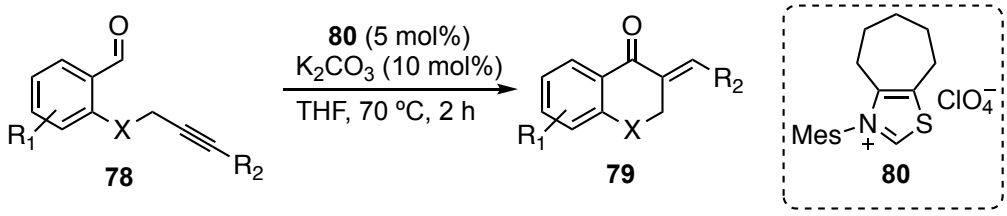

Scheme 12: Glorius' hydroacylation of tethered, unactivated alkynes.[34]

The intermolecular hydroacylation of cyclopropenes **82** to give acylcyclopropanes **83** with excellent diasterocontrol was achieved using N-mesityl substituted thiazolium **84** and triazolium **85** (Scheme 13).[35] Attempts to carry out the reaction using N-phenyl **86**

and N-pentafluorophenyl **87** substituted triazolium salts gave less than 5% yield. The reaction was developed further to be enantioselective and these authors found that increasing the electron donating ability of the *ortho*-substituted N-aryl triazolium from N-mesityl **88** to N-2,6-dimethoxyphenyl **89** triazolium salts resulted in greater yields and *ee*s of **83**.[36,37]

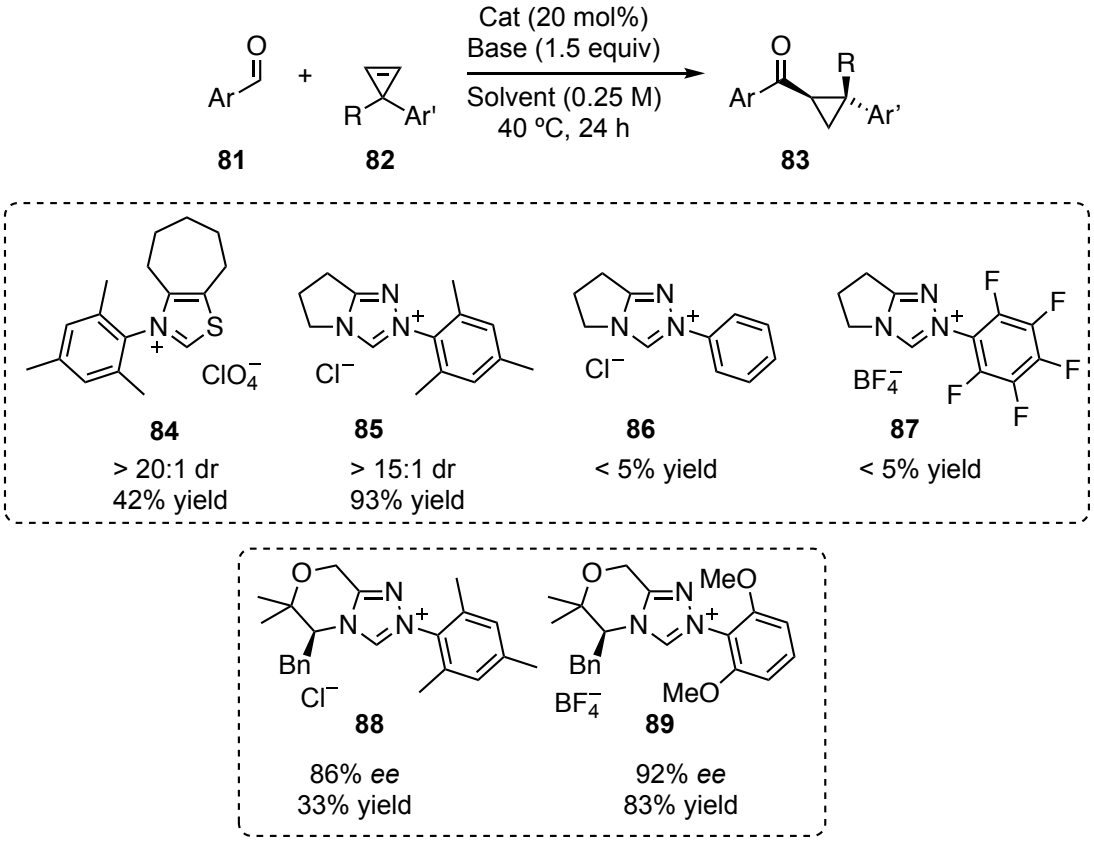

Scheme 13: Glorius' intermolecular hydroacylation of cyclopropenes, showing largest *ee*s and yields with electron donating *ortho*-disubstituted N-aryl triazolium salts.[35-37]

Glorius then reported the more challenging intermolecular hydroacylation of unactivated styrenes **91**, to give linear and branched products **92** and **93**, respectively (Scheme 14).[38] Again, the N-2,6-dimethoxyphenyl triazolium salt **95** was superior to the N-mesityl triazolium salt **94**. Electronics and sterics play a role in efficiency of catalysis in this transformation, however, the mechanistic underpinning is not clear.

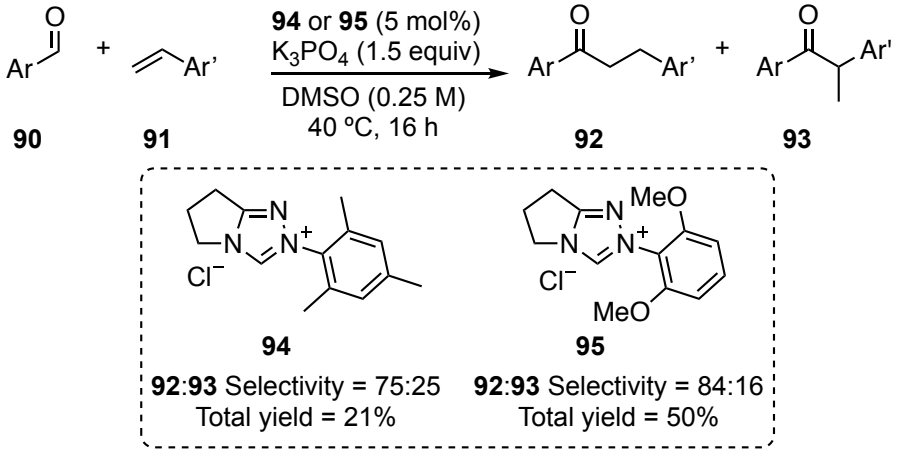

Scheme 14: Glorius' intermolecular hydroacylation of styrenes.[38]

1.2.2 Homoenolate intermediates

Nucleophilic attack of an NHC **97** upon an α,β-unsaturated aldehyde **96** provides a means of converting the initially electrophilic a^3 Michael acceptor synthon **96** into nucleophilic d^3 synthon **98** (Scheme 15). NHC-bound homoenolates **98** (d^3 synthons) can then be used to make 1,4-difunctionalised compounds via umpolung chemistry. This leads to useful intermediates synthetically and recent advances have led to their use in the synthesis of γ-butyrolactones, spiro-γ-butyrolactones, and γ-lactams, all of which are important for the synthesis of biologically active molecules.

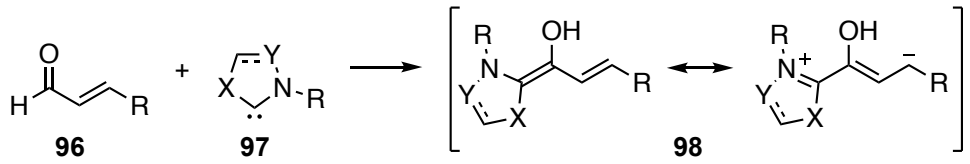

Scheme 15: Umpolung of a Michael acceptor to give a homoenolate (a^3 synthon into a d^3 synthon).

The first NHC-catalysed homoenolate reactions were reported independently by Bode[39] and Glorius[40] in 2004. These authors prepared γ-butyrolactones **101**, products of C-O bond forming reactions, using aldehydes or ketones **99** and enals **100**. The reactions gave good yields using imidazolium precatalyst **102** (Scheme 16).

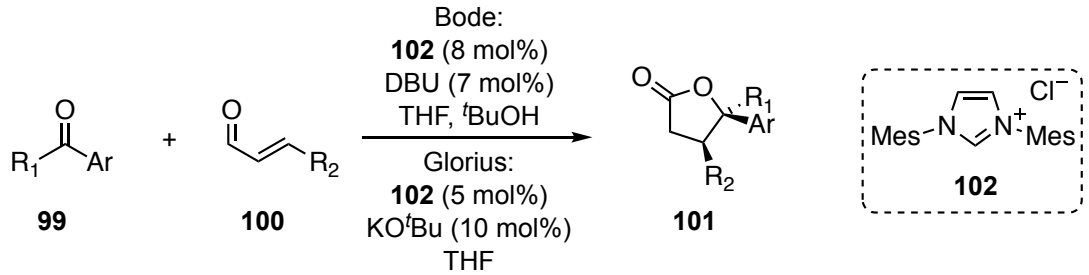

Scheme 16: First NHC-catalysed homoenolate reactions in the synthesis of γ-butyrolactones.[39,40]

Another example of oxygen heterocycle synthesis is Nair's preparation of a range of spiro-γ-butyrolactones, **105**, exploiting homoenolate chemistry of a number of suitable aromatic enals **104** towards 1,2-cyclohexandione **103**, catalysed by imidazolium precatalyst **106** (Scheme 17).[41] A 74% yield of a single diastereoisomer was obtained with an enal bearing an Ar = *para*-fluorophenyl substituent. This highlights the synthetic potential such catalysts have in the field of natural product synthesis to access chiral quaternary carbon derivatives.

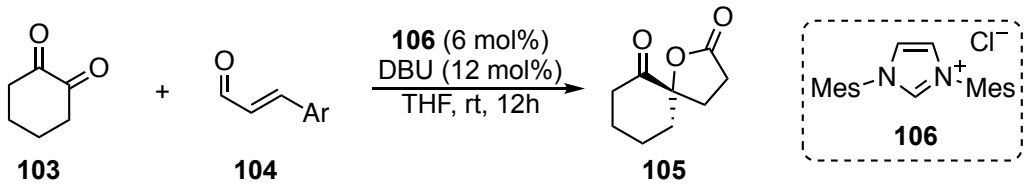

Scheme 17: Synthesis of spiro-γ-butyrolactones.[41]

Nitrogen heterocycle synthesis is also possible via homoenolate chemistry. A range of γ-lactams **109** were prepared from enal **107** and N-sulfonyl imines **108** using imidazolium precatalyst **110** (Scheme 18). Reaction with electron rich N-4-methoxybenzene sulfonyl imine **108** was found to give the desired *cis* diasteromeric product **109** in good yields and with moderate to good selectivities.[42]

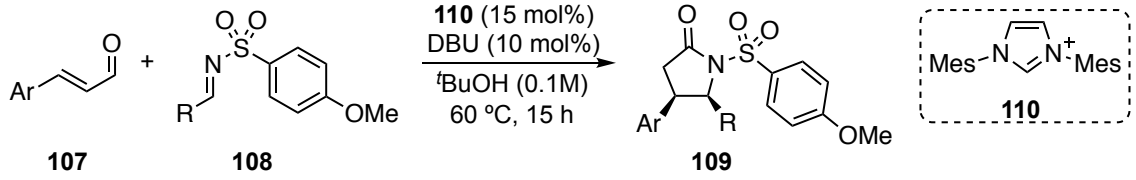

Scheme 18: N-heterocycle synthesis via a homoenolate intermediate.[42]

In an attempt to use homoenolate chemistry to access cyclopentanones **115**, Nair serendipitously formed a 1,3,4-trisubstitutedcyclopentene ring **112** from an enal **111** and chalcone **112** (Scheme 19).[43]

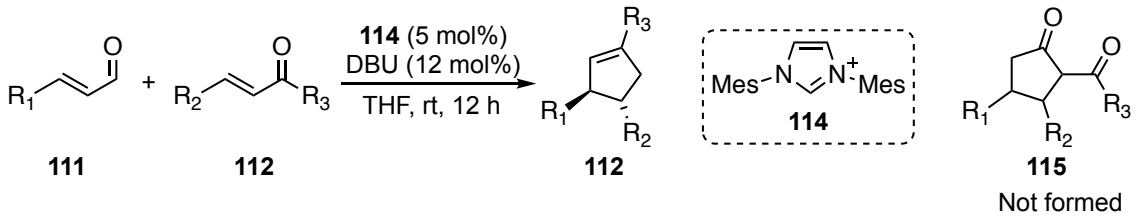

Scheme 19: Unexpected carbocycle product formed via homoenolate intermediate.[43]

The mechanism that was proposed is shown in Scheme 20.[43] Following the formation of homoenolate **116**, conjugate addition to chalcone **112** and proton transfer generates an enolate **117**. This enolate can attack the terminal carbonyl to give **118**. Attack of the

alkoxide **118** at the carbonyl to give **119** and ejection of the carbene **114'** gives a β-lactone **120**, which undergoes decarboxylation to give cyclopentene **113**.

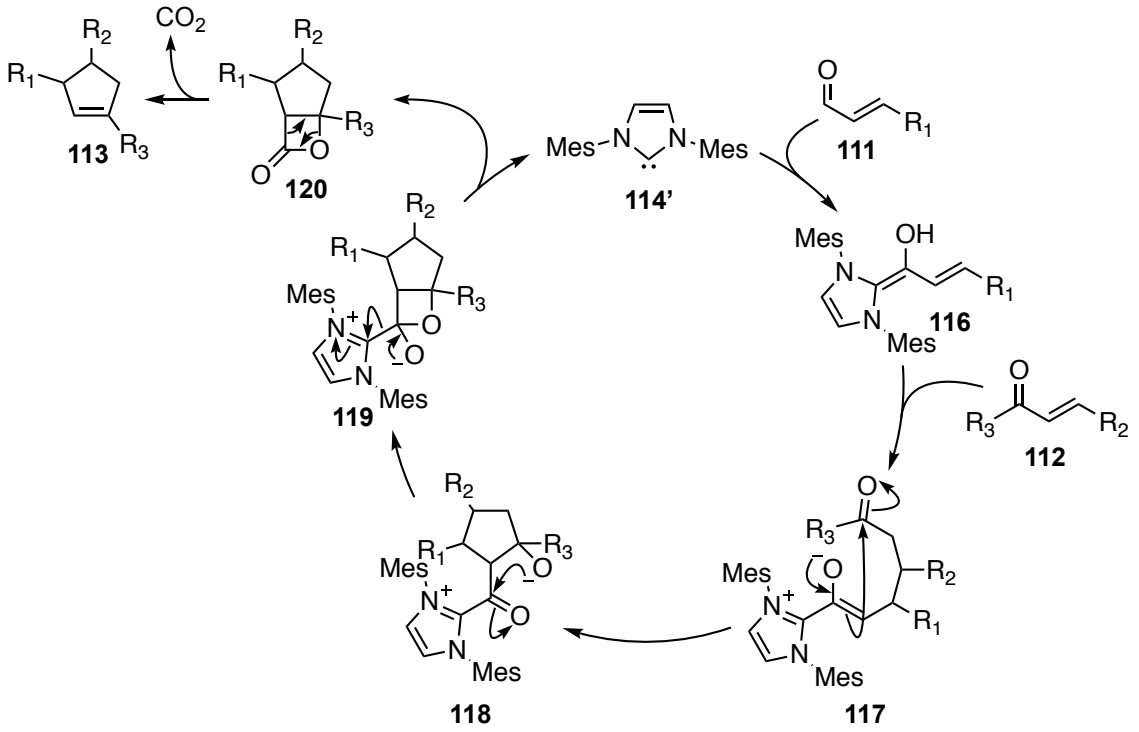

Scheme 20: Nair's proposed mechanism of carbocycle synthesis via homoenolate intermediate.[43]

In 2013, Chi expanded on this reaction by activating the β-carbon of a saturated ester **121** rather than an unsaturated enal (Scheme 21). This reaction expands the scope of homoenolate chemistry by applying a challenging "inert" β-carbon in the construction of C-C bonds to yield cyclopentenes **123**, catalysed by triazolium **124**.[44]

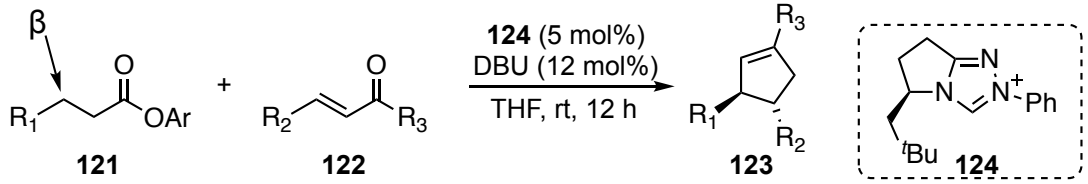

Scheme 21: Activation of an "inert" β-carbon in carbocycle synthesis.[44]

Scheidt utilised homoenolate chemistry for the conversion of an α,β-unsaturated aldehyde **125** into a saturated ester **127** by first trapping the homoenolate with a proton source, and subsequent attack of a nucleophile **126** at the electrophilic carbonyl group (Scheme 22). Two alcohols were used to give the desired product, one acting as a proton source and the other as a nucleophile. Benzimidazolium precatalyst **128** was found to be more effective than thiazolium **129** or triazolium **130**.[45]

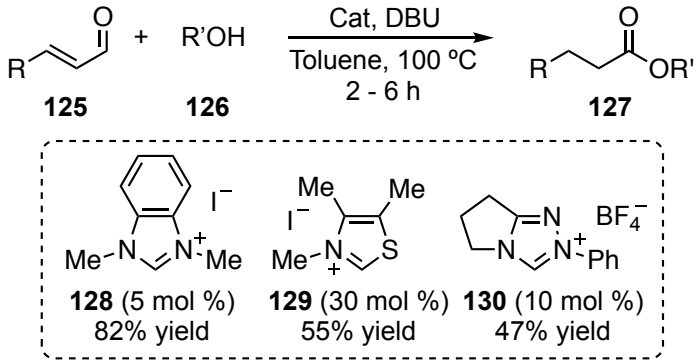

Scheme 22: Conversion of α,β-unsaturated aldehyde into a saturated ester.[45]

1.2.3 Enolate intermediates

The first example of an NHC-catalysed Diels-Alder reaction was reported by Bode in 2006, in which enals **131** was coupled with α,β-unsaturated imine **132** yielding dihydropyridinone **134** with excellent yields (up to 90%) and up to 99.5% *ee* (Scheme 23).[46] The highest conversion and selectivity was obtained used triazolium precatalyst **139**. The selectivity for dihydropyridinone **134** relies on protonation of the homoenolate **140** at the β to give enolate **141** and finally a Diels-Alder reaction with a protected imine (Scheme 24). The alternative product is derived from nucleophilic attack of homoenolate **140** upon protected imine **132** to give γ-lactam **133**.

The mechanistic reasons for (1) the superiority of the electron rich *ortho*-disubstituted N-mesityl triazolium salts **137** and **139**, compared to N-phenyl **136** and N-4-methoxyphenyl **138** and (2) the use of the more electron withdrawing triazolium precatalysts to effect β protonation are not clear.

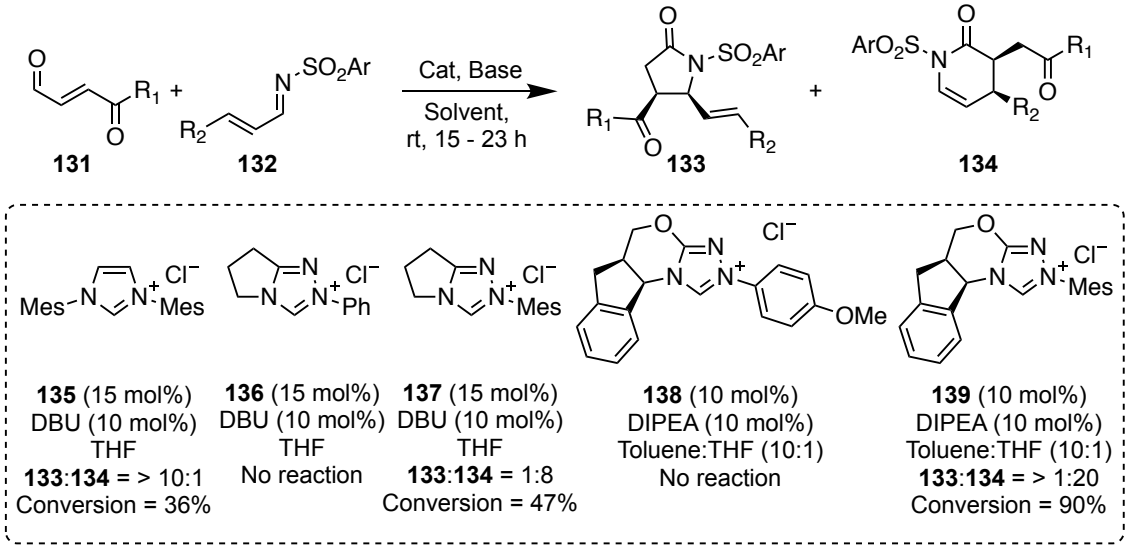

Scheme 23: Triazolylidene-catalysed azadiene Diels-Alder reaction which, goes via enolate intermediate.[46]

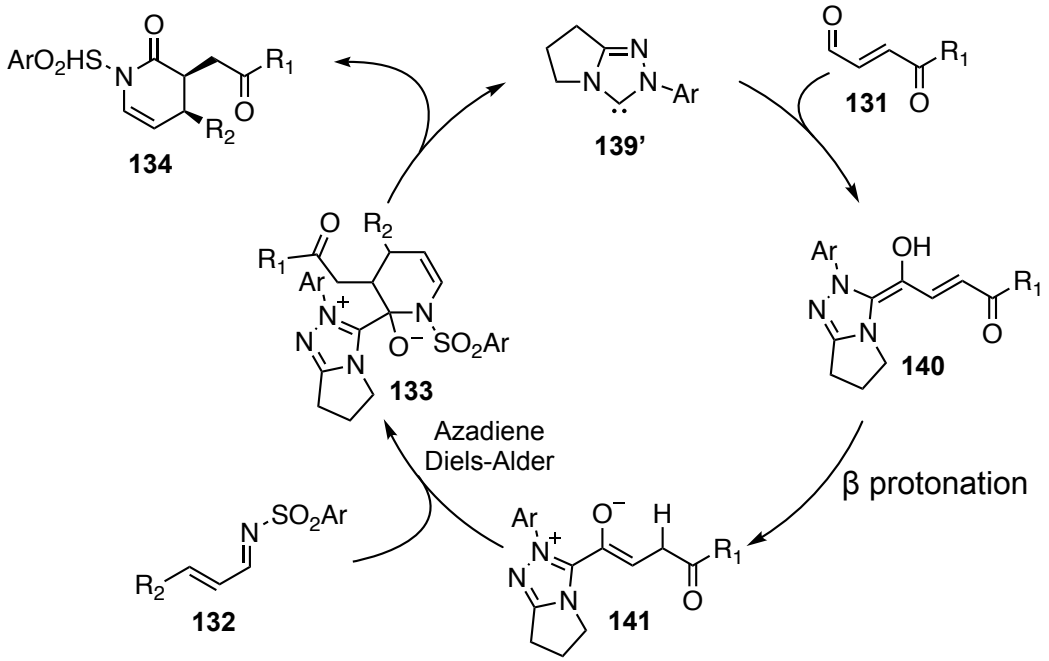

Scheme 24: Bode's proposed mechanism of dihydropyridinone synthesis via enolate intermediate and azadiene Diels-Alder reaction.[46]

1.2.4 Acyl azolium intermediates

Rovis reported the conversion of α-haloaldehydes **143** into acylating agents **146**, where the addition of a series of primary and secondary alcohols **144** gave a series of saturated esters **145** (Scheme 25).[47] These reactions utilise good leaving groups at the α-position of **143**, and subsequent tautomerisation gives an acyl azolium intermediate **146**. However, no comment was made on why the triazolium catalyst **149** was favoured over thiazolium **148** and imidazolium **147**.

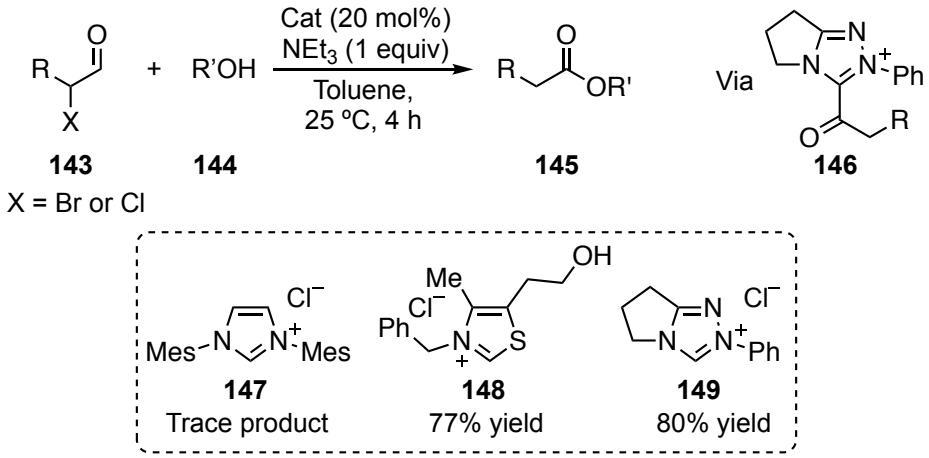

Scheme 25: Conversion of α-haloaldehydes into saturated esters.[47]

1.3 Mechanistic work

This section describes some of the mechanistic work which has been carried out on three steps of the benzoin condensation: (1) azolium deprotonation, (2) hydroxyaryl adduct formation and (3) BI formation and reaction.

1.3.1 Azolium ion deprotonation

In a typical NHC reaction, the reactive carbene is generated *in situ* with the aid of a base. Most of the pK_a data that exist for the major azolium scaffolds have been determined in DMSO or water, however, there is one example in THF.[48] The equilibrium pK_a values of thiazoliums,[49] imidazoliums[48,50,51,52] and triazoliums[53] have been determined in DMSO. Thiazolium salts have been shown to form the hydroxyl adduct and ring open in basic aqueous solution.[54] In addition, given the relatively high pK_a values found in DMSO, it has been necessary to determine kinetic pK_a values in aqueous solution. These have been determined for a range of thiazoliums,[55] imidazoliums[56,57] and triazoliums[58,59] salts. Mayr and co-workers have also studied the nucleophilicities of triazolium, imidazonium and imidazolium salts in THF at 20 ºC using a range of reference electrophiles.[60]

Previous work in the O'Donoghue research group has looked at the kinetic acidities of a range of triazolium precatalysts **150** to give NHC **151** (Scheme 26), which are particularly common in contemporary NHC-organocatalysis. Adopting methodology used by Jencks for a range of thiazolium salts,[55,61,62] and by Richard for a range of imidazolium salts,[57] an H/D exchange method was used to determine second order rate constants for deprotonation (k_{-p}) and these were used to estimate kinetic pK_a values.[58,59] The estimation was based on the assumption that reprotonation of the NHC (k_p) is limited only by the rate constant for solvent reorganisation.

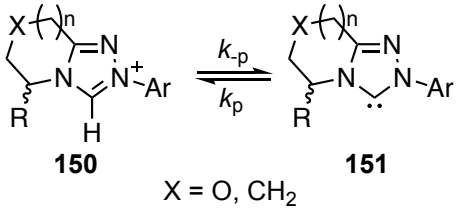

Scheme 26: Proton transfer equilibrium which involves deprotonation of triazolium salt to give triazolyldene.

Unexpected pD – log k_{ex} profiles were obtained for *ortho*-halo (**152 - 154**), *ortho*-pyrimidinyl (**158**) and *ortho*-pyridyl (**159**) triazolium salts. In addition to the mechanism of H/D exchange which is first order in deuteroxide ion above pD ~ 1, an

additional pathway of H/D exchange was observed which led to an upward bend in the pD – log k_{ex} profiles. A slight upward bend was also observed for N-4-fluorophenyl and N-4-cyanophenyl triazolium salts, however, this behaviour was not discussed. In the case of *ortho*-halo (**152** - **154**, Figure 3) and *ortho*-pyrimidinyl (**158**, Figure 4) triazolium salts, a mechanism that was proposed to be responsible for this kinetic behaviour was a protonation at N1 **157** at low pD which gives a more labile C(3)-H and leads to faster rate of exchange. It was suggested that N1 protonation was capable of reducing electrostatic repulsions between the lone pairs of electrons on N1 and the *ortho*-heteroatom substitutents on the N-aryl ring (**156**, Figure 3). In the case of the *ortho*-pyridyl triazolium salt (**159**, Figure 4), a mechanism was proposed which involved N1 protonation in conjunction with an intramolecular general base catalysis (GBC) role for the pyridyl substituent (**160** or **161**, Figure 4).

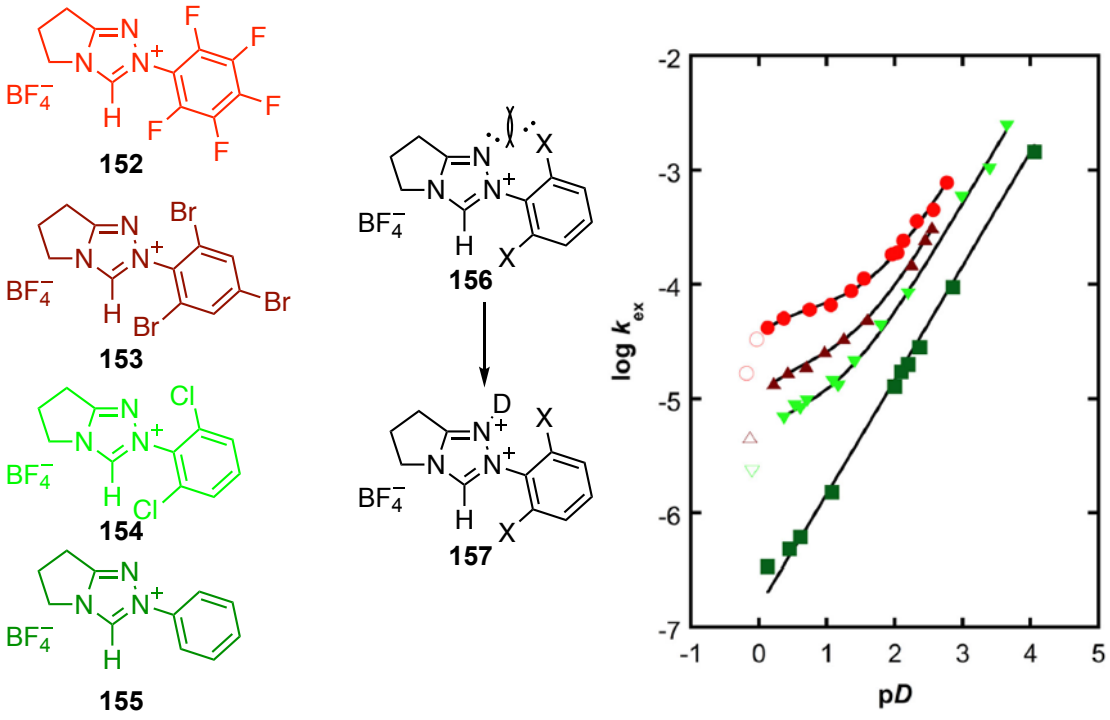

Figure 3: pD – log k_{ex} profile for a range of *ortho*-halogenated N-aryl substituents, with the profile for N-Ph shown for comparison.[58,59] (Reproduced with permission of Wiley publications. Copyright © 2014 John Wiley & Sons, Ltd)

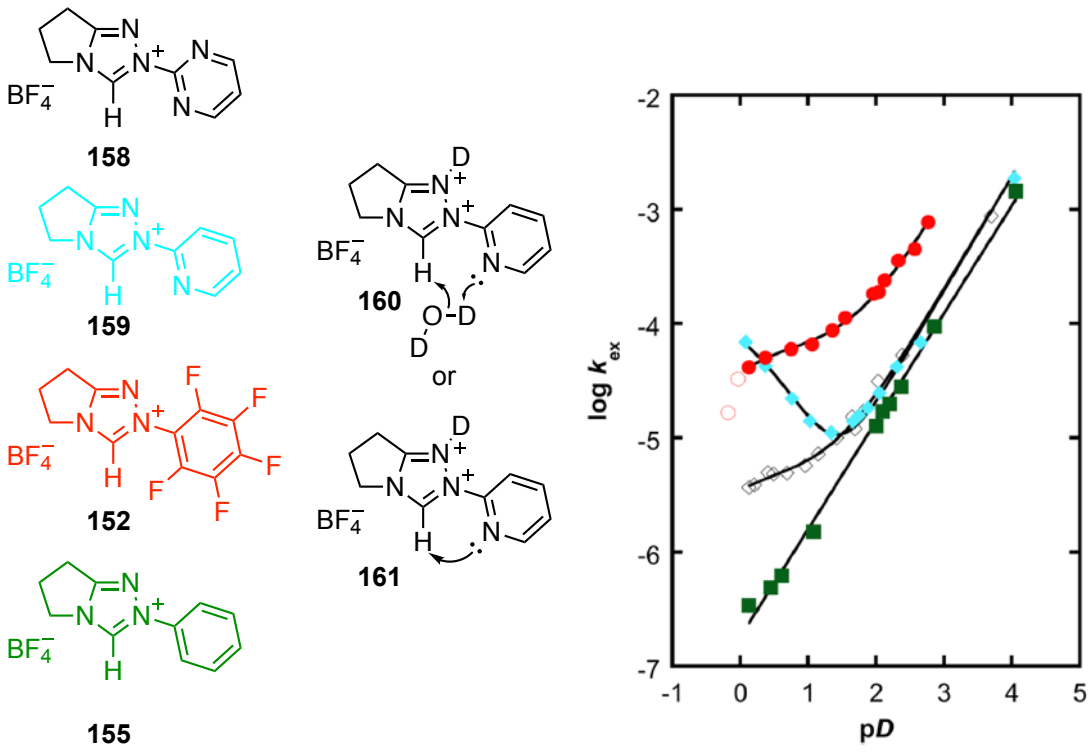

Figure 4: pD – log k_{ex} profile for N-pyridyl and N-pyrimidinyl substituents, with the profile for N-Ph and N-C_6F_5 shown for comparison.[58,59] (Reproduced with permission of Wiley publications. Copyright © 2014 John Wiley & Sons, Ltd)

The mechanistic implications of these behaviours on NHC-catalysis are not clear and require further study, but it has been shown that *ortho*-substituted N-aryl triazolium salt precatalysts are particularly favourable in catalysis. This leads to the first set of questions this thesis attempts to answer:

(1) What is the effect of *ortho*-oxygen substituents on the mechanism of C(3)-H/D exchange?

(2) What is the effect of a more basic *ortho*-pyridyl substituent on the acid-catalysed pathway for exchange, and what can we learn about N-pyridyl substituents in general?

(3) How do the N-aryl substituents affect the solid state dihedral angles between triazolium and N-aryl rings?

(4) What can DFT calculations tell us about the barriers for rotation of the N-aryl ring?

(5) What can the Hammett correlation tell us about the C(3)-H/D exchange mechanism?

1.3.2 Hydroxyaryl adduct formation

Breslow's postulated mechanism of the thiazol-2-ylidene-catalysed benzoin condensation[8] has been widely accepted and is used to rationalise product outcomes in new transformations.[4] The mechanism (Scheme 1) involves the initial attack of the NHC **4** on an aldehyde **5** to give, after proton transfer, a hydroxyaryl adduct **7**. Deprotonation of this adduct gives an enaminol **8**, usually termed the Breslow intermediate (BI). This key step inverts the reactivity of the aldehyde to yield a d^1-nucleophile.

However, the discovery that when thiazolium salts **163** are treated with base in non-aqueous solvents, they dimerise to give bis(thiazol-2-ylidenes) **165** (Scheme 27), given the name Wanzlick dimers,[63] has led to two alternative mechanisms of the benzoin condensation.

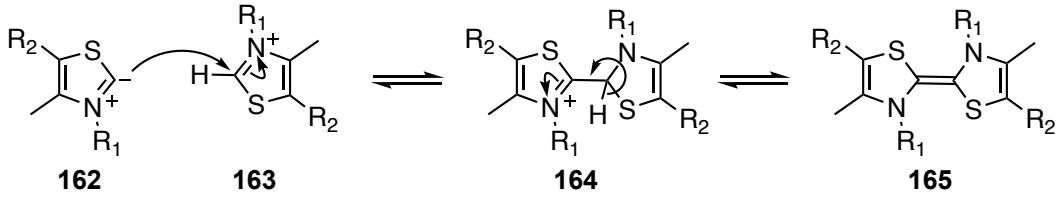

Scheme 27: Dimerisation of thiazolium salts in the presence of base in non-aqueous solvents.

Lemal suggested that attack of the nucleophilic enamine **166** upon the electrophile is followed by a fragmentation **167** to give hydroxyaryl adduct **169** and carbene **168** (Scheme 28).[64] The adduct **169** would then react onwards in the way proposed by Breslow.[8]

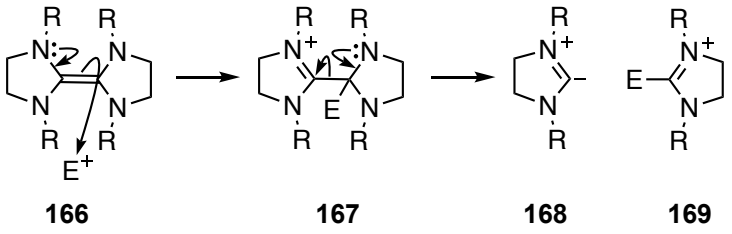

Scheme 28: Dissociation of dimer 166 to give adduct 169 and carbene 168.

Inspired by Lemal's work, López-Calahorra proposed an alternative mechanism,[65,66,67,68] where the adduct formed from the reaction of the bis(thiazol-2-ylidene) dimer with aryl aldehyde **170** does not fragment, but is deprotonated to give the reactive carbanion **171** (Scheme 29).

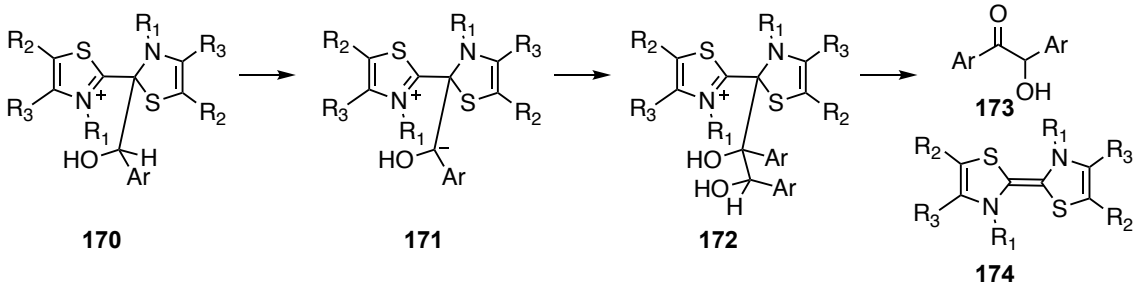

Scheme 29: Mechanism of benzoin condensation proposed by López-Calahorra, which goes via bis(thiazol-2-ylidene) dimer.[65-68]

Breslow strongly disagreed with López-Calahorra's mechanism and stated that data obtained for the benzoin condensation in DMSO from his laboratory,[69] and that of Pandit,[70] and even the data obtained by López-Calahorra[67] showed that the reaction is first order in thiazolium salt.[71] In addition, no dimer **174** was observed by NMR spectroscopy.[69] Formation of dimer **174** from thiazolium salt should have shown second order kinetics unless all of thiazolium salt had been completely converted to dimer **174**. Breslow also questioned the likelihood of the carbanion **171** formed from deprotonation of the adduct **170**, where resonance stabilisation is not possible (cf the BI, which is stabilised by resonance into the azolium ring). In light of these contentions, the community has favoured Breslow's mechanism given in Scheme 1.

The order of the thiazolyl-catalysed benzoin condensation in benzaldehyde has been reported to be first order,[72,73] second order[67,74,75,] or a mixture of both.[69]

Leeper[73] used initial rate studies at low catalyst concentration relative to benzaldehyde, to show that the benzoin thiazolylidene-catalysed benzoin condensation is first order in benzaldehyde over the concentration range 0.1 – 1.7 M. Experiments were also carried out at stoichiometric concentrations of thiazolium precatalyst. Concentration profiles showing the decrease in precatalyst and aldehyde, and the increase and subsequent decrease of the hydroxyaryl adduct as benzoin was formed were obtained by ^{1}H NMR spectroscopy. The overall finding of this work was that hydroxyaryl adduct formation, deprotonation and subsequent onwards reaction of the BI are all partly rate limiting.

Triazolylidene catalysis is widely reported in the literature, and attempts have been made to explain the efficiency of the triazolium scaffold, and the potential role of the N-aryl substituent. Bode and co-workers noted that, in a side by side comparison, N-mesityl imidazoliums **175** are favoured in reactions involving homoenolate intermediates whereas N-mesistyl triazoliums **176** are favoured in reactions involving acyl anion and enolate intermediates (Figure 5).[76]

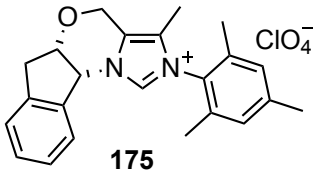

175

Imidazolium precatalyst: Favoured in homoenolate reactivity

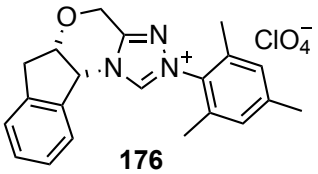

176

Triazolium precatalyst: Favoured in acyl anion and enolate reactivity

Figure 5: Comparison between N-mesityl imidazolium and triazolium salts in catalytic transformations.[76]

Bode and co-workers later attempted to rationalise the effects of the N-mesityl substituent (compared to N-pentafluorophenyl) and why relatively electron rich and sterically bulky N-mesityl triazolium salts are superior in reactions with enals. These authors concluded that (1) the formation of the hydroxyaryl adduct with enals is irreversible with N-mesityl triazolium salts and reversible with N-pentafluorophenyl salts and (2) sterically hindered N-aryl triazolium salts lead to relatively fast and irreversible formation of the BI due to relief of steric hindrance of the hydroxyaryl adduct.[77] However, no kinetic or equilibrium data was obtained and it is not clear whether there is a reduction in steric hindrance on formation of the BI or its relevance to the observed reactivity. It is also not clear how these authors concluded that the rate limiting step for the N-pentafluorophenyl triazolium salt is BI formation, whereas for the N-mesityl triazolium salt, the rate limiting step is onwards attack of the BI, without kinetic data.

The kinetics of the formation of hydroxyaryl adducts from triazolium precatalysts were studied previously within the O'Donoghue research group. Leeper's methodology[73] was used to study the reactions using catalytic[78] and stoichiometric[25,79] quantities of the triazolium salt precatalyst.

Under catalytic conditions, the benzoin condensation is (1) first order in triazolium salt precatalyst, (2) first order in benzaldehyde at low benzaldehyde concentrations (< 0.5 M) when triazolium salt concentration was 12 mM and (3) zero order in benzaldehyde at higher concentrations. These findings are consistent with rate limiting deprotonation and/or reaction of the BI.[78]

Under stoichiometric catalyst conditions, it was found that (1) equilibrium constants for the formation of hydroxyaryl adducts **179** (Scheme 30 and Table 1) are larger for *ortho*-substituted aryl aldehydes **178** than non-*ortho*-substituted aldehydes (2) equilibrium constants for the formation of hydroxyaryl adducts **179** (Scheme 30 and Table 1)) are

larger for *ortho*-substitued triazolium precatalysts **177** (3) rate constants for hydroxyaryl adduct formation **182** (Scheme 31 and Table 2) are greater for *ortho*-methoxybenzaldehyde **181** (R_1 = OMe, R_2 = H) than benzaldehyde using N-phenyl triazolium precatalyst **180**.[25,79]

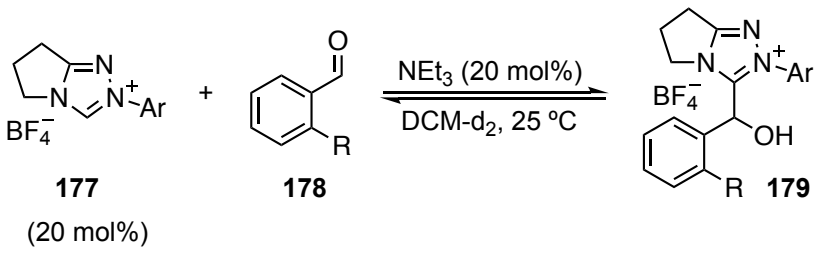

177 (20 mol%) **178** **179**

Scheme 30: Equilibria for hydroxyaryl adduct formation.[25]

Table 1: Equilibrium constants (*K*, M^{-1}) for hydroxyaryl adduct formation.[25]

Triazolium precatalyst	Aldehyde (R)	*K* / M^{-1}
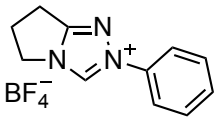	H	3
	OMe	56
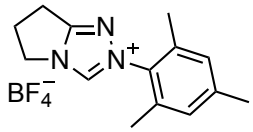	H	31
	OMe	143
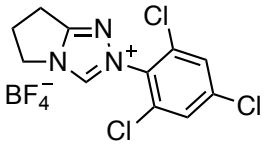	H	39
	OMe	601

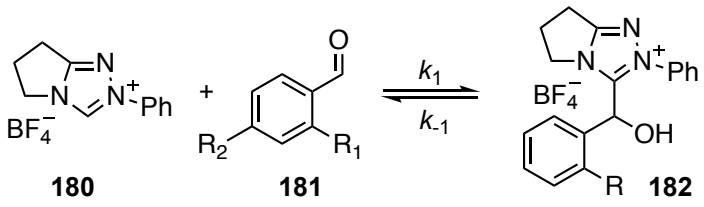

180 **181** **182**

(In triethylamine buffered CD_3OD at 25 ºC)

Scheme 31: Measurement of rate and equilibrium constants for hydroxyaryl adduct formation.[25]

Table 2: Measurement of rate and equilibrium constants for hydroxyaryl adduct formation.[25]

Aldehyde	k_1 / M^{-1} s^{-1}	k_{-1} / s^{-1}	*K* / M^{-1}
R_1 = H R_2 = H	1.33×10^{-2}	1.17×10^{-3}	11.4
R_1 = OMe R_2 = H	3.44×10^{-2}	2.92×10^{-4}	118
R_1 = H R_2 = OMe	2.86×10^{-3}	1.49×10^{-3}	1.92

In the context of cross-benzoin condensations,[17-24] these findings indicate that the product outcome is not determined by the initial adduct forming step. This leads to the second set of questions that this thesis attempts to answer:

(1) What is the effect of the triazolium N-aryl substituent on the rate and equilibrium constants for hydroxyaryl adduct formation/dissociation?

(2) What is the effect of the *ortho*-methoxy substituent in the reaction with a range of N-aryl triazolium salts?

1.3.3 Breslow intermediate formation

1.3.3.1 Studies related to enzyme catalysis

Prior to the intense interest in NHC organocatalysis that started about 20 years ago, the BI was of interest in the context of thiamine dependent enzyme catalysis and therefore much of the early work was centred on understanding the proton transfer from thiazolium salts.

Using irreversible iodination, combined with UV-vis spectrophotometry, Washabaugh reported pK_a estimates and a structure-reactivity relationship of N3-substituted thiazolium-based hydroxyaryl adducts **183**.[80,81] General base catalysis was observed and a Brønsted plot gave a slope of $\beta \geq 0.9$ which represents a late transition state where proton transfer is nearly complete. In the reverse direction, $\alpha = 0.1$, which represents diffusion controlled reprotonation of BI **184**.

These systems show a large inductive reaction constant of $\rho_I = 22 \pm 3$, which is consistent with a reaction involving the formation of a planar, delocalised BI rather than a localised carbanion (Figure 6). This is compared to reaction constants for C(2)-H/D exchange of a range of N3 substituted thiazolium salts **185**, which has a reaction constant of $\rho_I = 8.4 \pm 0.2$,[55] and detritiation of substituted acetylenes **187**, which has a reaction constant of $\rho_I = 8.0 \pm 0.5$.[82] These systems will contain a negative charge in a localised orbital (sp^2 and sp, respectively) that cannot delocalise into a π-system (Figure 6, **186** and **188**). No upward deviation in the Hammett correlation for proton transfer catalysed by phosphate dianion for less bulky R substituents suggest that delocalisation of the electrons from the carbon atom is independent of size of R.

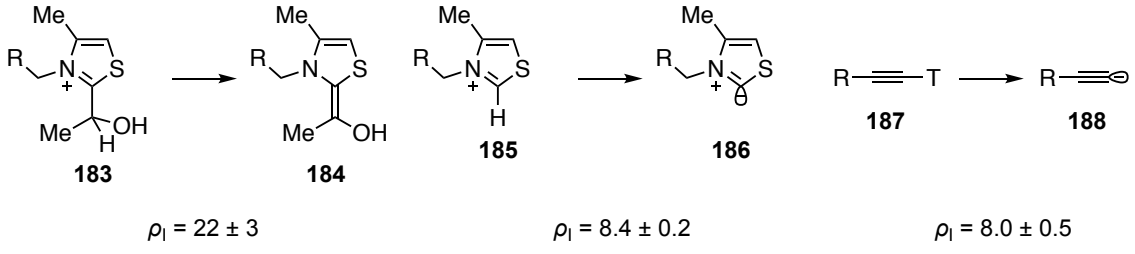

Figure 6: Hammett reaction constants for deprotonation and detritiation of carbon acids.

Since it was not possible to directly observe and measure the concentration of the BI **190** (Scheme 32), a pK_a was estimated using a ratio of rate constants for forward and reverse reactions.* Using the estimated value for the solvent-catalysed proton transfer, $k_{H2O} \leq 8.9 \times 10^{-11}$ s^{-1}, and the rate constant for diffusion controlled reprotonation by H_3O^+ (based on values obtained for reprotonation of amines and cyanide by H_3O^+), k_p = 2×10^{10} M^{-1} s^{-1},[83] a p$K_a \geq 20.4$ was estimated for this system.

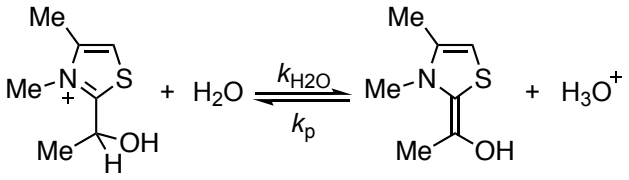

189 **190**

Scheme 32: Estimation of kinetic pK_a of hydroxyethyl adduct 189.[80]

Washabaugh also reported a proton transfer study of a thiazolium-benzaldehyde hydroxyaryl adduct **191** using a combination of ^{1}H NMR spectroscopy, detritiation and irreversible iodination (Scheme 33).[84] A pK_a of 15 ± 1 was estimated based on these data. GBC was observed and a Brønsted plot gave a slope of β = 0.95 which represents a late transition state where proton transfer is nearly complete. However, rate constants that were determined for reprotonation of **192** by buffer acids were independent of the pK_a of the buffer and well below the diffusional limit, at $k_{BH} = 10^{4\pm1}$ M^{-1} s^{-1}. This would suggest that the Brønsted β value was overestimated. Primary isotope effects of k_H/k_D = 1.5 ± 0.1 and k_H/k_T = 1.8 ± 0.1 were found, which obey the Swain-Schaad equation[85] with y = 1.5 ± 0.2.† The theoretical value expected for primary isotope effects, which are maximised when proton transfer is rate limiting, is 1.44. Clearly, proton transfer is at least partly rate-limiting, and this has been attributed to a requirement of the buffer acid to first desolvate. However, an alternative explanation, which the authors did not consider, is that in comparison with acetaldehyde-derived **189**, which may exhibit diffusion-controlled reprotonation, the phenyl ring may provide a more extended delocalised electron system that may reduce the kinetic basicity of **192**.

---

* $pK_a = -log\left(\frac{k_{H_2O}}{k_p}\right)$

† The Swain-Schaad equation is: $\log_{10}\left(\frac{k_H}{k_T}\right) = y \log_{10}\left(\frac{k_H}{k_D}\right)$ where $y = \frac{\left(\frac{1}{\mu_{CH}}\right)-\left(\frac{1}{\mu_{CT}}\right)}{\left(\frac{1}{\mu_{CH}}\right)-\left(\frac{1}{\mu_{CD}}\right)}$ and μ is the reduced mass of C-H, C-D or C-T bonds.

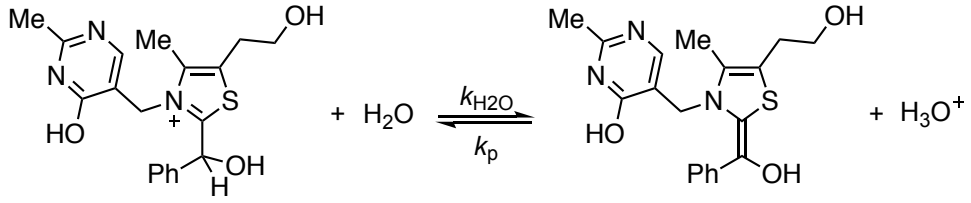

191 **192**

Scheme 33: Deprotonation of hydroxyethyl adduct based on oxythiamine.[84]

In 1997, Jordan and co-workers used stopped flow spectrophotometry to transiently generate the BI in aqueous solution from thiamine model compounds **196** (Scheme 35).[86] Model compounds were designed such that there was a methyl group at N3 and the hydroxyl group was protected as the methyl ether. The use of a methyl group at N3 reduces the number of hydrolysis reactions compared to thiamine **193**, which also undergoes intramolecular attack of nucleophilic exocyclic 4'-amino group on the pyrimidine ring at C(2).[87] Two pathways are known to exist for hydroxide ion-mediated ring opening of thiamine **193**: hydroxide ion attack at C(2) to form a hydrate followed by ring opening to give thiol **194**; and nucleophilic attack by the exocyclic 4'-amino group on the pyrimidine ring at C(2) which gives ring opened **195** (Scheme 34).[88] The use a methyl ether at the acidic carbon rather than a hydroxyl group prevents dissociation of the adduct to give the aryl aldehyde and thiazolylidene.

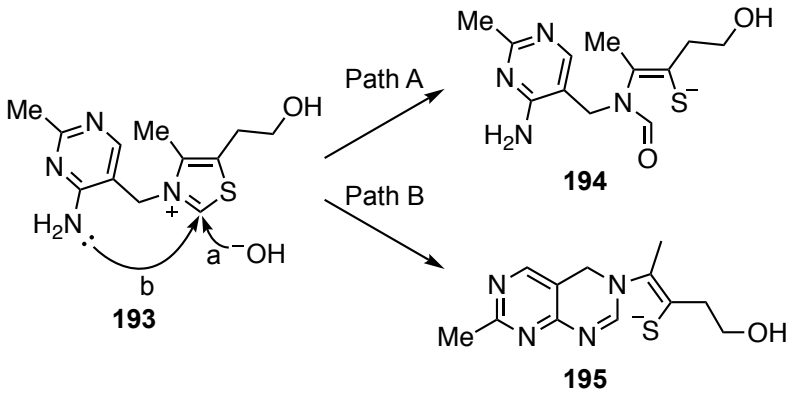

193

Scheme 34: Ring opening reactions of thiamine which may go via two pathways.[88]

The study was predicated on the estimate of the pK_a of the thiazolium (Scheme 33) of 15 ± 1 and therefore if the BI had a relatively large extinction coefficient, a small amount should be detectable in hydroxide solution near pH 14.

Following the addition of aqueous sodium hydroxide solution (not at constant ionic strength), the change in absorbance was monitored as a function of time for the reaction of thiazolium ion **196** (R = H). The progress curves in Figure 7 show the absorbance at 380 nm which was attributed to the formation and decay of the BI. The absorbance

increases at the beginning of the reaction in proportion to the addition of various concentrations of sodium hydroxide. A decrease in the absorbance is then observed, which was attributed to decomposition of **196** and reprotonation of BI **197**. The data were fitted to a series of rate equations to extract rate constants for deprotonation, reprotonation and decomposition. No other evidence was presented to confirm unambiguously that the absorbance traces were indeed due to a deprotonation followed by decomposition and reprotonation.

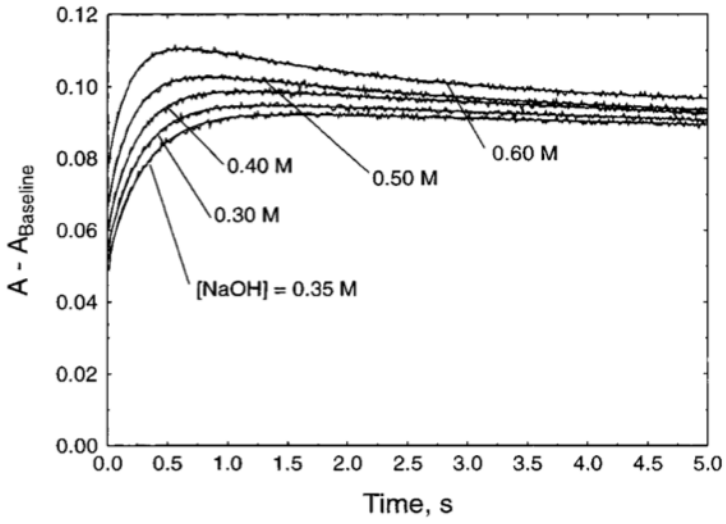

Figure 7: Change in absorbance for reaction of 196 (R = H, 3.40 mM) with aqueous sodium hydroxide at 25 °C.[86] (Reproduced with permission of ACS publications. Copyright © 1997 American Chemical Society).

A competing ring-opening reaction occurred and the ring opened product **198** was characterised by ^{1}H NMR spectroscopy. The decay in the absorbance trace (Figure 7) was partly attributed to the formation of this product (Scheme 35, k_3).

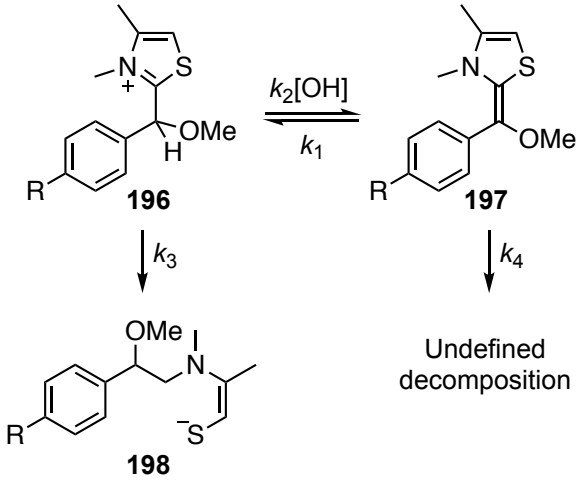

	R = H	R = $^{+}$NMe$_3$
k_1 / s^{-1}	1	300 - 540
k_2 / M^{-1} s^{-1}	0.019	18 - 42
k_3 / M^{-1} s^{-1}	0.5	3.4
k_4 / M^{-1} s^{-1}	7.11	-
pK_a	15.7	15.0 - 15.5

Scheme 35: Proposed kinetic model for proton transfer and decomposition with rate constants and a pK_a estimates of C(2α)-H where R = H and $^{+}$NMe$_3$.[86]

The proposed kinetic model for proton transfer and decomposition is shown in Scheme 35. The rate constants for deprotonation of the adduct **196** (k_2, M^{-1} s^{-1}), reprotonation of BI **197**, (k_1, s^{-1}), hydroxide ion dependent ring opening of the adduct **196** (k_3, M^{-1} s^{-1}), and decomposition of BI **197** to a product that was not characterised, (k_4, M^{-1} s^{-1}) are also shown in Scheme 35.

Three questions arise from these results: (1) why should the reverse protonation of the cationic R = $^{+}NMe_3$ substituted BI be ≥ 300 times faster than the neutral R = H BI? (2) Why is an undefined decomposition reaction of the neutral R = H BI required to give acceptable data fitting when the likely more reactive R = $^{+}NMe_3$ substituted BI would be predicted be more susceptible to decomposition? (3) How were the rate constants for decomposition and reprotonation pathways separated from the decrease in absorbance traces without independent analysis of the rate of decomposition?

To estimate the pK_a of C(2α)-H in both systems, the equation pK_a = pK_w – log (k_2 / k_1) was used, which combines the rate constant for hydroxide ion-dependent removal of the proton (k_2, M^{-1} s^{-1}) with the rate constant for the reverse reprotonation (k_1, s^{-1}) and the equilibrium constant for the autoionisation of water, $K_w = 10^{-14}$.

1.3.3.2 Studies related to organocatalysis

Berkessel[89] and co-workers attempted to generate the BI based on the triazolium ion scaffold **199** with propanal **200** (Scheme 36). In a 1:1 ratio of NHC:aldehyde, only the keto tautomer **201** of the BI was observed at equilibrium. This product was stable enough to be isolated by column chromatography. Attempts to generate a BI analogue **202** from the keto form **201** in the presence of base and silylating agent failed, only yielding silyl enol ether **203**.

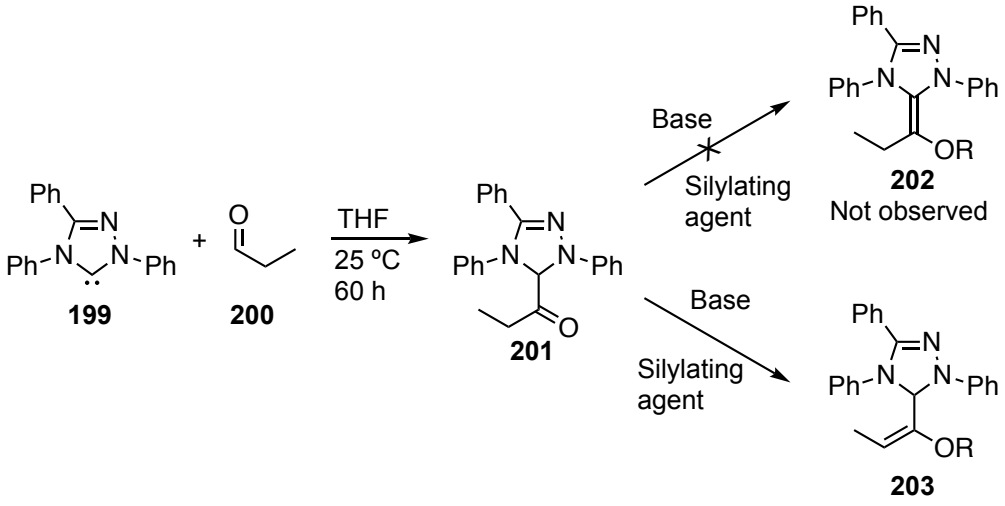

Scheme 36: Generation of the keto tautomer of the BI.[89]

Further attempts to generate the the keto tautomer were performed in the presence of a large excess of aldehyde relative to NHC (10:1). This led to the formation of a new species that was proposed to be spiro-dioxolane **205**. These authors suggested that this was a resting state in the acyloin condensation with a mechanism shown in Scheme 37.[89]

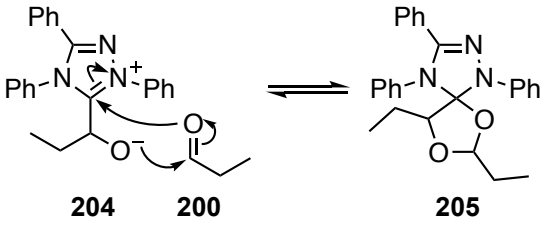

Scheme 37: Mechanism of spiro-dioxolane formation proposed by Berkessel and co-workers.[89]

Rovis and co-workers isolated aza-BI analogues **208** and **210** (Scheme 38) after reacting N-tribromophenyl triazolium salt **206** and either iminium ion **207** (to give aza-BI **208**) or iminium ion **209** (to give aza-homoenolate **210**).[90]

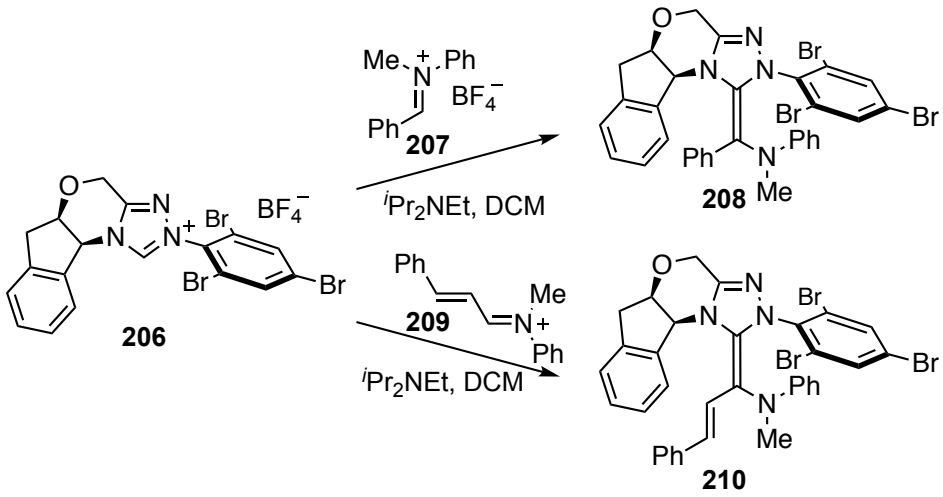

Scheme 38: Formation and isolation of aza-BI and aza-homoenolates by Rovis and co-workers.[90]

The aza-BI **208** was reacted with aldehyde **211**, yielding the intramolecular Stetter product **212** (Scheme 39), demonstrating the reversibility of aza-BI formation (**208** - **206'**). However, these results do not prove the catalytic relevance of this type of intermediate.

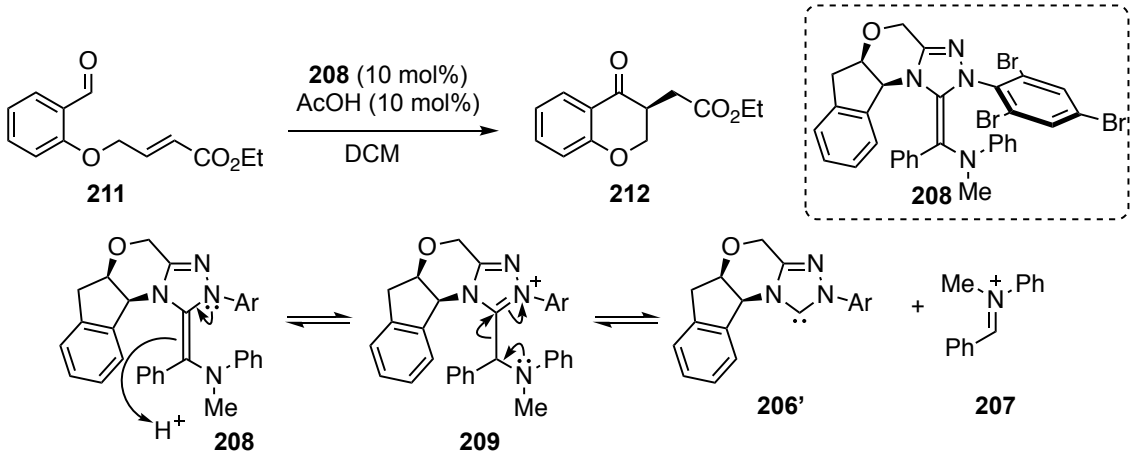

Scheme 39: Catalytic activity of aza-BI involves initial dissociation to give NHC 206' which participates in the intramolecular Stetter reaction.[90]

Berkessel and co-workers reported the generation and reaction of BIs and showed them to be catalytically relevant.[91] They reasoned (Figure 8) that using a saturated NHC, greater stability could be imparted in the reactive intermediate. Using an unsaturated imidazolium system, attack of BI **213** on an electrophile was thought to return the aromaticity to the imidazolium ring (**214**). In the case of a saturated system (**215**), re-aromatisation is not possible (**216**). A range of BIs **219** were prepared by mixing NHC **217** with an equal amount of a range of aldehydes **218** in anhydrous THF with rigorous exclusion of oxygen.

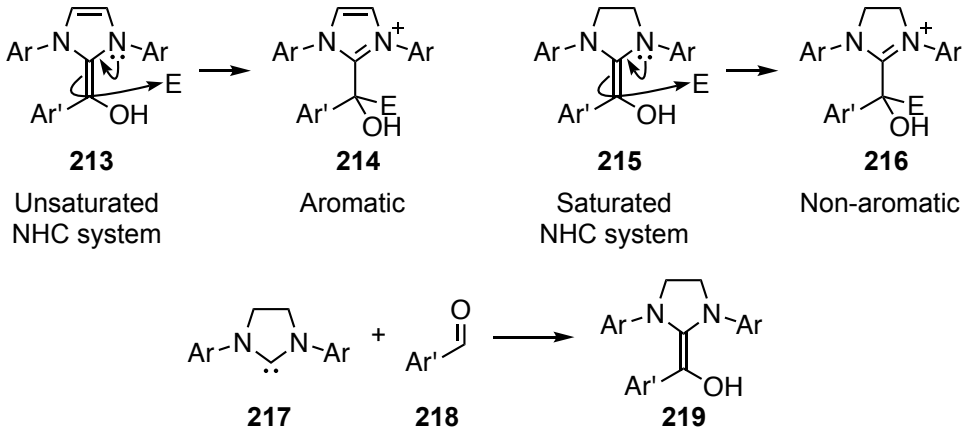

Figure 8: Formation of BIs from saturated imidazolinylidene NHCs.[91]

The catalytic relevance of this intermediate was demonstrated by mixing BI **220** with aldehyde **223** (Scheme 40). These authors had independently made BI **224** from aldehyde **223**, and so could observe by NMR spectroscopy the rapid equilibration between BIs **220** and **224**. Interestingly, these results showed that BI **224** was favoured compared to **220** but, in addition to the trace of homo-coupled benzoin product **226**, only cross product **225** was obtained. This result has significant implications for the

control of chemoselectivity in cross benzoin condensations as it demonstrates that onwards attack of the BI could determine the product outcome. However, it is not clear (1) why the BI **224** is favoured over unsubstituted **220**; (2) why the BI **220** attacks **223** to give the cross product **225** and (3) why only trace homo-coupled benzoin **226** is observed.

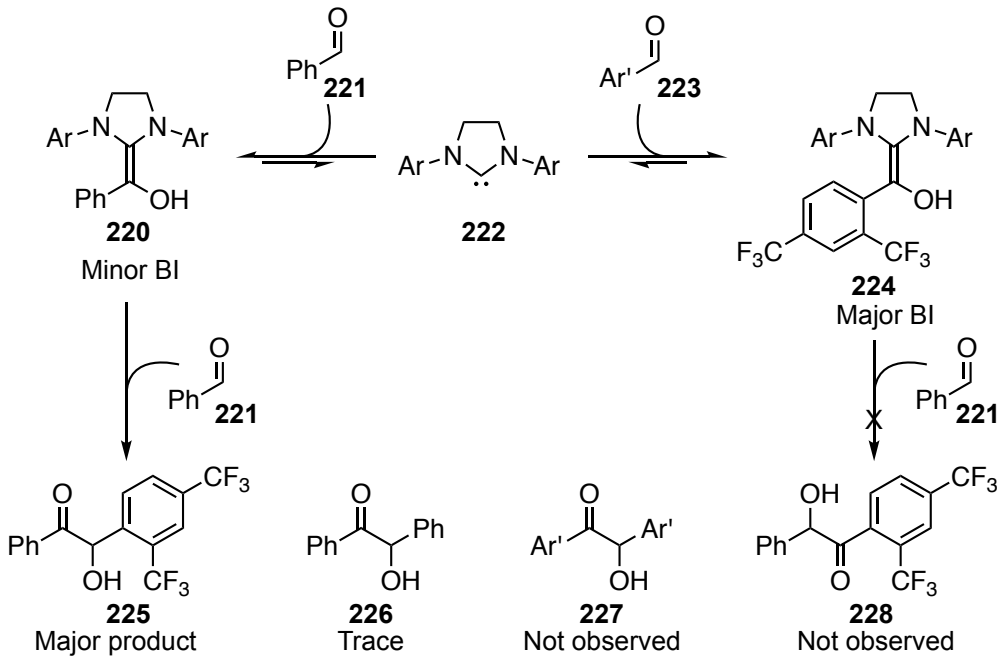

Scheme 40: Catalytic activity of BI 220 in the presence of aldehyde 223 to give 225 as the major cross product.[91]

Also in 2012, during a Master's research project within the O'Donoghue research group, Maguire[92] studied a methylated adduct **229**, derived from an N-phenyl-substituted triazolium ion (Scheme 41). Adopting the methodology used by Jordan, stopped flow UV-vis spectrophotometry (not at constant ionic strength) showed an absorbance increase at a longer wavelength than the starting material which could be consistent with BI **230**. However, uncharacterised side reactions, which may include ring opening of the triazolium ring,[93] meant that an accurate pK_a could not be determined.

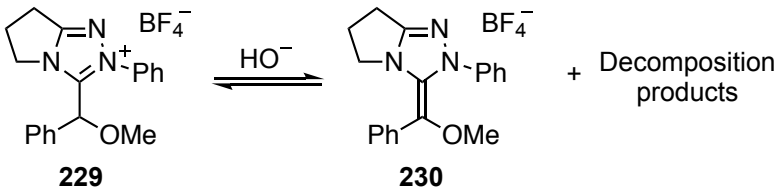

Scheme 41: Attempts to generate O-methylated BI from triazolylidene scaffold by stopped flow UV-vis spectrophotometry.[92]

Mayr[94] studied the nucleophilicities of a range of BIs derived from thiazolium, imidazolium and triazolium scaffolds. O-Methylated BI analogues **231** – **234** (Figure 9) were prepared by deprotonation of the O-methylated hydroxyaryl adducts using NaH and catalytic KO^{t}Bu in anhydrous THF. Evaporation of the solvent and extraction into anhydrous toluene yielded O-methylated BIs based on thiazolium **231** and **232**, imidazolium **233** and triazolium **234** systems. These systems could be stored in an argon glovebox at – 30 °C for several weeks. The nucleophilicities of these systems were studied using stabilised benzhydrylium ions, which are reference electrophiles that Mayr and his group have used extensively, to present a reactivity scale. Using an excess of nucleophile under anhydrous conditions, the absorbance change of the reference electrophile was followed using stopped flow UV-vis spectrophotometry. Relative reactivities of the O-methylated BIs are shown in Figure 9. While these studies are informative, no electrophiles that are synthetically relevant to NHC catalysis were studied.

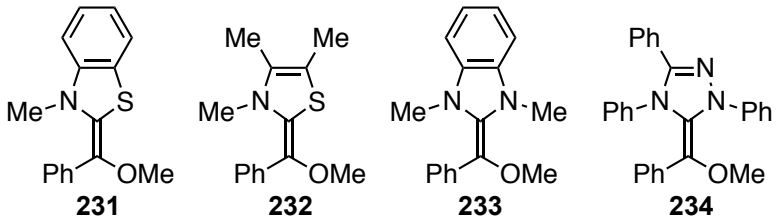

Figure 9: Mayr's scale of relative nucleophilicities of O-methylated BIs derived from various NHC scaffolds.[94]

In 2013, Berkessel and co-workers reported the X-ray crystal structures of three acyl anion BIs **235** – **237**, one homoenolate BI **238** and three azolium enolates **239** – **241** (Figure 10).[95] These structures demonstrate interesting structural characteristics: (1) R groups attached to the NHC scaffold lie nearly perpendicular to the plane of the NHC ring and (2) the dihedral angle (abcd) is relatively insensitive to the substituents on the aryl ring.

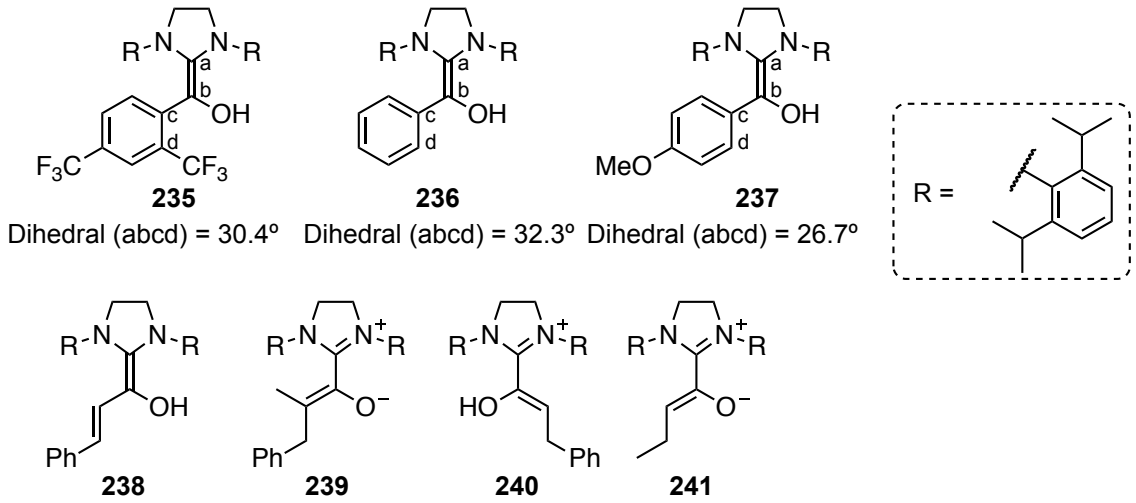

Figure 10: X-ray crystal structures obtained for three acyl anion BIs, two homoenolate BIs and two azolium enolates.[95]

These workers also studied the onwards reactions of the preformed homoenolates **238** with benzaldehydes **242** to give γ-butyrolactone **243**, and preformed azolium enolate **244** with enone **245**, to give γ,δ-unsaturated δ-lactones **246** (Scheme 42).[96]

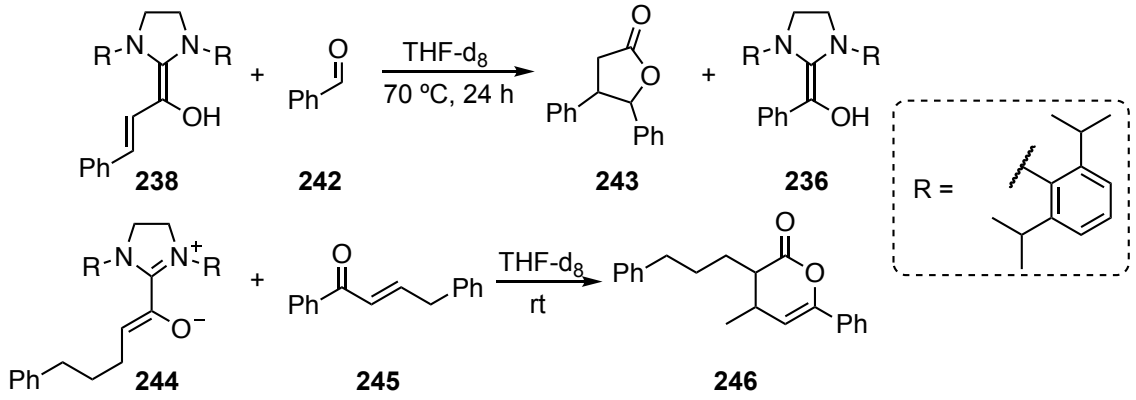

Scheme 42: Reactions of preformed homoenolate 238 and azolium enolate 244.[96]

Berkessel and co-workers reported, in 2016, new *ortho*-alkyl substituted triazolium salt precatalysts **250a** and **250b** that were capable of catalysing the recalcitrant redox esterification of α- and β-substituted α,β-enals **247** (Scheme 43). The authors attributed the success of the new precatalysts to the stabilising dispersion interactions between *ortho*-alkyl substituents and the enol of the BI.[97,98] This is likely a consequence of the large dihedral angles between *ortho*-substituted N-aryl and the azolylidene rings.

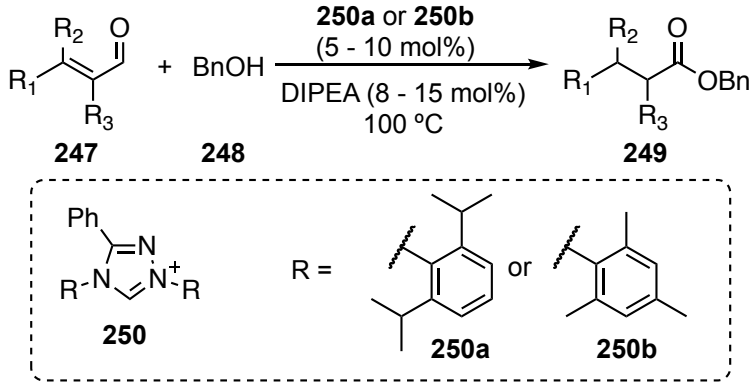

Scheme 43: Development of *ortho*-alkyl substituted triazolium salts for the challenging redox esterification of α- and β-substituted α,β-enals.[96]

Using double ^{13}C labelling experiments, Berkessel and co-workers were recently able to identify, by NMR spectroscopy, the BI based on the unsaturated benzimidazolylidene **251** (Figure 11) and thiazolylidene **254** (Scheme 44).[99] The benzimidazolylidene **251** was proposed to stabilise the enol of the BI through dispersion interactions with the *ortho*-alkyl substituents. An X-ray crystal structure was obtained for the benzimidazolylidene BI with Ar = 2,4-bis-trifluoromethylphenyl, and demonstrates that the nucleophilicity of this BI is likely to be sterically hindered by the *ortho*-CF_3 substituent.

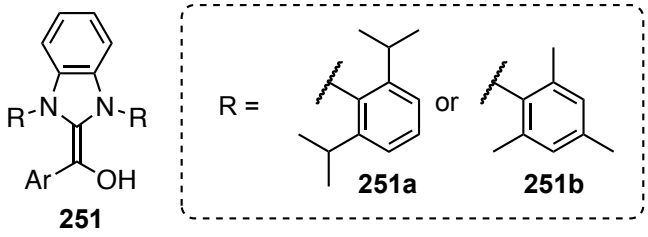

Figure 11: BI based on benzimidazolylidene scaffold, with *ortho*-alkyl N-aryl substituents which are proposed to stabilise the BI through dispersive interactions with the enol.[99]

In the case of the thiazolylidene BI, using an *ortho*-alkyl N-aryl substituent failed to yield the BI. However, using the N-methyl-substituted thiazolylidene, with a ^{13}C label at C2, these authors demonstrated that dimer **252** is formed, and in the presence of electron withdrawing aldehyde **253**, gives the desired BI **254** (Scheme 44).

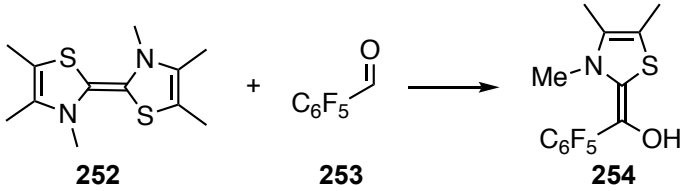

Scheme 44: Formation of the BI derived from N-methyl substituted thiazolylidene, starting from dimer 252.[99]

These studies represent the state of the art in terms of our understanding of BI formation and reaction. However, the third set of questions this thesis attempts to answer are:

(1) Is it possible to determine a pK_a of the conjugate acid of the BI based on triazolium salt precatalysts?
(2) What are the *ortho*-substituted-aldehyde effects in the formation and reaction of the BI?

1.4 Summary and aims

The foregoing examples in section 1.2 demonstrate that NHCs show great promise as tunable, highly selective (chemo, regio and stereo), efficient organic catalysts in umpolung and normal reactivity. The benzoin condensation has served as a test bed for designing new catalysts, however, the focus of more recent literature is the application of NHCs to the discovery of new reactions. In this regard, screening based approaches are still common because it is not entirely clear how the structures of both the N-aryl ring and aldehyde substrate affect reactivity.

This thesis describes attempts to understand how *ortho*-substituents on both the N-aryl ring and aryl aldehyde affect selectivity, and has direct implications for the understanding of crossed benzoin condensations and also the choice of current and design of new catalyst systems.

Chapter 2 describes (1) the effect of *ortho*-substituents on the N-aryl ring in the triazolium deprotonation step, (2) the effect of *ortho*-substituents on the N-aryl ring on the solid state structure and (3) the use of DFT calculations and Hammett analysis to determine the structural features that favour a rapid deprotonation step.

Chapter 3 describes (1) the effect of *ortho*-substituents on the N-aryl ring in the hydroxyaryl adduct forming step, (2) the effect of an *ortho*-methoxy substituent in the hydroxyaryl adduct forming step and (3) the use of Hammett analysis to determine the structural features of the NHC and the aryl aldehyde that favour hydroxyaryl adduct formation.

Chapter 4 describes (1) the effect of *ortho*-substituents on the N-aryl ring in the BI forming step and (2) attempts to quantify the rate constant of reprotonation of the BI derived from the most hydrolytically stable adduct.

Chapter 2: Triazolium ion deprotonation

2.1 Aims

Pseudo first order rate constants for C(3)-H/D exchange of four *ortho*-heteroatom N-aryl triazolium salts were obtained (Figure 12). H/D exchange kinetics provide not only kinetic acidities and pK_a estimates, but also straightforward probes to quantify and mechanistically assess *ortho*-substituent effects. Data for *ortho*-pyridyl triazolium **258** was reported previously, but additional data points are described here and the kinetic fittings and mechanisms are re-evaluated. To further inform catalyst design, X-ray crystal structures for a wide range of triazolium salts were obtained, and Hammett correlations and DFT calculations were used to assess the effect of N-aryl substituents on proton transfer (Figure 13). These data provide clear insight into the inherent electronic and steric substituent effects, that could aid future catalyst design.

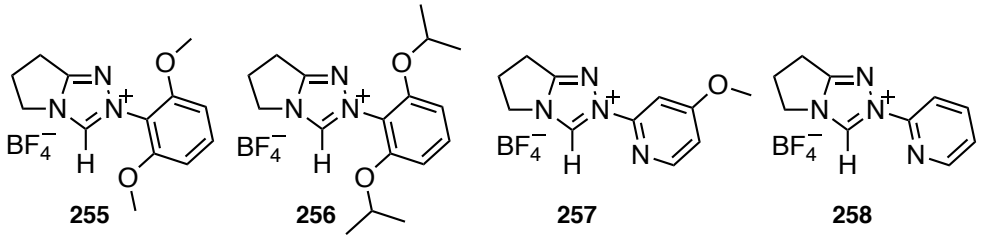

Figure 12: Triazolium salts studied in C(3)-H/D exchange kinetics.

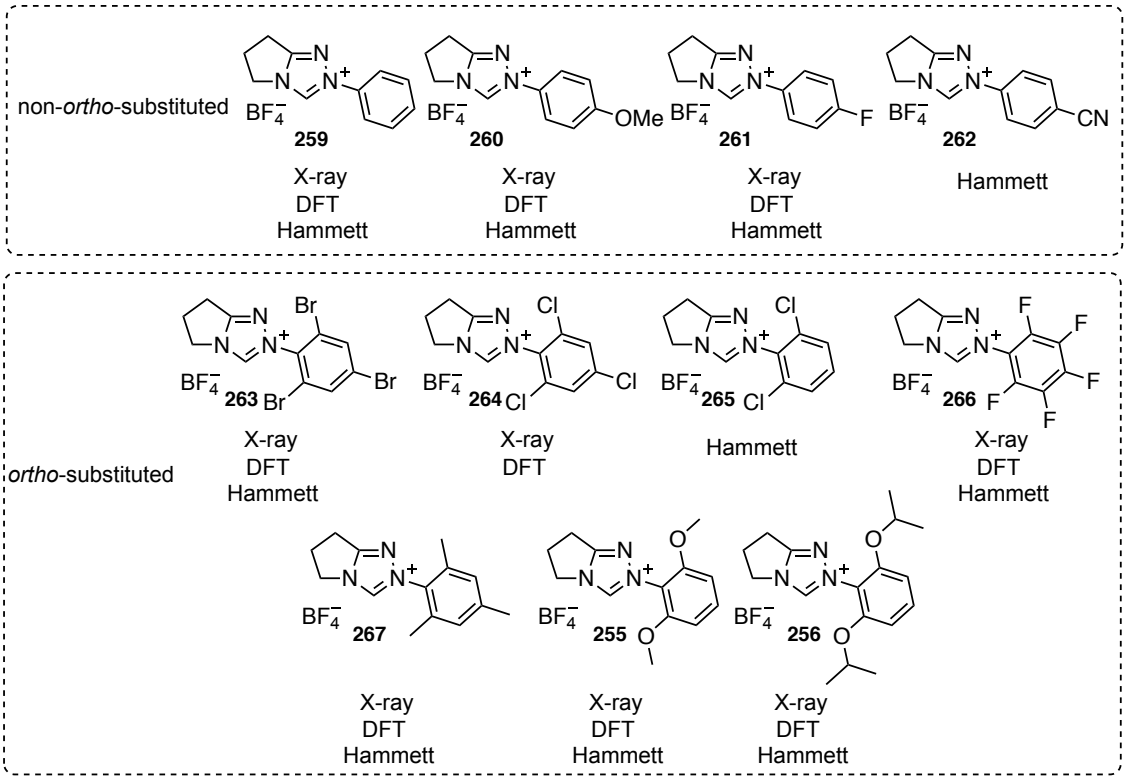

Figure 13: The range of triazolium salts that were crystallised and analysed by DFT calculations and Hammett correlations.

2.2 Results and discussion

2.2.1 Synthesis of triazolium Salts

The general strategy for preparing triazolium salts used in this study is shown in Scheme 45. Methylation of 2-pyrrolidone **268** with Me_3OBF_4 in anhydrous DCM overnight gave amidate **269**. Formation of amidrazones **272** required either aryl hydrazines **271** or aryl hydrazinium chlorides **270** (which were neutralised and extracted into organic solvent). The formation of amidrazones **272** was monitored by LCMS. Once the aryl hydrazine **271** had been consumed, the solvent was removed under reduced pressure and amidrazone **272** was used in the next step without purification. Refluxing amidrazone **272** in $CH(OEt)_3$ gave cyclised triazolium salts **273** which was monitored by LCMS. Evaporation of the solvent followed by either precipitation with ethyl acetate/diethyl ether or column chromatography using DCM/MeOH gave triazolium salts **273**. The yields of triazolium salts over the three or four steps starting from 2-pyrrolidinone **268** are shown in Table 3.

In the case of *ortho*-alkoxy and *ortho*-pyridyl salts **255** – **257**, aryl hydrazines were not commercially available and the synthesis of these hydrazine precursors are described in sections 2.2.1.1 and 2.2.1.2.

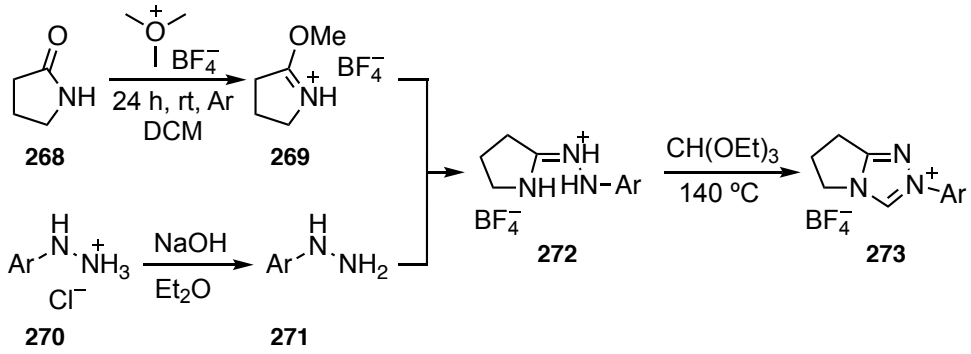

Scheme 45: General strategy for preparation of triazolium salts 273.

Table 3: Yields of triazolium salts starting from 2-pyrrolidone 268.

Triazolium salt	Yield	Triazolium salt	Yield
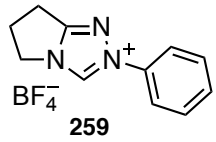 **259**	55%	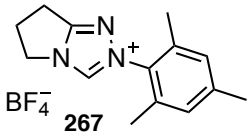 **267**	35%
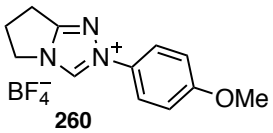 **260**	48%	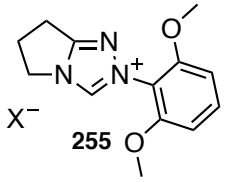 **255**	8% (X = Cl) 11% (X = BF_4)
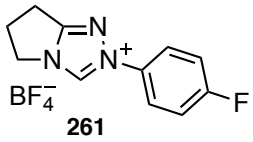 **261**	42%	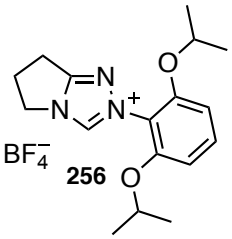 **256**	13%
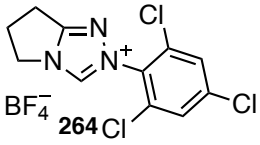 **264**	22%	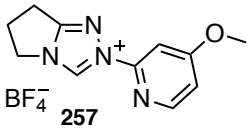 **257**	6%
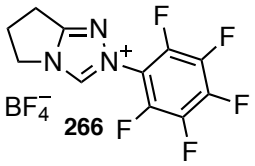 **266**	49%		

2.2.1.1 Precursor for *ortho*-alkoxy triazolium salts

Initially, attempts were made to diazotise 2,6-dimethoxyaniline **274** followed by *in situ* reduction of the intermediate diazonium salt **275,** to give the required aryl hydrazinium chloride **276** (Scheme 46). A number of conditions were used (see Appendix 1), which were adapted from the synthesis of 2,6-dimethylphenyl hydrazine from 2,6-dimethylphenyl aniline.[100,101] However, there was no evidence for the formation of aryl hydrazinium chloride **276** and an alternative strategy was used.

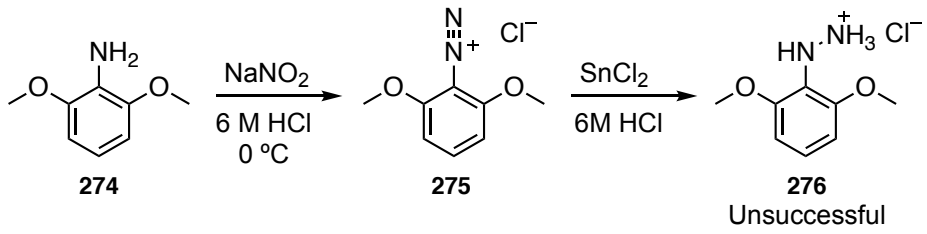

274 **275** **276**
Unsuccessful

Scheme 46: Unsuccessful diazotisation of 2,6-dimethoxyaniline in the attempted synthesis of 2,6-dimethoxypheyl hydrazinium chloride.

In light of the diazotisation strategy being unsuccessful, a route via a Boc-protected hydrazine was explored (Scheme 47).[36,102] Lithiation of 1,3- dimethoxybenzene **277** (where R = Me) followed by the addition of di-*tert*-butyl diazo-1,2-dicarboxylate (DBAD), quenching with AcOH and flash column chromatography gave the protected aryl hydrazine **278** (where R = Me) as a white solid following slow evaporation of ethyl acetate. The mixture exists as an approximately 1.8:1 mixture of rotamers. This is confirmed by ^{1}H-^{1}H EXSY NMR spectroscopy, and is in agreement with the literature.[36]

This method worked equally well for the 2,6-diisopropoxy-substituted Boc-protected aryl hydrazine **278** (R = ^{i}Pr in Scheme 47), which was purified by column chromatography to give a yellow oil.

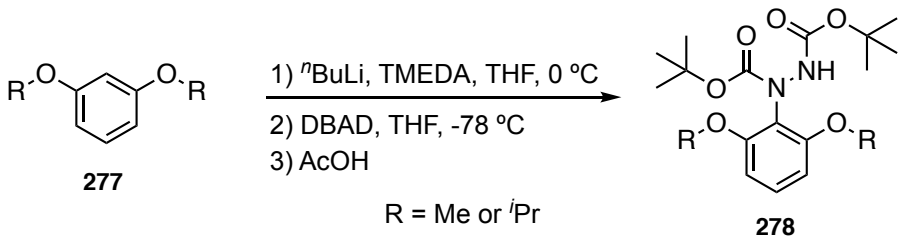

Scheme 47: Synthesis of Boc-protected aryl hydrazine from 1,3-dialkoxybenzene.

Removal of the protecting groups was achieved under anhydrous conditions by stirring the Boc-protected hydrazine **278** with HCl (4 M in 1,4-dioxane) in methanol for 4 h at room temperature. The solvent was evaporated to give the hydrazine hydrochlorides **270**, which were used in the next step without purification (Scheme 48), where conversion to the hydrazinium chloride was confirmed for both R = Me and ^{i}Pr, by LCMS.

For the synthesis of the N-2,6-dimethoxyphenyl triazolium salt **255**, the method initially followed was Glorius' procedure (Scheme 48).[36] This method involved neutralising amidate **269** to give imino ether **279**, and adding hydrazinium hydrochloride **281** directly to imino ether **279**. The resulting triazolium salt **283** had a chloride, rather than a tetrafluoroborate counterion, and was purified by column chromatography.

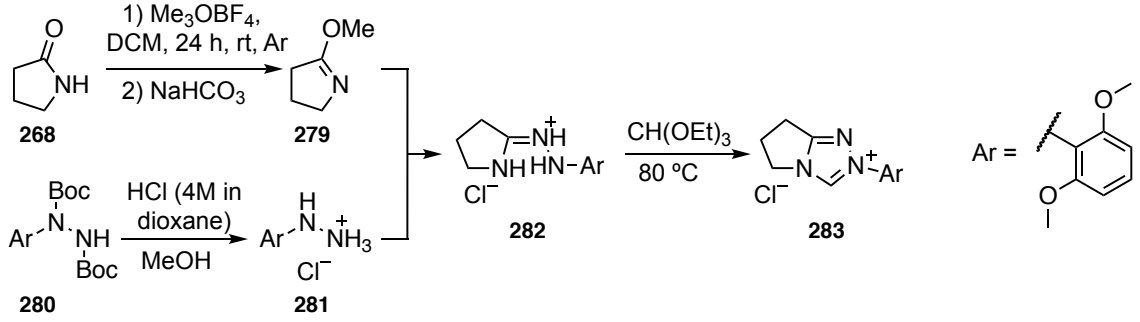

Scheme 48: Synthesis of the chloride salt of the N-2,6-dimethoxyphenyl triazolium salt.

The low yield and challenging column purification[‡] then led to the study of the instability of the 2,6-dimethoxyphenyl hydrazine. To determine approximately how unstable the deprotonated dimethoxyphenyl hydrazine was, a mixture of one equivalent of NaOH (relative to the hydrazinium chloride) and DCM-d_2 were added to the hydrazine hydrochloride. The DCM layer was separated and a ^{1}H NMR spectrum was obtained. The sample was left in the NMR tube for a further 19 h in a thermostated water bath at 25 ºC and another ^{1}H NMR spectrum was obtained. The aryl region of the ^{1}H NMR spectrum of the hydrazine is shown in Figure 14. After 19 h, a decrease in the triplet signal due to the aromatic *para* proton at 6.95 ppm is accompanied by an increase in a triplet signal at 7.21 ppm. The free aryl hydrazine has an approximate half-life of $t_{1/2}$ ~ 36 h. Although the free hydrazine is more unstable than the HCl salt, it appeared to be sufficiently stable on the timescales of our attempted transformations.

In order to facilitate chromatography, the syntheses of triazolium salts where R= Me and ^{i}Pr were adapted – the hydrazinium chloride **281** was neutralised and added directly to amidate **269** as shown in Scheme 45, yielding the BF_4 salt. Column chromatography of the final product was easier with the less charge dense counter ion. The yields obtained were still low but are an improvement on Glorius' method.

[‡] The more charge dense chloride counterion leads to a more deshielded C(3)-H proton in $CDCl_3$ and lower R_f on silica, compared to the less charge dense tetrafluoroborate counterion.

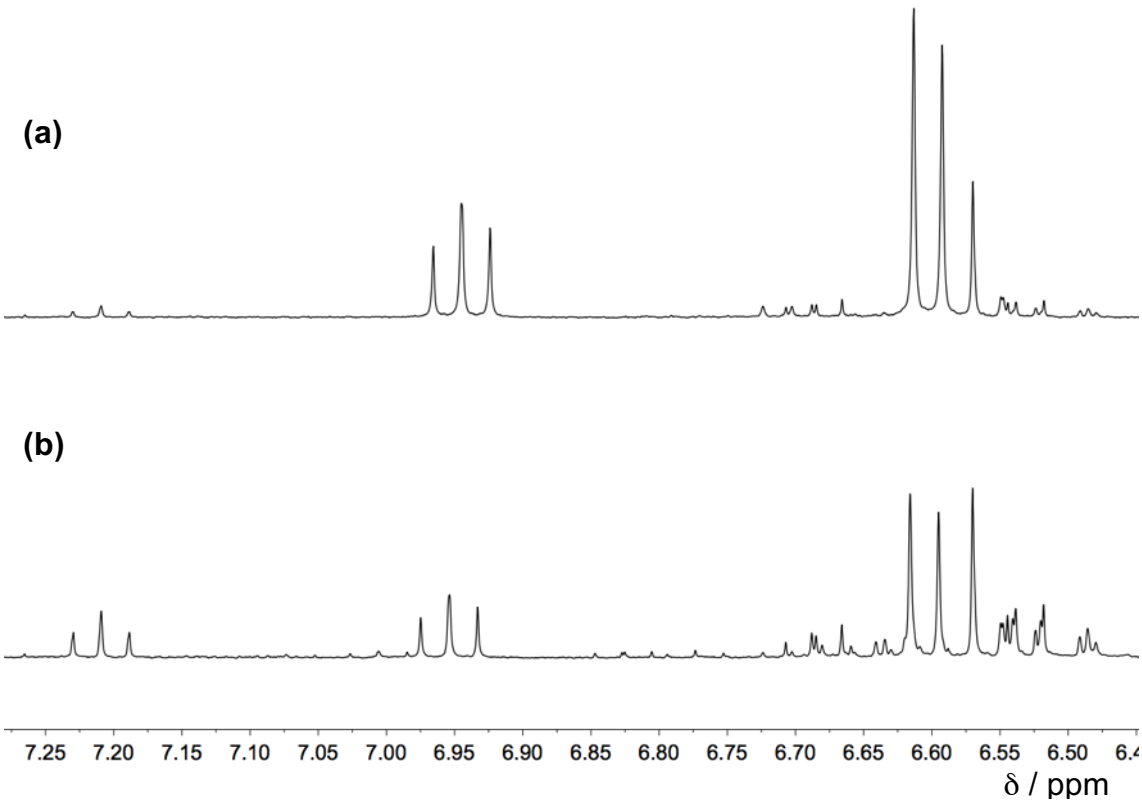

Figure 14: ^{1}H NMR spectra in DCM-d_2 of the aromatic region of 2,6-dimethoxyphenylhydrazine showing the decomposition of the deprotonated hydrazine. The spectra were taken (a) shortly after extraction of the neutralised hydrazinium salt into DCM-d_2 and (b) after 19 h at 25 ºC.

2.2.1.2 Precursor for more basic *ortho*-pyridyl substituent

To gain insight into the mechanism of C(3)-H/D exchange observed for N-pyrid-2-yl triazolium salt **258**,[59] the aim was to prepare a triazolium salt with an N-pyridyl ring bearing an electron donating substituent. For this, the synthesis of a pyridyl hydrazine with an electron donating substituent attached was required. Initially, attempts were made to carry out a nucleophilic aromatic substitution upon 2-chloro-4-methoxypyridine **284** with hydrazine monohydrate (Scheme 49). This method is reported to work well for more activated aromatic rings, such as 2-chloropyridine[103] and 2-chloropyrimidine,[59,104] but there are no reports of this transformation upon less S_NAr activated systems. The details of these attempts are shown in Table 4. It is clear that the pyridine is not electrophilic enough for this reaction, with only a trace of product being observed under forcing conditions (entries 4 and 6).

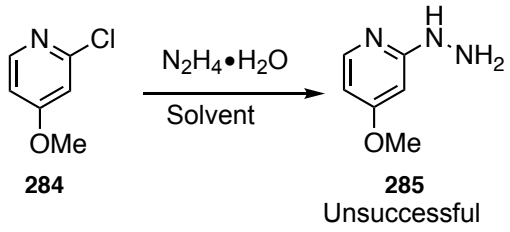

Scheme 49: Attempted synthesis of 2-hydrazino-4-methoxypyridine 284 by nucleophilic aromatic substitution.

Table 4: Summary of conditions employed for the attempted synthesis of 2-hydrazino-4-methoxypyridine 285 by nucleophilic aromatic substitution.

Entry	Conditions	Observations
1	$N_2H_4 \bullet H_2O$ (10 equiv) Solvent: EtOH (c = 0.2 M), T = 80 ºC	No reaction
2	$N_2H_4 \bullet H_2O$ (10 equiv) Solvent: EtOH (c = 0.2 M), T = 100 ºC	No reaction
3	$N_2H_4 \bullet H_2O$ (10 equiv) Solvent: EtOH (c = 1 M), T = 80 ºC	No reaction
4	$N_2H_4 \bullet H_2O$ (10 equiv) Solvent: EtOH (c = 1 M), T = 100 ºC	Trace product observed by ESI-MS
5	$N_2H_4 \bullet H_2O$ (10 equiv), Neat T = 80 ºC	No reaction
6	$N_2H_4 \bullet H_2O$ (10 equiv), Neat T = 100 ºC	Trace product observed by ESI-MS

One possible solution to the low reactivity of electron rich chloropyridine **284** is to use a more electrophilic nitro-substituted chloropyridine, followed by reduction of the nitro group with H_2 and Pd/C which would yield an electron rich amino substituted hydrazinopyridine. Following literature procedures, 2-hydrazino-3-nitropyridine **287**[105,106] and 2-hydrazino-5-nitropyridine **290**[107] were prepared in 88% and 76% yield, respectively (Scheme 50). For each compound, it was possible to reduce the nitro group to an amino group using H_2 and Pd/C, where ESI-MS was used to monitor the reaction.

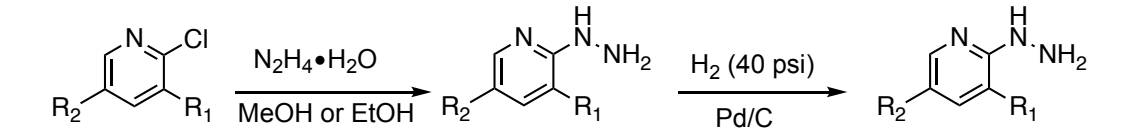

286 ($R_1 = NO_2$, $R_2 = H$) **287** ($R_1 = NO_2$, $R_2 = H$) **288** ($R_1 = NH_2$, $R_2 = H$)

289 ($R_1 = H$, $R_2 = NO_2$) **290** ($R_1 = H$, $R_2 = NO_2$) **291** ($R_1 = H$, $R_2 = NH_2$)

Scheme 50: Preparation of 2-hydrazino nitro- and amino-pyridines.

Attempts to prepare the triazolium salts from either aryl hydrazine derived from nitropyridine or 2-hydrazino-5-aminopyridine (Scheme 51) were unsuccessful. In each case, it was possible to generate the amidrazone **272**, but either a small conversion (< 5%) or an inability to purify the ring-closed product by precipitation or column chromatography meant that each synthesis was unsuccessful.

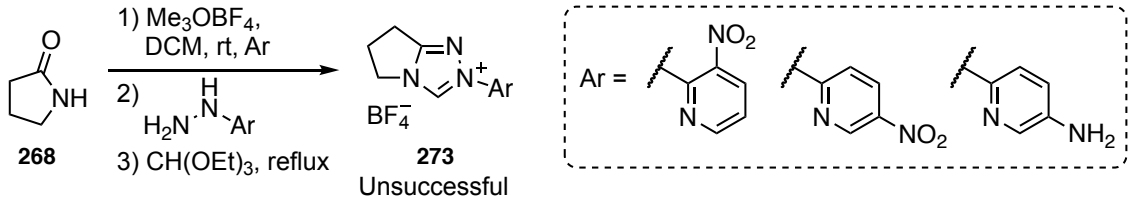

Scheme 51: Attempted synthesis of nitro or amino substituted N-pyridyl triazolium salts.

No literature procedure existed for the synthesis of 2-hydrazino-4-nitropyridine, and adapting the procedures used for 2-hydrazino-3-nitropyridine and 2-hydrazino-5-nitropyridine did not yield any of the desired hydrazinopyridine. Since it was clear that the triazolium salts could not be made easily with a nitro substituent, a new strategy was required.

Revisiting 2-chloro-4-methoxypyridine **284**, a Buchwald-Hartwig amination[108] was successfully used with benzophenone hydrazone **292**, a crystalline, dry hydrazine derivative (Scheme 52). The Pd-catalysed reaction gave the desired product **293** in 99% yield after column chromatography. The resulting compound **293** was then converted to the hydrazinium chloride using HCl at 90 ºC and neutralised with NaOH to yield the desired aryl hydrazine **285**. This hydrazine was relatively unstable and was used without further purification in the synthesis of the desired triazolium salt **257**.

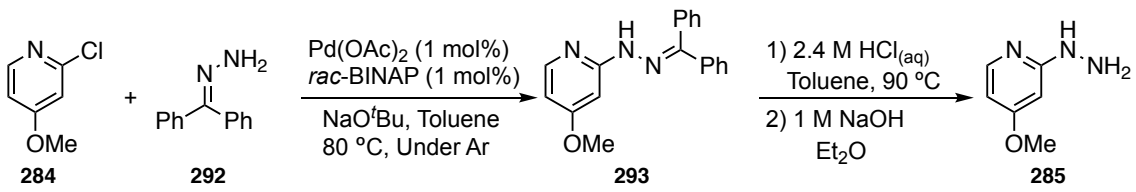

Scheme 52: Buchwald-Hartwig amination of 2-chloro-4-methoxypyridine 284, followed by deprotection and deprotonation to give aryl hydrazine 285.

2.2.2 Kinetics of C(3)-H/D exchange

The kinetic procedures for the measurement of rate constants for C(3)-H/D exchange (Scheme 53) for triazolium salts **255** – **258** were identical to those reported previously and are described in the experimental section.[58,59]

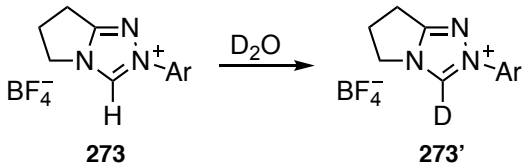

Scheme 53: C(3)-H/D exchange studied in D_2O by ^1H NMR spectroscopy.

Exchange reactions were carried out between pD 0 – 4 at 25 ºC and I = 1.0 M (KCl). Reactions were initiated by addition of a pre-equilibrated solution (0.75 mL), containing

internal standard (tetramethylammonium deuteriosulphate) and buffer or DCl, directly to the rigorously dried triazolium salt. The final substrate and internal standard concentrations in the D_2O reaction solutions were 10 mM and 0.83 mM, respectively. Reaction solutions in NMR tubes were incubated at 25 ºC in a thermostatted water bath. pD values were recorded at the beginning and end of each reaction and were found to be constant within error (± 0.05). The progress of each C(3)-H/D exchange reaction was followed by ^{1}H NMR spectroscopy during the disappearance of 75-90% of the C(3)-H signal of each substrate. There was no change in the integrated areas of the signals due to all other protons of triazolium salts **255** – **258** during this period, and no appearance of new signals, consistent with the absence of any parallel decomposition or hydrolysis reactions under the reaction conditions. ^{1}H NMR spectra were integrated using MestreNova following a first order phase correction and a baseline correction using a 6th order Bernstein polynomial.

The observed pseudo first order rate constants for C(3)-H/D exchange, k_{ex} (s^{-1}), were obtained from the gradients of the slopes of the natural log of the fraction of unexchanged substrate, f (s), against time according to Eqn. (1). f (s) was determined from Eqn. (2), where A_{C3H} and A_{std} are the integrated areas of the singlet due to the C(3)-H of the triazolium salt and the singlet at 3.3 ppm due to the twelve equivalent non-exchangeable[109] protons of the internal standard, tetramethylammonium deuteriosulphate.

$$ln\{f(\mathrm{s})\} = -k_{ex}t \quad (1)$$

$$f(\mathrm{s}) = \frac{(\mathrm{A_{C3H}/A_{std}})_t}{(\mathrm{A_{C3H}/A_{std}})_0} \quad (2)$$

Semi-logarithmic plots with associated pseudo first order rate constants for C(3)-H/D exchange, k_{ex} (s^{-1}), are given in Appendix 1. A representative NMR spectral overlay, and semi-logarithmic plot are shown for N-2,6-dimethoxyphenyl triazolium salt in the next section (2.2.2.1).

2.2.2.1 *Ortho*-alkoxy N-aryl triazolium salts 255 and 256

Representative ^{1}H NMR spectra obtained at three time points during C(3)-H/D exchange at pD = 1.08 for N-2,6-dimethoxyphenyl triazolium salt **255** is shown in Figure 15. C(3)-H/D exchange results in the disappearance of the ^{1}H NMR signal corresponding to the proton at the C(3) position at 9.64 ppm. The signal corresponding to the internal standard, tetramethylammonium deuteriosulphate, is observed at 3.10

ppm. No change in the integrals of all other signals, or the appearance of new signals, were observed during these experiments.

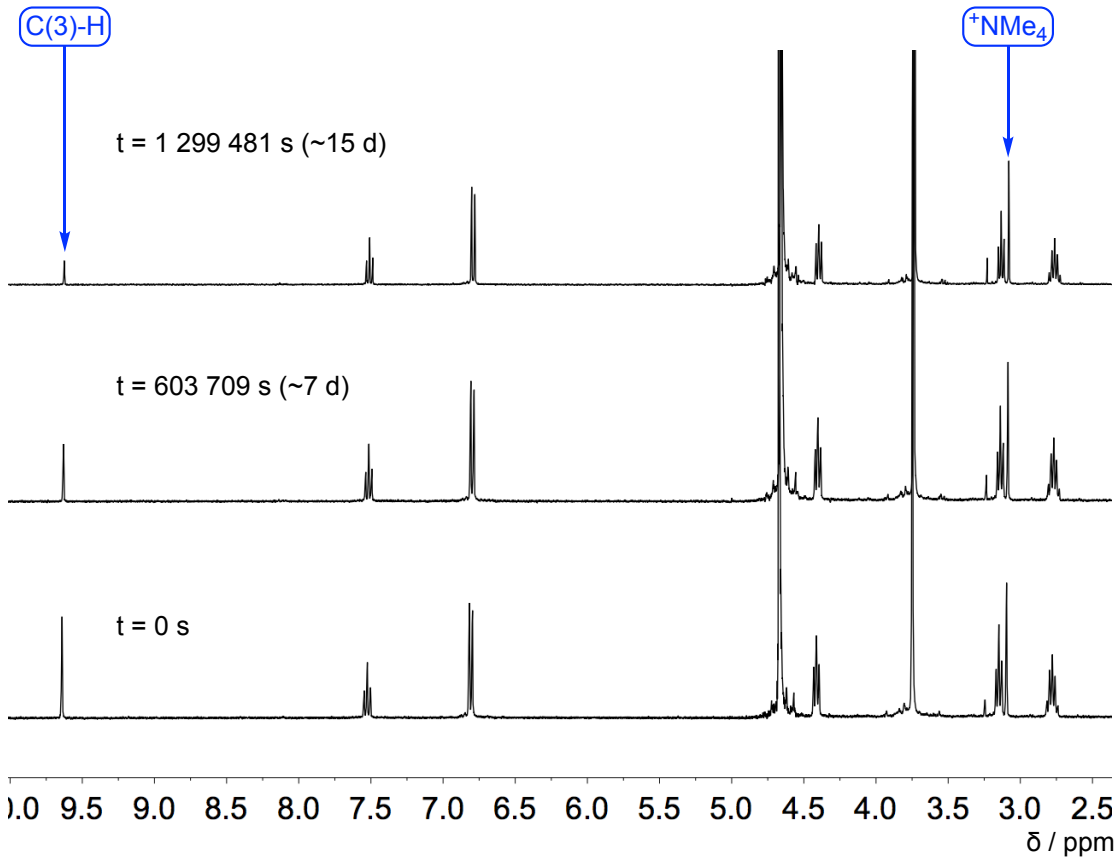

Figure 15: Representative ^{1}H NMR spectra at 400 MHz of N-2,6-dimethoxyphenyl triazolium salt 255 (10 mM, pD 1.08) obtained during C(3)-H/D exchange (s, 9.64 ppm) in D_2O at 25 °C and I = 1.0 M (KCl).

A semi-logarithmic plot of the fraction of unexchanged substrate against time is shown in Figure 16. The gradient gives the pseudo first order rate constant for C(3)-H/D exchange, k_{ex} (s^{-1}), at a given pD. The semi-logarithmic plots, pseudo first order rate constants and experiments at different buffer concentrations, for a range of pD values are given in Appendix 1.

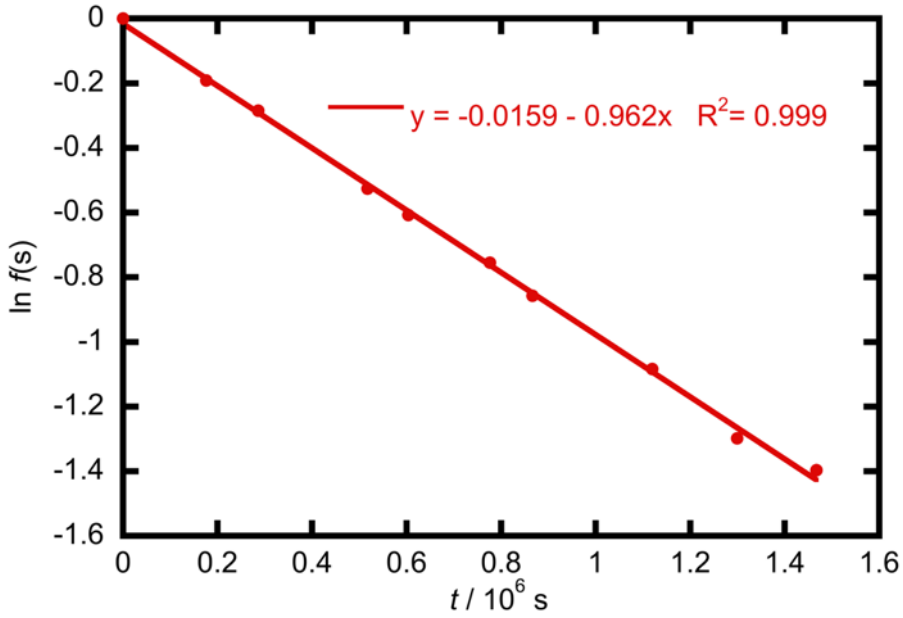

Figure 16: Semi-logarithmic plot of the fraction of unexchanged substrate against time for C(3)-H/D exchange reaction of N-2,6-dimethoxyphenyl triazolium salt 255 at 25 °C in D_2O at pD 1.08 and I = 1.0 M (KCl). The gradient gives the pseudo first order rate constant for exchange, k_{ex} = (9.62 ± 0.13) × 10^{-6} s^{-1}, at pD 1.08.

Buffer catalysis of H/D exchange for *ortho*-alkoxy triazolium salts **255** and **256** was found to be insignificant (Appendix 1), as was the case in all previous studies of azolium ion conjugate acids of N-heterocyclic carbenes.[56-59] Figure 17 shows the pD – log k_{ex} profiles for *ortho*-alkoxy triazolium salts **255** and **256**.

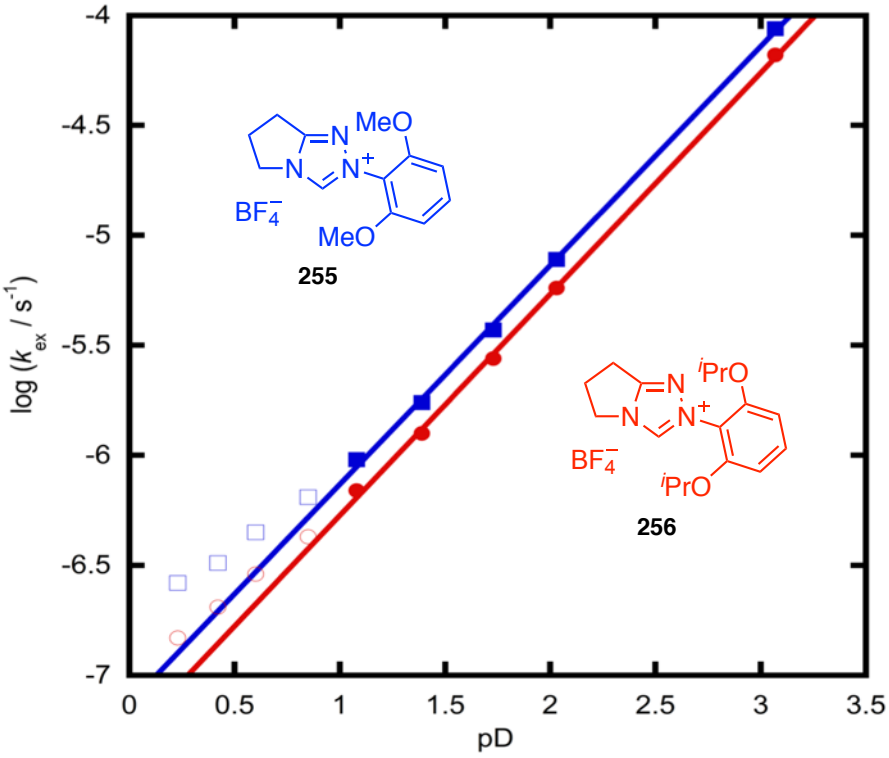

Figure 17: pD – log k_{ex} profile for C(3)-H/D exchange for N-2,6-dimethoxyphenyl 255 (■) and N-2,6-diisopropoxyphenyl 256 (●) triazolium salts. The points are experimental, the solid lines are the fittings through the solid points for pD > 1 to Eqn. (3). Open symbols show additional data that were not included in the fitting.

Both *ortho*-alkoxy systems **255** and **256** show a linear dependence of log k_{ex} on pD at pD > 1 with a slope of +1. A unit slope indicates a first order dependence on deuteroxide ion concentration. General base catalysis has been shown to be insignificant for triazolium salts **255** and **256** meaning that exchange in this region goes via a specific base catalysed mechanism. General base catalysis of exchange has been found to be insignificant for N-phenyl **259** and N-4-fluorophenyl **261** triazolium salts.[58] A slight upward bend is present as pD decreases below pD 1 (open symbols in Figure 17) which is indicative of an additional pathway for H/D exchange that is outcompeting the specific base catalysed mechanism. Second order rate constants for deuteroxide ion catalysed exchange, k_{DO} (M^{-1} s^{-1}), were obtained by fitting the data for pD > 1 to Eqn. (3), which is derived from the mechanism shown in Scheme 54, and the data are shown in Table 5. In this equation, $K_w = 10^{-14.87}$ is the ion product of D_2O at 25 °C[110] and $\gamma_{DO} = 0.72$ is the activity coefficient for deuteroxide ion under our experimental conditions.[111]

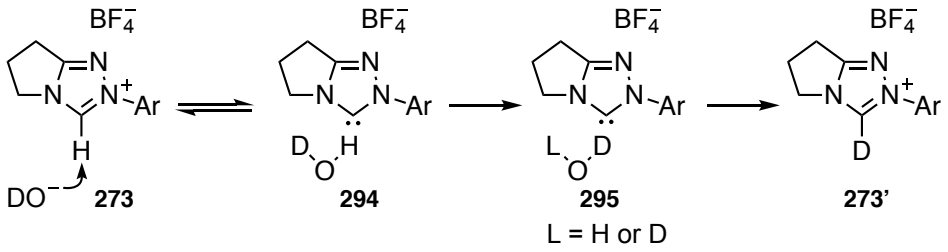

Scheme 54: Deuteroxide ion catalysed C(3)-H/D exchange.

$$\log (k_{ex}) = log\left(\frac{k_{DO}K_W}{\gamma_{DO}}\right) + pD \quad (3)$$

Table 5: Second order rate constants for deuteroxide ion-catalysed C(3)-H/D exchange (k_{DO}, M^{-1} s^{-1}) and carbon acid pK_a^{C3} values in aqueous solution at 25 °C and ionic strength, I = 1.0 M (KCl).

Salt	k_{DO} ($M^{-1}s^{-1}$)[a]	pK_a^{C3} [c]
N-Phenyl **259**[b]	6.82 (± 0.13) × 10^7	17.5
N-Mesityl **267**[b]	5.29 (± 0.07) × 10^7	17.7
N-2,6-Dimethoxyphenyl **255**	3.87 (± 0.07) × 10^7	17.8
N-2,6-Diisopropoxyphenyl **256**	2.87 (± 0.13) × 10^7	17.9

[a]Values of k_{DO} (M^{-1} s^{-1}) were obtained by fitting log k_{ex} – pD data to Eqn. (3). [b]Taken from R. S. Massey *et al*.[58] [c]pK_a^{C3} values were obtained by application of Eqn. (7).

The mechanism of specific base catalysed H/D exchange involves the initial removal of C(3)-H by deuteroxide ion to give an intimate ion pair **294**. This complex may either return to unexchanged triazolium ion **273**, or solvent reorganisation may occur, which allows for the delivery of a deuteron to the carbene at C(3). This process may involve either the rotation of the molecule of DOH formed during C(3)-H proton removal, or exchange with D_2O from bulk solvent (**295**), and it is essentially irreversible in deuterated solvent. Finally, deuteronation of carbene **295** gives the exchanged product **273'**.

Table 5 also shows previously reported rate constants for N-phenyl **259** and N-mesityl **267** triazolium salts for comparison.[58] The trends in rate constants are in agreement with the electronic effects of the N-aryl substituents on kinetic acidity of C(3)-H: as the substituent becomes increasingly electron donating, the second order rate constant for H/D exchange, k_{DO} (M^{-1} s^{-1}), decreases and therefore pK_a increases.

The absence of a downward bend in the pD – log k_{ex} profile at low pD means that if deuteronation at N1 of the triazolium ring is likely to occur, the pK_a^{N1} < 0 and therefore cannot be determined with certainty. Previously, pD – log k_{ex} profiles for *ortho*-heteroatom substituted triazolium ions[58,59] were fitted to an equation which allowed for a downward bend to occur near pD 0. Attempts to fit the same rate law to the *ortho*-alkoxy triazolium salts **255** and **256** led to large errors in pK_a^{N1} and therefore k_{DO} (shown in Appendix 1). The downward bend was proposed to be due to a deuteronation

at N1 of the triazole ring (**157**), where a pK_a^{N1} may be estimated from the crossing point of the arms of the downward bend. pK_a^{N1} values were estimated to be -0.04, -0.11 and -0.18 for N-2,4,6-tribromophenyl **263**, N-2,6-dichlorophenyl **265** and N-pentafluorophenyl **266** triazolium salts, respectively.[58,59]

The proposal of N1 deuteronation was made previously to account for an additional mechanism which goes via a dicationic triazolium ion **157**. N1 deuteronation would be expected to occur for all triazolium ions if the pD is low enough. However, *ortho*-halo triazolium salts caused an increase in pK_a^{N1} – this is counterintuitive since electron withdrawing halo substituents would be expected to decrease pK_a^{N1}. This increase in pK_a^{N1} was attributed to a reduction in lone pair – lone pair repulsion between N1 and the *ortho*-halo substituents **156**. Based on electronic arguments, one might expect that the pK_a^{N1} would increase with electron donating ability. *Ortho*-alkoxy N-aryl triazolium ions **255** and **256** show a slight upward bend between pD 0 – 1, but the absence of any downward bend in the pD range would suggest the pK_a^{N1} for both *ortho*-alkoxy substituents is lower than *ortho*-halo substituents. Another explanatation is therefore required to explain the upward bends observed for all *ortho*-heteroatom substituted triazolium salts.

To find an explanation and attempt to relate this to synthetic applications, a range of analyses were carried out and are described in sections 2.2.3 – 2.2.7. First, an examination of the chemical shifts C(3)-H as a function of pD for non-*ortho*-substituted N-phenyl **259**, and *ortho*-substituted N-pentafluorophenyl **266**, N-2,6-dialkoxyphenyl **255** and **256**, and N-pyrimidinyl **313** triazolium salts was made (Figure 24 in section 2.2.3). A range of triazolium salts were crystallised and crystal structures were obtained (section 2.2.4). Finally, DFT calculations were carried out to investigate how the energy of the molecule varies with the dihedral angle between the triazolium and N-aryl ring (section 2.2.5). These data suggest that N1 protonation is not necessarily required to explain the kinetic data for C(3)-H/D exchange (section 2.2.6). In addition, whatever is responsible for the kinetic behaviour below pD 1 is not what is responsible for their superiority in catalytic applications (section 2.2.7 – 2.2.8).

2.2.2.2 *Ortho*-pyridyl N-aryl triazolium salts 257 and 258

Figure 19 shows the pD – log k_{ex} profiles for N-5-methoxypyrid-2-yl triazolium salt **257** in comparison with previous data for N-pyrid-2-yl triazolium salt **258**. Additional data points were obtained between pD 3 – 4 for the N-pyrid-2-yl triazolium salt **258** to assess the substituent effects on the deuteroxide ion catalysed mechanism. The data for both

triazolium salts show regions of slopes of -1, 0 and +1. The distinctive acid catalysed exchange that was present for N-pyridyl triazolium salt **258** between pD 0 – 1.3 is present in the N-5-methoxypyrid-2-yl triazolium salt **257**, but is present between pD 0 – 2.

The data for the N-5-methoxypyrid-2-yl triaolium salt **257** also reveal the presence of a pD-independent region between the acid and base catalysed slopes. Fitting the data in the pD – log k_{ex} profile to a mechanism which excluded pD-independent exchange was less satisfactory (Figure 18).

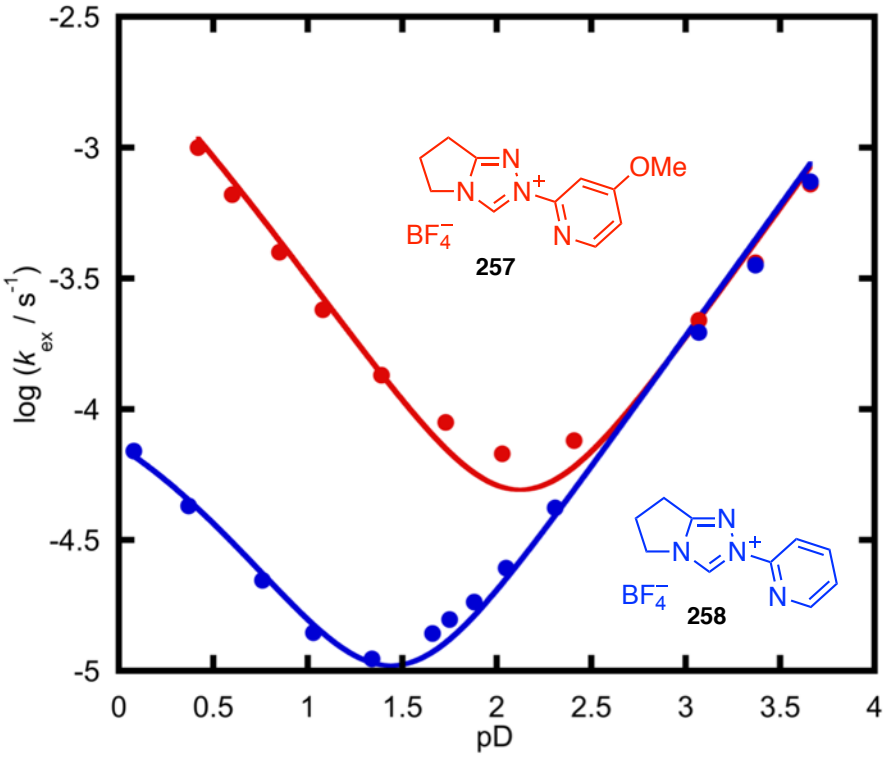

Figure 18: pD – log k_{ex} profile for C(3)-H/D exchange for N-5-methoxypyrid-2-yl 257 (●) and N-pyrid-2-yl 258 (●) triazolium salts, which includes a substrate ionisation term (K_a^{N1}, leading to the onset of a downward bend at pD ~ 0) but excludes a pD-independent term (in between the slopes of -1 and +1). The points are experimental, the solid curve calculated using Eqn. (4).

$$\log(k_{ex}) = log\left[\frac{k_I(10^{-pD}) + K_a^N\left(\frac{k_{DO}K_W}{\gamma_{DO}}\right)10^{pD}}{K_a^N + 10^{-pD}}\right] \quad (4)$$

The absence of a downward bend also suggested that the equation for the N-pyrid-2-yl triazolium salt **258** needed to be re-evaluated. The data for both pyridyl systems have been fitted to rate equations which show three mechanisms in operation: specific acid, pD-independent and specific base catalysed exchange.

Second order rate constants for DO^- and D_3O^+, and pseudo first order rate constant for pD-independent catalysed exchange were obtained by fitting the data between pD 0 -

3.7 to Eqn. (5) and they are shown in Table 6. In Eqn. (5), k_{D3O} (M^{-1} s^{-1}) is the second order rate constant for acid catalysed exchange and k_{D2O} (s^{-1}) is the pseudo first order rate constant for pD-independent exchange.

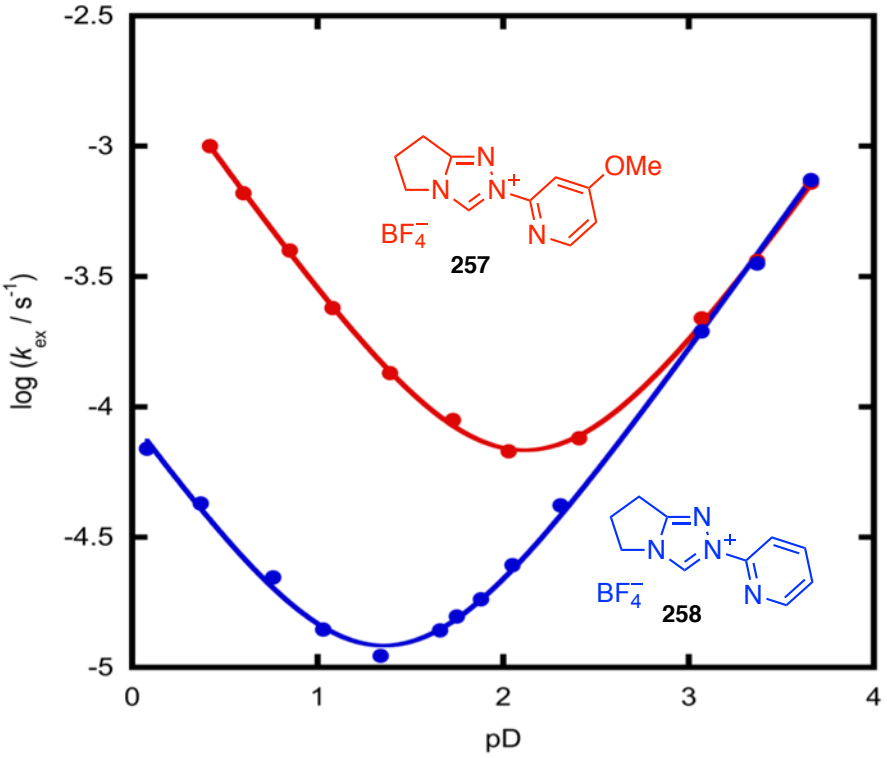

Figure 19: pD – log k_{ex} profile for C(3)-H/D exchange for N-5-methoxypyrid-2-yl 257 (●) and N-pyrid-2-yl 258 (●) triazolium salts. The points are experimental, the solid curve calculated using Eqn. (5).

$$\log(k_{ex}) = log\left[k_{D_3O}(10^{-pD}) + k_{D_2O} + \left(\frac{k_{DO}K_W}{\gamma_{DO}}\right)10^{pD}\right] \quad (5)$$

Table 6: Second order rate constants for deuteroxide ion-catalysed (k_{DO}, M^{-1} s^{-1}), specific acid catalysed (k_{D3O}, M^{-1} s^{-1}) and pD-independent C(3)-H/D exchange (k_{D2O}, s^{-1}) and carbon acid pK_a^{C3} values in aqueous solution at 25 °C and constant ionic strength, I = 1.0 M (KCl).

Triazolium Salt	k_{D3O} (M^{-1} s^{-1})[a]	k_{D2O} (s^{-1})[a]	k_{DO} (M^{-1} s^{-1})[a]	pK_a^{C3} [b]
N-pyrid-2-yl **258**	8.3 (± 0.4) × 10^{-5}	4.8 (± 0.5) × 10^{-6}	8.7 (± 0.3) × 10^{7}	17.4
N-5-methoxypyrid-2-yl **257**	2.55 (± 0.05) × 10^{-3}	2.92 (± 0.19) × 10^{-5}	8.0 (± 0.2) × 10^{7}	17.5

[a]Values of k_{D3O} ($M^{-1}s^{-1}$), k_{D2O} (s^{-1}) and k_{DO} ($M^{-1}s^{-1}$) were obtained by fitting log k_{ex} – pD data to Eqn. (5)
[b]pK_a^{C3} values were obtained by application of Eqn. (7).

The rate constants for DO^- catalysed exchange are 1.04 × 10^{12} and 3.14 × 10^{10} – fold larger than D_3O^+ catalysed exchange for N-pyrid-2-yl **258** and N-5-methoxypyrid-2-yl **257** triazolium salts, respectively. The difference in log(k_{D3O}) between the two triazolium salts is 1.49, which is very similar to the change in pK_a between pyridine and 4-methoxypyridine (ΔpK_a = 1.45). This is evidence that the pyridyl ring is involved in the acid catalysed region of C(3)-H/D exchange either as an intramolecular general base or as a titratable group. The value of k_{DO} is slightly smaller for N-5-methoxypyrid-2-yl

257, which is the opposite of what be expected based on the σ_m value of a methoxy substituent (σ_m = +0.115). One explanation for this discrepancy is that the relatively fast rates of exchange in the pD 3 – 4 region and insufficient data points in this region means that the curve fitting software cannot accurately describe the specific base catalysed region. A comparison of three points between pD 3 – 4 show that the values are very similar and that the N-5-methoxypyrd-2-yl **257** and N-pyrid-2-yl **258** salts shows the same rates of exchange within error.

Eqn. (5) describes three mechanisms of C(3)-H/D exchange which are in operation. The third term describes the mechanism with a slope of +1, shown in Scheme 54. The first and second terms – acid catalysed and pD-independent exchange, respectively – may be described by a number of kinetically equivalent pathways, shown in Figure 20 and Figure 21, respectively. Each mechanism will be discussed in turn, but the most likely mechanisms operating in the regions of -1 and 0 slopes are shown in dotted boxes.

2.2.2.2.1 Acid catalysed mechanism for N-pyridyl triazolium salts

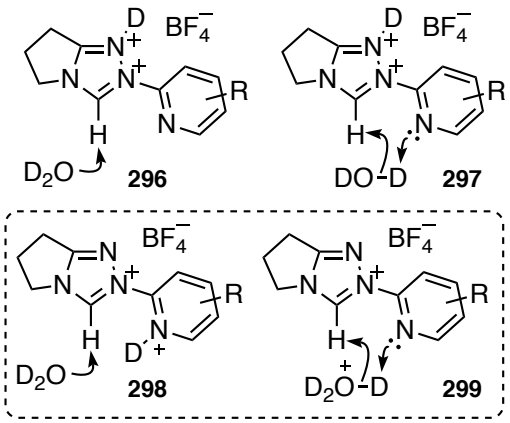

Figure 20: Kinetically equivalent mechanisms for acid catalysed exchange of N-pyridyl triazolium salts. Options 298 and 299, highlighted in the dotted box, are the most likely mechanisms that are operating in the acid catalysed region.

Option **296** in Figure 20 describes a scenario where N1 becomes deuteronated followed by solvent mediated exchange. This option seems unlikely because the difference in $\log(k_{D3O})$ is very similar to the ΔpK_a between the pyridyl rings. This directly implicates the pyridyl nitrogen in C(3)-H/D exchange. However, the pyridyl substituent would not be expected to dramatically increase pK_a^{N1} of the triazolium ring compared to more electron donating and withdrawing substituents.[58,59] Intramolecular H-bonding between a deuteronated N1 and the pyridyl substituent could cause a slight increase in pK_a^{N1} but $\Delta\log(k_{D3O}) \approx \Delta pK_a$ between the pyridyl substituents and this suggests the deuteron resides on the pyridyl nitrogen.

Option **297** describes the previously proposed mechanism[58,59] which goes via N1 deuteronation in conjunction with intramolecular general base catalysis by the pyridyl ring. The conformation of the pyridyl ring in this mechanism (cf. X-ray structural and DFT analysis in sections 2.2.4 and 2.2.5, respectively) would not necessarily require N1 deuteronation to reduce electrostatic repulsion between the lone pairs of electrons on N1 and the pyridyl nitrogen.

Options **298** and **299** involve two possibilities which cannot be distinguished on the current kinetic data, since they describe different extents of deuteron transfer to the pyridyl substituent in the transition state for C(3)-H removal. Option **298** involves complete deuteronation in the transition state for C(3)-H removal. This deuteronation at the pyridyl nitrogen may well be stabilised by an intramolecular H-bond with the triazolium N1. Option **299** describes either partial deuteronation in the transition state for C(3)-H removal or a concerted deuteronation at the pyridyl nitrogen and C(3)-H removal by D_2O. Chemical shift analysis of C(3)-H (Figure 24 in section 2.2.3) and the aromatic protons on the pyridyl ring indicate a substrate deuteronation is occurring, which causes these signals to deshield at pD < 2. Positive charges usually de-shield nearby protons, which may explain the increased chemical shift C(3)-H as pD decreases.

Attempts were also made to fit the data to the three terms (acid, pD-independent and base catalysed mechanisms) which included a low pD ionisation term (Ka^N, which may correspond to either N1 of the triazolium ring or the pyridyl nitrogen) shown in Eqn. (6). This additional term would allow a downward bend at pD ≤ 0 with an associated K_a^N value. These fittings were less satisfactory, as there is no downward deviation of the data near pD 0 (i.e. as the pD decreases in the acid catalysed region, the slope has a gradient of -1, and does not change to 0). This means that the fitting programme is guessing where the downward bend occurs, with estimates of pKa^N << 0 made, and so the Ka^N term was excluded from kinetic fitting. This suggests that the pKa^N, whether on the triazolium or pyridyl nitrogen of either triazolium salt, is ≤ -2.

$$\log\left(k_{ex}\right) = log\left[\frac{K_a^N k_{D_3O}(10^{-pD}) + K_a^N k_{D_2O} + K_a^N\left(\frac{k_{DO}K_W}{\gamma_{DO}}\right)10^{pD}}{K_a^N + 10^{-pD}}\right] \qquad (6)$$

2.2.2.2.2 pD-Independent mechanism for N-pyridyl triazolium salts

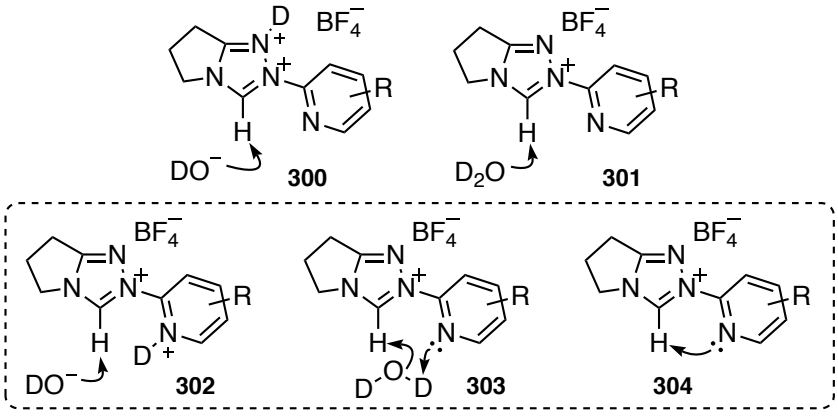

Figure 21: Kinetically equivalent mechanistic options for pD-independent C(3)-H/D exchange for N-pyridyl triazoliums. Options 302, 303 and 304 are the most likely mechanisms that are operating.

pD-Independent C(3)-H/D exchange has been included into the fitting of N-5-methoxypyrid-2-yl **257** and for the existing data points for N-pyrid-2-yl **258** triazolium salts. Possible mechanisms consistent with pD-independent C(3)-H/D exchange for N-pyrid-2-yl **258** and N-5-methoxypyrid-2-yl **257** triazolium salts are shown in Figure 21.

Option **300** describes a scenario where N1 becomes deuteronated followed by deuteroxide ion mediated exchange. This mechanism is less likely as the conformation of the pyridyl ring in this mechanism (cf. X-ray structural and DFT analysis in sections 2.2.4 and 2.2.5, respectively) would not necessarily require N1 deuteronation to reduce electrostatic repulsion between the lone pairs of electrons on N1 and the pyridyl nitrogen.

Option **301** describes the D_2O mediated exchange and may be excluded because the rate constants for solvent catalysed exchange, k_{D2O}, reported previously for *ortho*-halo and *ortho*-pyrimidinyl triazolium salts require impossibly large reverse rate constants for reprotonation to give the same pK_a values obtained from k_{DO}. Values of k_{H3O+} = (1.7 – 5.0) × 10^{12} M^{-1} s^{-1} are required to obtain the same pK_a^{C3} values obtained from Eqn. (7), which far exceed diffusion controlled rate consants of ~ 10^{10} M^{-1} s^{-1}.[55,58,59]

Options **302**, **303** and **304** are therefore the likely mechanisms of exchange, although the kinetic data do not allow a distinction between them. Option **302** describes complete deuteronation of the pyridyl nitrogen in the transition state for C(3)-H removal which is mediated by deuteroxide ion. Option **303** describes either partial deuteronation in the transition state for C(3)-H removal or a concerted deuteronation at N1 and C(3)-H removal by deuteroxide ion. Option **304** describes the direct deprotonation of C(3)-H by the pyridyl nitrogen.

Figure 24 (section 2.2.3) shows the difference in the chemical shift between C(3)-H and the signal for the non-exchanging internal standard, tetramethylammonium deuteriosulphate, Δδ / ppm, for N-5-methoxypyrid-2-yl triazolium salt **257**. The same trend is also observed for the aromatic pyridyl signals (not shown). The increase in Δδ as pD decreases below 1, is consistent with either a substrate titration or the formation of an intra- or intermolecular H-bond. Since there are titratable atoms on this triazolium salt, and hydrogen bonding would not be expected to increase as the pD decreases, it is reasonable to conclude that this is most likely evidence of substrate titration.

2.2.2.3 Estimation of carbon acid pK_a^{C3} values

Estimating the pK_a^{C3} of C(3)-H can be achieved by combining the equations for hydroxide ion mediated deprotonation of a carbon acid **273** to give carbene **305** and the autoionisation of water, K_w. This gives an equation that can be solved for the pK_a^{C3} value in water, Eqn. (7), which is derived from Scheme 55.

$$pK_a^{C3} = pK_w + log\frac{k_{HOH}}{k_{HO}} \quad (7)$$

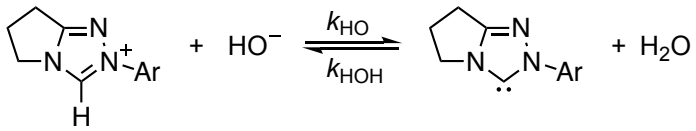

273 **305**

Scheme 55: Equilibrium for deprotonation by hydroxide ion of triazolium salt 273 at C(3).

The value of k_{HO} can be estimated from the experimental value of k_{DO} using a secondary kinetic isotope effect. To determine the appropriate correction, it is necessary to look at the steps involved in C(3)-H/D exchange. Exchange of a proton for a deuteron involves three distinct steps.[§] The first step is proton removal by a basic species to give a reactive intermediate (with associated rate constant k_{-p}). This is followed by a solvent reorganisation step (k_{reorg}), which is a process that involves the solvent structure rearranging to the development (or removal) of charge in the transition state and the intermediate formed from such a step. Finally, reprotonation (k_p) of the reactive intermediate by solvent gives the exchanged product.

Previous studies of proton transfer from thiazolium ions found evidence for the internal return of the transferred hydron.[62] Using an analysis developed by Streitweiser,[112] Jencks found that a negative deviation from the Swain – Schaad relationship,[113] with an

[§] Diffusion together and apart, which form part of an Eigen mechanism for proton transfer are not included in these three steps.

ideal value of $y = 3.34$, was due to a decreased observed primary isotope effect which is evidence for internal return. Values for k_p / k_{reorg} were found to increase with decreasing acidity of the thiazolium ion (Figure 22). A schematic diagram of the free energies vs reaction coordinates is also shown in Figure 22, where the upper pathway qualitatively represents the more electron rich N-methyl thiazolium salt **306** and the lower coordinate qualitatively represents the more electron poor N-cyanomethyl thiazolium salt **308**.

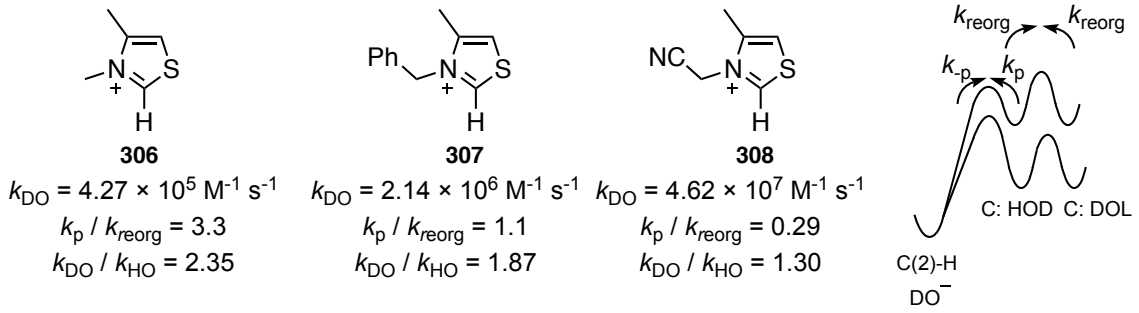

Figure 22: Second order rate constants for deuteroxide ion catalysed C(2)-H/D exchange, and ratios of rate constants k_p/k_{reorg} and k_{DO}/k_{HO}, for three thiazolium salts obtained by Jencks.[62] Also shown is a qualitative free energy reaction coordinate profile for the thermodynamically unfavourable proton transfer from C(2)-H to deuteroxide ion in D_2O.

Internal return of the transferred hydron becomes more important as the kinetic acidity of the thiazolium ion decreases. Jencks observed general base catalysis (GBC) by a series of oxygen containing bases and amine bases for a series of thiazolium ions, with $\beta = 0.95$ suggesting rate limiting diffusional separation (a transition state in which proton transfer is almost complete). The rates of solvent reorganisation and of internal return are both partially rate limiting.

While studying the kinetic and thermodynamic acidities of a series of simple imidazolium ions, Amyes[57] found that GBC of exchange was absent and that imidazolium ions **309 – 312** (Figure 23) had smaller kinetic acidities (20 – 8000-fold) than 3–methyl–4–methylthiazolium ion **306** (k_{DO} = 4.27 × 10^5 M^{-1} s^{-1}). Given the trend observed for a series of thiazolium ions in Figure 22, this would suggest that C(2)-H/D exchange would likely be more limited by solvent reorganisation (i.e., representing the upper reaction coordinate in Figure 22).

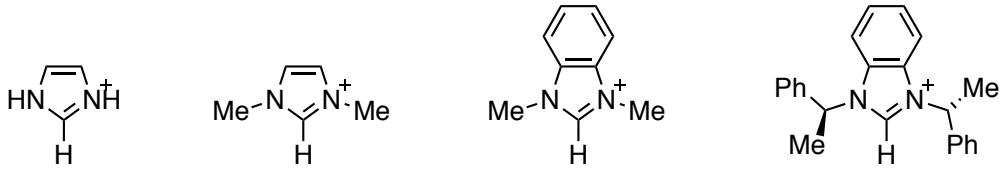

309	**310**	**311**	**312**
k_{DO} = 36.9 M^{-1} s^{-1}	k_{DO} = 247 M^{-1} s^{-1}	k_{DO} = 5.74 × 10^3 M^{-1} s^{-1}	k_{DO} = 1.48 × 10^4 M^{-1} s^{-1}
pK_a = 23.8	pK_a = 23.0	pK_a = 21.6	pK_a = 21.2

Figure 23: Second order rate constants for deuteroxide ion catalysed C(2)-H/D exchange and pK_a value obtained by Amyes and co-workers.[57]

GBC of exchange would be expected if the transfer of the proton to a general base, k_{-p}, was rate limiting. Since GBC was found to be insignificant for triazolium salts **255** and **256** and for previously reported triazolium salt **259** and **261**,[58,59] it may be concluded that the rate limiting step is solvent reorganisation. The secondary kinetic isotope effect of k_{DO} / k_{HO} = 2.4,[114,115] which is the maximum possible value determined using deuterium fractionation factors, is then used to obtain the second order rate constant for hydroxide ion catalysed exchange for all four triazolium salts.

The rate constant for solvent reorganisation, k_{reorg}, has been correlated previously[56-59] to the dielectric relaxation time of pure water at 25 ºC. Studies into proton transfer from methanol to singlet diphenyl carbene found that the time constant for proton transfer is τ = 9.0 ps (k_{MeOH} = 1.1 × 10^{11} s^{-1}) which correlates well to the solvation time for methanol, of 1.5 × 10^{11} s^{-1}.[116] The dielectric relaxation time of pure water at 25 °C has been found to be 8.27 ps.[117] The addition of KCl, which is used to maintain ionic strength in our kinetic measurements, has been found to cause a decrease in the dielectric relaxation time of water by 7.9%.[118,119,120] This has been rationalised in terms of the increased mobility of the dipoles of the solution resulting from a more broken structure. This justifies the use of an order of magnitude estimate value of k_{reorg} = 10^{11} s^{-1}.[121, 122]

In the reverse direction, proton transfer to the carbene is thermodynamically favourable. In an Eigen mechanism, a thermodynamically favourable proton transfer is likely to have a diffusion controlled encounter rate limiting step.[123] The reorganisation step may indeed be just the rotation of a molecule of HOD into the correct position to deliver a deuteron back to the carbene. This would be expected to be at least as fast as the diffusion together of two molecules in solution (which have second order rate constants of the order of about 10^{10} M^{-1} s^{-1}) since the triazolylidene is surrounded by ~55.4 M D_2O, but rotation of the molecule of HOD in the intimate ion pair will still require restructuring of surrounding solvent molecules which were hydrogen bonded to the

deuteroxide ion. From the principle of microscopic reversibility, this would imply that k_{reorg} must be rate limiting in reverse direction, therefore $k_{reorg} = k_{HOH} = 10^{11}$ s^{-1}.

The equilibrium constant for the autoionisation of water[110] is given by $K_W = 10^{-14}$. This value is obtained from a pure solution of water at I = 0 M. Under our experimental conditions, an ionic strength of 1.0 M (KCl) was used. The autoionisation of water will be sensitive to the ionic strength as it involves the generation of charged species from a neutral solution. For comparison with published pK_a values, it is assumed that $K_W = 10^{-14}$.

The C(3)-H pK_a^{C3} values for the two alkoxy (**255** and **256**) and two pyridyl (**257** and **258**) triazolium salts are given in Table 5 and Table 6, respectively. The two alkoxy triazolium salts **255** and **256** are the most basic triazolium systems reported so far, and this can be attributed to the electron-donating ability of alkoxy systems which stabilize the cationic ground state. Sterics may also contribute to the observed reactivity – isopropoxy groups are typically more electron donating, but in the *ortho*-positions may cause poorer overlap of the oxygen lone pair with the N-aryl π-system. This would explain the higher chemical shift difference for isopropoxy vs methoxy substituents – the inductive electron withdrawing effect is more dominant for isopropoxy due to steric interactions and this causes the C(3)-H to appear more deshielded (section 2.2.3). The same steric interactions may slow the rate of C(3)-H/D exchange.

As for the N-pyridyl triazolium salts (**257** and **258**), placing a methoxy substituent in a *meta* position relative to the triazolium ring would be expected to cause k_{DO} to increase relative to the unsubstituted N-pyridyl triazolium salt **258**. There is a 7% decrease in k_{DO} which falls outside the error value. Three data points were compared at the same pD for both pyridyl systems and it is clear that the difference is small. This discrepancy may be due to the fitting of the pD – log k_{ex} profiles to three mechanisms with insufficient data points in the specific base catalysed region.

2.2.3 Chemical shift analysis

The effect of pD on the chemical shift difference, Δδ / ppm, between C(3)-H and the internal standard, tetramethylammonium deuteriosulphate, for N-phenyl **259**, N-pentafluorophenyl **266**, N-pyrimidinyl **313**, N-2,6-dimethoxyphenyl **255**, N-2,6-diisopropoxyphenyl **256** and N-5-methoxyprid-2-yl **257** triazolium salts are shown in Figure 24. These data show that as pD decreases, Δδ for N-5-methoxyprid-2-yl **257** increases indicating either a substrate deuteronation or the formation of an intra or

intermolecular hydrogen bond. All other salts show a slight decrease Δδ which is inconsistent with a substrate deuteronation near pD 0, although it doesn't rule out a substrate deuteronation in the Hammett acidity region at pD < 0.

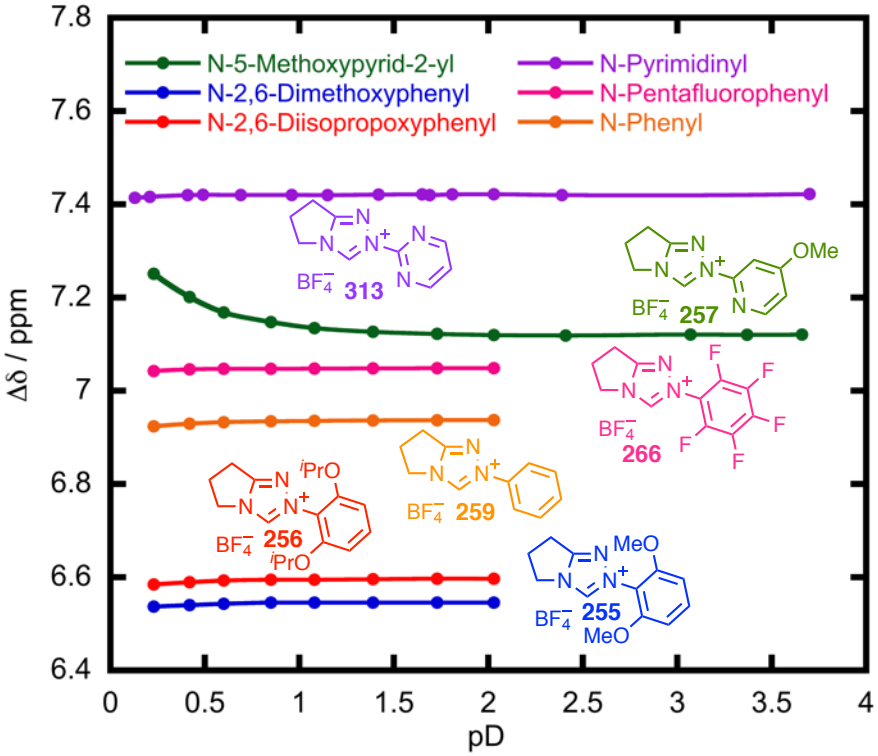

Figure 24: The effect of pD on the chemical shift difference between C(3)-H and the internal standard signal due to twelve non-exchangeable protons on tetramethylammonium deuteriosulphate.

Interestingly, the change in chemical shift of C(3)-H for all triazoliums is the opposite of what would be expected from protonation at N1. The chemical shift is more or less constant above pD 1. Below pD 1, as pD decreases, the chemical shift of C(3)-H relative to the internal standard signal decreases slightly. N1 deuteronation near pD 0 is therefore not consistent with the kinetic data and chemical shifts of all triazolium salts, and an alternative explanation is required.

An interaction between the lone pair of electrons on the *ortho*-substituents and the cationic π-system of the triazolium ring **314** (Figure 25) may be expected to lead to a shielding of the C(3)-H signal. This would also have the effect of stabilising the positive charge and therefore decreasing the acidity which is not what is observed in the kinetic data. No change in chemical shift of the methyl protons attached to the oxygen atoms of N-2,6-dimethoxyphenyl as a function of pD would suggest that this is not a significant factor causing the upward bend.

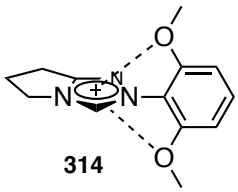

314

Figure 25: Potential cationic stabilising effect which may shield the ^{1}H NMR signal of C(3)-H, but which cannot explain enhanced rate constant for C(3)-H/D exchange.

Another possibility is that, in addition to the electron withdrawing *ortho*-substituted N-aryl triazoliums, N-4-fluorophenyl **261** and N-4-cyanophenyl **315** triazolium ions[58,59] (Figure 26) also show a significant upward bend in the pD – log k_{ex} profile for C(3)-H/D exchange, and solvation may be a key factor. Electron withdrawing N-aryl rings possess different electrostatic potential surfaces to electron donating N-aryl rings (**316** and **317**, Figure 26).[124] This may lead, particularly in the case of multiply halo-substituted N-aryl rings, to differing solvation effects. The reason why this occurs only below pD 1 may be due to the changing solvent structure as the concentration of the ionic salt KCl is no longer in large excess of D_3O^+. The standard molar Gibbs energy of hydration for H^+ and K^+ are -1056 and -304 kJ mol^{-1},[125] respectively, and this may lead to a change in the localised structure of the solvent around the triazolium salt. However, there is no direct evidence for (or against) this hypothesis.

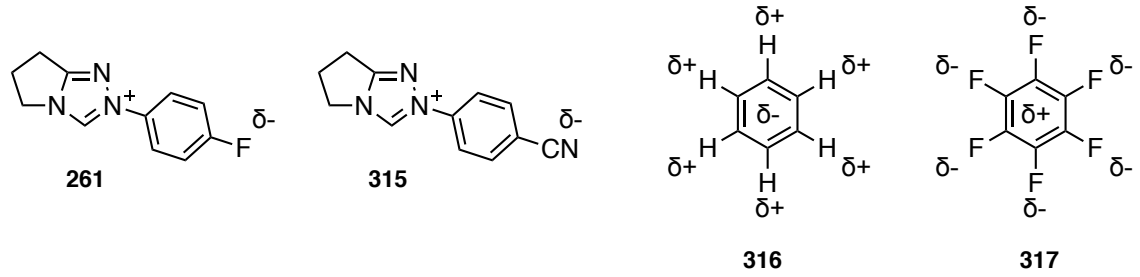

261 315 316 317

Figure 26: Electron withdrawing triazolium salts 261 and 315 also display upward bends in pD – log k_{ex} profiles,[58,59] which may be a result of differing solvation effects upon the N-aryl ring. Electron withdrawing hexafluorobenzene 317 displays a reversed electrostatic potential surface to benzene 316.

One final possibility is that the kinetic fitting placed a downward bend at a relatively high pD i.e. the actual p$K_a^{N1} \leq -2$. This downward bend would not be accessible under ideal solution conditions in the pD region. The chemical shift data could corroborate this, but without a downward bend in the pD – log k_{ex} profile or an increase in the chemical shift of the C(3)-H signal, it is not possible to prove unambiguously that N1 protonation is causing the upward bend. X-ray crystal structures (section 2.2.4) show that *ortho*-substituted N-aryl rings have larger dihedral angles and a protonation at N1 may not be necessary to reduce lone pair – lone pair repulsions.

2.2.4 X-ray structural analysis

To further inform our mechanistic interpretation, X-ray crystal structures were obtained for a range of triazolium salts discussed in section 2.2.1. In addition, the N-2,4,6-tribomophenyl triazolium salt **263** that had been prepared previously within the O'Donoghue group was also crystallised.[58,59] To obtain crystals suitable for X-ray crystallography, the triazolium salts were dissolved in either methanol or acetonitrile in a 7 mL glass vial and allowed to evaporate slowly. The structures obtained are compared with the literature crystal structure for N-phenyl triazolium salt **259**.[126] The ORTEP diagrams, as well as the chemical structure, for four structural classes are shown as follows: non-*ortho*-substituted are shown in Figure 27; *ortho*-pyridyl-substituted are shown in Figure 28; *ortho*-halo-substituted are shown in Figure 29; *ortho*-alkyl- and *ortho*-alkoxy-substituted are shown in Figure 30. Attempts to crystallise N-pyrimidinyl **313** and N-2,6-diisopropoxyphenyl **256** triazolium salts were unsuccessful in a range of conditions.

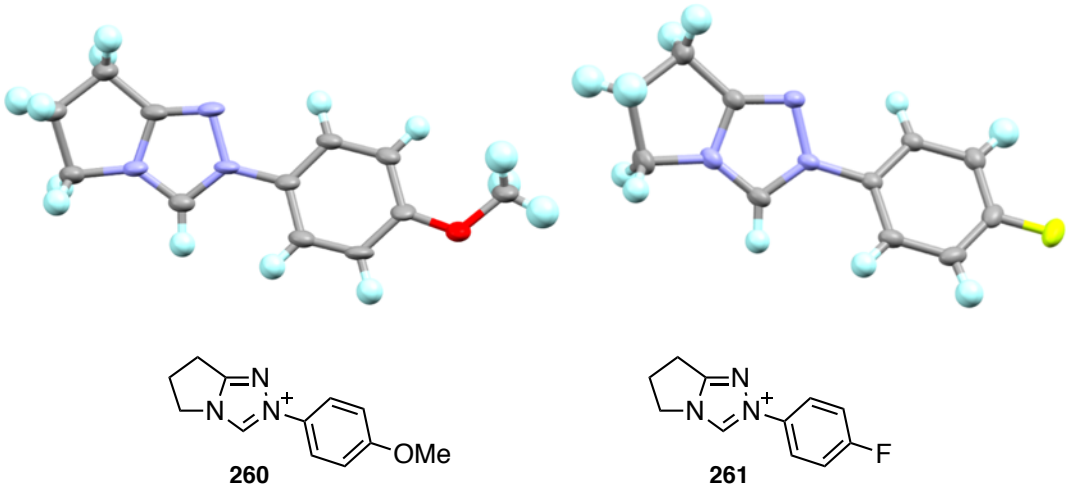

Figure 27: ORTEP diagrams for non-*ortho*-substituted triazolium salts.

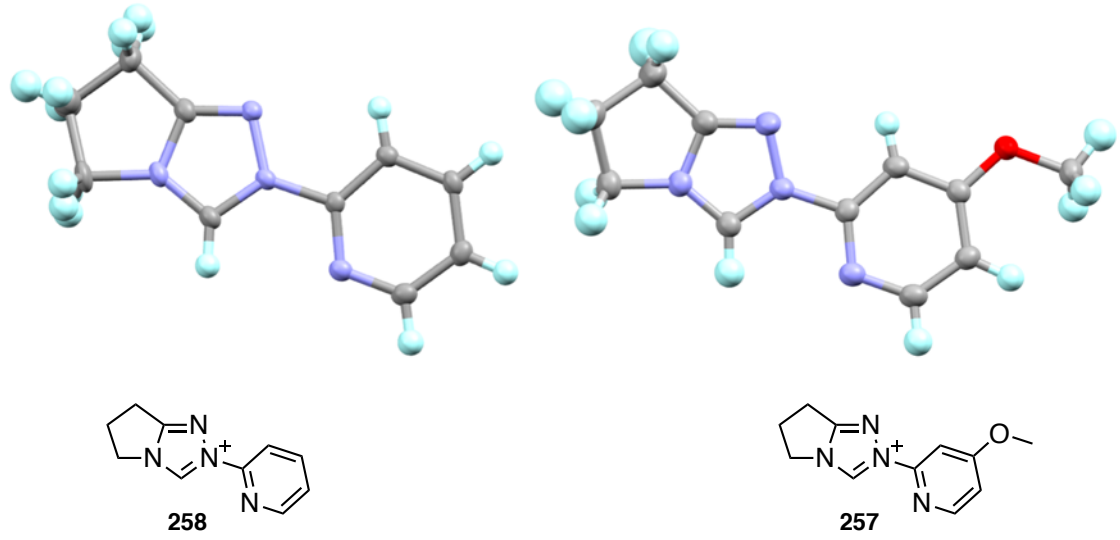

Figure 28: ORTEP diagrams for *ortho*-pyridyl-substituted triazolium salts.

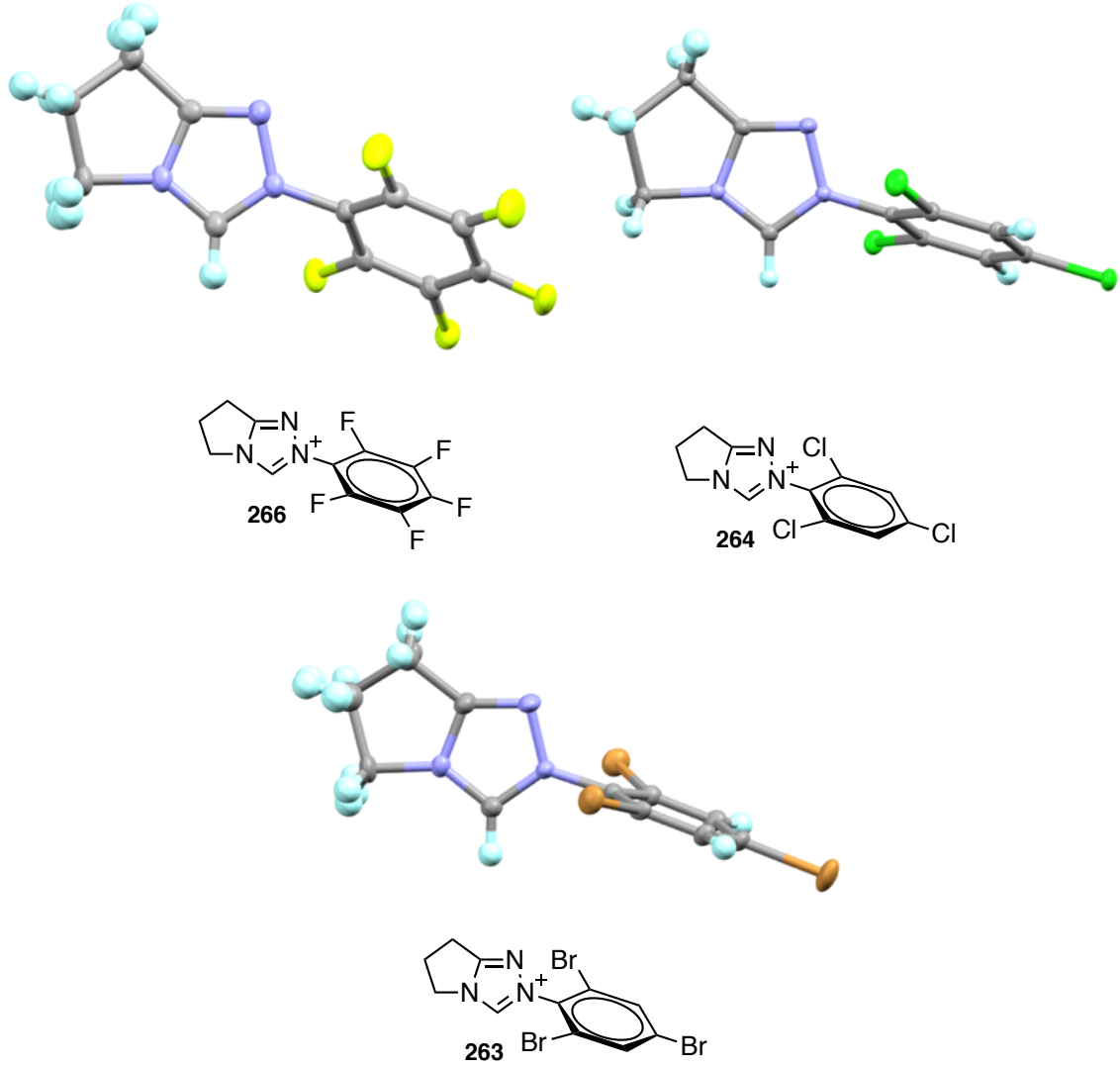

Figure 29: ORTEP diagrams for *ortho*-halo-substituted triazolium salts.

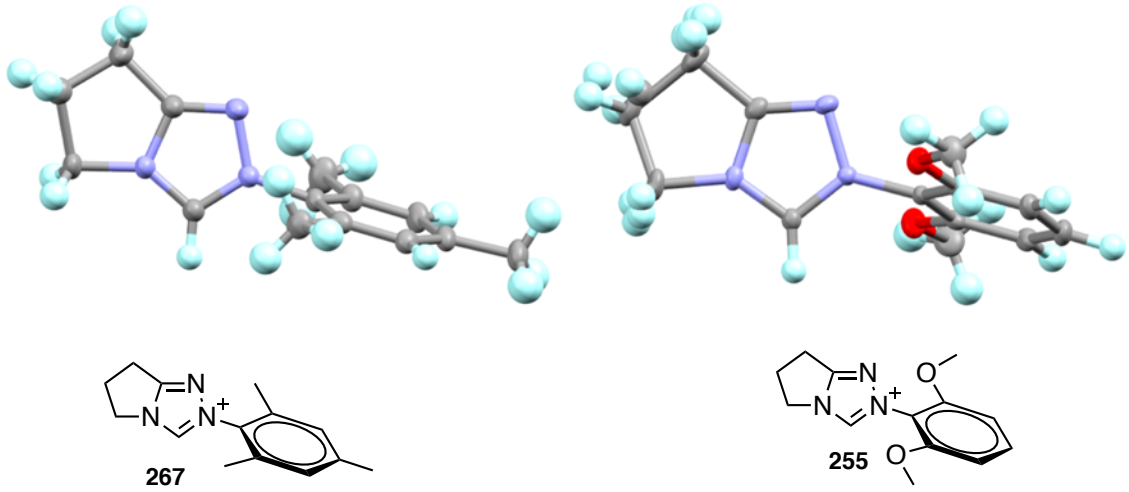

Figure 30: ORTEP diagrams for *ortho*-alkyl- and *ortho*-alkoxy-substituted triazolium salts.

It was then possible to study the effect of varying the N-aryl ring on the length and dihedral angles between the triazolium and N-aryl rings. The length is defined as the distance between N2 and C_{ipso} of the aryl ring, and the dihedral angle, θ, is defined as the angle between N1-N2 of the triazole ring and C_{ipso}-C_{ortho} of the N-aryl ring (Figure 31). For symmetrical N-aryl rings, the choice of C_{ortho} was made to give a dihedral angle of $|\theta| \leq 90°$. The two parameters are compared in Table 7. Shown in Table 8 are the same parameters compared for three hydroxyaryl adducts[79] derived from N-phenyl triazolium ion.

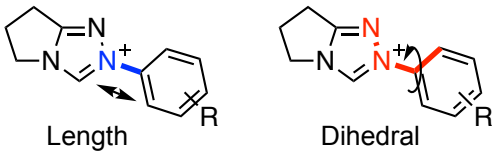

Figure 31: Definitions of bond length and dihedral angles between the triazolium and N-aryl rings. The bond length is highlighted in bold blue. The dihedral angle, θ, is highlighted in bold red.

Table 7: Bond length and torsion angles between the triazolium and N-aryl rings obtained from X-ray crystal structures of triazolium salts.

Triazolium Salt	N2-C_{ipso} length / Å	N1-N2-C_{ipso}-C_{ortho} Dihedral, θ / °	Triazolium Salt	N2-C_{ipso} length / Å	N1-N2-C_{ipso}-C_{ortho} Dihedral, θ / °
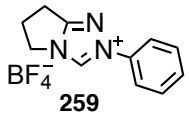 **259**	1.435	19.45	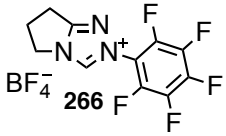 **266**	1.429	62.0
 **260**	1.435	16.1	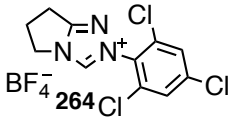 **264**	1.4264	73.71
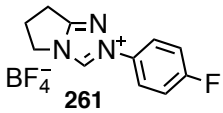 **261**	1.428	25.2	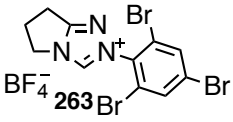 **263**	1.430	89.6
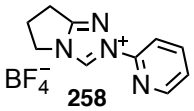 **258**	1.431	6.5	 **267**	1.441	79.51
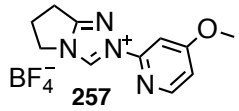 **257**	1.429	10.3	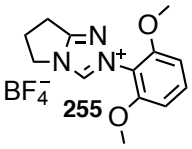 **255**	1.433	76.63

Table 8: Bond length and torsion angles between the triazolium and N-aryl rings obtained from X-ray crystal structures of hydroxyaryl adducts obtained by O'Donoghue and co-workers.[79]

Hydroxyaryl Adduct	N2-C_{ipso} length / Å	N1-N2-C_{ipso}-C_{ortho} Dihedral, θ / °
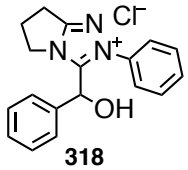 **318**	1.437	67.95
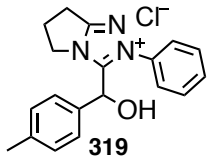 **319**	1.437	65.14
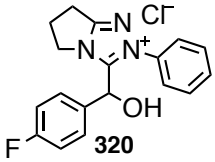 **320**	1.439	65.51

All triazolium salts (Table 7) show only a small variation in bond lengths, ranging from (1.4264 - 1.441 Å). There is no trend between the van der Waals radii of the substituents on the N-aryl rings and the bond length. However, the dihedral angles are affected dramatically by the presence or absence of *ortho*-substituents on the N-aryl ring. In general, non-*ortho*-substituted N-aryl rings have much smaller dihedral angles (16.1 –

25º) than *ortho*-substituted N-aryl rings which have much larger dihedral angles (62.0 – 89.6º).

For *ortho*-halo N-aryl rings, the dihedral angle increases in the order F < Cl < Br, which reflects the increased size and therefore increased steric and electrostatic interactions with the triazolium ring (N1 and C(3)-H). *Ortho*-pyridyl N-aryl rings have low dihedral angles (≤ 10.3º) which are lower than non-*ortho*-substituted N-aryl rings. The pyridyl nitrogen is also positioned towards C(3)-H rather than N1 of the triazolium ring (i.e. as drawn in Table 7). This may be caused by reduced steric interactions with C(3)-H **321** and/or a stabilising hydrogen bond between the pyridyl nitrogen with C(3)-H **322** (Figure 32). N-Mesityl **267** and N-2,6-dimethoxyphenyl **255** triazoliums have relatively large dihedral angles of 79.51 and 76.63º, respectively. Steric interactions between the *ortho*-methyl groups and the triazolium ring explain the large dihedral angle for N-mesityl. The large N-2,6-dimethoxyphenyl dihedral angle is likely caused by the same steric interactions and electrostatic repulsions between the *ortho*-alkoxy substituents with N1 of the triazolium ring.

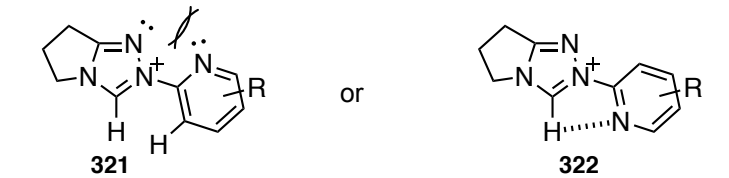

321
Destabilising electrostatic interactions

322
Stabilising intramolecular H-bond

Figure 32: The conformation of the N-pyridyl triazolium salts may be due to a destabilising steric/electrostatic interaction 321 and/or a stabilising intramolecular H-bond 322.

Table 8 shows the dihedral angles between the N-phenyl and triazolium ring for three hydroxyaryl adducts **318** – **320**.[79] The angles are ≥ 65.14º, which is in contrast to the dihedral angle for the N-phenyl triazolium salt **259** which has a dihedral angle of 19.45º. To allow the approach of the aldehyde in the hydroxyaryl adduct forming step, the N-aryl ring must rotate out of plane with the triazolium ring. This will be discussed in more detail in implications for catalysis and chapter 3, where *ortho*-substituted N-aryl triazolium salts usually show enhanced reactivity in catalysis, which is attributed to the larger dihedral angles of the N-aryl ring.

2.2.5 DFT dihedral angle calculations

DFT calculations were carried out to investigate the effect of the dihedral angle between the triazolium and N-aryl rings on the calculated energy, for all triazolium ions shown in Table 7. Calculations were also performed on the ylid/carbene of each triazolium ion,

and also on the proposed dication formed on N1 protonation with *ortho*-heteroatom substituents (Figure 33). The graphs for the ylid/carbene and dication calculations are given in Appendix 1, but the important results are described later in this section. The energy as a function of dihedral angle (N1-N2-C_{ipso}-C_{ortho}) was studied using Gaussian 09[127] on the Durham University Hamilton HPC.[128] The level of theory used was B3LYP/6-31(g), using redundant internal coordinates, with solvent methanol being modelled using an implicit polarisable continuum model (PCM). Calculations were run using 5º steps starting from a dihedral angle of 0º.

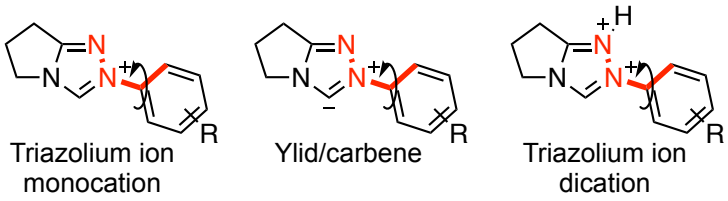

Figure 33: Calculations of energies as a function of dihedral angle of triazolium ion, ylid/carbene and triazolium dication.

2.2.5.1 Triazolium ion monocation calculations

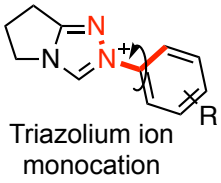

The data are shown in Figures 34– 37 are for all triazolium ions where an X-ray crystal structure could be obtained.

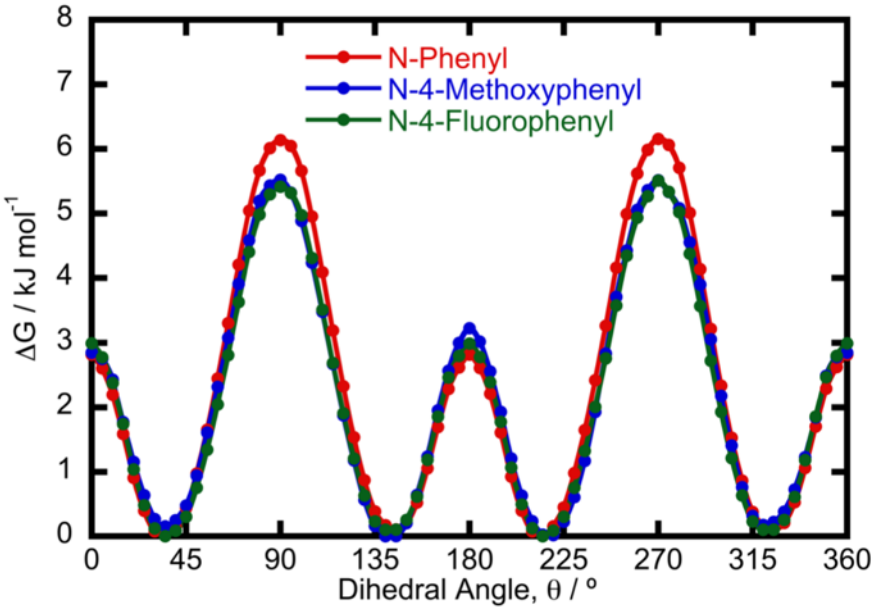

Figure 34: Effect of dihedral angle between N-aryl and triazolium rings on the calculated energy of non-*ortho*-substituted N-aryl triazolium ions using B3LYP/6-31(g) and PCM solvent methanol. Points are calculated energies; solid curve is an interpolation between data points.

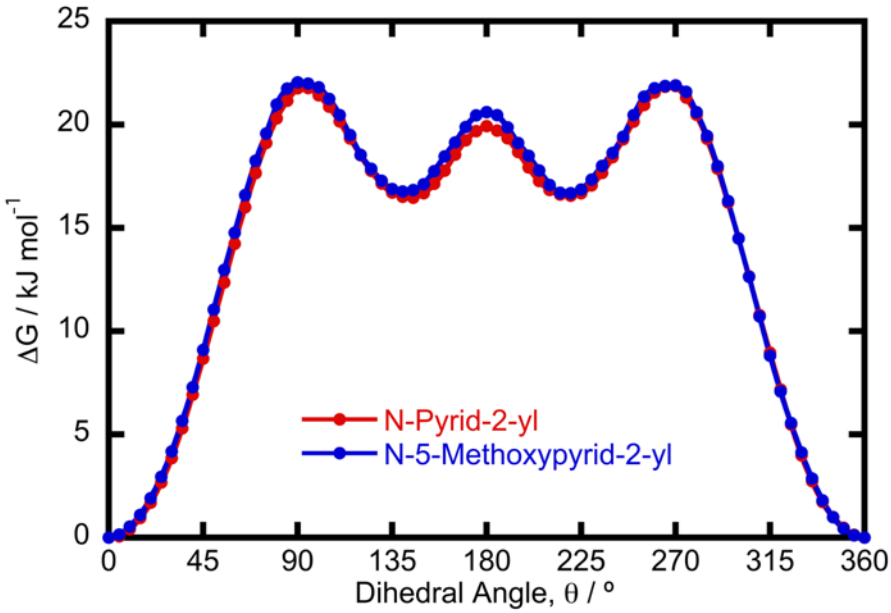

Figure 35: Effect of dihedral angle between N-aryl and triazolium rings on the calculated energy of *ortho*-pyridyl-substituted N-aryl triazolium ions using B3LYP/6-31(g) and PCM solvent methanol. Points are calculated energies; solid curve is an interpolation between data points.

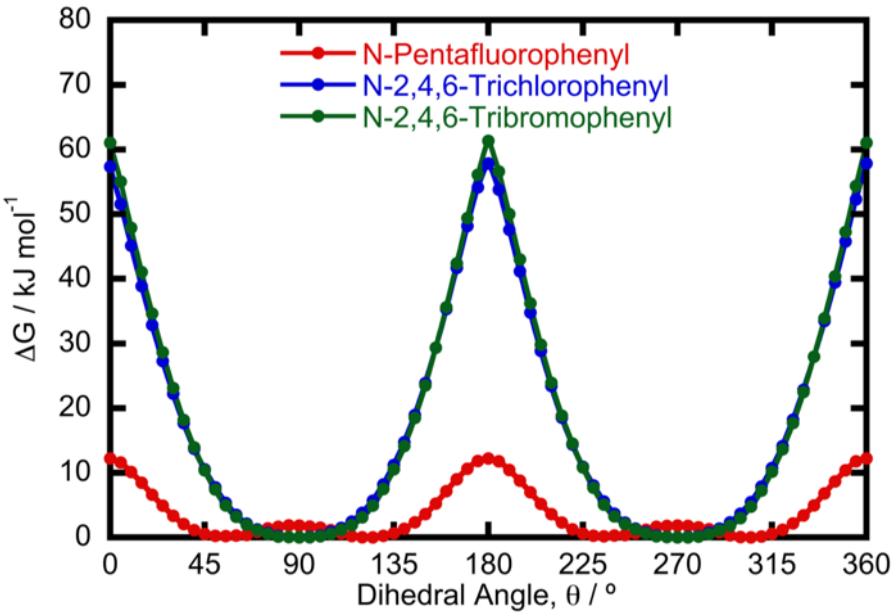

Figure 36: Effect of dihedral angle between N-aryl and triazolium rings on the calculated energy of *ortho*-halo-substituted N-aryl triazolium ions using B3LYP/6-31(g) and PCM solvent methanol. Points are calculated energies; solid curve is an interpolation between data points.

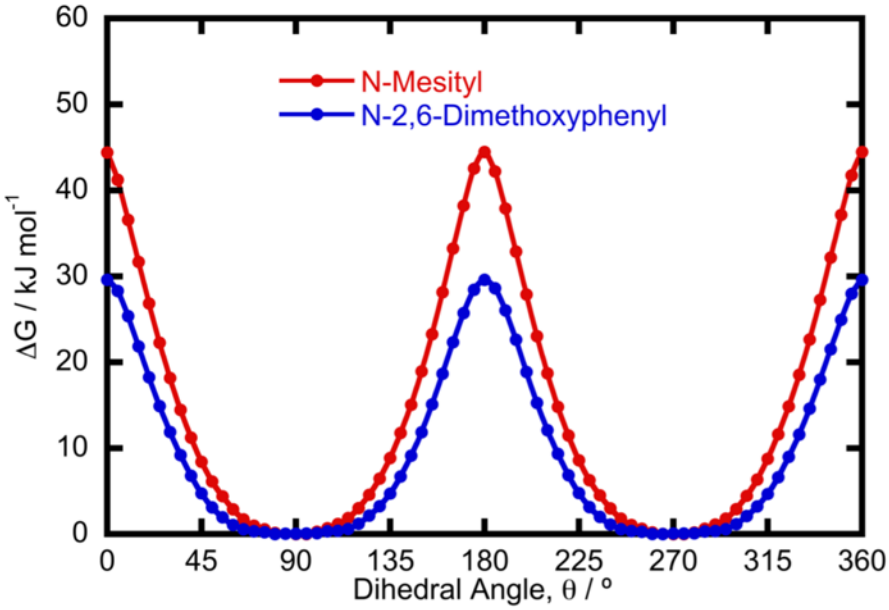

Figure 37: Effect of dihedral angle between N-aryl and triazolium rings on the calculated energy of *ortho*-alkyl and *ortho*-alkoxy-substituted N-aryl triazolium ions using B3LYP/6-31(g) and PCM solvent methanol. Points are calculated energies; solid curve is an interpolation between data points.

A summary of the dihedral angle at the global energy minimum and the free rotation possible at 298 K are given in Table 9. The angles of free rotation were determined by linear interpolation of the two closest data points to an energy of RT = 2.48 kJ mol^{-1}, which is the thermal energy at 298 K.

Table 9: Dihedral angles at the global energy minimum and the range of angles accessible at 298 K.

Triazolium ion	Global energy min. / º	Free rotation at 298 K / º	Triazolium ion	Global energy min. / º	Free rotation at 298 K / º
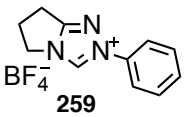 **259**	35	6.5 – 60.2	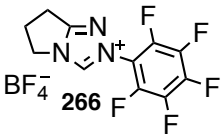 **266**	55	≥ 33.4
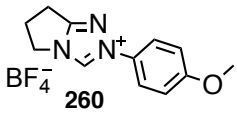 **260**	40	10.7 – 63.7	 **264**	90	≥ 64.5
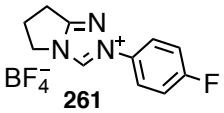 **261**	35	8.7 – 62.8	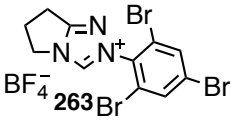 **263**	90	≥ 62.9
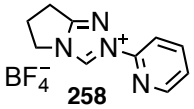 **258**	0	≤ 24.0	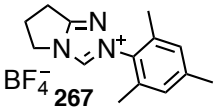 **267**	85	≥ 61.8
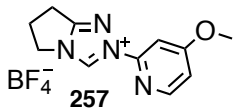 **257**	0	≤ 22.7	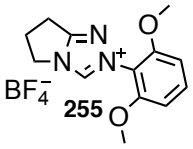 **255**	80	≥ 52.8

[a]DFT dihedral angle calculations were studied using B3LYP/6-31(g) level of theory using redundant internal coordinates, with solvent methanol being modelled using an implicit polarisable continuum model (PCM). [b]Free energy of rotation is defined as the range of dihedral angles that are below thermal energy at 298 K (RT = 2.48 kJ mol^{-1}).

All three non-*ortho*-substituted triazolium salts show global energy minima between 35 – 40º which presumably minimises interactions between the *ortho*-hydrogens of the N-aryl ring with C(3)-H and N1 of the triazolium ring **323** (Figure 38). X-ray crystal structural analysis of all three non-*ortho*-substituted triazolium salts (Table 7) typically gave smaller dihedral angles than the global energy minima, however free rotation at 298 K typically allows angles ≤ 63.7º. An energy maximum appears at 90º i.e. when the triazolium and N-aryl rings are orthogonal.

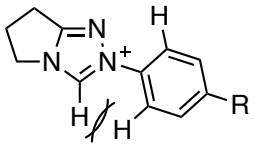

323
R = H, OMe, F

Figure 38: Steric interactions which prevent complete planarity between triazolium and N-aryl rings in non-*ortho*-substituted triazolium salts.

Ortho-pyridyl triazolium salts display conformations in which the pyridyl nitrogen is pointing towards C(3)-H, with a global energy minimum at 0º and free rotation of ≤ 24º. Like non-*ortho*-substituted triazolium salts, there is a global energy maximum at 90º

and a local energy maximum at 180º presumably due to the previously described steric/electrostatic repulsions (Figure 32).

Ortho-halo, *ortho*-alkyl and *ortho*-alkoxy triazolium salts typically adopt larger dihedral angles of ≥ 33.4º for pentafluorophenyl and ≥ 52.8 for the remaining triazolium salts. Interestingly, the pentafluorophenyl triazolium salt shows a local energy maximum at 90º. This may be due to unfavourable electrostatic interactions between the lone pairs of electrons on the *ortho*-fluorine substituents and the π-orbitals of the triazolium ring. The other *ortho*-substituted triazolium salts have a global energy minimum at 90º and an energy maximum at 0º.

2.2.5.2 Carbenes/ylides formed by deprotonation of triazolium ions

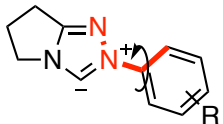

Ylid/carbene

Graphs for these calculations are given in Appendix 1. The dihedral global energy angle minimum for non-*ortho*-substituted systems (**324**, Figure 39) changes from 35 – 40º in the triazolium monocation to 0º in the carbene. There is also an increase in the barrier for rotation from ~ 6 kJ mol^{-1} in the triazolium monocations to > 13 kJ mol^{-1} in the carbenes.

The *ortho*-pyridyl-substituted systems (**325**, Figure 39) show a global energy minimum at 180º in the carbene compared to 0º in the triazolium monocation. This may be due to increased electrostatic repulsions repulsions between the pyridyl lone pair and the lone pair of electrons at C(3).

Ortho-halo, *ortho*-alkyl and *ortho*-alkoxy substituted systems (**326**, Figure 39) show no qualitative change in the shape of the energy graphs as a function of dihedral angle, between the triazolium ion and carbene.

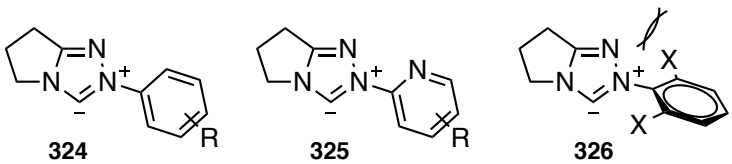

324 **325** **326**

Figure 39: Representation of the most stable conformers for carbenes/ylides.

2.2.5.3 Triazolium ion dications

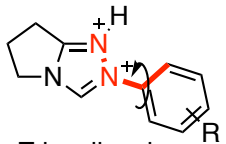

Triazolium ion dication

Graphs for these calculations are given in Appendix 1. These calculations were performed on triazolium salts which have N-aryl *ortho*-heteroatom substituents, where N-phenyl substituted triazolium salt was used as a control.

In the case of N-phenyl triazolium dication (**327**, Figure 40), a global energy maximum occurs at a dihedral angle of 0º compared with 90º for the monocation. This may be attributed to steric hindrance between the *ortho*-hydrogens of the phenyl ring and the proton at N1.

Ortho-pyridyl triazolium dications (**328**, Figure 40) show a global energy minimum at 180º compared to 0º in the triazolium monocation. This may be due to a stabilising intramolecular H-bond between the pyridyl lone pair and the proton at N1.

Ortho-halo triazolium dications (**329**, Figure 40) show a global energy maximum at 0º which is also observed in the monocations, although in the case of N-pentafluorophenyl system, it is reduced from ~ 12 to ~ 7 kJ mol^{-1}. This suggests that although there is slight stabilising effect only in the case of the N-pentafluorophenyl system, the interaction between N1-H and the *ortho*-halo substituents is still unfavourable.

Interestingly, in the case of the N-2,6-dimethoxyphenyl system (**330**, Figure 40), there is a stabilising interaction between N1-H and the *ortho*-alkoxy substituents. The global energy minimum changes from 90º in the triazolium monocation to 15º in the dication suggesting the presence of an intramolecular H-bonding interaction.

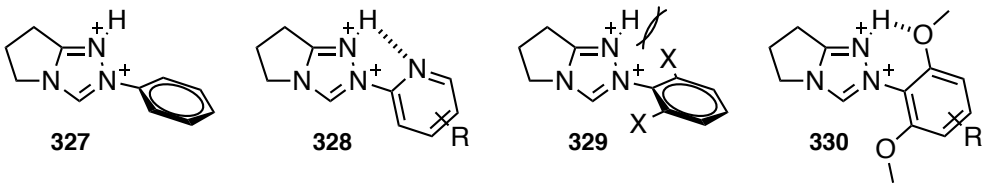

Figure 40: Representation of the most stable conformers for triazolium dications with *ortho*-heteroatom substituents.

2.2.6 Is N1 protonation occurring?

N1 protonation was previously proposed for describing the additional pathways for C(3)-H/D exchange for *ortho*-halo-substituted triazolium salts as a means of reducing

lone pair – lone pair repulsions between N1 and the *ortho*-halo substituents. The X-ray crystal structures for these triazolium salts indicates that the dihedral angle between the triazolium and N-aryl rings are typically ≥ 62º. The DFT global energy minima for the three triazolium salts are ≥ 55º. Based on these results, it seems unlikely that the triazolium and N-aryl rings would become coplanar, where the electrostatic repulsion would be significant.

Calculations were also carried out on dications of N-aryl *ortho*-heteroatom systems. Although there appears to be a stabilising interaction between N1-H and the *ortho*-substituents for *ortho*-pyridyl and N-2,6-dimethoxyphenyl systems, this is not observed for *ortho*-halo systems.

A chemical shift analysis for the N-pentafluorophenyl triazolium salt (Figure 24) shows that there is no evidence for an N1 deuteronation in the pD region which would lead to an increase in the chemical shift of C(3)-H. This of course does not rule out an N1 deuteronation in the Hammett acidity region (pD < 0). Fluorine is the smallest halogen substituent in the series and displayed the smallest dihedral angles in the X-ray crystal structure (Table 7) and DFT calculations (Table 9). It may be predicted that the N-pentafluorophenyl triazolium salt would have the greatest tendency to become coplanar out of the three halogenated triazolium salts. If an N1 protonation is occurring, it is likely to have a $pK_a^{N1} \leq -2$ which is not accessible under ideal solution conditions.

The crystal structures and DFT calculations for the *ortho*-pyridyl triazolium salts show that the lowest energy conformations are when the pyridyl nitrogen is pointing away from N1. There would not be a requirement for a protonation at N1 to reduce electrostatic repulsions with the *ortho*-pyridyl N-aryl ring.

Based on electronic arguments, *ortho*-alkoxy substituents would be expected to increase the pK_a^{N1}. But again the larger dihedral angles in the solid state structure and DFT calculation, as well as a slight decrease in the chemical shift of C(3)-H (Figure 24) would suggest that if an N1 protonation is occurring, it would also have a $pK_a^{N1} \leq -2$.

While the additional pathways pose interesting mechanistic questions, the next question then is how relevant are these additional pathways for C(3)-H/D exchange to synthetic applications of these NHC precatalysts? The triazolium salts are usually deprotonated *in situ* with the aid of an organic or inorganic base in a large range of organic solvents, conditions where triazolium protonation to give a dication would be unlikely.

The next section looks at a Hammett correlation for the second order rate constants for deuteroxide ion catalysed C(3)-H/D exchange, k_{DO} (M^{-1} s^{-1}). These results help rationalise why *ortho*-substituted N-aryl triazoliums are superior to non-*ortho*-substituted N-aryl triazoliums in catalysis.

2.2.7 Hammett correlation

To provide additional insight into the observed reactivity of *ortho*-substituted triazolium salts, a Hammett plot was made using second order rate constants for the *ortho*-alkoxy triazolium salts reported here, and previously reported non-*ortho*- and *ortho*-substituted triazolium salts.[58,59] The σ and k_{DO} values are shown in Table 10. Figure 41 shows the correlation between Hammett substituent constants, σ, and the second order rate constants for C(3)-H/D exchange, k_{DO} (M^{-1} s^{-1}). In this plot, σ_{para} values were used for *ortho*-substituents and we have assumed that (1) for multiply substituted triazolium salts, Hammett substituent constants are approximately additive[129] and (2) the large dihedral angles for *ortho*-substituted N-aryl rings means that steric and H-bonding effects on C(3)-H/D exchange are not significant. An excellent correlation is found separately for *ortho* and non-*ortho*-substituted N-aryl rings, with reaction constants of ρ = + 0.79 (R^2 = 0.991) and + 0.96 (R^2 = 0.997), respectively.

Table 10: Hammett substituent constants, σ, and logarithimic (base 10) second order rate constants for deuteroxide ion catalysed exchange, k_{DO} (M^{-1} s^{-1}), used in the Hammett correlation shown in Figure 41.

Triazolium Salt	σ	log (k_{DO} / M^{-1} s^{-1})	Triazolium Salt	σ	log (k_{DO} / M^{-1} s^{-1})
 **260**	σ_p = -0.27	7.62[a]	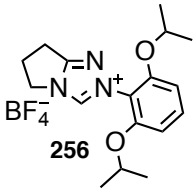 **256**	2 × σ_p = -0.90	7.46
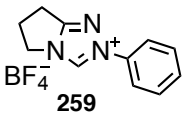 **259**	0	7.83[a]	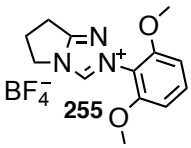 **255**	2 × σ_p = -0.54	7.59
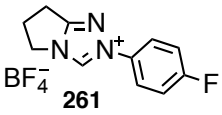 **261**	σ_p = 0.062	7.94[a]	 **267**	2 × σ_p = -0.51	7.72[a]
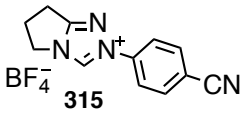 **315**	σ_p = 0.66	8.50[a]	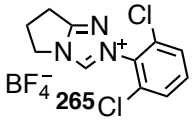 **265**	2 × σ_p = 0.454	8.43[b]
			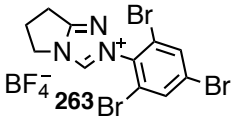 **263**	3 × σ_p = 0.696	8.63[b]
			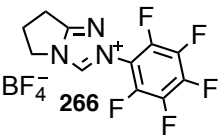 **266**	($3 \times \sigma_p$) + ($2 \times \sigma_m$) = 0.86	8.83[a]

[a]Values of k_{DO} (M^{-1} s^{-1}) were taken from R. S. Massey *et al.*[58] [b]Values of k_{DO} (M^{-1} s^{-1}) were taken from D. E. Tucker *et al.*[59]

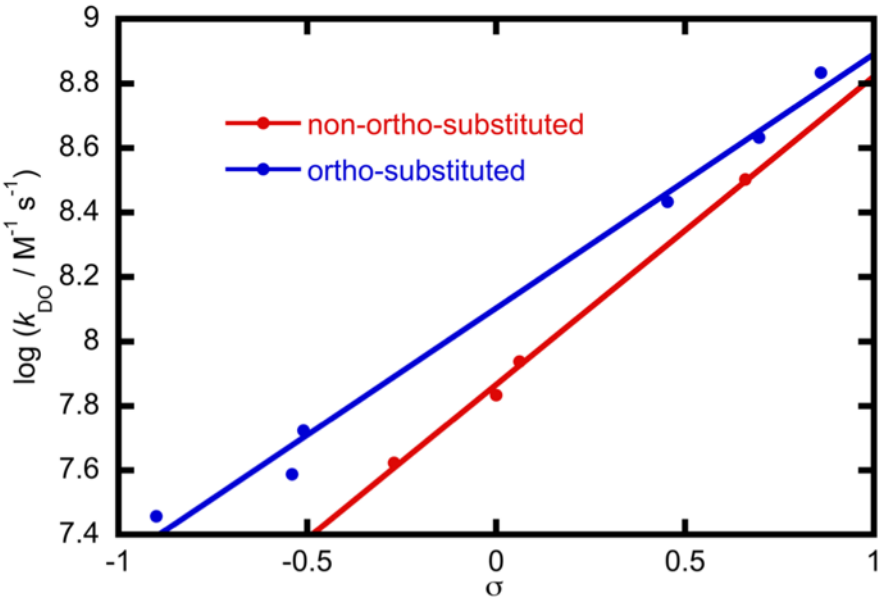

Figure 41: Hammett plot showing the relationship between second order rate constants for deuteroxide ion catalysed exchange, k_{DO} (M^{-1} s^{-1}), and Hammett constants for non-*ortho*-substituted (●) and *ortho*-substituted (●) triazolium salts.

Non-*ortho*-substituted triazoliums display a reaction constant of ρ = +0.96 which suggests that C(3)-H/D exchange is only mildly less sensitive to substituents than in the case of benzoic acid dissociation. The distance between the substituents and the site of negative charge is approximately the same as in benzoic acid **332** (Figure 42). However, the lone pair of electrons in the carbene reside in an sp^2 hybridised orbital on C(3) which cannot be stabilised by delocalisation.

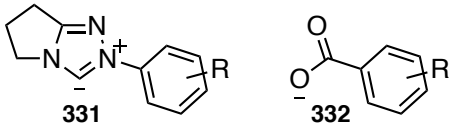

331 **332**

Figure 42: Similar distance between developing negative charge from R substituted aryl ring in triazolium ion and benzoic acid.

Ortho-substituted triazoliums display a smaller reaction constant of ρ = +0.79 which indicates a lower sensitivity to substituents than non-*ortho*-substituted N-aryl triazoliums. This weaker sensitivity may be due to the over estimation of substituent constants caused by partial cancellation – the effect of each substituent may be smaller due to the presence of multiple substituents. This would have the effect of decreasing $|\sigma_{Total}|$ values and therefore increasing the gradient of the slope. The weaker sensitivity may also be due to the fact that π-orbital overlap between the two rings is poorer than in the non-*ortho*-substituted triazolium salts. Resonance between the two rings leads to a greater sensitivity to the substituent.

Scheme 56 shows two of the resonance structures that are possible for non-*ortho*-substituted N-aryl triazoliums (**334** and **335**). The same resonance is not possible for *ortho*-substituted N-aryl triazoliums and so the transmission of polar effects is purely through the σ-bond between N2 and C_{ipso}. The Hammett ρ values for acid dissociation of substituted β-phenylpropionic acid **336** and *trans*-cinnamic acid **337** (Figure 43) are +0.21 and +0.47,[130] respectively, and is due to greater transmission of polar effects via the double bond connecting the carboxylic acid to the aryl ring.

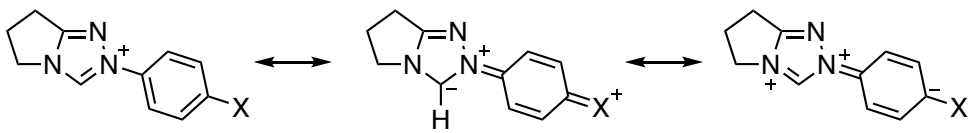

333 **334** **335**

Scheme 56: Resonance structures possible for non-*ortho*-substituted triazolium salts demonstrating a possible ground state stabilisation for non-*ortho*- substituents.

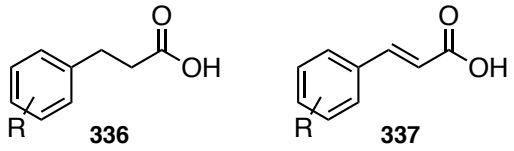

Figure 43: Hammett ρ values for acid dissociation of substituted β-phenylpropionic acid and *trans*-cinnamic acid.[130]

The slope for *ortho*-substituted N-aryl triazoliums lies above that for non-*ortho*-substituted triazolium salts. This may either be due to greater ground state destabilisation of the ground state triazolium or stabilisation of the transition state for *ortho*-substituted triazoliums compared to non-*ortho*-substituted triazoliums, which has the overall effect of lowering the energy barrier for deprotonation.

2.2.7.1 Ground state or transition state effect?

The kinetic data and DFT calculations using a dihedral scan do not allow us to unambiguously attribute the observed rate constants to a predominantly ground or transition state effect, but both options are briefly discussed.

In terms of a predominantly ground state effect, at 298 K there is enough thermal energy for non-*ortho*-substituted N-aryl triazoliums to adopt dihedral angles between 10 – 60º, with an energy minimum between 35 – 40º. This would allow sufficient overlap between the molecular orbitals between the triazolium and N-aryl rings. N-2,4,6-trichlorophenyl **264**, N-2,4,6-tribromophenyl **263** and N-mesityl **267** triazoliums are able to adopt dihedral angles between 65 – 90º, while N-2,6-dimethoxyphenyl **255** can adopt angles between 55 – 90º. Increased steric and electrostatic repulsions between *ortho*-substituents and the triazolium ring prevent N-aryl triazoliums from adopting a dihedral angle that would allow resonance between the two rings. Since *ortho*-substituted N-aryl triazoliums cannot benefit from a resonance stabilising effect, the cationic charge of the triazolium is both less sensitive to substituents on the N-aryl ring and also more localised. This leads to increased lability of C(3)-H.

Alternatively, a transition state stabilisation for *ortho*-substituted N-aryl triazoliums may be responsible for the rate enhancement. On deprotonation, a negative charge resides in an sp^2 hybridised orbital on C(3) which cannot be stabilised by delocalisation. Since the lone pairs on adjacent nitrogen atoms are more localised in the triazolium ring, this may lead to a greater stabilising effect through greater donation into the empty p orbital of C(3). Non-*ortho*-substituted triazolium salts would allow the lone pair on

N2 to participate in resonance in both rings and this may destabilise the carbene relative to *ortho*-substituted triazolium salts.

DFT calculation of the dihedral angle energies of the carbene/ylide suggests that the lowest energy conformation of the deprotonated triazolium salt has a dihedral angle θ = 0º. There is also a larger barrier to rotation for non-*ortho*-substituted triazolium salts compared to the ground state. If it is more stabilising to be planar in the intermediate, and therefore the transition state, and the C(3)-H/D exchange kinetics show that there is a smaller barrier to deprotonation for *ortho*-substituted triazolium salts then the effect is more likely to be a ground state destabilisation effect.

2.2.8 Implications for catalysis

In general, it has been found that *ortho*-substituted triazolium salts lead to enhanced equilibrium constants for adduct formation with aryl aldehydes.[25,79] Considering the initial proton transfer equilibria discussed here and results on hydroxyaryl adduct formation discussed in chapter 3, this is likely due to the steric effects in *ortho*-substituted triazoliums. Structural and kinetic data suggest that *ortho*-substituted N-aryl triazoliums destabilise the triazolium ion relative to the transition state for deprotonation. This leads to a higher concentration of reactive carbene in solution. The larger dihedral angles between the rings also assist the approach of the electrophile, which is usually an aryl aldehyde.

X-ray crystal structures of hydroxyaryl adducts formed from N-phenyl catalyst with three aryl aldehydes[79] show that the N-phenyl ring has rotated from 19.45 to 65 – 68º. It may be suggested that non-*ortho*-substituted N-aryl rings stabilise the triazolium ground state to a greater extent than *ortho*-substituted N-aryl rings. The rate of deprotonation is slowed due to a resonance stabilising effect between the two rings, something that is less possible for *ortho*-substituted N-aryl rings. Once the carbene/ylide has formed, there is an energetic penalty that non-*ortho*-substituted triazoliums must pay to rotate the N-aryl ring to accommodate the approach of the electrophile. For steric and electronic reasons, *ortho*-substituted N-aryl rings do not need to pay the same energetic penalty and so aid a faster nucleophilic addition.

The additional pathways for C(3)-H/D exchange which are evident for some of the triazoliums at lower pD present interesting questions on mechanism, but it has been concluded that if N1 protonation is occurring, it has a $pK_a^{N1} \leq -2$. Under synthetic conditions where a base or basic buffer are in use, it is unlikely that a protonation at N1

would be significant. A protonation at N1 does not explain the advantage *ortho*-substituents on the N-aryl ring have in catalysis.

Ortho-pyridyl triazolium salts appear to increase the rate of deprotonation via either an intramolecular deprotonation (direct or via solvent) or by initial protonation of the pyridyl nitrogen to give a more reactive dicationic triazolium salt. For N-5-methoxypryid-2-yl triazolium salt, specific base catalysis is the dominant mechanism above pD 2. Whether intramolecular deprotonation would occur under synthetic conditions depends on the choice of base and solvent. Further work could explore the potential of intramolecular bases for increasing the rates of carbene and Breslow intermediate formation.

2.3 Conclusions and future work

While it has been clear for some time that *ortho*-substituted N-aryl rings are advantageous in catalysis, the reason for this phenomenon has not been well understood. In an attempt to aid catalyst design/choice, it is proposed that non-*ortho*-substituted triazoliums are stabilised relative to *ortho*-substituted triazoliums. Additional pathways for C(3)-H/D exchange that are evident for *ortho*-heteroatom N-aryl triazoliums raise interesting mechanistic questions, but it may be concluded that whatever is causing this is not primarily responsible for the catalytic advantage observed for *ortho*-substituted N-aryl triaoliums. *Ortho*-substituted N-aryl triazoliums are destabilised by rotation of the N-aryl ring away from planarity with the triazolium ring. The same rotation also accounts for relatively faster rates of addition into electrophiles (chapter 3).

Chapter 3: Hydroxyaryl adduct formation

3.1 Aims

This chapter details the rate and equilibrium constants obtained for hydroxyaryl adduct formation based on three non-*ortho*-substituted (**259** - **261**) and four *ortho*- (**267**, **341**, **255** and **256**) N-aryl triazolium salts (Figure 44) and three aryl aldehydes: benzaldehyde, *para*- and *ortho*-methoxybenzaldehyde (**338** – **340**, Figure 44). Although kinetic studies were attempted for **264** and **266**, it was found that these triazolium ions decompose under these reaction conditions.

Initially, ^{1}H and ^{13}C NMR chemical shifts of the three aryl aldehydes are examined to gain information on the electron density of the molecules, particularly at the carbonyl carbon (Figure 44). *Ortho*-methoxybenzaldehyde is a crystalline solid, and so an X-ray crystal structure and DFT calculation could be used to study whether the enhanced rate and equilibrium constants previously observed[25] for formation of the hydroxyaryl aryl adduct with *ortho*-methoxybenzaldehyde is a ground state destabilisation effect. Next, the effect of the N-aryl substituent of the triazolium salt, on the rate and equilibrium constants are studied (Scheme 57). Taken together, the data provides insight into the observed reactivity and equilibria.[25,79]

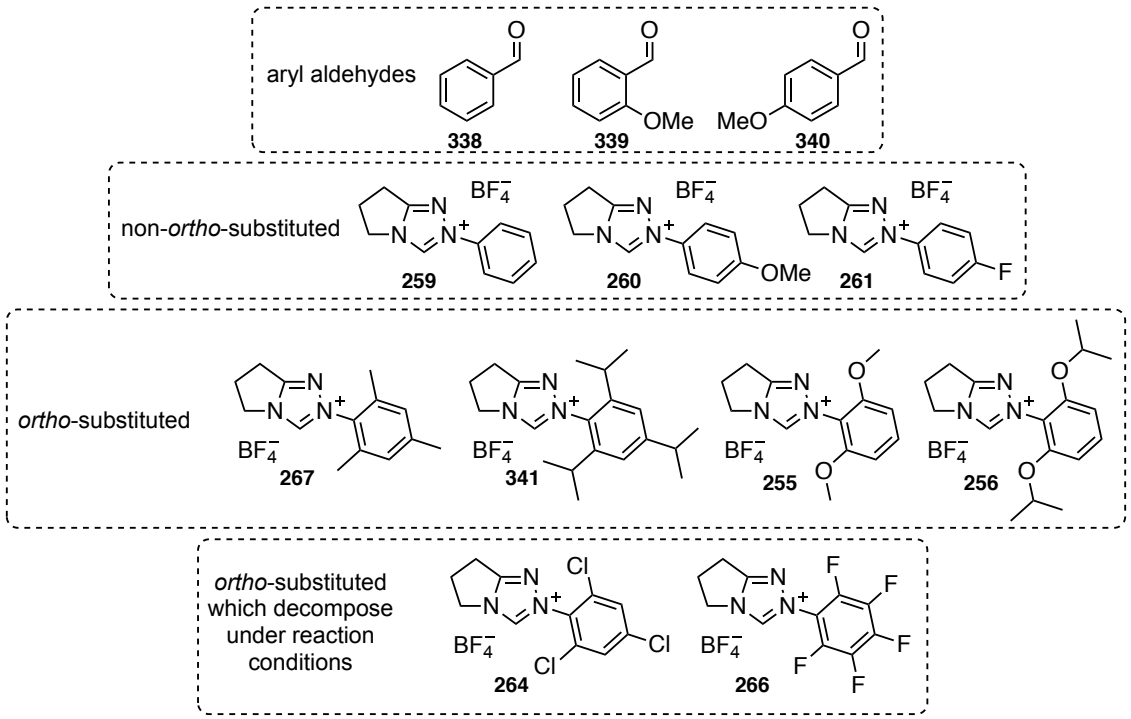

Figure 44: Aryl aldehydes and non-*ortho*- and *ortho*-substituted triazolium salts studied in this chapter. Also shown are two triazolium salts (264 and 266) which were unstable under these reaction conditions and therefore reliable data could not be obtained for these triazolium salts.

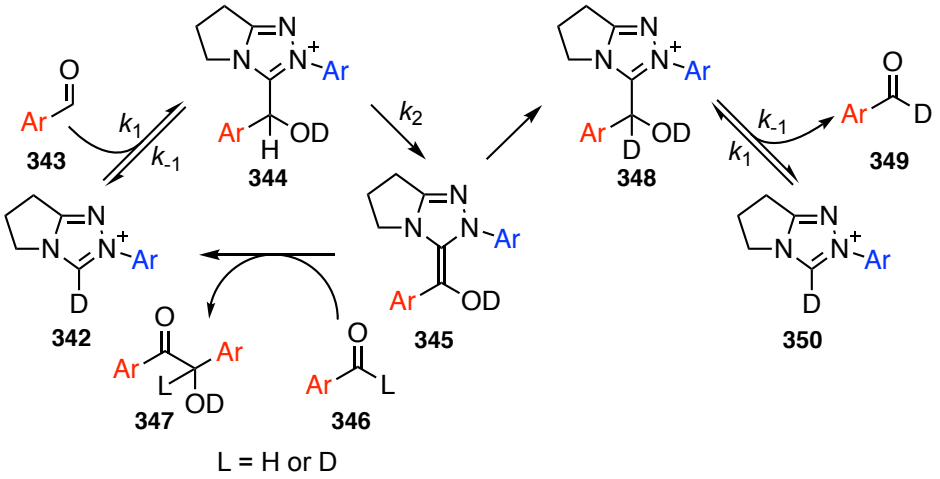

Scheme 57: Mechanism of the benzoin condensation studied in this chapter, with the three rate constants which can be obtained (k_1, k_{-1} and k_2).

3.2 Results and discussion

3.2.1 Aldehyde structure

The ^{1}H and ^{13}C NMR chemical shifts of the three aryl aldehydes are shown in Table 11. The aldehydic proton (H^1) decreases in chemical shift in the order *ortho*-methoxybenzaldehyde **339** > benzaldehyde **338** > *para*-methoxybenzaldehyde **340**. This order may either be due to the inductive electron withdrawing effect of the *ortho*-methoxy substituent, or a small degree of intramolecular H-bonding (Figure 45). This may initially be construed as *ortho*-methoxybenzaldehyde **339** being more electrophilic than benzaldehyde **338**. However, the aldehydic carbon (C^1) signal decreases in the order benzaldehyde **338** > *para*-methoxybenzaldehyde **340** > *ortho*-methoxybenzaldehyde **339**. This suggests that the order of electrophilicity follows the order benzaldehyde **338** > *para*-methoxybenzaldehyde **340** > *ortho*-methoxybenzaldehyde **339**.

Table 11: ^{1}H and ^{13}C NMR chemical shifts for the three aryl aldehydes studied obtained in CD_3OD at 25 °C.

Position	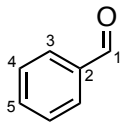		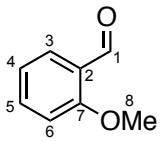		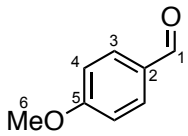	
	^{1}H / ppm	^{13}C / ppm	^{1}H / ppm	^{13}C / ppm	^{1}H / ppm	^{13}C / ppm
1	9.98	192.8	10.39	189.8	9.82	191.4
2	-	136.6	-	124.6	-	129.9
3	7.88-7.91	129.2	7.74	127.7	7.85	131.7
4	7.56	128.7	7.03	120.3	7.07	114.1
5	7.66	134.2	7.15	111.8	-	165.0
6	-	-	7.61	136.1	3.88	54.8
7	-	-	-	162.1	-	-
8	-	-	3.93	54.9	-	-

[a]^{1}H and ^{13}C NMR chemical shifts were referenced using the methanol-d_4 solvent signals at 3.31 and 49.00 ppm, respectively.

The resonance structures that are consistent with the chemical shifts in Table 11 are shown in Figure 45. The more electron rich C^1 and C^2 of *ortho*-methoxybenzaldehyde suggest that the deshielding of H^1 is mostly due to intramolecular H-bonding with the *ortho*-methoxy substituent.

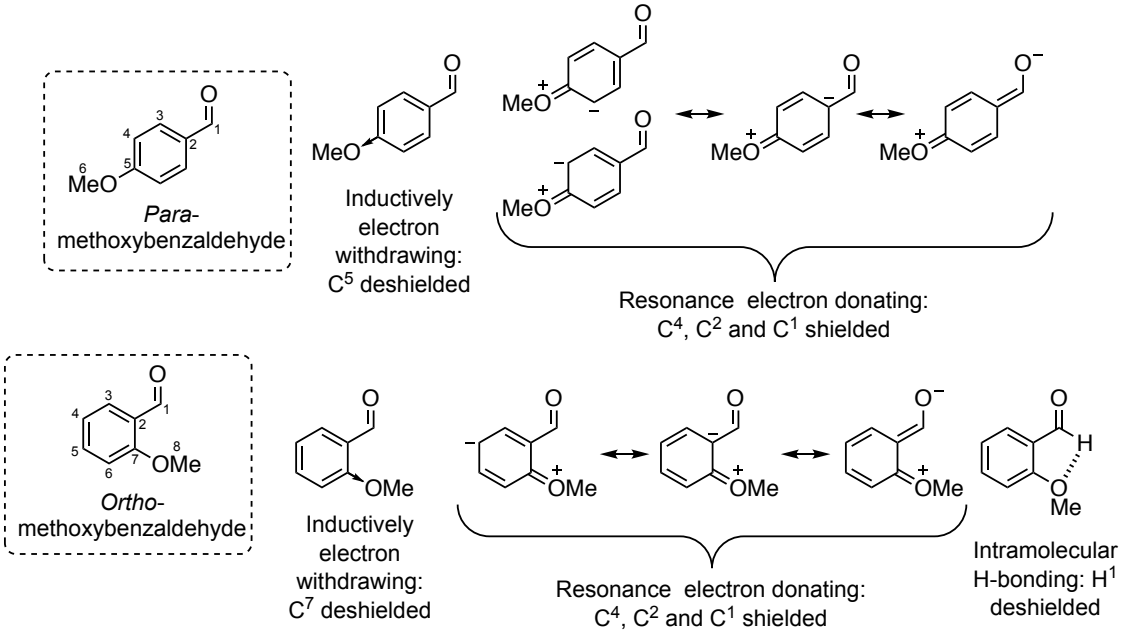

Figure 45: The effect of the methoxy substituent in *para*- and *ortho*-methoxybenzaldehyde on the ^{1}H and ^{13}C NMR chemical shifts, with deshielding and shielding referenced relative to values for benzaldehyde.

As *ortho*-methoxybenzaldehyde **339** is a crystalline solid, an X-ray crystal structure was obtained. Figure 46 shows the ORTEP diagram obtained with two dihedral angles, relative to the plane of the aryl ring, for the carbonyl and *ortho*-methoxy substituent. The carbonyl dihedral angle (O1-C7-C1-C6) is 4.9º, which suggests that the *ortho*-methoxy substituent does not cause the carbonyl to rotate out of the plane of aryl ring. The *ortho*-methoxy substituent also adopts a conformation which allows the lone pair of electrons at sp^3 hybridised O2 to overlap with the aryl π-system.

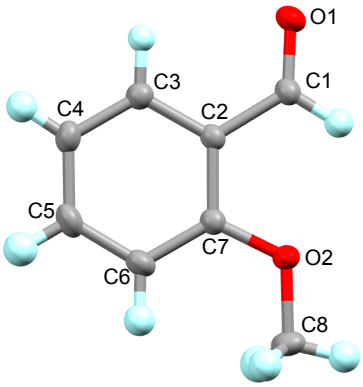

Dihedral angles:

O1-C1-C2-C3 = 4.9º

C8-O2-C7-C6 = 4.1º

Figure 46: ORTEP diagram of *ortho*-methoxybenzaldehyde showing relevant dihedral angles.

The energy as a function of the carbonyl dihedral angle (O1-C1-C2-C3) was studied using DFT calculations in Gaussian 09[127] using the Durham University Hamilton HPC.[128] The level of theory used was B3LYP/6-31(g), using redundant internal coordinates and with solvent methanol modelled using an implicit polarisable continuum model (PCM). Calculations were run using 5º steps starting from a dihedral angle of 0º. The results are shown in Figure 47 and clearly demonstrate the energetic preference for the carbonyl to remain coplanar with the aryl ring. The global energy minimum is a dihedral angle (O1-C1-C2-C3) of 0º, with an additional local minimum at 180º.

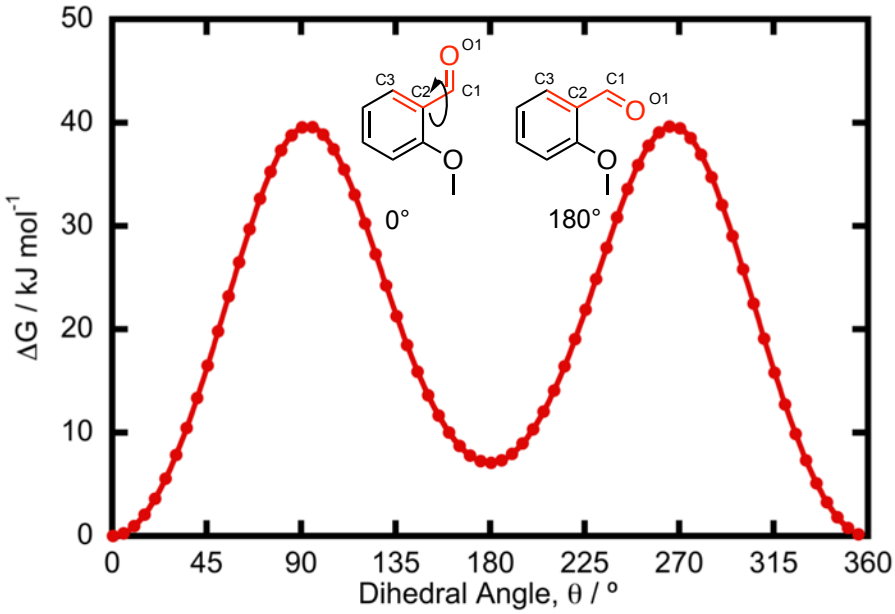

Figure 47: Effect of dihedral angle between O1-C1 and C2-C3 on the energy of *ortho*-methoxybenzaldehyde using B3LYP/6-31(g) and PCM solvent methanol. Points are calculated energies; solid curve is an interpolation between data points.

The X-ray crystal structure and DFT calculations of *ortho*-methoxybenzaldehyde demonstrate that the enhanced rate constant[79] observed for addition of the N-phenyl triazolyl carbene to *ortho*-methoxybenzaldehyde compared to benzaldehyde is unlikely to be a ground state destabilisation effect. An alternative reason for the rate enhancement will be suggested later in the text. The next section gives the results of the effects of *ortho*- and non-*ortho*-substituted N-aryl triazolium substituents on the rate and equilibrium constants associated with the adduct formation/dissocation, and the rate constant for formation of the Breslow Intermediate (BI).

3.2.2 Hydroxyaryl adduct formation

The formation of 3-(hydroxyaryl)azolium adducts under stoichiometric conditions from four *ortho*-substituted catalysts (N-mesityl **267**, N-2,4,6-triisopropylphenyl **341**,[131] N-2,6-dimethoxyphenyl **255** and N-2,6-diisopropoxyphenyl **256**) and three non-*ortho*-substituted catalysts (N-phenyl **259**, N-4-methoxyphenyl **260** and N-4-fluorophenyl **261**) with three aryl aldehydes (benzaldehyde **338**, *ortho*- **339** and *para*-methoxybenzaldehyde **340**) were followed in buffered CD_3OD at 25 °C by ^1H NMR spectroscopy. The conditions were chosen to match those used previously.[25,73]

Based on previous kinetic work on the thiazolylidene[73] and triazolylidene catalysed benzoin condensation[78] described in chapter 1, the following assumptions are made: (1) at stoichiometric concentrations of triazolium salt precatalyst, the reaction is first order with respect to triazolium salt and aryl aldehyde and (2) triethylamine is required as a

catalytic base in both formation and dissociation of the hydroxyaryl adduct and therefore k_1 is a pseudo second order rate constant and k_{-1} is a pseudo first order rate constant.

The procedure for initiating kinetic experiments was as follows: triazolium precatalyst and triethylamine buffer were dissolved in CD_3OD and incubated at 25 °C and the kinetics were initiated by transferring this solution to the aryl aldehyde, and transferring to an NMR tube. Final concentrations of triazolium salt and aryl aldehyde were equal at 0.08 M, while the concentration of the basic and acidic forms of the triethylamine buffer were 0.107 and 0.053 M, respectively. A calculated pD was determined from the chemical shift of the quartet due to the protons on triethylamine adjacent to the nitrogen atom, where the triethylammonium pK_a = 10.78 in methanol.[132] Reaction solutions in NMR tubes were thermostatted in the NMR spectrometer at 25 °C, and the progress of the reaction was followed for 12 – 16 hours with spectral acquisitions made at approximately 4 minute intervals.

Concentrations of triazolium salt precatalyst, aryl aldehyde, 3-(hydroxyaryl)azolium adduct and benzoin product were determined by converting relevant integrals for isolated signals to concentrations using the known initial concentration of triazolium salt precatalyst. ^{1}H NMR signals were generally chosen that were resolved from adjacent signals. An NMR overlay for the reaction between N-phenyl triazolium salt **259** and *ortho*-methoxybenzaldehyde **339** is shown in Figure 48. In this figure the signals due to total concentrations of triazolium salt (A_T), aldehyde (B_T) and hydroxyaryl adduct (C_T) are highlighted with reference to Scheme 58. Also shown are the signals due to the aldehydic proton (B_H) and the C(α)-H of the hydroxyaryl adduct (C_H), both of which are H/D exchangeable, and also the C-H of the benzoin product (D_H).

In this reaction (Figure 48), the signal due to the catalyst (A_T) overlaps that due to one of the diastereotopic hydroxyaryl adduct protons (C_T^{α}). To determine the total concentration of catalyst, the integral of the signal due to the non-overlapping diasterotopic proton (C_T^{β}) was subtracted from the total integral of the catalyst and the overlapping diastereotopic proton ($A_T + C_T^{\alpha}$) according to Eqn. (8). It is assumed that there is a 1:1 ratio of these diastereotopic protons, which is observed for related reactions where this signal overlap does not occur.

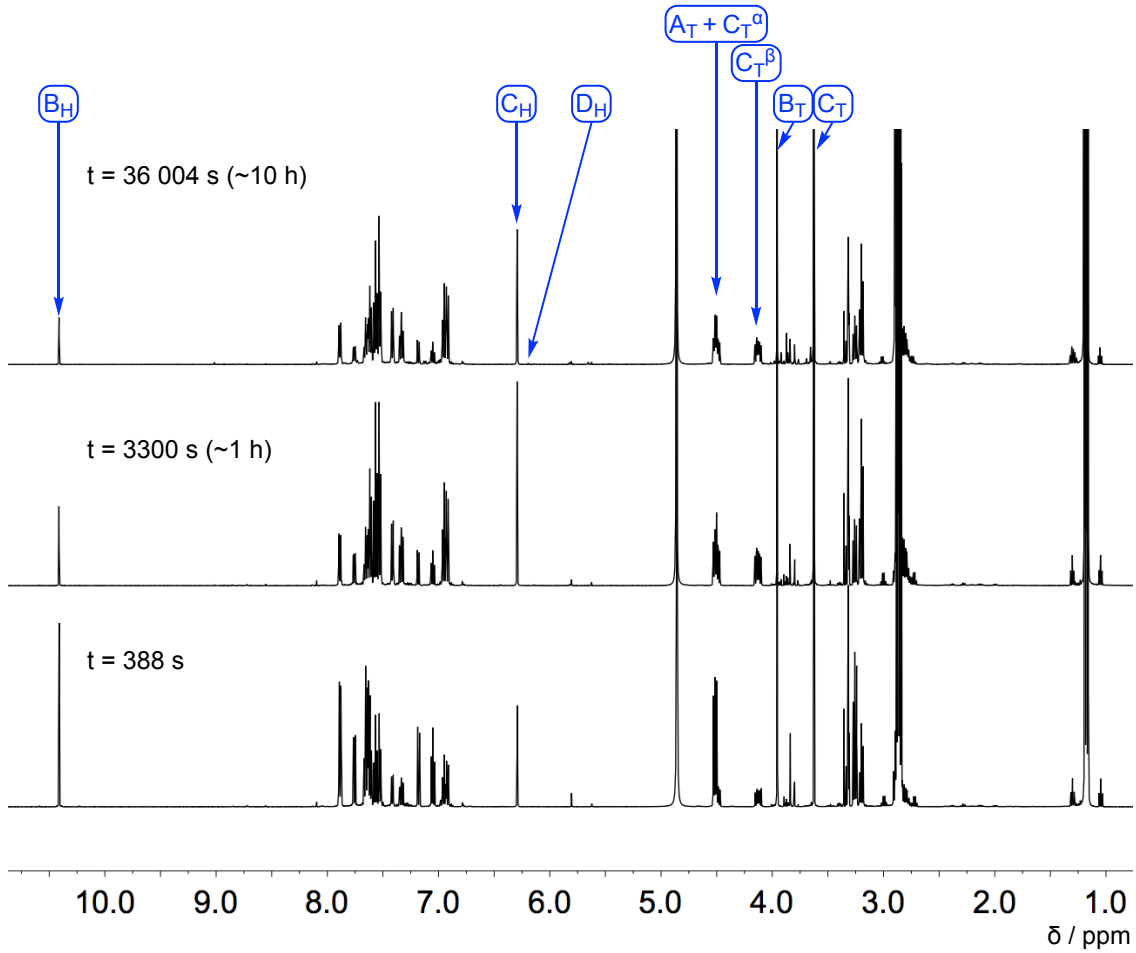

Figure 48: Representative ^{1}H NMR spectral overlay for the reaction between N-phenyl triazolium salt 259 and *ortho*-methoxybenzaldehyde 339 in CD_3OD at 25 °C taken at t = 388, 3300 and 36 004 seconds.

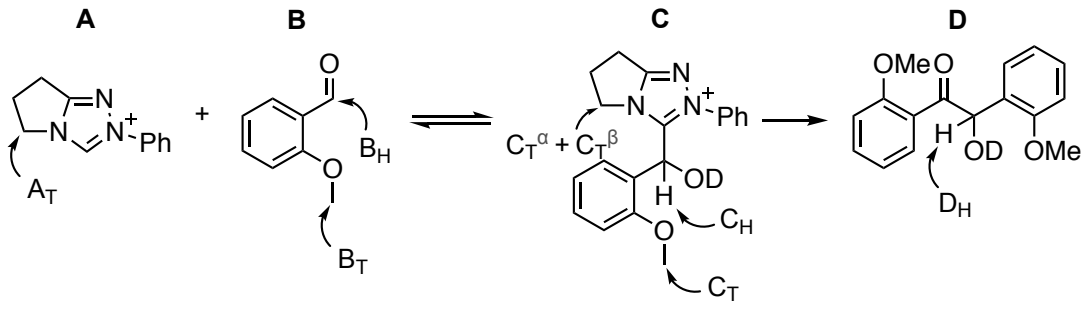

Scheme 58: ^{1}H NMR signals monitored during the reaction progress.

$$A_T = (A_T + C_T^{\alpha}) - C_T^{\beta} \tag{8}$$

The triazolium catalysts shown in Table 12 were stable under the reaction conditions. It was therefore assumed that the total concentration of catalyst ($[A_T]_t$) and hydroxyaryl adduct ($[C_T]_t$) at time *t* were equal to the initial concentration of triazolium salt ($[A_T]_{t=0}$), as no additional catalyst-derived species are present, as described by Eqn. (9).

The concentrations of N-phenyl triazolium precatalyst **259**, *ortho*-methoxybenzaldehyde **339**, hydroxaryl adduct and benzoin were determined according to equations 10 – 15. The method of determining concentrations for all other combinations of triazolium salt and aldehyde was adapted based on the signals that were integrated easily. The concentration of aldehyde and benzoin product were determined relative to this value.

$$[A_T]_{t=0} = [A_T]_t + [C_T]_t = 0.08M \tag{9}$$

$$[A_T] = \left\{ \frac{\frac{(A_T + C_T^{\alpha}) - C_T^{\beta}}{2}}{\frac{(A_T + C_T^{\alpha}) - C_T^{\beta}}{2} + \frac{C_T}{3}} \right\} \times 0.08M \tag{10}$$

$$[B_T] = \left\{ \frac{\frac{B_T}{3}}{\frac{(A_T + C_T^{\alpha}) - C_T^{\beta}}{2} + \frac{C_T}{3}} \right\} \times 0.08M \tag{11}$$

$$[B_H] = \left\{ \frac{B_H}{\frac{(A_T + C_T^{\alpha}) - C_T^{\beta}}{2} + \frac{C_T}{3}} \right\} \times 0.08M \tag{12}$$

$$[C_T] = \left\{ \frac{\frac{C_T}{3}}{\frac{(A_T + C_T^{\alpha}) - C_T^{\beta}}{2} + \frac{C_T}{3}} \right\} \times 0.08M \tag{13}$$

$$[C_H] = \left\{ \frac{C_H}{\frac{(A_T + C_T^{\alpha}) - C_T^{\beta}}{2} + \frac{C_T}{3}} \right\} \times 0.08M \tag{14}$$

$$[D_H] = \left\{ \frac{D_H}{\frac{(A_T + C_T^{\alpha}) - C_T^{\beta}}{2} + \frac{C_T}{3}} \right\} \times 0.08M \tag{15}$$

The rate constants for the formation, k_1 (M^{-1} s^{-1}), and dissociation, k_{-1} (s^{-1}), of the 3-(hydroxybenzyl)azolium adducts were determined from fitting software (Berkeley Madonna[**]), where a simplified version of the model shown in Scheme 57 was used. The model only takes into account the total concentration of triazolium salt, aryl aldehyde, hydroxaryl adduct and benzoin-H, where the ^{1}H NMR signals chosen did not H/D exchange under these reaction conditions. This model is shown in Scheme 59.

[**] Berkeley Madonna only gives the RMS error associated with the fitting of experimental data.

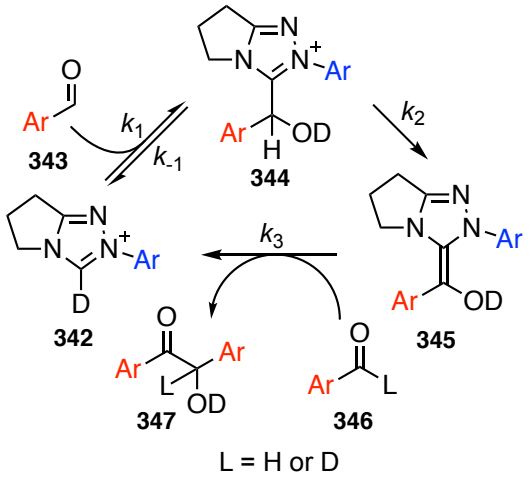

Scheme 59: Mechanistic model used to calculate k_1, k_{-1} and k_2 in this study.

Equilibrium constants for formation of the 3-(hydroxybenzyl)azolium adducts could also be estimated from the concentrations of adduct, aldehyde and catalyst at the steady state, Eqn. (16). A reliable value can only be obtained when there is no depletion of the hydroxyaryl adduct as it reacts onwards to give benzoin.

$$K_1 = \frac{[Adduct]}{[Catalyst][Aldehyde]} \tag{16}$$

This can be used as an alternative method for obtaining k_1 which involves integrating a pseudo-second order rate equation for a reaction approaching equilibrium.[133] There was good agreement between the rate constant (k_1) and equilibrium constant (K_1) obtained by either method (within ± 10%). In some cases, some benzoin product is formed before an equilibrium is established, which is the drawback of using this method.

In all reactions involving benzaldehyde **338**, the rate of benzoin formation was necessary to allow data fitting. No benzoin product was observed for reactions of *ortho*-methoxybenzaldehyde **339**. For *para*-methoxybenzaldehyde **340**, benzoin product was observed in the presence of N-phenyl **259** and N-4-fluorophenyl **261** triazolium salts.

The BI **345** was not observed under these reaction conditions, and so the fitting model was modified to allow hydroxyaryl adduct **344** and aldehyde **346** to form benzoin **347** and regenerate the catalyst **342** (i.e. k_2 and k_3 were combined into a single step). The value of k_2 was obtained from the slope of a semi logarithmic plot of the integral of C(α)-H at time t, relative to the integral of this signal at its largest value, at or near to equilibrium, Eqn. (17). The plot for the N-phenyl triazolium and *ortho*-methoxybenzaldehyde adduct is shown in Figure 50. The value of k_2 was determined according Eqn. (17).

$$ln\left(\frac{[Add-H]_t}{[Add-H]_e}\right) = -k_2 t \quad (17)$$

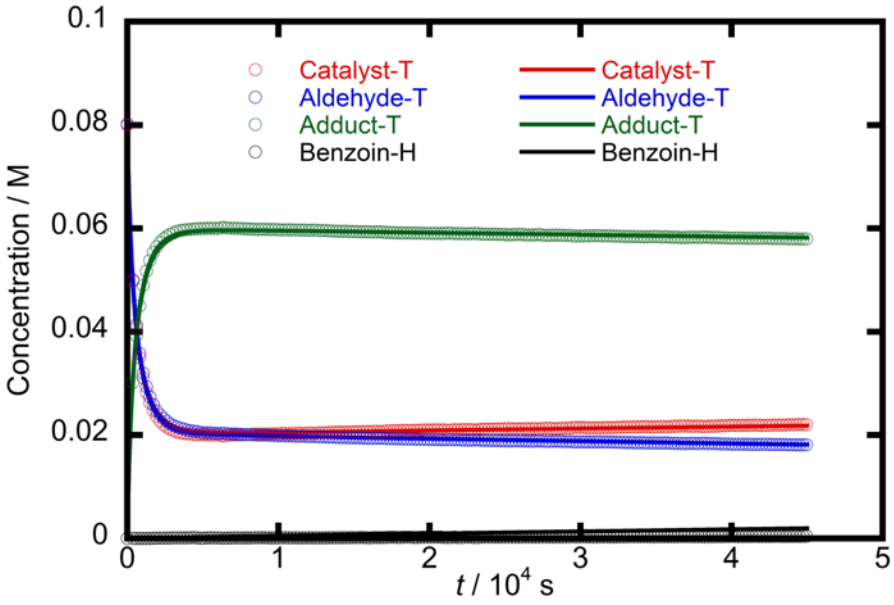

Figure 49: Concentration profile for the reaction between N-phenyl triazolium salt 259 and *ortho*-methoxybenzaldehyde 339 at 25 °C in CD_3OD. Open circles represent the total concentrations of triazolium salt (Catalyst-T), aryl aldehyde (Aldehyde-T) and hydroxyaryl adduct (Adduct-T), and the concentration of benzoin with H at the 2-position (Benzoin-H). The solid line is the fitting obtained using Berkeley Madonna.

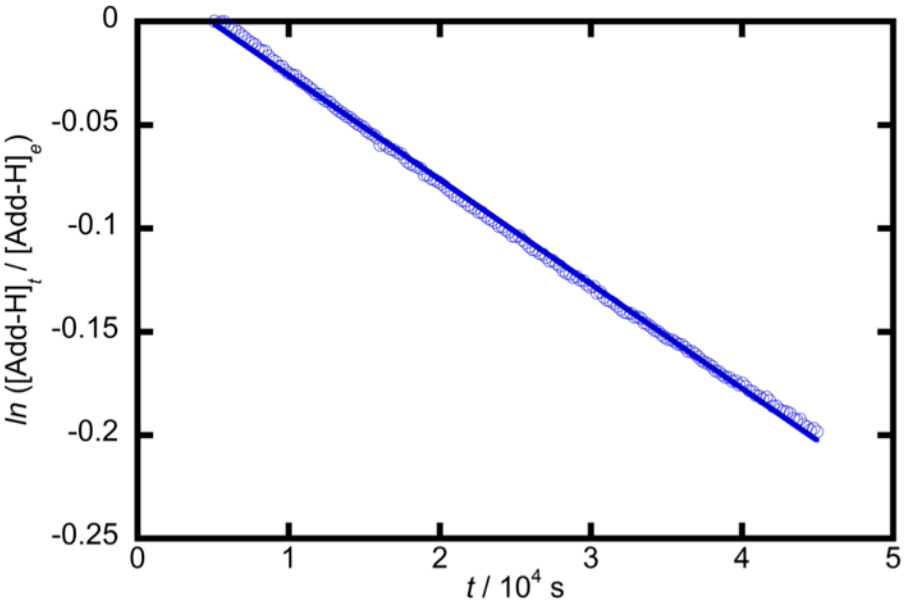

Figure 50: Determination of k_2 from the slope of a semi-logarithmic plot of the concentration of the C(α)-H signal at time *t*, relative to the integral of this signal at its largest value, at or near to equilibrium.

The concentration profiles and semi-logarithmic plots for all the reactions studied are given in Appendix 2. Equilibrium constants, K_1 (M^{-1}), and rate constants for formation, k_1 (M^{-1} s^{-1}), and dissociation, k_{-1} (s^{-1}), of the hydroxyaryl adduct **344** and formation of BI **345**, k_2 (s^{-1}), are given in Table 12.

N-Pentafluorophenyl **266** and N-2,4,6-trichlorophenyl **264** triazolium salts were unstable under the reaction conditions. The N-pentafluorophenyl triazolium salt **266** decomposed to ~ 50% and N-2,4,6-trichlorophenyl **264** to ~ 70% of the starting concentrations in 12 hours. LCMS suggests that the possible products were the hydrate **348** (or more likely the equivalent amide on either nitrogen **349** or **350**) and the amidrazone **351** (Figure 51). Attempts to generate the MeO-adduct in separate experiments from the N-pentafluorophenyl **266** and N-phenyl **259** triazolium precatalysts in refluxing 0.5 M NaOMe in methanol only led to amidrazone and other decomposition products. An attempt was made to follow adduct formation between N-pentafluorophenyl catalyst **266** and benzaldehyde **338**, however, the approach to equilibrium proved too fast to follow at 25 °C.

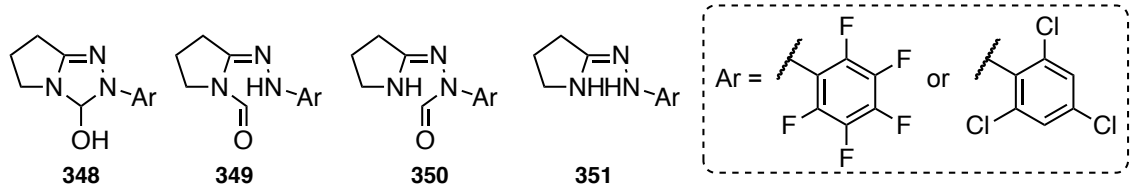

Figure 51: Potential decomposition products for N-pentafluorophenyl 266 and N-2,4,6-trichlorophenyl 264 triazolium salts under our reaction conditions.

Table 12: Rate constants and equilibrium constants for formation of hydroxyaryl adducts and BI formation in buffered CD_3OD at 25 °C.

	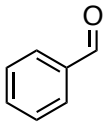 **338**	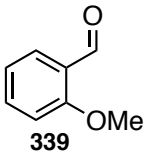 **339**	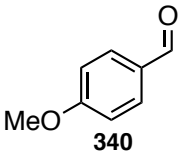 **340**
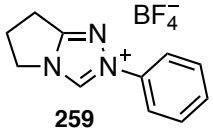 **259**	pD^{calc} = 10.87 K_1 = 13.5 M^{-1} $k_1 = 9.86 \times 10^{-3}$ M^{-1} s^{-1} $k_{-1} = 7.30 \times 10^{-4}$ s^{-1} $k_2 = 7.35 \times 10^{-6}$ s^{-1}	pD^{calc} = 10.92 K_1 = 147 M^{-1} $k_1 = 2.11 \times 10^{-2}$ M^{-1} s^{-1} $k_{-1} = 1.44 \times 10^{-4}$ s^{-1} $k_2 = 5.05 \times 10^{-6}$ s^{-1}	pD^{calc} = 10.92 K_1 = 2.38 M^{-1} $k_1 = 1.80 \times 10^{-3}$ M^{-1} s^{-1} $k_{-1} = 7.56 \times 10^{-4}$ s^{-1} $k_2 = 2.67 \times 10^{-6}$ s^{-1}
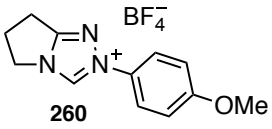 **260**	pD^{calc} = 11.11 K_1 = 25.1 M^{-1} $k_1 = 9.53 \times 10^{-3}$ M^{-1} s^{-1} $k_{-1} = 3.79 \times 10^{-4}$ s^{-1} $k_2 = 8.25 \times 10^{-6}$ s^{-1}	pD^{calc} = 11.05 K_1 = 221 M^{-1} $k_1 = 1.46 \times 10^{-2}$ M^{-1} s^{-1} $k_{-1} = 6.61 \times 10^{-5}$ s^{-1} $k_2 = 3.56 \times 10^{-6}$ s^{-1}	pD^{calc} = 11.12 K_1 = 3.45 M^{-1} $k_1 = 1.85 \times 10^{-3}$ M^{-1} s^{-1} $k_{-1} = 5.37 \times 10^{-4}$ s^{-1} $k_2 = 4.80 \times 10^{-7}$ s^{-1}
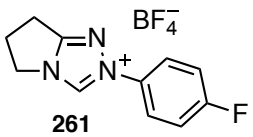 **261**	pD^{calc} = 11.04 K_1 = 18.0 M^{-1} $k_1 = 2.92 \times 10^{-2}$ M^{-1} s^{-1} $k_{-1} = 1.62 \times 10^{-3}$ s^{-1} $k_2 = 2.10 \times 10^{-5}$ s^{-1}	pD^{calc} = 11.05 K_1 = 231 M^{-1} $k_1 = 5.15 \times 10^{-2}$ M^{-1} s^{-1} $k_{-1} = 2.23 \times 10^{-4}$ s^{-1} $k_2 = 1.40 \times 10^{-5}$ s^{-1}	pD^{calc} = 11.09 K_1 = 2.97 M^{-1} $k_1 = 5.10 \times 10^{-3}$ M^{-1} s^{-1} $k_{-1} = 1.72 \times 10^{-3}$ s^{-1} $k_2 = 3.28 \times 10^{-6}$ s^{-1}
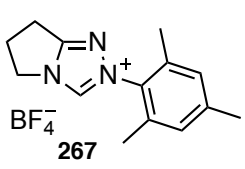 **267**	pD^{calc} = 10.73 K_1 = 129 M^{-1} $k_1 = 9.32 \times 10^{-3}$ M^{-1} s^{-1} $k_{-1} = 7.21 \times 10^{-5}$ s^{-1} $k_2 = 3.53 \times 10^{-6}$ s^{-1}	pD^{calc} = 10.72 K_1 = 392 M^{-1} $k_1 = 1.23 \times 10^{-2}$ M^{-1} s^{-1} $k_{-1} = 3.14 \times 10^{-5}$ s^{-1} $k_2 = 5.65 \times 10^{-7}$ s^{-1}	pD^{calc} = 10.80 K_1 = 22.8 M^{-1} $k_1 = 2.04 \times 10^{-3}$ M^{-1} s^{-1} $k_{-1} = 8.94 \times 10^{-5}$ s^{-1} $k_2 = 2.01 \times 10^{-6}$ s^{-1}
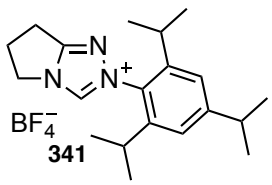 **341**	pD^{calc} = 10.97 K_1 = 129 M^{-1} $k_1 = 1.48 \times 10^{-2}$ M^{-1} s^{-1} $k_{-1} = 1.15 \times 10^{-4}$ s^{-1} $k_2 = 5.27 \times 10^{-6}$ s^{-1}	pD^{calc} = 11.07 K_1 = 1236 M^{-1} $k_1 = 2.25 \times 10^{-2}$ M^{-1} s^{-1} $k_{-1} = 1.82 \times 10^{-5}$ s^{-1} k_2 = -	pD^{calc} = 10.99 K_1 = 21.0 M^{-1} $k_1 = 3.01 \times 10^{-3}$ M^{-1} s^{-1} $k_{-1} = 1.43 \times 10^{-4}$ s^{-1} $k_2 = 1.55 \times 10^{-6}$ s^{-1}
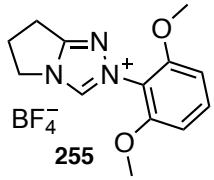 **255**	pD^{calc} = 11.04 K_1 = 434 M^{-1} $k_1 = 7.12 \times 10^{-3}$ M^{-1} s^{-1} $k_{-1} = 1.64 \times 10^{-5}$ s^{-1} $k_2 = 2.59 \times 10^{-6}$ s^{-1}	pD^{calc} = 11.03 K_1 = 2135 M^{-1} $k_1 = 6.15 \times 10^{-3}$ M^{-1} s^{-1} $k_{-1} = 2.88 \times 10^{-6}$ s^{-1} k_2 = -	pD^{calc} = 11.01 K_1 = 67.9 M^{-1} $k_1 = 1.46 \times 10^{-3}$ M^{-1} s^{-1} $k_{-1} = 2.15 \times 10^{-5}$ s^{-1} $k_2 = 9.61 \times 10^{-7}$ s^{-1}
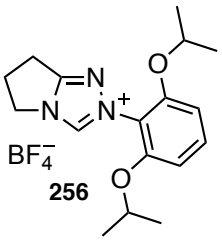 **256**	pD^{calc} = 11.00 K_1 = 107 M^{-1} $k_1 = 2.79 \times 10^{-3}$ M^{-1} s^{-1} $k_{-1} = 2.61 \times 10^{-5}$ s^{-1} $k_2 = 1.26 \times 10^{-6}$ s^{-1}	pD^{calc} = 10.92 K_1 = 1566 M^{-1} $k_1 = 1.55 \times 10^{-3}$ M^{-1} s^{-1} $k_{-1} = 9.90 \times 10^{-7}$ s^{-1} k_2 = -	pD^{calc} = 10.99 K_1 = 54.2 M^{-1} $k_1 = 6.18 \times 10^{-4}$ M^{-1} s^{-1} $k_{-1} = 1.14 \times 10^{-5}$ s^{-1} k_2 = -

[a]Starting concentrations: triazolium salt (0.08 M), aldehyde (0.08 M) in CD_3OD and 0.160 M NEt_3:$HNEt_3$ buffer (2:1). [b]Values of k_1 and k_{-1} were determined using Berkeley Madonna global fitting software and K_1 determined from the ratio $K_1 = k_1/k_{-1}$. [c]Values of k_2 were obtained from the slope of the semi-logarithmic plots of the signal due to C(α)-H according to the equation $\ln([\text{Add-H}]_t / [\text{Add-H}]_e) = -k_2 t$, where $[\text{Add-H}]_t$ is the integral of C(α)-H at time t, and $[\text{Add-H}]_e$ is the integral of C(α)-H at the peak concentration (i.e. once equilibrium had been established between carbene, aldehyde and hydroxyaryl adduct). [d]pD values were calculated based on the chemical shift of the quartet due to the CH_2 signal of the buffer, relative to the chemical shifts in the free base and fully protonated states, using the solvent signal at 3.31 ppm as reference. [d]Rate and equilibrium constants for **341** in combination with **338**, **339** and **340** were obtained by Jiayun Zhu.

3.2.3 General trends in K_1, k_1 and k_{-1}

The trend in equilibrium constants that are common to all catalysts is that K_1 decreases in the order *ortho*-methoxybenzaldehyde **339** > benzaldehyde **338** > *para*-methoxybenzaldehyde **340**. The forward rate constant for adduct formation, k_1, shows the same trend for non-*ortho*-substituted and *ortho*-alkyl substituted N-aryl triazolium salts. However, the order of k_1 changes for *ortho*-alkoxy substituted triazolium salts: benzaldehyde **338** > *ortho*-methoxybenzaldehyde **339** > *para*-methoxybenzaldehyde **340**.

The observed value for the forward rate constants for hydroxyaryl adduct formation, k_1 (M^{-1} s^{-1}), represents both the initial deprotonation of the catalyst and therefore the pre-equilibria for carbene formation (see chapter 2), and the addition step to give the hydroxyaryl adduct. Higher k_1 values may be due either to a higher kinetic acidity of the triazolium salt, or a lower concentration of a more basic and nucleophilic carbene, or a combination of the two. The concentration of the carbene from N-4-fluorophenyl **261** is greater than N-4-methoxyphenyl **260**, however the greater nucleophilicity of N-4-methoxyphenyl **260** negates some of the advantage the N-4-fluorophenyl **261** catalyst has in the adduct forming step. The general observed trend is that as Hammett σ increases for a more electron withdrawing N-aryl substituent, so does the value of k_1, which is consistent with a dependence on the NHC forming step.

The k_1 values for *para*-methoxybenzaldehyde **340** are lower than either of the two other aldehydes in combination with all catalysts, reflecting the lower electrophilicity of the aldehyde due to the electron donating *para*-methoxy substituent. This is reflected in the chemical shifts of the aldehydic proton (H^1) and carbon (C^1) of *para*-methoxybenzaldehyde **340**, compared to benzaldehyde **338**. The faster k_1 values for *ortho*-methoxybenzaldehyde **339** compared to benzaldehyde **338** are surprising given the fact that the aldehydic carbon (C^1) is more shielded than the other aryl aldehydes. Interestingly, the aldehydic proton (H^1) of *ortho*-methoxybenzaldehyde **339** is the most deshielded out of the three aldehydes.

For non-*ortho*-substituted (**259** – **261**) and *ortho*-alkyl-substituted (**267** and **341**) triazolium salts, the large increase in K_1 from benzaldehyde **338** to *ortho*-methoxybenzaldehyde **339** is due partly to an increase in k_1 (1.32 – 2.13-fold) and partly to a decrease in k_{-1} (56.4 – 86.2%). For *ortho*-alkoxy-substituted triazolium salts (**255** and **256**), the large increase in K_1 from benzaldehyde **338** to *ortho*-

methoxybenzaldehyde **339** is due to a small decrease in k_1 (13.6 – 44.4%) but a larger decrease in k_{-1} (82.4 – 96.2%).

3.2.4 Trends for benzaldehyde and *para*-methoxybenzaldehyde

In chapter 2, it was shown that there is a relationship between Hammett substituent constants, σ, and the second order rate constants for H/D exchange, k_{DO} (M^{-1} s^{-1}). Positive ρ values were observed for both *ortho*- and non-*ortho*-substituted triazolium salts, although *ortho*- substituted triazolium salts display a lower sensitivity to substituents, which can be explained by higher torsional angle of the N-aryl ring. *Ortho*-substituted N-aryl rings also display larger k_{DO} than predicted by the trend line for non-*ortho*-substituted N-aryl rings suggesting a destabilisition of the ground state. Non-*ortho*-substituted triazoliums can adopt a planar conformation that stabilises the ground state compared to *ortho*-substituted N-aryl rings. X-ray crystal structures demonstrate that *ortho*-substituted N-aryl rings adopt larger torsional angles than non-*ortho*-substituted N-aryl rings. However, the N-aryl ring must rotate (Figure 52) to allow the approach to the aryl aldehyde which is demonstrated by the change in torsion angle for N-phenyl triazolium salt (19.45°) on forming hydroxyaryl adducts (65.14 – 67.95° for benzaldehyde, *para*-methylbenzaldehdye and *para*-fluorobenzaldehyde).

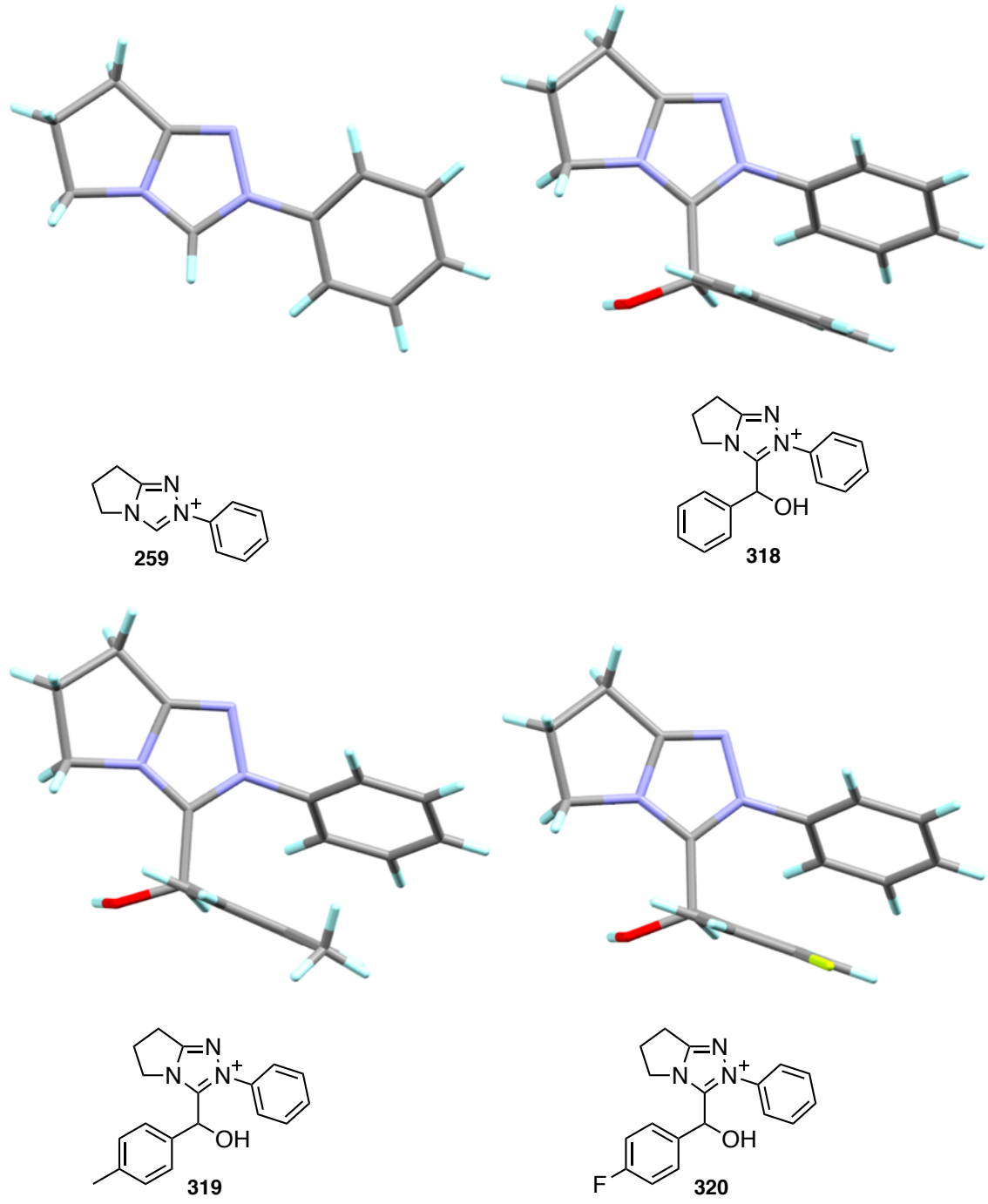

Figure 52: X-ray crystal structures of N-phenyl triazolium salt 259 (obtained by Smith and co-workers[126]) and the hydroxyaryl adducts formed with benzaldehyde, *para*-fluoro- and *para*-methyl-benzaldehyde (obtained by O'Donoghue and co-workers[79])

The same trends in k_1, k_{-1} and k_2 are observed for the reaction of all seven catalysts with benzaldehyde **338** and *para*-methoxybenzaldehyde **340**. However, from benzaldehyde **338** to *para*-methoxybenzaldehyde **340**, there is a relatively large decrease in k_1 (77.8 – 82.5%) but a relatively smaller increase in k_{-1} (< 1.42-fold). The extent of the disappearance of C(α)-H, which gives an estimate of k_2, needed to be considered particularly for the more electron donating catalysts. The k_2 data for *ortho*- and non-*ortho*-substituted N-aryl rings appear to fall on the same trendline. However, the C(α)-

H signal only decreased to ≥ 89% of the starting value for the *ortho*-alkyl and *ortho*-alkoxy triazolium salts.

Figure 53 and Figure 55 show Hammett plots for the rate constant for hydroxyaryl adduct formation, k_1 (M^{-1} s^{-1}), of benzaldehyde **338** and *para*-methoxybenzaldehyde **340**, respectively, with the seven catalysts used in this study. With too few data points to gain meaningful ρ values, these plots are used as a graphical guide to show the effects of N-aryl substituents on k_1. The features which are common to the Hammett plot obtained for second order rate constants for C(3)-H/D exchange in chapter 2 are that (1) there is a positive slope for both *ortho*- and non-*ortho*-substituted triazolium catalysts and (2) the data for *ortho*-substituted N-aryl triazoliums lie above that of the non-*ortho*-substituted N-aryl triazoliums. The factors which affect the the acidity of C(3)-H also affect the rate constant for hydroxyaryl adduct formation. The more acidic triazolium salts lead to higher concentrations of NHC, which leads to a faster rate constant for addition. This is offset slightly, as observed for non-*ortho*-substitued triazoliums, by the greater NHC nucleophilicity for the less acidic azoliums. *Ortho*-substituted N-aryl triazoliums are destabilised relative to non-*ortho*-substituted N-aryl triazoliums as no resonance is possible between the two rings. This leads to a relatively high rate constant for C(3) proton removal. To accommodate the incoming aryl aldehyde, the N-aryl ring must rotate, and this energetic penalty for non-*ortho*-substituted triazolium salts results in lower k_1 values (Scheme 60). *Ortho*-substituted N-aryl triazolium salts adopt larger dihedral angles (≥ 62°) than non-*ortho*-substituted N-aryl triazolium salts (≤ 25.2º). Rate constants could not be obtained for N-pentafluorophenyl and N-2,4,6-trichlorophenyl triazolium salts **266** and **264** under our reaction conditions. *Ortho*-alkoxy triazoliums provide the closest models in terms of steric and electrostatic effects for these *ortho*-halo triazolium salts. It is also apparent is that *ortho*-substituted N-aryl triazoliums show a better correlation with σ.

Figure 54 and Figure 56 show Hammett plots for the rate constant for hydroxyaryl adduct dissociation, k_{-1} (s^{-1}), of benzaldehyde and *para*-methoxybenzaldehyde, respectively, with the seven catalysts used in this study. Again, these plots are used as a graphical guide, and that there are not enough data points to give a reliable ρ value. These plots show that (1) there is a positive slope for both *ortho*- and non-*ortho*-substituted catalysts and (2) the data for *ortho*-substituted N-aryl triazoliums now lie below that of the non-*ortho*-substituted N-aryl triazoliums. In general, k_{-1} increases as σ increases – as the N-aryl ring becomes more electron withdrawing, the hydroxyl group

becomes more acidic and the carbene becomes a better leaving group. This trend is in agreement with pK_a estimates for the triazolium salts. The rate constants for non-*ortho*-substituted triazoliums are expected to be greater due to the increased stability of the planar triazolium and N-aryl rings in the catalyst compared to the rotated N-aryl ring in the hydroxyaryl adduct (Scheme 61).

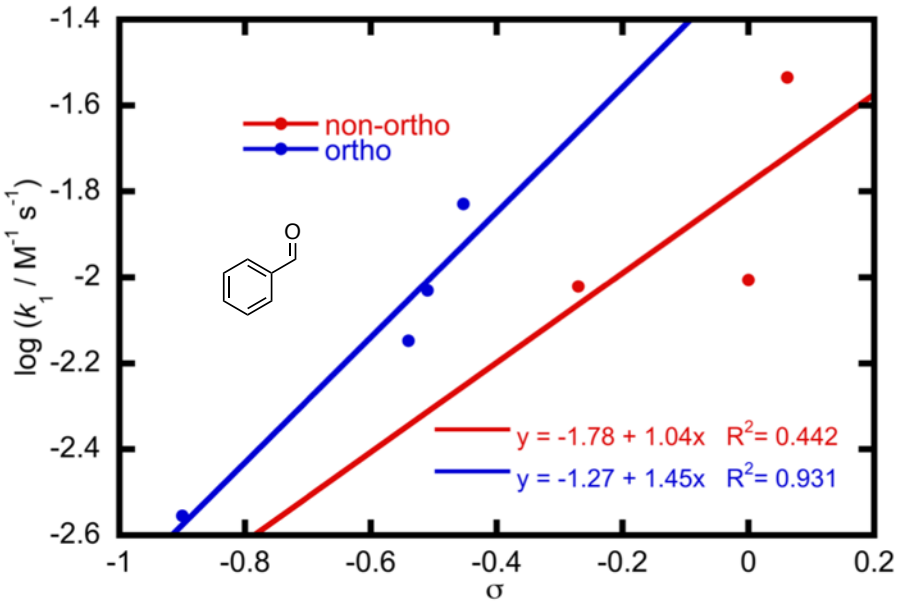

Figure 53: Hammett plot showing the relationship between the pseudo second order rate constants for formation of the hydroxyaryl adduct from triazolium salt and benzaldehyde, k_1 (M^{-1} s^{-1}), and Hammett constants for non-*ortho*-substituted (•) and *ortho*-substituted (•) triazolium salts.

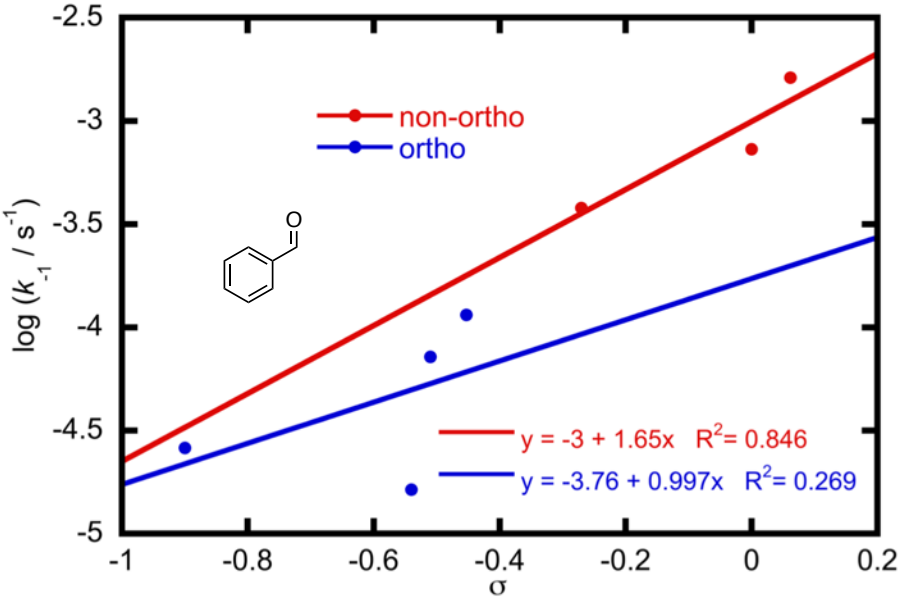

Figure 54: Hammett plot showing the relationship between the pseudo first order rate constants for dissociation of the hydroxyaryl adduct to give triazolium salt and benzaldehyde, k_{-1} (s^{-1}), and Hammett constants for non-*ortho*-substituted (•) and *ortho*-substituted (•) triazolium salts.

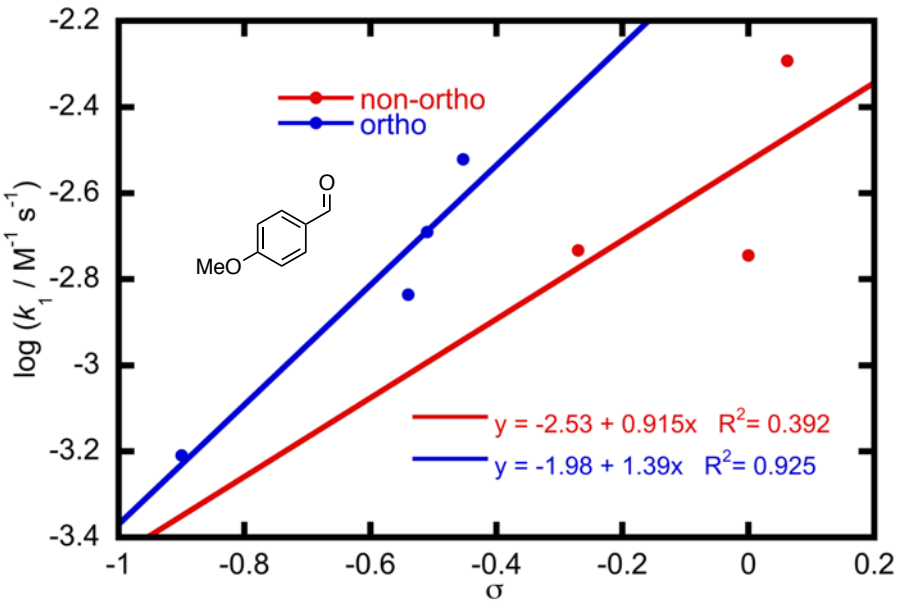

Figure 55: Hammett plot showing the relationship between the pseudo second order rate constants for formation of the hydroxyaryl adduct from triazolium salt and *para*-methoxybenzaldehyde, k_1 (M^{-1} s^{-1}), and Hammett constants for non-*ortho*-substituted (•) and *ortho*-substituted (•) triazolium salts.

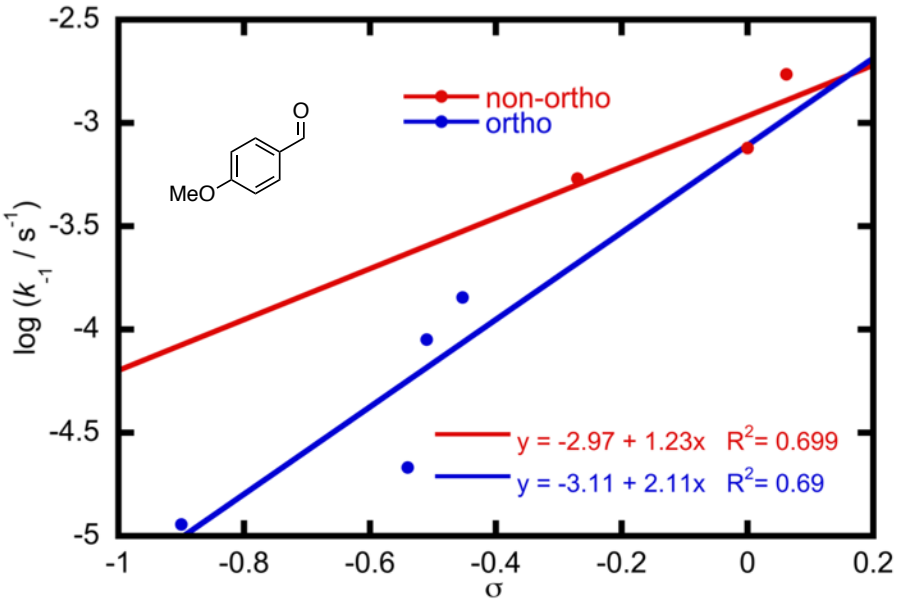

Figure 56: Hammett plot showing the relationship between the pseudo first order rate constants for dissociation of the hydroxyaryl adduct to give triazolium salt and *para*-methoxybenzaldehyde, k_{-1} (s^{-1}), and Hammett constants for non-*ortho*-substituted (•) and *ortho*-substituted (•) triazolium salts.

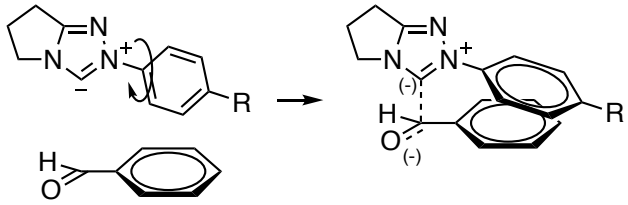

Scheme 60: Non-*ortho*-substituted N-aryl triazoliums show slower k_1 values because of an energetic penalty that must be paid by rotating the N-aryl ring to accommodate the approach of the incoming aryl aldehyde.

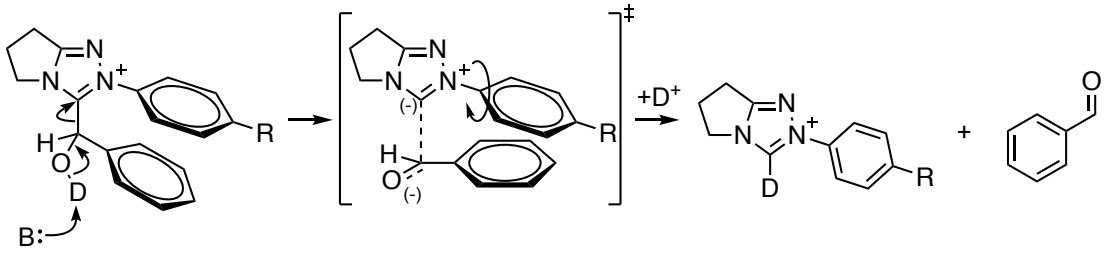

Scheme 61: Non-*ortho*-substituted triazolium salts lead to enhanced k_{-1} values towards a planar triazolium and and N-aryl ring conformation.

The values of k_2 are sensitive to the pD of the solution. Generally, for non-*ortho*-substituted N-aryl triazoliums, a +ρ value is obtained when varying the N-aryl ring of the triazolium salt, and that k_2 is larger for benzaldehyde than it is for *para*-methoxybenzaldehyde. Reliable k_2 values could not be obtained for *ortho*-substituted N-aryl triazoliums – the extent of the disappearance of the C(α)-H signal for N-mesityl, N-2,6-dimethoxyphenyl and N-2,6-diisopropoxyphenyl was 11, 6 and 2 %, respectively.

3.2.5 Trends for *ortho*-methoxybenzaldehyde

Figure 57 and Figure 58 show Hammett plots for the rate constants for hydroxyaryl adduct formation, k_1 (M^{-1} s^{-1}), and dissociation, k_{-1} (s^{-1}), respectively, of *ortho*-methoxybenzaldehyde **339** with the seven triazolium salt precatalysts used in this study. These plots are used as a graphical guide to show the effects of N-aryl substituents on k_1 and k_{-1}. The correlation between k_1 and k_{-1} with σ is generally poorer than in the case of benzaldehyde and *para*-methoxybenzaldehyde. However, the trend in k_1 is similar to that observed for benzaldehyde (Figure 53) and *para*-methoxybenzaldehyde (Figure 55). The poorer correlation between k_{-1} and σ (Figure 58) for *ortho*- compared to non-*ortho*-substituted N-aryl triazolium salts suggests that steric effects are dominating in the dissociation step.

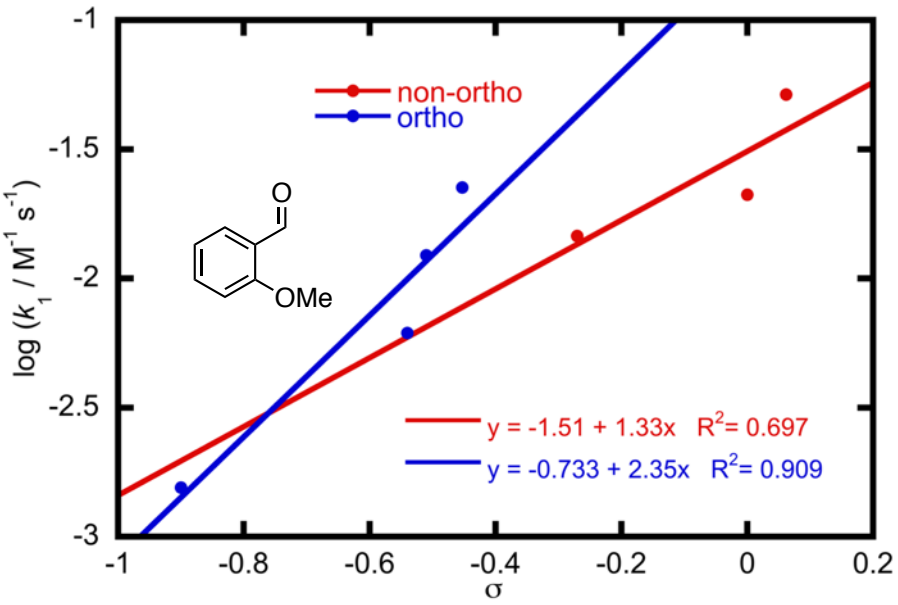

Figure 57: Hammett plot showing the relationship between the pseudo second order rate constants for formation of the hydroxyaryl adduct from triazolium salt and *ortho*-methoxybenzaldehyde, k_1 (M^{-1} s^{-1}), and Hammett constants for non-*ortho*-substituted (•) and *ortho*-substituted (•) triazolium salts.

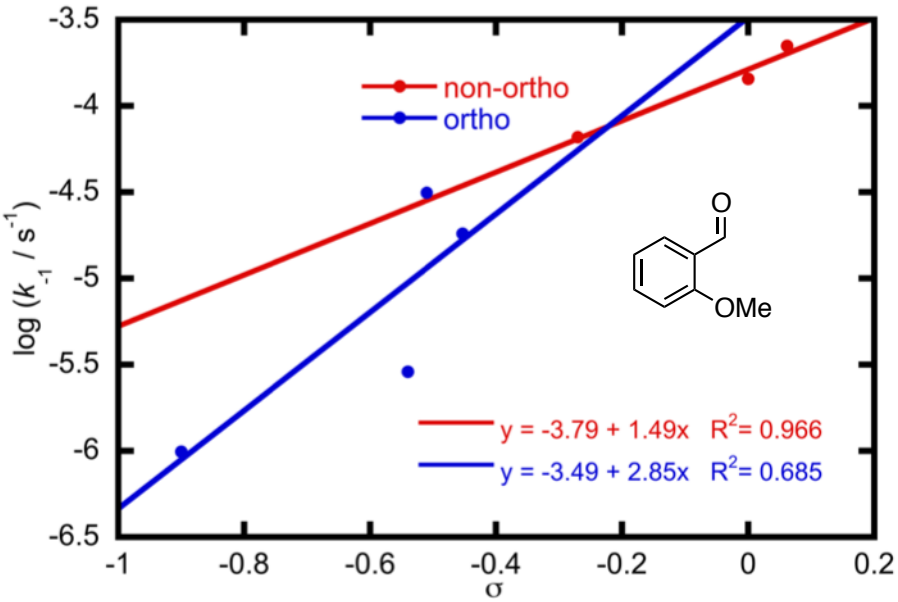

Figure 58: Hammett plot showing the relationship between the pseudo first order rate constants for dissociation of the hydroxyaryl adduct to give triazolium salt and *ortho*-methoxybenzaldehyde, k_{-1} (s^{-1}), and Hammett constants for non-*ortho*-substituted (•) and *ortho*-substituted (•) triazolium salts.

3.2.6 Comparison between benzaldehyde and *ortho*-methoxybenzaldehyde

Table 13 shows the structures of almost all of the catalysts used in this study, along with the relative rate constants (k_1^{rel}, k_{-1}^{rel} and k_2^{rel}) for *ortho*-methoxybenzaldehyde relative to benzaldehyde. The length is defined as the distance between N2 and C_{ipso} of the aryl ring, and the dihedral angle, θ, is defined as the angle between N1-N2 of the triazole

ring and C_{ipso}-C_{ortho} of the N-aryl ring (Figure 59). For symmetrical N-aryl rings, the choice of C_{ortho} was made to give a dihedral angle of $|\theta| \leq 90°$.

Non-*ortho*-substituted and *ortho*-alkyl N-aryl triazoliums show k_1^{rel} ranging from 1.52 – 2.14 while *ortho*-alkoxy N-aryl triazoliums show k_1^{rel} ranging from 0.56 – 0.86. $k_{-1}^{rel} < 1$ for all catalysts studied.

The relative value k_2^{rel} for all catalyst systems were > 1. For the non-*ortho*-substituted catalysts, the value of k_2 decreases in the order benzaldehyde > *ortho*-methoxybenzaldehyde > *para*-methoxybenzaldhyde. This may be due to the inductively electron withdrawing effect of the *ortho*-methoxy substituent compared to the *para*-methoxy substituent. The steric and resonance electron donating effects of the *ortho*-methoxy group also causes k_2 values to be lower than for benzaldehyde.

The general trend for the effect of catalyst on k_2 value is that as Hammett σ increases, so does the value of k_2. These electronic effects of the N-aryl ring and are in the same order as observed for the kinetic acidities of the parent azolium ions.[58,59] The extent of H/D exchange and onwards reaction of the BI were slow for *ortho*-substituted triazoliums. The integral of C(α)-H signal only decreased to ≥ 89% of the original value and so the slow reactions for *ortho*-alkoxy and *ortho*-alkyl-substituted triazoliums are less reliable under our reaction conditions.

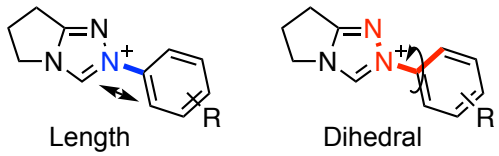

Figure 59: Definition of the length between N2 and C_{ipso} and the dihedral angle between the two rings, θ, defined as the angle between N1-N2 and C_{ipso}-C_{ortho}.

Table 13: Bond length and torsion angles between the triazolium and N-aryl rings obtained from X-ray crystal structures. Also included are relative rate constants (k_1^{rel}, k_{-1}^{rel} and k_2^{rel}) for *ortho*-methoxybenzaldehyde relative to benzaldehyde.

	N2-C$_{ipso}$ length / Å	N1-N2-C$_{ipso}$-C$_{ortho}$ Dihedral angle, θ / °	k_1^{rel}	k_{-1}^{rel}	k_2^{rel}
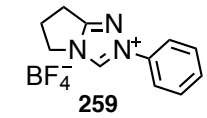 **259**	1.435	19.45	2.14	0.20	0.69
 **260**	1.435	16.1	1.53	0.17	0.43
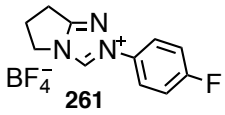 **261**	1.428	25.2	1.76	0.14	0.67
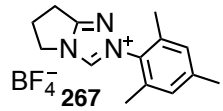 **267**	1.441	79.51	1.32	0.44	0.16
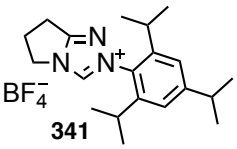 **341**	-	-	1.52	0.16	< 0.16
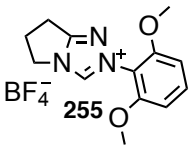 **255**	1.433	76.63	0.86	0.18	< 0.16
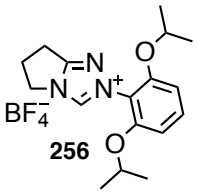 **256**	-	-	0.56	0.04	< 0.16
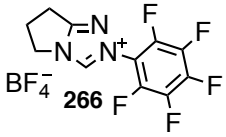 **266**	1.429	62.0	-	-	-
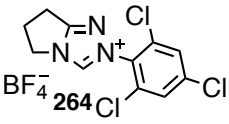 **264**	1.4264	73.71	-	-	-
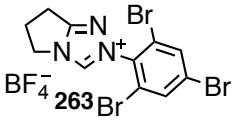 **263**	1.430	89.6	-	-	-

[a] k_{rel} values are defined as the ratio of rate constants for *ortho*-methoxybenzaldehyde relative to benzaldehyde.

3.2.6.1 Rationalising observed ratios

It was previously reported that the N-phenyl catalyst adds into *ortho*-methoxybenzaldehyde with a faster rate constant than benzaldehyde and suggested that the *ortho*-methoxy group may distort the carbonyl of the aldehyde out of plane with the

aromatic ring, therefore increasing the electrophilicity of the carbonyl.[25] We have repeated the experiments here, and also obtained additional data for two other non-*ortho*- and four *ortho*-substituted triazolium salts. ^{1}H and ^{13}C NMR chemical shifts, X-ray crystal structure and DFT dihedral angles demonstrate that there is unlikely to be any distortion of the carbonyl out of the plane of the aromatic ring due to the *ortho*-methoxy substituent which would lead to a ground state destabilisation of *ortho*-methoxybenzaldehyde compared to benzaldehyde. DFT calculations (Figure 47) shows that the thermal energy at 298 K would allow no more than 15-20° rotation out of plane of the aryl ring, which would not be expected to be a significant contributor to the observed rate constants for addition.

Ortho-alkyl and non-*ortho*-substituted N-aryl triazoliums display $k_1^{rel} \geq 1$, whereas *ortho*-alkoxy N-aryl triazoliums display $k_1^{rel} \leq 1$. It is clear that steric hindrance cannot explain the difference between *ortho*-alkyl and *ortho*-alkoxy triazolium salts.

In chapter 4, the synthesis and kinetic study of a series of methylated hydroxyaryl adducts are described. The chemical shifts of these adducts are shown in Figure 60. The chemical shifts of C(α)-H under the reaction conditions described in this chapter are shown in Figure 61. These chemical shifts and the structural analysis described in the previous chapter may be used to rationalise the observed kinetic trends.

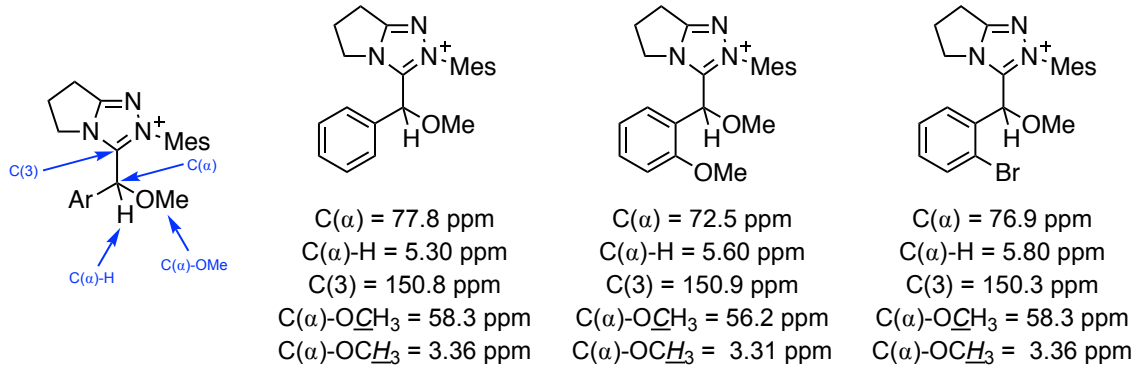

Figure 60: ^{1}H and ^{13}C NMR chemical shifts of three methylated hydroxyaryl adducts which are described in more detail in Chapter 4.

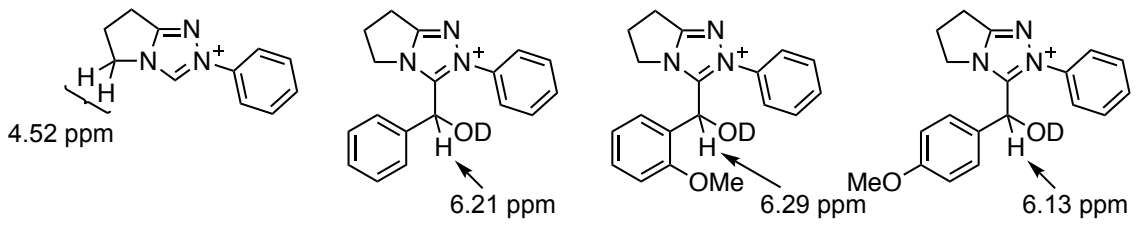

Figure 61: ^{1}H NMR chemical shifts of C(α)-H signal of the hydroxyaryl adducts using the N-phenyl catalyst for all three aryl aldehydes.

An explanation that may rationalise the enhanced k_1 values for *ortho*-methoxybenzaldehyde for non-*ortho*- and *ortho*-alkyl-substituted triazolium salts may be due to the intramolecular hydrogen bonding between the *ortho*-methoxy substituent and what is initially the aldehydic proton and becomes C(α)-H in the hydroxyaryl adduct. In the aldehyde, intramolecular H-bonding is consistent with the observed chemical shifts for C^1 and H^1 of *ortho*-methoxybenzaldehyde (Figure 45): C^1 and C^2 are shielded but H^1 is deshielded. The lone pair of electrons on the methoxy oxygen are sp^3 hybridised which means that the H-bonding is less than optimal – the lone pair of electrons are not in the same plane of the aryl ring and therefore the plane of the aldehydic C-H. However, in the hydroxyaryl adduct, the initial aldehydic proton rotates out of the plane of the aryl ring as C^1 changes hybridisation from sp^2 to sp^3. This allows the formation of a five membered envelope conformation **352**, which leads to more effective hydrogen bonding. As the hydroxyaryl adduct forms, the strength of the hydrogen bond increases as the geometry improves. This has the effect of increasing k_1^{rel} for non-*ortho* and *ortho*-alkyl substituted triazolium salts.

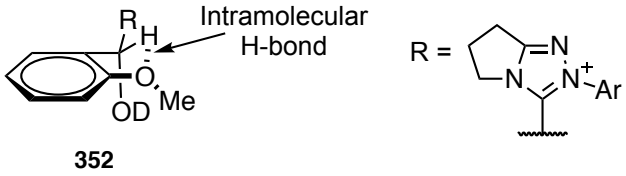

352

Figure 62: Towards a potentially improved intramolecular H-bond in the hydroxyaryl adduct based on *ortho*-methoxybenzaldehyde.

The alternative hydrogen bonding between the hydroxyl group, C(α)-OH, and the *ortho*-methoxy group had been considered previously.[25] However, in the transition state leading to the hydroxyaryl adduct, a partial negative charge will reside on the carbonyl oxygen atom (Figure 63). Although solvation of this charge may occur by H-bonding to solvent MeOD or buffer acid, the lone pair of electrons on the *ortho*-methoxy substituent would not be expected help attenuate the charge build up. This would lead to an electrostatic repulsion **353**, highlighted in red in Figure 63, and would not be expected to lead to a transition state stabilisation. A rate decrease rather than increase would then be expected if the intramolecular hydrogen bonding was due to the forming hydroxyl rather than C(α)-H.

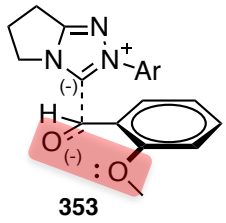

353

Figure 63: Electrostatic repulsion between the *ortho*-methoxy substituent in the transition state for hydroxyaryl adduct formation. H-bonding between C(α)-OH and the *ortho*-methoxy substituent is therefore not responsible for the rate enhancement for *ortho*-methoxybenzaldehyde.

This situation is different for *ortho*-alkoxy substituents, which possess lone pairs of electrons in the *ortho*- position of the N-aryl ring. The relative rate consant $k_1^{rel} < 1$ for *ortho*-alkoxy triazolium salts may be rationalised in terms of the electrostatic repulsion between the *ortho*-oxygen atoms of the N-aryl ring and the approaching *ortho*-methoxy substituent on the aryl aldehyde (Figure 64). This repulsion outweighs the beneficial intramolecular hydrogen bond which forms in the hydroxyaryl adduct.

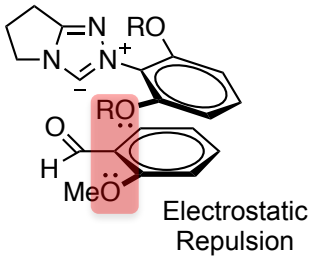

Figure 64: Electrostatic repulsions (highlighted in red) between *ortho*-alkoxy N-aryl substituents and *ortho*-methoxy substituent of incoming aryl aldehyde.

The ratio $k_1^{rel} > 1$ for non-*ortho* and *ortho*-alkyl-substituted triazolium salts may therefore be rationalised in terms of a transition state stabilisation effect. The development of a more optimal H-bond in the hydroxyaryl adduct stabilises the transition state for the addition. This evidently outweighs the small ground state destabilisation caused by a less electrophilic aldehyde – C^1 is more shielded for *ortho*-methoxybenzaldehyde than it is for benzaldehyde. Electrostatic repulsion between *ortho*-alkoxy substituents on both triazolium and aldehyde may explain why $k_1^{rel} < 1$ for triazolium salts with *ortho* substituents bearing lone pairs of electrons, which outweighs the stabilising H-bond in the hydroxyaryl adduct. It may be predicted that *ortho*-halo triazolium salts also display $k_1^{rel} \leq 1$.

The k_{-1} values for *ortho*-methoxybenzaldehyde are smaller than for benzaldehyde for two likely reasons: (1) steric hindrance for deprotonating the hydroxyl group and (2) the resonance electron donating effect of the *ortho*-methoxy substituent which makes C(α) more electron rich and therefore the hydroxyl less acidic. Methylated hydroxyaryl

adducts were prepared for studying the formation of the BI in chapter 4. The chemical shifts of these adducts are shown Figure 60, and show that the ^{13}C NMR chemical shifts for C(α) and C(α)-OMe are lower for the *ortho*-methoxybenzaldehyde adduct, indicating that the hydroxyl group at C(α) is less acidic. This NMR chemical shift analysis helps explain why the equilibrium constants for hydroxyaryl adduct formation are larger for *ortho*-methoxybenzaldehyde than benzaldehyde – a smaller k_{-1} leads to a larger K_1 since $K_1 = k_1 / k_{-1}$.

For all catalysts where a k_2 value could be obtained for both benzaldehyde and *ortho*-methoxybenzaldehyde, the ratio of these rate constants was $k_2^{rel} < 1$. This demonstrates that the *ortho*-methoxy group has a steric effect, since the chemical shift for *ortho*-methoxybenzaldehyde and the C(α)-H of the adduct based on this aldehyde are greater than benzaldehyde and the adduct based on benzaldehyde.

The chemical shifts of the C(α)-H signal of the hydroxyaryl adducts based on the N-phenyl catalyst, under these reaction conditions are shown in Figure 61. The same order of chemical shifts is observed for all catalysts studied. The shifts were compared relative to the CH_2 signal on the catalyst as an internal standard. The chemical shift is greater for the *ortho*-methoxybenzaldehyde adduct suggesting either an inductive electron withdrawing effect or an intramolecular H-bond. These trends are also shown in the chemical shifts of the methylated adducts in Figure 60. The rate constant for deprotonation of this adduct, k_2, is larger for the benzaldehyde adduct. So despite the apparent increased lability of the proton, steric hindrance and the presence of an intramolecular H-bond is slowing the rate of proton removal. This steric hindrance may be of the incoming base or the formation of a planar BI, or a combination of the two effects.

These results suggest that there is a higher concentration of the BI derived from benzaldehyde **354** compared to *ortho*-methoxybenzaldehyde **355**. ^{1}H and ^{13}C NMR chemical shifts of methylated adducts (Figure 60) show that the C(α)-H signal is more deshielded for *ortho*-methoxybenzaldehyde than benzaldehyde, but that C(α) is more shielded for *ortho*-methoxybenzaldehyde, which suggests that the BI based on *ortho*-methoxybenzaldehyde **355** is more basic (Figure 65). This also suggests that the deshielding of C(α)-H is caused predominantly by an intramolecular hydrogen bond, which has the effect of stabilising the hydroxyaryl adduct and therefore the transition state leading to it.

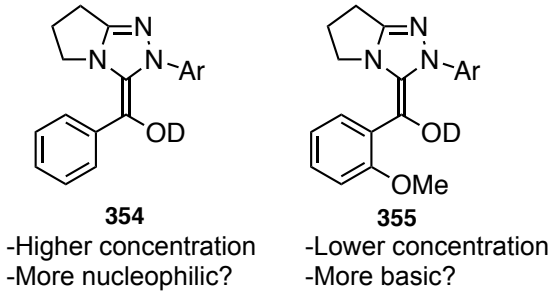

354
-Higher concentration
-More nucleophilic?

355
-Lower concentration
-More basic?

Figure 65: Properties of the BI for adducts based on benzaldehyde vs *ortho*-methoxybenzaldehyde.

3.3 Implications for catalysis

The results obtained in this, and the previous chapter, indicate that *ortho*-substituted N-aryl triazoliums are beneficial in promoting (1) relatively fast rate of C(3)-H transfer, (2) faster rate constants for hydroxyaryl adduct formation, (3) slower rate constants for hydroxyaryl adduct dissociation and (4) larger equilibrium constants for hydroxyaryl adduct formation.

Rate constants for formation of adducts from *ortho*-methoxybenzaldehyde clearly point to the potential of exploiting intramolecular H-bonding. This evidently causes the equilibrium constants for hydroxyaryl adduct formation to be greater for adducts formed from the less electrophilic *ortho*-methoxybenzaldehyde compared to benzaldehyde. Any aryl aldehyde which could exploit the formation of a more optimal H-bond could help bias the chemoselectivity of this step. The use of N-aryl triazolium salts with *ortho*-heteroatoms bearing lone pairs of electrons, such as *ortho*-halo-substituted, may lead to increased electrostatic repulsion with the incoming *ortho*-oxygen lone pair and this may also be exploited to favour a specific crossed product.

Relatively slow formation of the BI from adducts formed from *ortho*-methoxybenzaldehyde and perhaps *ortho*-substituted aryl aldehydes in general clearly begin to bias the product based on the initial attack of the less sterically hindered benzaldehyde.

Onwards attack of the BI is then likely to be governed by another trade off of electronics and sterics – attack at *ortho*-methoxybenzaldehyde would benefit from the stabilising intramolecular hydrogen bond, but may be sterically hindered due to the *ortho*-substituents on the N-aryl and aldehyde rings, where the BI is likely to adopt a conformation closer to **357** than to **356** (Figure 66). A similar conformation was observed in the solid state,[95] and a reasonable conclusion from this is that onwards

attack of the BI from the *ortho*-substituted aldehyde adduct is prohibitively slow due to steric hindrance.

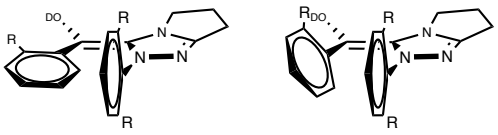

356 **357**

Figure 66: Possible conformations of the BI. Steric interactions between the two aromatic rings in the hydroxyaryl adduct may mean a conformation similiar to 357 is more likely (cf. X-ray crystal structures of hydroxyaryl adducts).

3.4 Conclusions and future work

To conclude, the ^{1}H and ^{13}C NMR chemical shifts of benzaldehyde, *ortho*- and *para*-methoxybenzaldehyde have been studied, and the findings suggest that the electrophilicity (based on the carbonyl carbon) follows the order benzaldehyde > *para*-methoxybenzaldehyde > *ortho*-methoxybenzaldehyde. The aldehydic proton decreases in chemical shift from *ortho*-methoxybenzaldehyde > benzaldehyde > *para*-methoyxbenzaldehyde which suggests that there is a degree of intramolecular H-bonding between the aldehydic proton and the *ortho* oxygen lone pair. X-ray crystal structure analaysis and DFT calculation of *ortho*-methoxybenzaldehyde suggest that the methoxy substituent is not causing a distortion of the carbonyl out of the plane of the aromatic ring, and any previously reported rate enhancements for *ortho*-methoxybenzaldehyde cannot be adequately explained by a ground state destabilisation.[25]

Rate constants for hydroxyaryl adduct formation and dissociation were obtained for the three aryl aldehydes with three non-*ortho*- and four *ortho*-substituted N-aryl triazolium salts. For reactions with benzaldehyde and *para*-methoxybenzaldehyde, the results are that (1) *ortho*-substituted N-aryl triazolium salts lead to enhanced rate constants for addition and (2) non-*ortho*-substituted N-aryl triazolium salts give enhanced rate constants for dissociation. This can be rationalised in terms of the rotational energies of the N-aryl substituent on the NHC. Non-*ortho*-substituted triazolium salts must rotate the N-aryl ring to accommodate the incoming aldehyde. As shown in chapter 2, there is a barrier to this rotation due to resonance stabilisation of a planar conformation. This energy penalty that must be paid for non-*ortho*-substituted triazolium salts results in relatively slower rate constants for addition. This resonance stabilisation also explains why the rate constants for dissociation are larger for non-*ortho*-substituted triazolium salts.

For reactions of the triazolium salts with *ortho*-methoxybenzaldehyde, the rate constants for addition were greater than with benzaldehyde for non-*ortho*- and *ortho*-alkyl-substituted triazolium salts, but smaller for *ortho*-alkoxy-substituted triazolium salts. This can be rationalised in terms of the formation of a more optimal intramolecular H-bond between C(α)-H, not C(α)-OH, and the *ortho*-oxygen lone pair which stabilises the transition state and hydroxyaryl adduct. *Ortho*-alkoxy-substituted N-aryl triazolium salts have increased electrostatic repulsions with the *ortho*-oxygen lone pair on the aldehyde, which explains why the reaction with benzaldehyde is faster in these cases.

Further work should be aimed at investigating the overall product outcomes of the crossed-benzoin condensations with catalysts studied in this chapter. To improve the Hammett plots, further work may also be aimed at increasing the number of triazolium salts studied by preparing the following: N-4-cyanophenyl, N-4-methylphenyl, N-4-trifluoromethylphenyl, N-4-chlorophenyl, N-4-bromophenyl, N-4-iodophenyl, N-4-isopropylphenyl, N-4-tertbutylphenyl.

Further work is required to investigate the nucleophilicity of the resulting BI as a means to predicting product outcomes in cross-benzoin condensations. The next chapter will detail the attempts to investigate the proton transfer and kinetic basicity of the O-methylated analogues shown in Figure 60.

Chapter 4: Breslow intermediate formation

4.1 Aims

To avoid, or at least minimise, competing decomposition reactions, new adducts will be studied. To prevent nucleophilic attack by hydroxide ion, two properties can be adjusted: increase the electron donating ability of the N-aryl substituent or aryl aldehyde and increase the steric hindrance through introducing bulky *ortho*-substituents on the N-aryl substituent or aryl aldehyde. Two independent methods may be used to determine the forward rate constant for deprotonation: (1) H/D exchange followed by ^{1}H NMR spectroscopy, which is inferred to go via a carbanion at C(α); (2) conventional and stopped flow UV-vis spectrophotometric studies of BI formation and decay under highly basic conditions. Rate constants for deprotonation (k_{HO}, M^{-1} s^{-1}) and reprotonation (k_{HOH}, s^{-1}) may then be combined in Eqn. (18) to yield a pK_a value in aqueous solution. In Eqn. (18), pK_w is the ionic product of water.

$$pK_a = pK_w + log\left(\frac{k_{HOH}}{k_{HO}}\right) \quad (18)$$

It is also necessary to investigate decomposition reactions by ^{1}H NMR spectroscopy and liquid chromatography electrospray mass spectrometry (LCMS) to ensure that processes occurring by UV-vis spectrophotometry are related to BI proton transfer. Experiments are also designed to attempt to obtain the reverse rate constant for reprotonation of the BI.

4.2 Results and discussion

4.2.1 Synthesis

A general scheme for the synthesis of a range of methylated hydroxyaryl adducts is shown in Scheme 62. The preparation of N-2,6-dimethoxyphenyl **255** and N-mesityl **267** triazolium salts was discussed in chapter 2. The route for preparing the triazolium salts is shown again in Scheme 62.

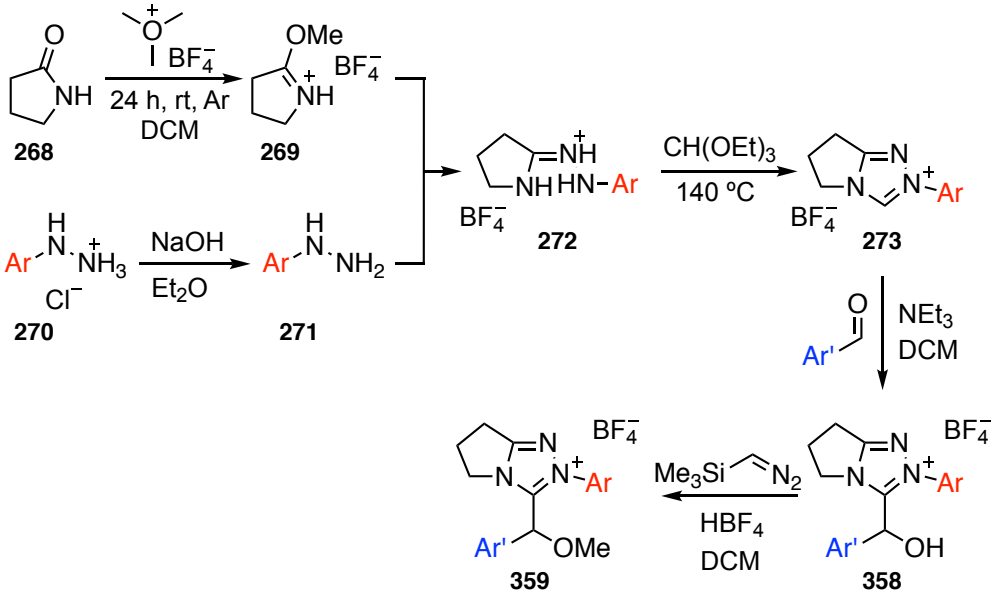

Scheme 62: General scheme for the synthesis of a range of methylated hydroxyaryl adducts.

4.2.1.1 Synthesis of hydroxyaryl adducts

The synthesis of the hydroxyaryl adducts **358** generally involved mixing triazolium salt **273** in anhydrous DCM and NEt_3 for approximately 15 minutes. The aryl aldehyde was added and stirred at room temperature in an inert atmosphere. Further details are given in the experimental section. The % conversions were determined by the ratio of signals of starting materials and products **360** – **365** (Table 14). The reactions were either quenched with aqueous HCl and extracted into DCM followed by evaporation *in vacuo*, or the solvent was evaporated *in vacuo* from the reaction mixture. These high conversions are in agreement with the equilibrium constants for hydroxyaryl adduct formation reported previously[25,79] and in chapter 3. The higher conversions for the N-2,6-dimethoxyphenyl **255** compared to the N-mesityl **267** triazolium system is also in agreement with the higher basicity of the N-2,6-dimethoxyphenyl substituted triazolium salt (chapter 2).

Table 14: Conversions obtained for hydroxyaryl adduct formation based on ratios of ^{1}H NMR spectroscopic signals.

	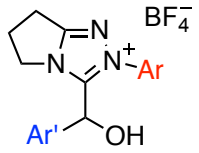	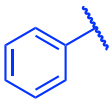	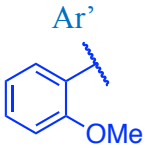	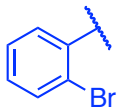
Ar	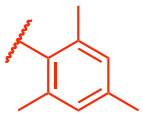	**360** 96%	**361** >99%	**362** 68%
	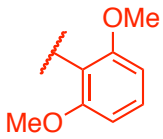	**363** >99%	**364** >99%	**365** >99%

4.2.1.2 Synthesis of methylated hydroxyaryl adducts

Previous work within the research group was aimed at preparing the methylated adduct **359** based on the N-phenyl triazolium catalyst **259** and benzaldehyde **338**.[92] Attempts to deprotonate the hydroxyaryl adduct formed *in situ* followed by a methylating agent (methyl iodide) failed to yield the desired product. Use of an analogue of Meerwein's salt (Me_3OBF_4) in either the presence or absence of a non-nucleophilic base also failed to yield the desired product, most likely due to the low nucleophilicity of the hydroxyl group. The method that worked best involved the use of a safer and easier to handle analogue of diazomethane – trimethylsilyl diazomethane (TMSDAM). This reagent has been used to methylate alcohols[134] and carboxylic acids[135,136] under acidic conditions. This was the method adopted for the methylation of the hydroxyaryl adducts. As observed previously,[79] a vast excess of TMSDAM was required to drive the reaction to completion. In all cases, HBF_4 was 48 wt. % in H_2O and TMSDAM was 2 M in hexanes.

Conversion to methylated products **366** – **379** was determined using ^{1}H NMR spectroscopy. Although methylation was successful for adducts based on the N-2,6-dimethoxyphenyl triazolium salt, attempts to purify the products **369** and **370** by reverse phase HPLC failed. Methylated adducts **366** – **368**, based on the N-mesityl triazolium catalyst **267**, were purified by standard silica flash column chromatography.

Table 15: Yields of methylated adducts starting from triazolium salt.

	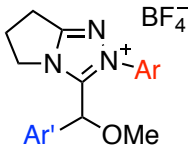	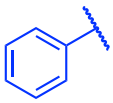		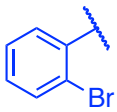
Ar	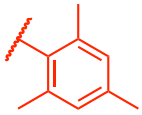	**366** 30%	**367** 30%	**368** 31%
	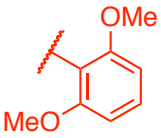	-	**369** Unable to purify	**370** Unable to purify

4.2.2 Mechanistic studies

Experiments were performed to study proton transfer and decomposition reactions of **359** (Scheme 63) using ^{1}H NMR spectroscopy, conventional and stopped flow UV-vis spectrophotometry and electrospray mass spectrometry. The results will be described in four sections: (1) Deprotonation I – C(α)-H/D exchange followed by ^{1}H NMR spectroscopy, (2) Depotonation II - UV/Vis spectrophotometric studies, (3) Stability studies and (4) Reprotonation - UV/Vis spectrophotometric studies.

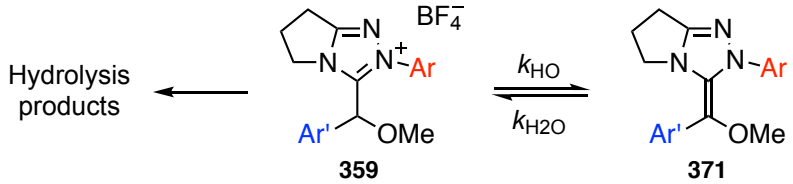

Scheme 63: Proton transfer equilibria and hydrolysis reactions studied in this chapter.

4.2.2.1 Kinetics – deprotonation I: C(α)-H/D exchange

The general method for determining the pseudo first order rate constant for C(α)-H/D exchange, k_{ex} (s^{-1}), is to monitor the disappearance of the integrated area of the C(α)-H signal as a function of time. The methodology was similar to that used in chapter 2 and that reported previously for azolium ion kinetic acidities.[55-59,61,62] C(α)-H/D exchange of **359** is inferred to go via carbanion formation **372** at C(α), which may delocalise to form the BI **371** (Scheme 64)

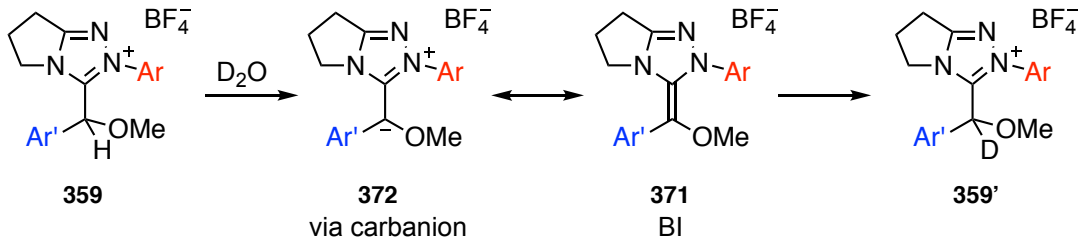

Scheme 64: C(α)-H/D is evidence of carbanion formation at C(α), which may delocalise to form the O-methylated BI 371.

Exchange reactions were carried out between pD 9 – 12 at 25 °C and I = 1.0 M (KCl). Reactions were initiated by addition of pre-equilibrated buffer solution (0.75 mL) containing internal standard (5 mM formate or 0.42 mM tetramethylammonium deuteriosulphate) to vials containing rigorously dried substrate (5 mM). Reactions were incubated in an NMR tube in a water bath thermostated at 25 °C and analysis by ^{1}H NMR spectroscopy was carried out at regular intervals. Fast reactions (with half-lives of less than 4 h) were thermostated at 25 °C directly in the NMR instrument. The progress of C(α)-H/D exchange was followed during the disappearance of 75 – 90% of the C(α)-H signal. There was no change in the integrated areas of signals due to all other protons during this period, and no appearance of new signals, consistent with the absence of any parallel decomposition or hydrolysis under the reaction conditions.

The fraction of unexchanged substrate, f(s), can be determined from Eqn. (19), where $A_{\mathrm{C\alpha H}}$ is the integrated area of the ^{1}H NMR signal due to the acidic proton, relative to the integrated area of the internal standard, A_{std}. In these experiments, either tetramethylammonium deuteriosulphate or potassium formate were chosen as the internal standard. ^{1}H NMR Spectra were integrated using MestreNova following a first order phase correction and a baseline correction using a 6$^{\mathrm{th}}$ order Bernstein Polynomial Fit. Reactions were pseudo first order, and the slope of a semi logarithmic plot of f(s) as a function of time gives the rate constant for exchange, k_{ex} (s^{-1}), as the gradient according to Eqn. (20).

$$f(\mathrm{s}) = \frac{(A_{\mathrm{C\alpha H}}/A_{\mathrm{std}})_t}{(A_{\mathrm{C\alpha H}}/A_{\mathrm{std}})_{t=0}} \tag{19}$$

$$\ln f(\mathrm{s}) = -k_{ex}t \tag{20}$$

A representative NMR spectral overlay (Figure 67), and semi-logarithmic plot (Figure 68) are shown for O-methylated adduct **366** in the next section (4.2.2.1.1). Semi-logarithmic plots, data from buffer catalysis studies and tabulated rate constants for the three compounds described in this chapter are given in Appendix 3.

4.2.2.1.1 Unsubstituted benzaldehyde adduct 366

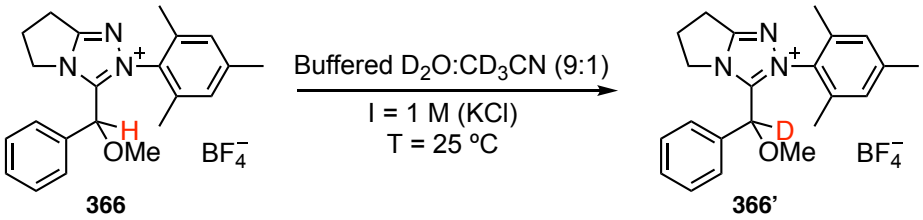

366 **366'**

Representative ^{1}H NMR spectra obtained at three time points during C(α)-H/D exchange at pD 10.40 are shown in Figure 67. C(α)-H/D exchange results in the disappearance of the ^{1}H NMR signal corresponding to the proton at the C(α)-H position at 5.53 ppm. The signal corresponding to the internal standard, tetramethylammonium deuteriosulphate, with its twelve equivalent non-exchangeable[137] protons is observed at 3.16 ppm.

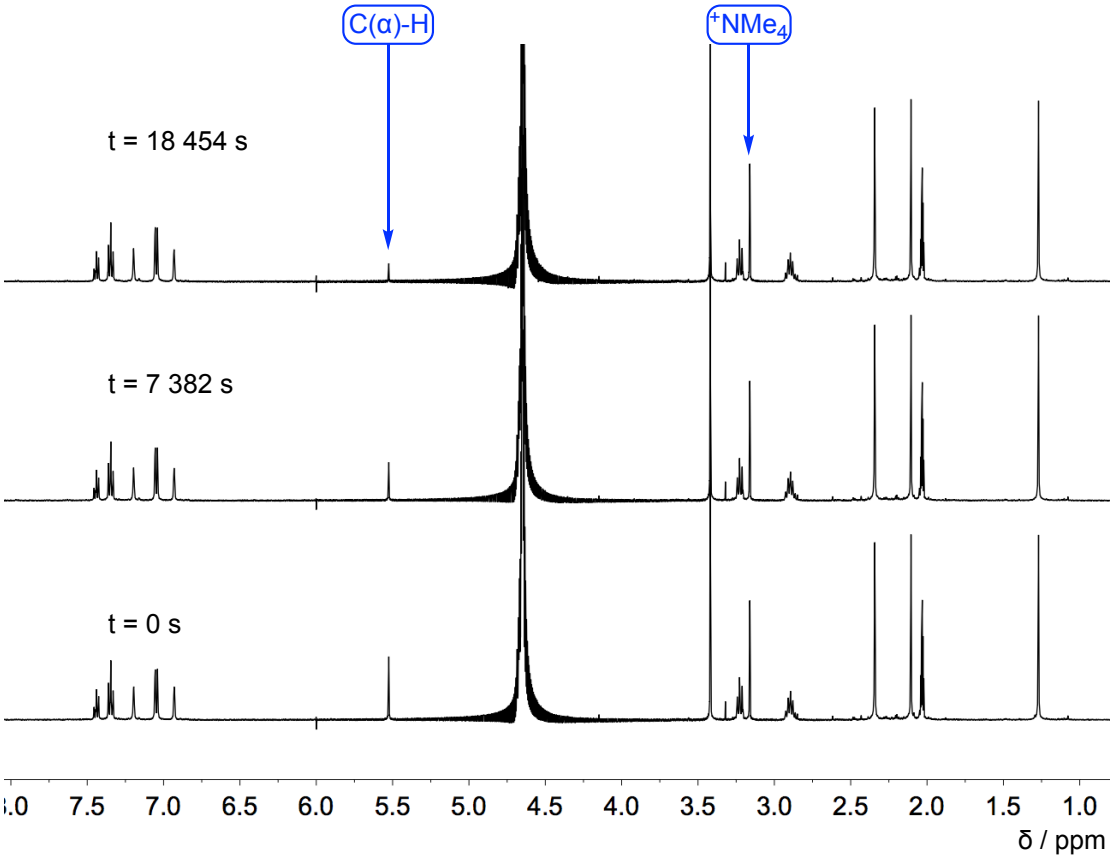

Figure 67: Representative ^{1}H NMR spectra at 500 MHz of adduct 366 (5 mM, pD 10.40) obtained during C(α)-H/D exchange (s, 5.53 ppm) in D_2O:CD_3CN (9:1) at 25 °C and I = 1.0 M (KCl).

A semi-logarithmic plot of the fraction of unexchanged substrate **366** against time is shown in Figure 68. The gradient gives the pseudo first order rate constant for C(α)-H/D exchange, k_{ex} (s^{-1}), at a given pD. Specific base catalysis was confirmed by kinetic

analysis where k_{ex} showed a kinetic dependence only on the concentration of deuteroxide ion, according to Eqn. (21).

$$k_{ex} = k_{DO}[DO] \tag{21}$$

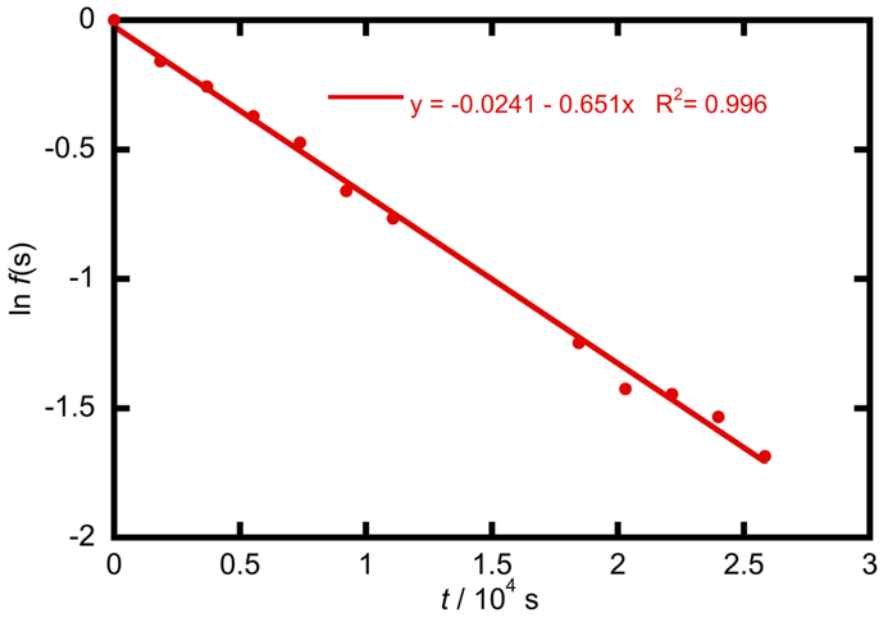

Figure 68: Semi-logarithmic plot of the fraction of unexchanged substrate against time for C(α)-H/D exchange reaction of adduct 366 at 25 °C in D_2O:CD_3CN (9:1) at pD 10.40 and I = 1.0 M (KCl). The gradient gives the pseudo first order rate constant for exchange, k_{ex} = (6.51 ± 0.12) × 10^{-5} s^{-1}, at pD 10.40.

4.2.2.1.2 *Ortho*-substituted benzaldehyde adducts 367 and 368

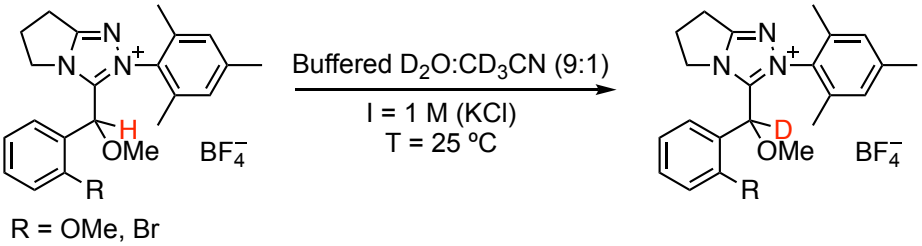

C(α)-H/D exchange was found to be general base catalysed for **367** and **368** (see Appendix 3). Pseudo first order rate constants for exchange were obtained at different total buffer concentrations at a given pD and constant ionic strength I = 1.0 M (KCl). Reactions were carried out at a range of pD. Extrapolation of the slope of rate constants at a given pD to zero buffer concentration gives the sum of the rate constants for pD-independent and deuteroxide ion catalysed exchange.

The low isolated yield of **368** meant that data could only be obtained for buffer independent rate constants for C(α)-H/D exchange at two concentrations of deuteroxide ion.

Figure 69 shows the plot of observed pseudo first order rate constants for buffer independent exchange as a function of deuteroxide ion concentration. The gradient of the slope gives the second order rate constant for deuteroxide ion catalysed exchange, k_{DO} (M^{-1} s^{-1}). The intercept for **367** and **368** go through 0 and so pD-independent exchange, k_0 (s^{-1}), was found to be insignificant. The rate equation is given in Eqn. (22).

$$k_{ex} = k_{DO}[DO] + k_{CO_3}[CO_3] \quad (22)$$

4.2.2.1.3 Determination of k_{DO}

The buffer independent pseudo first order rate constants have been plotted as a function of deuteroxide ion concentration in Figure 69. Second order rate constants for deuteroxide ion catalysed H/D exchange, k_{DO} (M^{-1} s^{-1}), are obtained from the slopes of these plots, according to Eqn. (21), and may be used as an estimate for the rate constant for deprotonation of the O-methylated adducts.

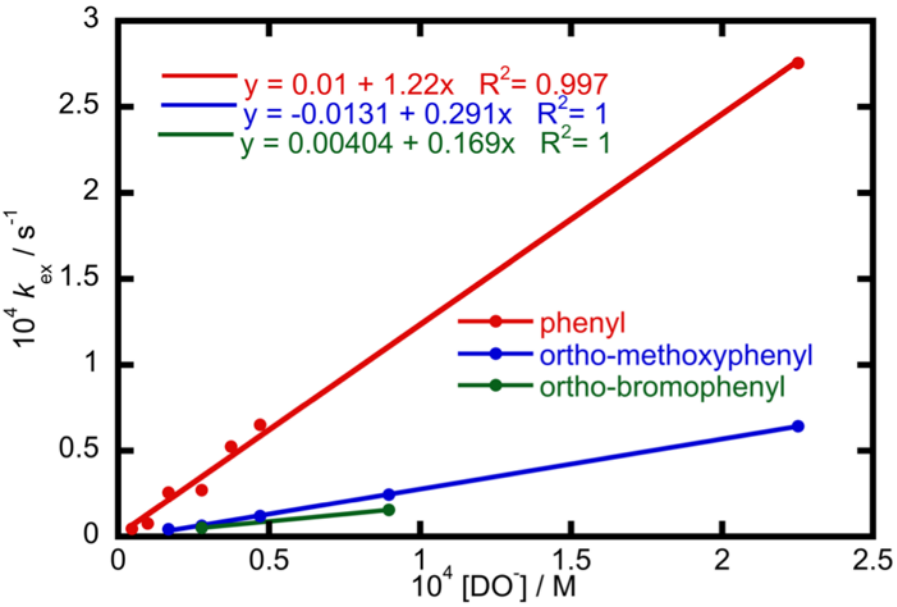

Figure 69: Second order plot of the pseudo first order rate constants for buffer independent C(α)-H/D exchange (k_{ex}, s^{-1}) as a function of deuteroxide ion concentration in aqueous solution (D_2O:CD_3CN 9:1) at 25 °C and ionic strength, I = 1.0 M (KCl).

Table 16: Second order rate constants for deuteroxide ion-catalysed C(α)-H/D exchange (k_{DO}, $M^{-1}s^{-1}$) in aqueous solution (D_2O:CD_3CN 9:1) at 25 °C and ionic strength, I = 1.0 M (KCl).

Adduct	k_{DO} (M^{-1} s^{-1}) [a]
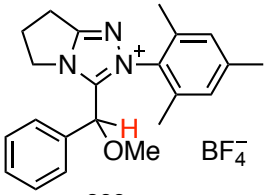 **366**	1.22 (± 0.03)
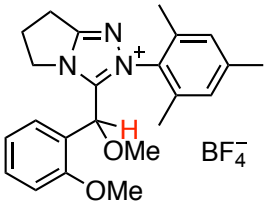 **367**	0.291 (± 0.003)
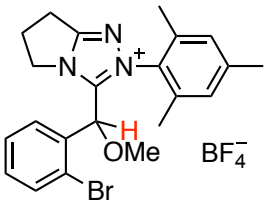 **368**	0.169[b]

[a]Values of k_{DO} (M^{-1} s^{-1}) obtained from the gradient of second order plot shown in Figure 69 by fitting data to Eqn. (21). [b]No standard error is reported as data was only obtained at two concentrations of deuteroxide ion.

4.2.2.1.4 Mechanism of C(α)-H/D exchange

The mechanism for triazolium salt C(3)-H/D exchange of triaozlium ions was previously found to be SBC.[58] The mechanism for C(α)-H/D for the phenyl adduct is also SBC, while the *ortho*-substituted adducts display weak GBC.

SBC involves an initial deprotonation at C(α)-H by deuteroxide ion to give an intimate ion pair **373**. This complex may either return to unexchanged H-adduct **359**, or undergo solvent reorganisation, which allows for the delivery of a deuteron back to the BI **374**. This may involve either the rotation of the molecule of DOH or exchange with D_2O from bulk solvent. This process is essentially irreversible in deuterated solvent when the initial concentration of H-adduct is low. Finally, deuteronation of BI **374** gives the exchanged product **359'**. As discussed in chapter 2, SBC of H/D exchange would mean that solvent reorganisation for H/D exchange is a rate limiting step. *Ortho*-substituted adducts display weak GBC of H/D exchange and so both the proton transfer and solvent reorganisation steps are partially rate limiting.

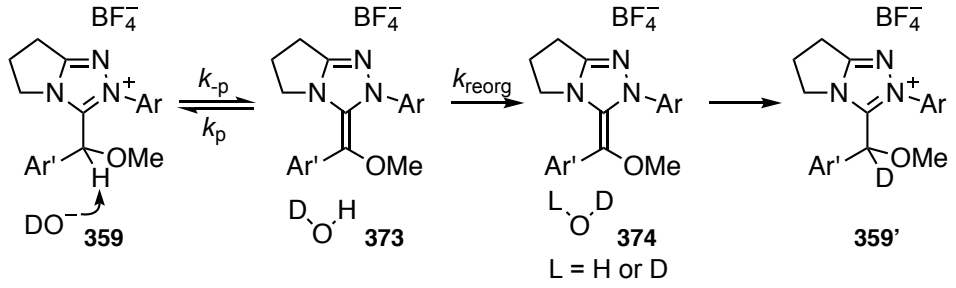

Scheme 65: Deuteroxide ion catalysed C(α)-H/D exchange.

The rate constants for H/D exchange for unsubstituted adduct **366** is > 4-fold larger than for the electron donating *ortho*-methoxy adduct **367** and electron withdrawing *ortho*-bromo adduct **368**. This could be because the *ortho*-substituted aldehydes are either (1) hindering the approach of the base or (2) too sterically hindered to become planar in the BI, or a combination of the two effects. The *ortho*-substituents of the aldehyde portion of the O-methylated adducts are relatively close to the reaction centre and it is therefore difficult to make comments on the electronic effects of the substituents on the rate constants for C(α)-H/D exchange.

It was previously found that varying the N-aryl substituent of the triazolium portion of the methylated adduct had a greater effect on the rate constant for C(α)-H/D exchange[79] than on C(3)-H/D exchange.[58] This can easily be seen on a Hammett plot, where the y-axis corresponds either to log (k_{ex}/s^{-1}) for C(α)-H/D exchange at a single pD = 10.9,[79] or log (k_{DO}/M^{-1} s^{-1}) for C(3)-H/D exchange.[58]

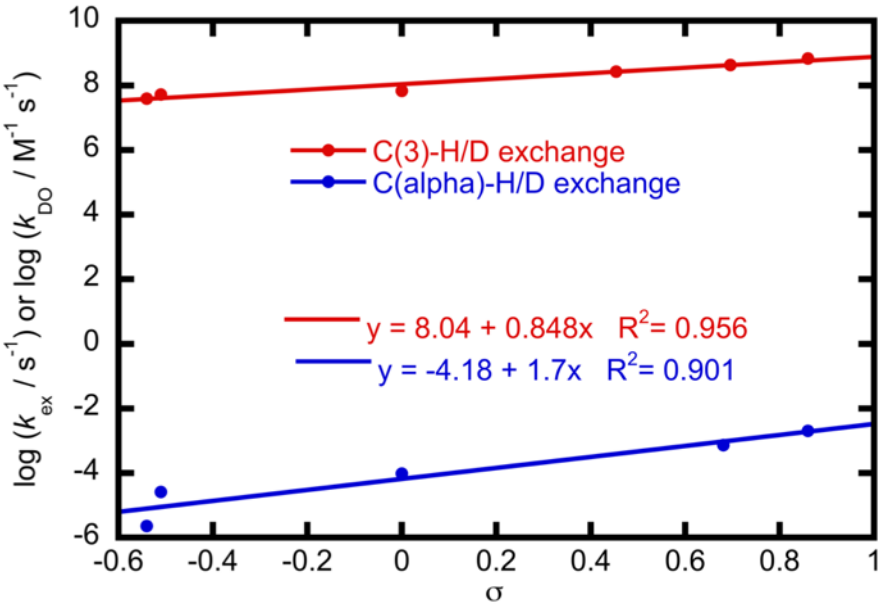

Figure 70: Hammett plot for C(3)-H/D and C(α)-H/D exchange, using values determined by O'Donoghue and co-workers.[58,59,79]

Two points of note are: (1) the gradient of the slope for C(α)-H/D is greater than for C(3)-H/D exchange and (2) the magnitude of the rate constants are greater for C(3)-H/D exchange than C(α)-H/D exchange (even after approximating a second order rate constant, k_{DO} (M^{-1} s^{-1}), assuming a first order dependence on deuteroxide ion, and dividing k_{ex} by [DO^-] at pD 10.9).

These finding are potentially consistent with a relatively delocalised BI **371** rather than a localised carbanion at C(α) **372**. The slower rate constants for C(α)-H/D exchange and presence of weak GBC may be a result of significant structural and electronic reorganisation, which includes reorganisation of the solvent. The absence of GBC and relatively fast second order rate constants for C(3)-H/D exchange, k_{DO} (M^{-1} s^{-1}), are consistent with 'normal' acid behaviour of a localised carbanion,[55,57,58,61,62] whereas the magnitude of second order rate constants for C(α)-H/D exchange (estimated at pD 10.9)[79] are consistent with slow proton transfers observed for carbon acids where delocalisation of the charge is occurring.[138]

The second order rate constants obtained here (Table 16) do not give evidence either for or against a planar or twisted aldehyde in the O-methylated BIs for *ortho*-substituted aldehydes. They do, however, show that steric hindrance near C(α)-H is a dominant factor in the deprotonation of the O-methylated adducts to give O-methylated BIs. Further work may be directed at investigating *ortho*-substituted aldehyde systems where a substituent on the *para*-position is varied.

Unlike the deprotonation of azolium ions to give ylid/carbenes, it is more difficult to predict a rate constant for reprotonation of the BI to estimate a pK_a because of the possibility that proton transfer back to C(α) is slow due to partial or complete delocalisation of the carbanion.

4.2.2.2 Kinetics – deprotonation II: UV-vis spectrophotometric studies

Based on the work by Jordan[86] and Maguire[92] it was anticipated that stopped flow UV-vis spectrophotometry would be required to study deprotonation, reprotonation and decomposition reaction rates. This was the method used here to follow the reactions up to a maximum time of 200 seconds. Data obtained by conventional UV-vis spectrophotometry for compound **367** (shown in Appendix 3) show that the absorbance increases are due to reaction and not due to instrument artefacts. Stopped flow UV-vis spectrophotometry involves the rapid mixing of solutions and following the absorbance changes as a function of time. The generation of a more conjugated system would be

predicted to result in an absorbance at a longer wavelength than the starting material. These experiments involved a 1:1 ratio of solution volumes, hence adducts were dissolved in H_2O:MeCN (8:2) at double the desired final concentration. Hydroxide solutions were prepared by diluting 1.000 M titrimetric standard solutions at a constant ionic strength I = 1.0 M (KCl). Following mixing, the final solvent composition was H_2O:MeCN (9:1) at I = 0.5 M (KCl), which although constant for all hydroxide ion concentrations, is half the value used in the NMR experiments. As noted in chapter 1, Jordan[86] and Maguire[92] did not maintain ionic strength.

Final concentrations of hydroxide and adduct quoted in this section are those of the final reaction mixture in the mixing chamber. In the case of each substrate, the following control experiments were performed:

1. Mixing of hydroxide solution with the H_2O:MeCN solution (8:2) used to dissolve the substrate (in the absence of substrate)
2. Mixing water with the H_2O:MeCN solution (8:2) of substrate.

These data show no change in absorbance at any wavelength as a function of time.

Rate constants and associated errors were obtained using the software program associated with the stopped flow spectrophotometer (Pro-Data SX).

4.2.2.2.1 *Ortho*-methoxybenzaldehyde adduct (367)

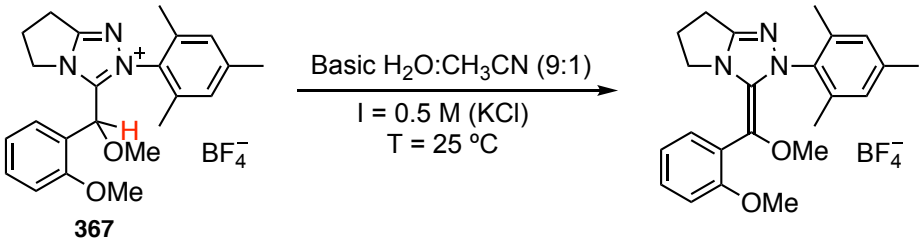

367

Stopped flow UV-vis spectra of methylated adduct **367** (0.625 mM) and 0.125 M NaOH in H_2O:MeCN (9:1) at four time points between 0 – 100 seconds is shown in Figure 71. A small absorbance increase is observed between 300 – 350 nm, with the largest change observed at 330 nm.

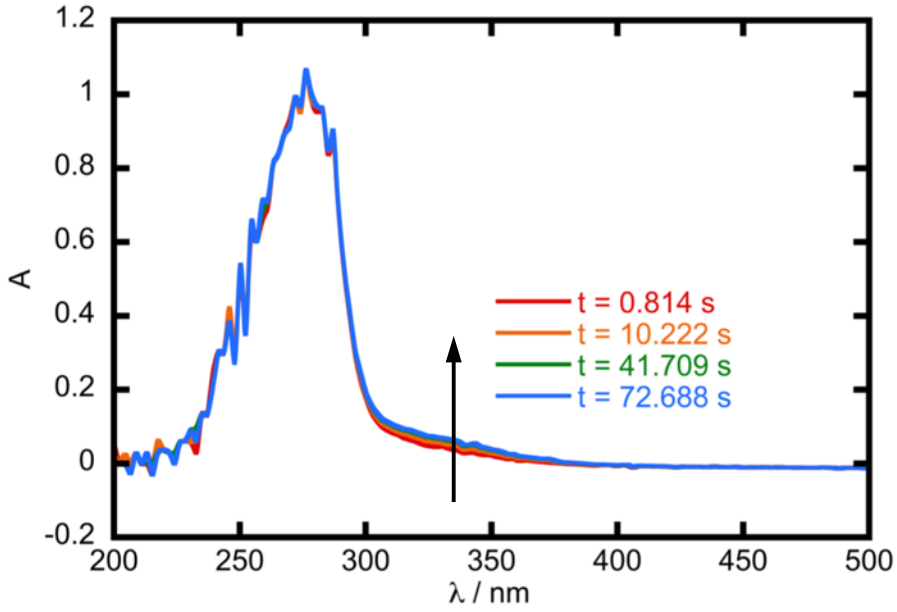

Figure 71: UV-vis spectra at four time points between 0 – 73 seconds for methylated adduct 367 (0.625 mM) in 0.125 M NaOH. Experiment was run in H_2O:MeCN (9:1).

The absorbance traces at 330 nm at four different concentrations of KOH at 25 °C in H_2O:MeCN (9:1) and I = 0.5 M (KCl) are shown in Figure 72. The data shown are absorbance traces following at least four runs so that consistent results were obtained. All data has been adjusted so that the absorbance at t = 0 is set to 0.

The shape of the function over the 200 seconds clearly shows additional processes in addition to pseudo first order kinetics. This is may be attributed to parallel decomposition reactions in hydroxide solution. The data were fitted to first order exponential functions for at least three half-lives of the faster of the two processes. The rate constants were then plotted as a function of hydroxide ion concentration (Figure 76) to obtain a second order rate constant for deprotonation, k_{HO} (M^{-1} s^{-1}), of 0.40 ± 0.02 M^{-1} s^{-1}. The similarity between rate constants obtained by NMR for C(α)-H/D exchange (k_{DO}) and UV-vis spectrophotometry (k_{HO}) provides confidence that a proton transfer process is being observed.

The 1.37-fold larger rate constant obtained in H_2O:MeCN at I = 0.5 M by UV-vis spectrophotometry compared to in D_2O:CD_3CN at I = 1.0 M by NMR spectroscopy may be ascribed to (1) a small primary solvent kinetic isotope effect and (2) a lower ionic strength. It may be expected that a decrease in ionic strength would destabilise the ground cationic state relative to the neutral transition state and therefore increase the rate constant. Rate constants for C(2)-H/D exchange of a range of thiazolium salts were found to increase with decreasing ionic strength.[62]

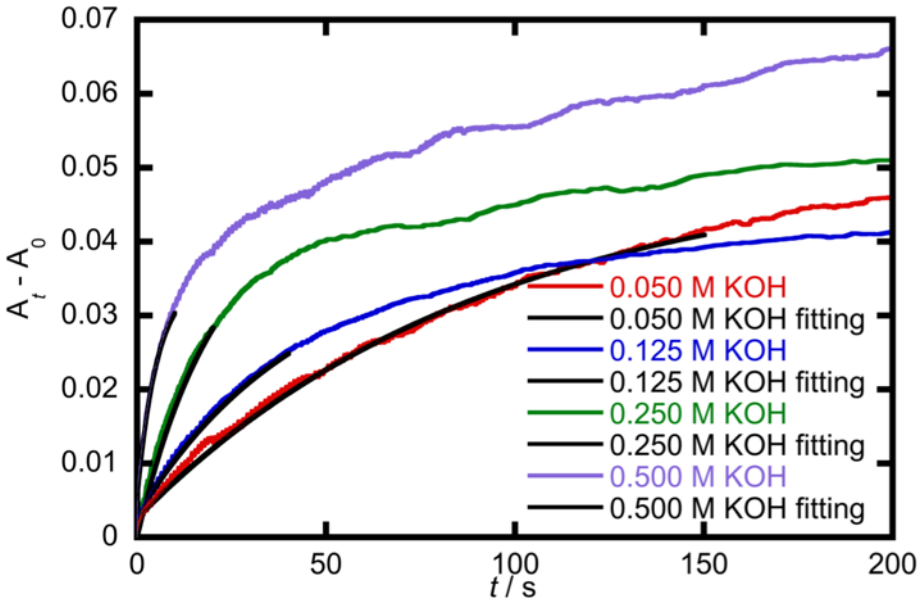

Figure 72: Stopped flow spectrophotometric traces at 330 nm obtained for methylated adduct 367 (0.625 mM) at four different hydroxide ion concentrations at 25 °C in H_2O:MeCN (9:1) and I = 0.5 M (KCl). All data are adjusted so that A = 0 at t = 0. Also shown are the first order exponential fittings for approximately three half-lives, obtained using the Pro-Data SX data associated with the stopped flow spectrometer. Rate constants obtained are given in Appendix 3.

4.2.2.2.2 Unsubstituted benzaldehyde adduct (366)

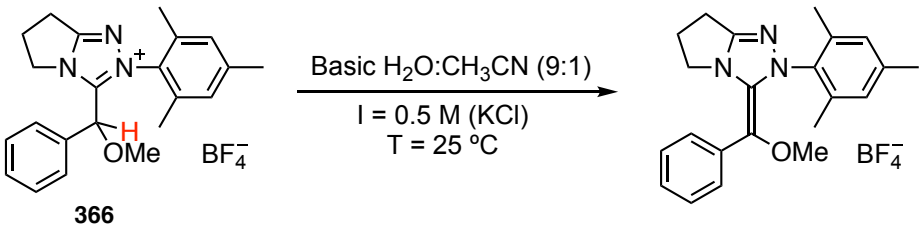

366

Stopped flow UV-vis spectra of methylated adduct **366** (2.5 mM) and 0.500 M KOH in H_2O:MeCN (9:1) at 25 °C at five time points is shown in Figure 73. A small absorbance increase is observed between 300 – 350 nm, with the largest change observed at 330 nm.

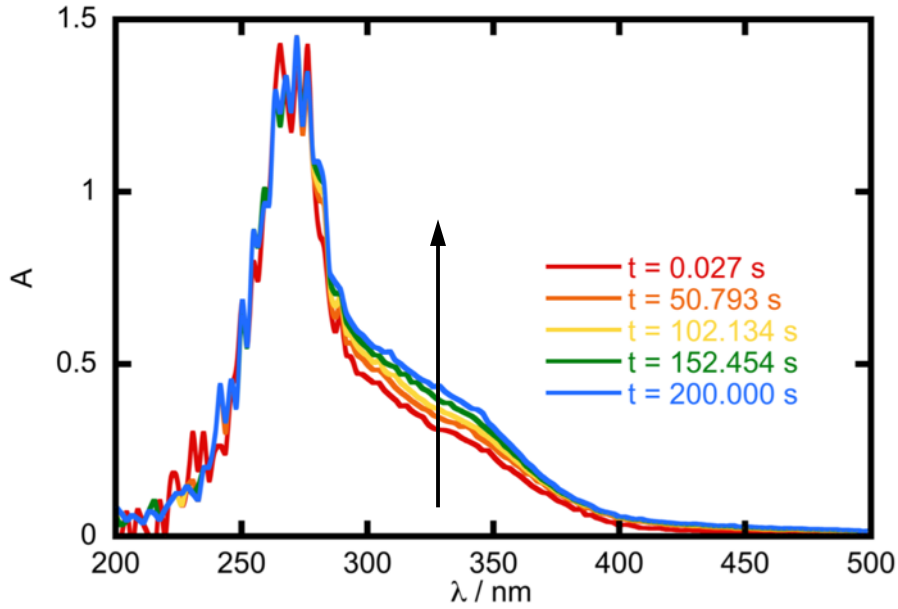

Figure 73: UV-vis spectra at five time points between 0 – 200 s for the reaction of methylated adduct 366 (2.5 mM) in 0.500 M KOH at 25 °C in H_2O:MeCN (9:1).

The results at 330 nm at 0.050 M and 0.375 M KOH at 25 °C in H_2O:MeCN (9:1) and I = 0.5 M (KCl) are shown in Figure 74. The data shown are absorbance traces following at least four runs so that consistent results were obtained.

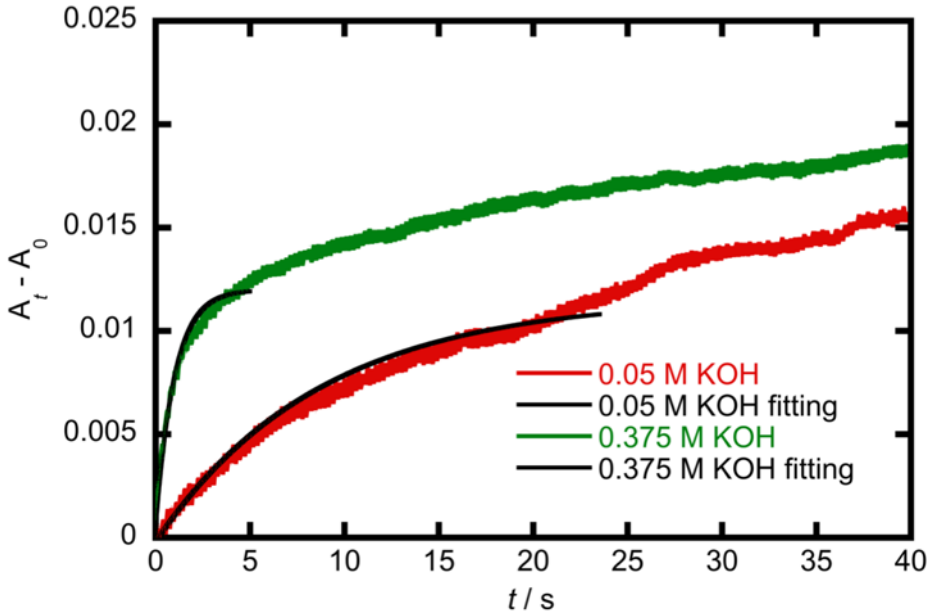

Figure 74: Stopped flow spectrophotometry traces at 330 nm of methylated adduct 366 (2.5 mM) in 0.05 M and 0.375 M KOH at 25 °C in H_2O:MeCN (9:1) and I = 0.5 M (KCl). Also shown are the first order exponential fittings for approximately three half-lives, obtained using the Pro-Data SX data associated with the stopped flow spectrometer. Rate constants obtained are given in Appendix 3.

The data in Figure 74 again show at least one additional process in addition to pseudo first order kinetics, which may be attributed to parallel decomposition reactions in hydroxide solution. The data were fitted to first order exponential functions for at least

three half-lives of the faster of the two (or more) processes. Unfortunately, reliable results could not be obtained at other concentrations of KOH due to spectrometer malfunction and insufficient material. The rate constants were then plotted as a function of hydroxide ion concentration (Figure 76) to obtain a second order rate constant for deprotonation, k_{HO} (M^{-1} s^{-1}), of 1.73 M^{-1} s^{-1}.

This value is 1.42-fold larger than the second order rate constant for C(α)-H/D exchange obtained in D_2O:CD_3CN at I = 1.0 M by NMR spectroscopy which, like the *ortho*-methoxybenzaldehyde adduct **367**, may be ascribed to (1) a small primary solvent kinetic isotope effect and (2) a lower ionic strength. The similarity in k_{HO}/k_{DO} ratios for adducts **366** and **367** allows us to be reasonably confident that a proton transfer process is being observed.

4.2.2.2.3 *Ortho*-bromobenzaldehyde adduct (368)

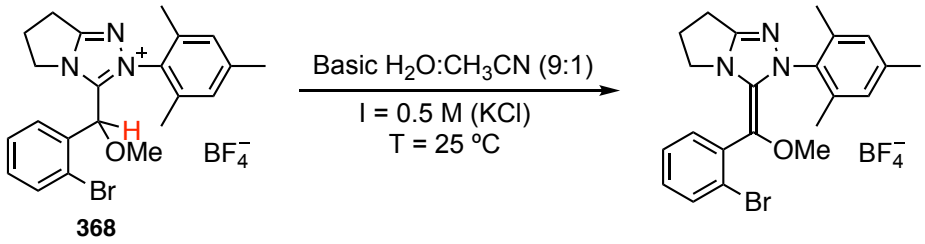

368

The absorbance traces at 330 nm at four concentrations of KOH at I = 0.5 M (KCl) and 25 ºC are shown in Figure 75. The absorbance traces were obtained following at least four drives of the drive syringes so that clean sample was mixed and results were consistent. All data has been adjusted so that the absorbance at t = 0 is set to 0. The data show an initial small increase in absorbance ($\Delta A \leq 0.004$) up to ~ 900 ms, followed by a smaller decrease up to ~ 5 s and then a gradual increase in absorbance. The change in absorbance values were much smaller than for adducts **367** (Figure 72) and **366** (Figure 74).

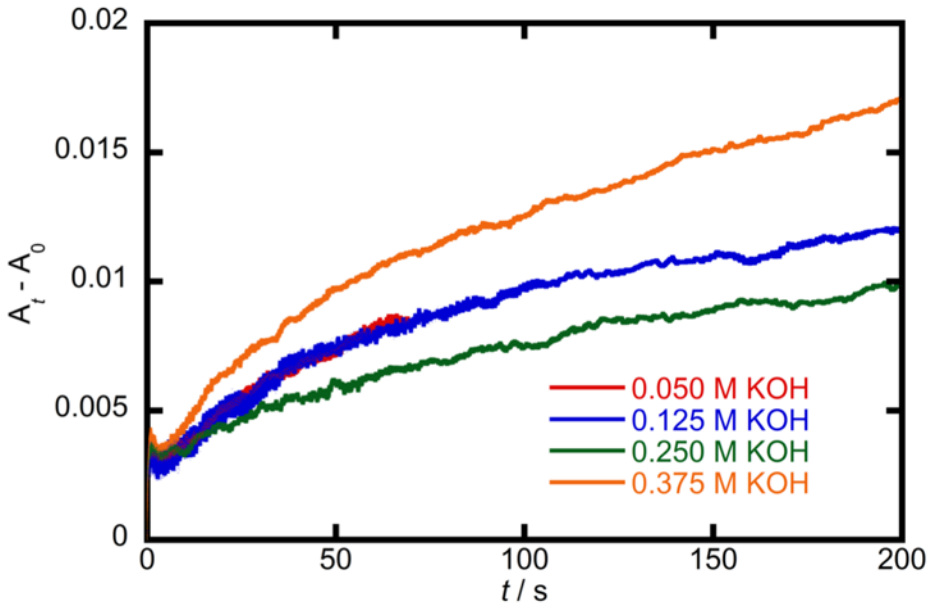

Figure 75: Stopped flow spectrophotometric traces at 330 nm obtained for methylated adduct 368 (0.625 mM) at four different hydroxide ion concentrations at 25 °C in H_2O:MeCN (9:1) and I = 0.5 M (KCl). All data are adjusted so that A = 0 at t = 0.

The data were fitted to single and to double exponential functions at t ≥ 4 s (fittings not shown for reasons to be described). Values for the rate constants in 0.05 M hydroxide would not converge and so no value could be obtained. Again, the slower process was at least 10 times slower than the faster process. The first order rate constants obtained from application of either of the two functions for the other three concentrations of KOH do not correlate with hydroxide ion concentration. This may either be due to decomposition reactions occurring or too dilute a sample of adduct (cf absorbance changes in Figure 75 are close to the noise level of the instrument). However, insufficient material meant that experiments at higher concentrations of adduct could not be performed.

4.2.2.2.4 Determination of k_{HO}

The pseudo first order rate constants, k_{obs} (s^{-1}), have been plotted as a function of hydroxide ion concentration in Figure 76. Second order rate constants for hydroxide ion catalysed deprotonation, k_{HO} (M^{-1} s^{-1}), are obtained from the slopes of these plots, according to Eqn. (23).

$$k_{obs} = k_{HO}[HO] \tag{23}$$

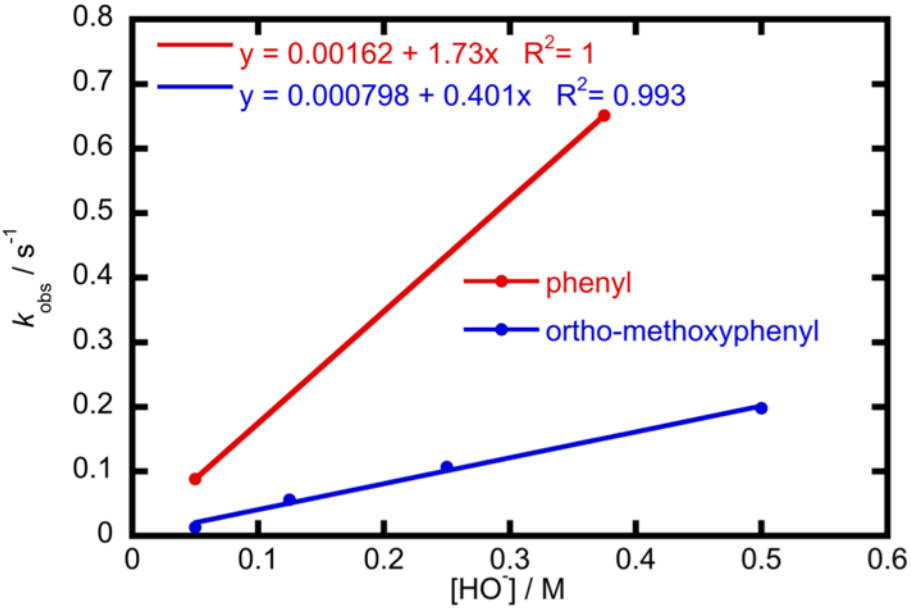

Figure 76: Second order plot of the pseudo first-order rate constants for the observed increase in absorbance (k_{obs}, s^{-1}) as a function of hydroxide ion concentration at 25 °C in H_2O:MeCN (9:1) and I = 0.5 M (KCl).

Table 17: Comparison of second order rate constants for hydroxide ion-catalysed deprotonation of C(α)-H (k_{HO}, $M^{-1}s^{-1}$) in aqueous solution (H_2O:MeCN 9:1) at 25 °C and ionic strength, I = 0.5 M (KCl), compared with the second order rate constants for deuteroxide ion-catalysed C(α)-H/D exchange (k_{DO}, $M^{-1}s^{-1}$) in aqueous solution (D_2O:CD_3CN 9:1) at 25 °C and ionic strength, I = 1.0 M (KCl).

Adduct	k_{HO} (M^{-1} s^{-1}) [a]	k_{DO} (M^{-1} s^{-1}) [b]	k_{HO} / k_{DO}
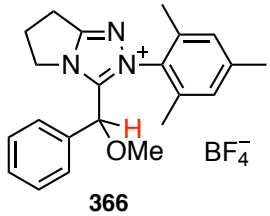 **366**	1.73[c]	1.22 (± 0.03)	1.42
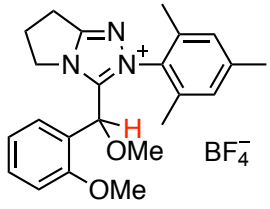 **367**	0.40 (± 0.02)	0.291 (± 0.003)	1.37
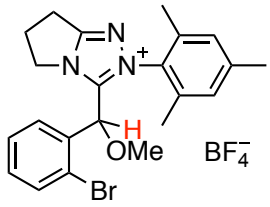 **368**	-	0.169[c]	-

[a]Values of k_{HO} (M^{-1} s^{-1}) obtained from the gradient of second order plot shown in Figure 76. by fitting data to Eqn. (23). [b]Values of k_{DO} (M^{-1} s^{-1}) obtained from the gradient of second order plot shown in Figure 69. by fitting data to Eqn. (21). [c]No standard error is reported as data was only obtained at two concentrations of hydroxide or deuteroxide ion.

4.2.2.3 Stability studies

The thiazolium compounds **196** studied by Jordan and co-workers decomposed in aqueous hydroxide solution, where clean ring opening was observed and the products were characterised by NMR spectroscopy.[86] C(2) in this case was clearly the most electrophilic position and the point of attack by hydroxide ion. When studying the deprotonation of these adducts in aqueous hydroxide solution by stopped flow spectrophotometry, these authors attributed a part of the decrease in absorbance after the initial rise (Figure 7) to this decomposition reaction.

With the triazolium systems studied here, and previously[92] there are two carbons on the triazolium ring which may be susceptible to attack. ^{1}H NMR spectra of the substrates mixed with deuteroxide ion were uninformative, most probably due to multiple decomposition reactions and low concentrations of each product. Electrospray mass spectrometry is another method for studying the decomposition products. This section briefly describes ^{1}H NMR and LCMS studies on the decomposition reactions and the implications for studying proton transfer.

4.2.2.3.1 Unsubstituted benzaldehyde adduct (366)

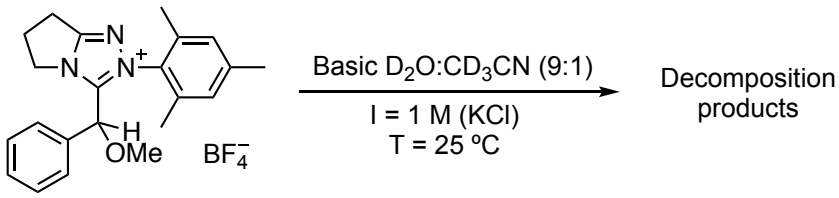

366

Reaction of methylated adduct **366** (5 mM) with 0.5 M KOD was followed by ^{1}H NMR spectroscopy in D_2O:CD_3CN (9:1) at 25 °C and I = 1.0 M (KCl). Formate was used as internal standard to enable any changes in the signals to be analysed. The signal corresponding to C(α)-H was not present in the first NMR spectrum as it had fully exchanged with deuterium. These conditions were chosen as they represented a similar set of conditions to that in C(α)-H/D exchange and UV-vis spectrophotometric experiments. A representative set of ^{1}H NMR spectra is shown in Figure 77.

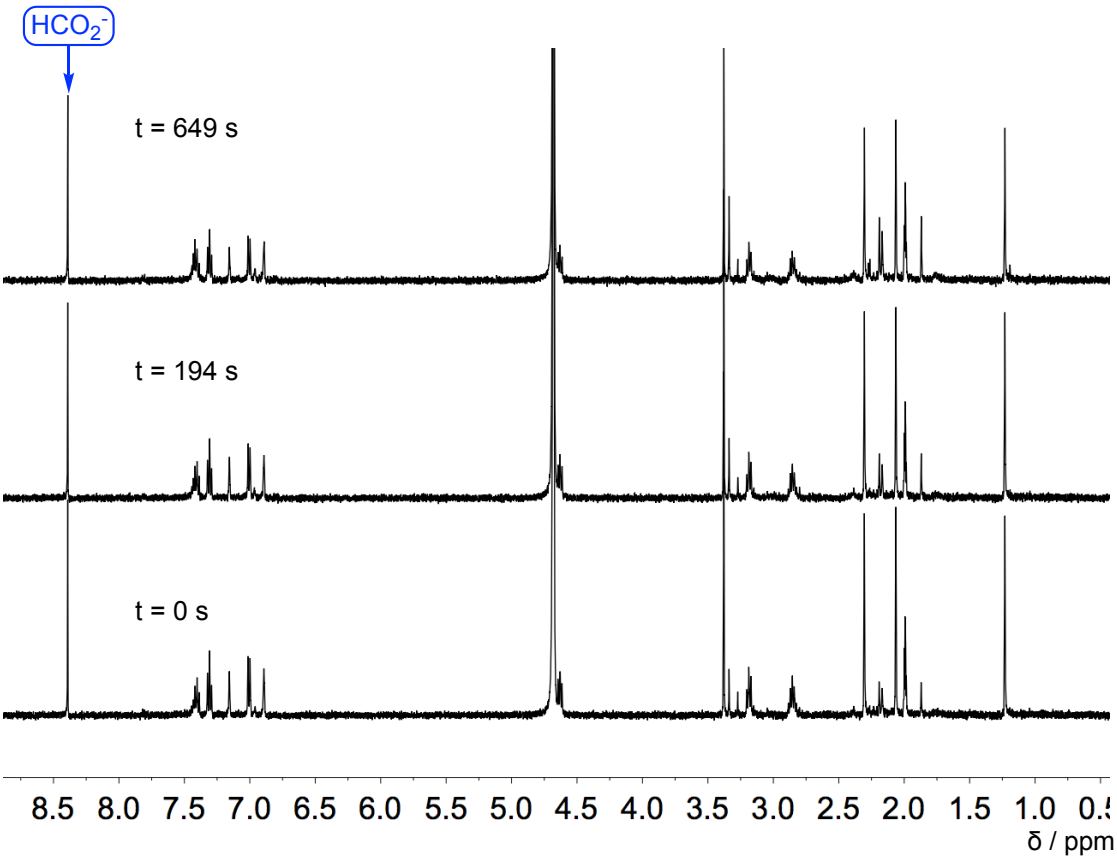

Figure 77: Representative ^{1}H NMR spectra at 400 MHz of O-methylated adduct 366 (5 mM) obtained in 0.5 M KOD in D_2O:CD_3CN (9:1) at 25 °C and I = 1.0 M (KCl).

The NMR spectra show only a small change is occurring in ~ 10 mins. There is no shift, or the appearance of, new signals at lower δ values that would be consistent with deprotonation and therefore shielding of the ^{1}H signals on the methylated adduct.

A semi-logarithmic plot of the fraction of starting material (deuterated), *f*(s), against time is shown in Figure 78. A rate constant at 0.5 M KOD was estimated to be k = (4.0 ± 0.5) × 10^{-4} s^{-1}, corresponding to a half-life of ~ 48 minutes. This could account for the additional process which is observed by stopped flow UV-vis spectrophotometry.

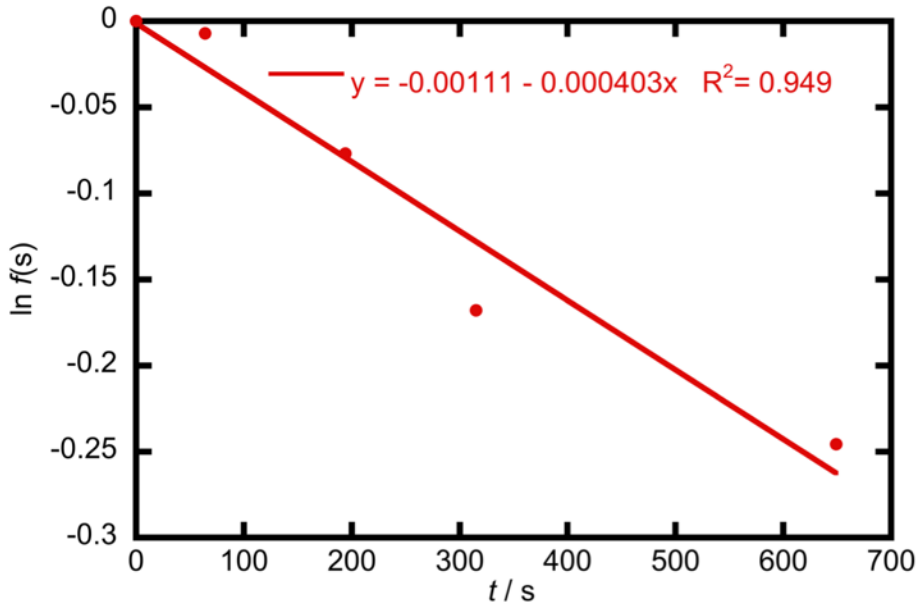

Figure 78: Semi-logarithmic plot of the fraction of starting material 366 (deuterated) against time in 0.5 M KOD obtained in D_2O:CD_3CN (9:1) at 25 °C and I = 1.0 M (KCl).

Electrospray mass spectrometry, used in conjunction with HPLC and UV-vis detection, showed no absorbance at 330 nm (Figure 79). A mass corresponding to a potential hydroxide adduct ($[M+H]^+$ = 367) through attack of deuteroxide ion at the triazolium ring, or the equivalent amides, is present (Figure 80). The likely structures corresponding to $[M+H]^+$ = 367 are shown in Figure 80. The *m*/*z* values of 366, 368 and 369 may be caused by the incorporation of H vs D at a number of sites. *m*/*z* values consistent with the aniline or hydrazine of the 2,4,6-trimethylphenyl group are not detected at any wavelength by LCMS. The conditions used in LCMS may have an impact on the resulting structures. Since a small amount of formic acid is used, any BI would be reprotonated and any acid sensitive hydrolysis products would potentially not appear in the chromatogram. Additional reactions may be possible once these ring opening reactions have occurred.

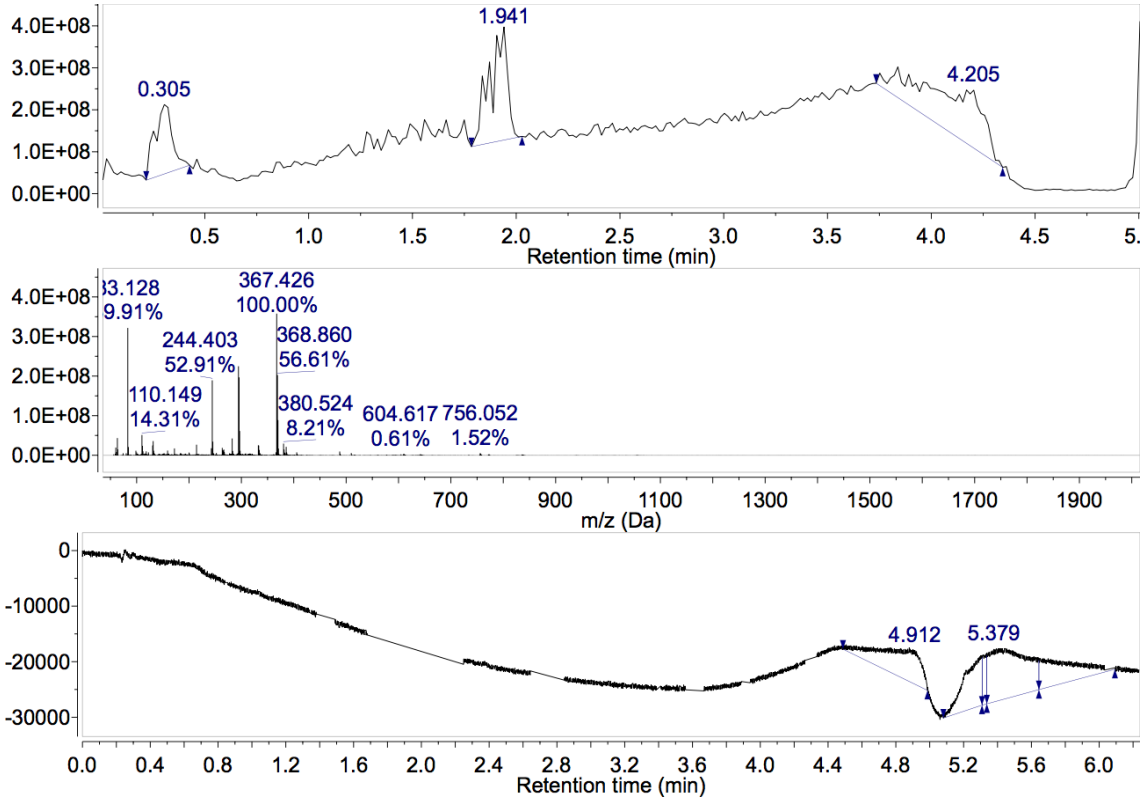

Figure 79: Electrospray chromatogram of methylated adduct 366 in 0.5 M KOH after ~ 90 minutes. (top) Total ion count chromatogram; (middle) mass spectrum of positive ions at a retention time of 1.78 – 2.01 mins; (bottom) UV-vis absorbance at 330 nm.

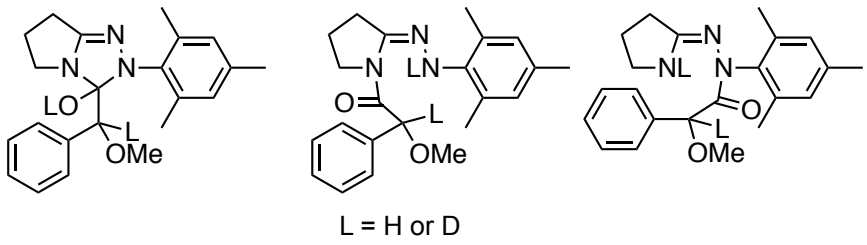

Figure 80: Structures of hydrate adduct and ring opened triazole rings that are consistent with $[M+H]^+$ = 367.

4.2.2.3.2 *Ortho*-methoxybenzaldehyde adduct (367)

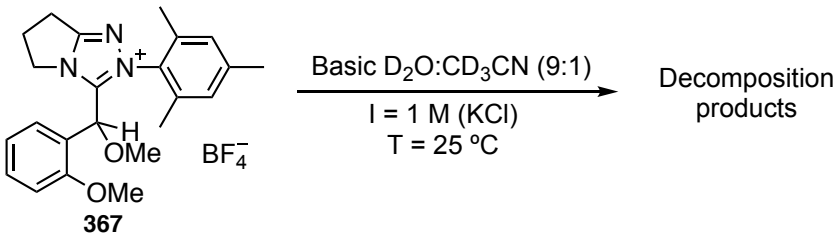

Reaction of methylated adduct **367** (5 mM) with 1.0 M KOD was followed by ^{1}H NMR spectroscopy in D_2O:CD_3CN (9:1) at 25 °C and I = 1.0 M (KCl). Tetramethylammonium deuteriosulphate was used as internal standard to enable any changes in the signals to be analysed. The signal corresponding to C(α)-H was not present in the first NMR spectrum as it had fully exchanged with deuterium. These

conditions were chosen as they represented a similar set of conditions to that in C(α)-H/D exchange and UV-vis spectrophotometric experiments. A representative set of ^{1}H NMR spectra is shown in Figure 81.

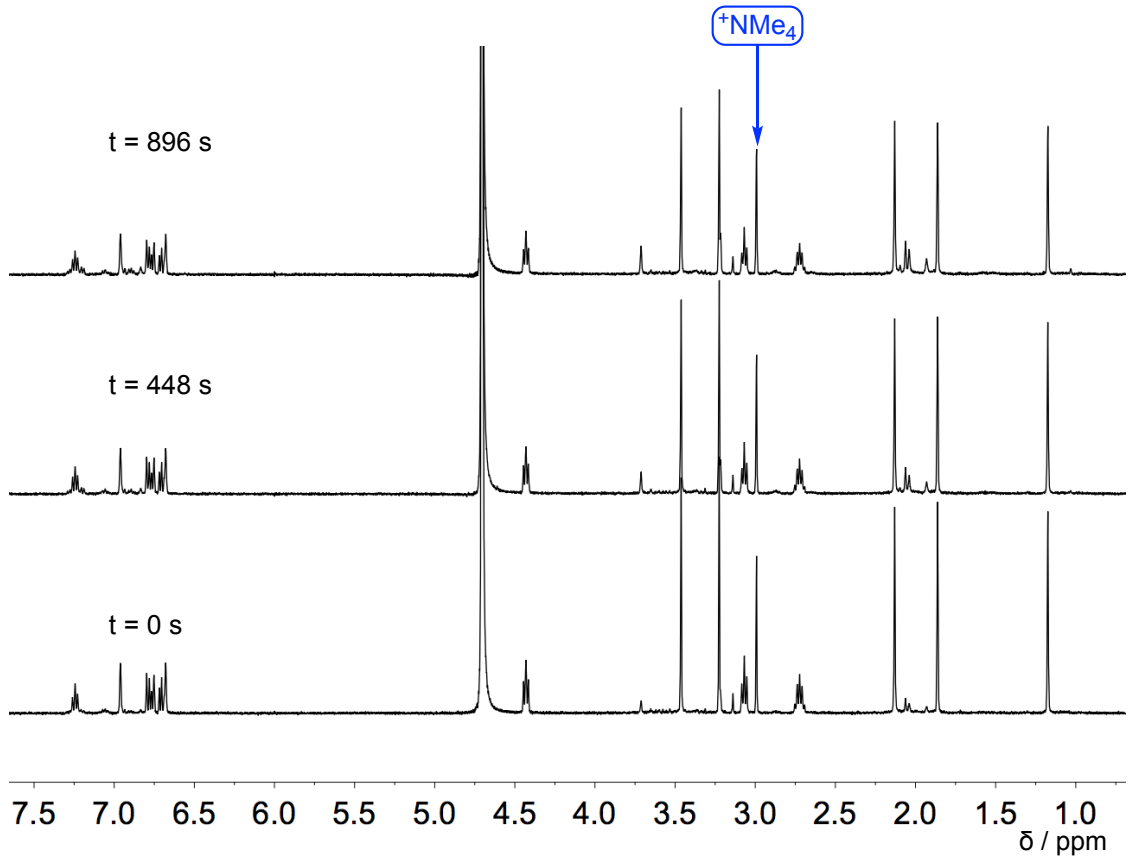

Figure 81: Representative ^{1}H NMR spectra at 400 MHz of O-methylated adduct 367 (10 mM) obtained in 1.0 M KOD in D_2O:CD_3CN (9:1) at 25 °C and I = 1.0 M (KCl).

The NMR spectra show only a small change is occurring in ~ 15 mins. There is no shift, or the appearance of, new signals at lower δ values that would be consistent with deprotonation and therefore shielding of the ^{1}H signals of the methylated adduct.

A semi-logarithmic plot of the fraction of starting material (deuterated), *f*(s), against time is shown in Figure 82. A rate constant at 1.0 M KOD was estimated to be $k = (1.661 \pm 0.011) \times 10^{-4}$ s^{-1}, corresponding to a half-life of ~ 70 mins. This could account for the additional process which is observed by stopped flow UV-vis spectrophotometry. This methylated adduct is more stable than the benzaldehyde adduct **366** which may be attributed to the electron donating ability and steric hindrance of the *ortho*-methoxy substituent.

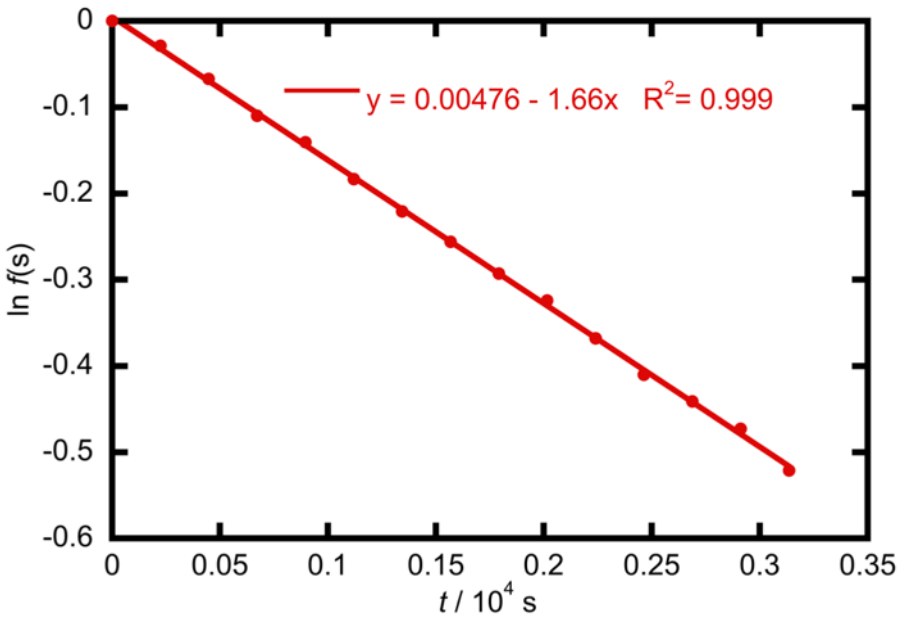

Figure 82: Semi-logarithmic plot of the fraction of substrate against time of adduct 367 in 1.0 M KOD at 25 ºC in D_2O:CD_3CN (9:1).

Using LCMS as previously described for adduct **366**, two peaks with an absorbance at 330 nm were detected, a bigger one at 0.23 – 0.36 mins and a smaller one at 2.96 – 3.02 mins. The first peak shows masses of 98, 123, 207, 291, 293 and 375 present (Figure 83), while the second peak shows masses of 65, 236, 239 and 261 present (not shown). The starting material appears with a retention time of 2.43 – 2.60 mins but shows no absorbance at 330 nm.

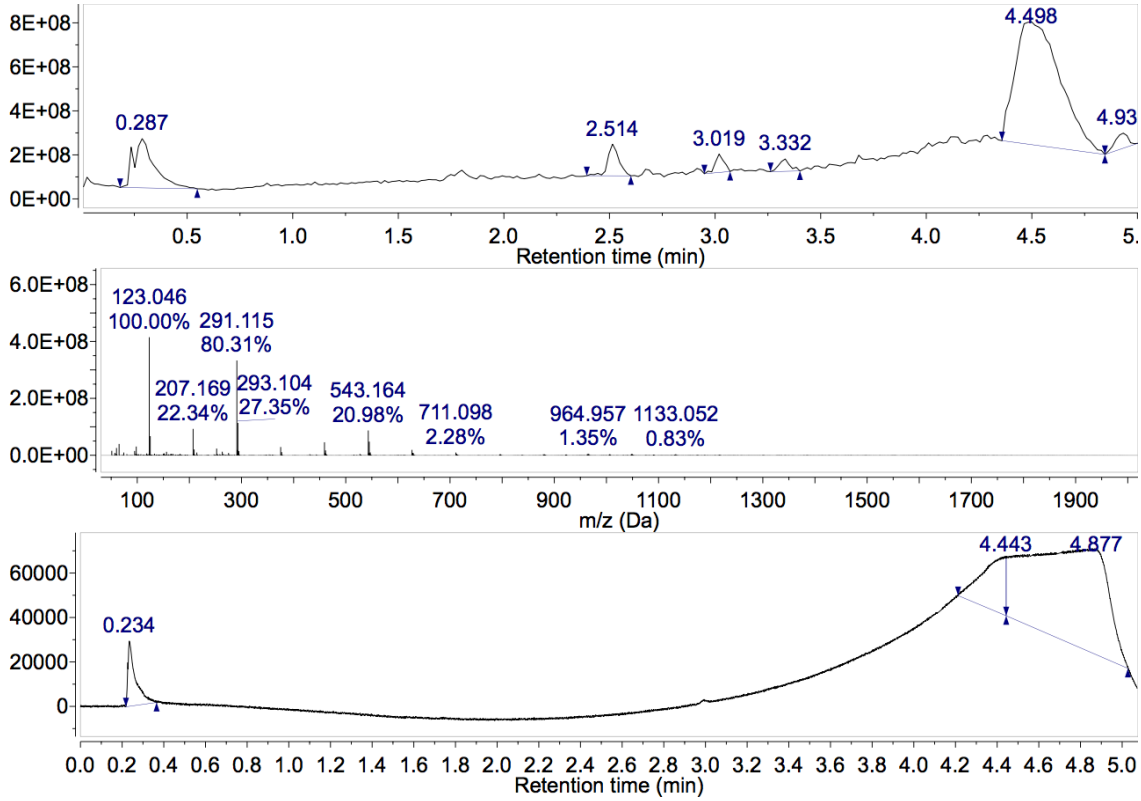

Figure 83: Electrospray chromatogram of methylated adduct 367 in 1.0 M KOH after ~ 90 minutes. (top) Total ion count chromatogram; (middle) mass spectrum of positive ions at a retention time of 0.23 – 0.36 mins; (bottom) UV-vis absorbance at 330 nm.

The masses cannot be assigned to any reasonable product of hydrolysis, some of which are shown in Figure 84. Possible products may include hydrate or ring opening of the triazolium ring ($[M+H]^+$ = 396), 2,4,6-trimethylphenyl hydrazine ($[M+H]^+$ = 151), 2,4,6-trimethylphenyl aniline ($[M+H]^+$ = 136), triazolium ion ($[M]^+$ = 228) or the hydrate of the triazolium ($[M+H]^+$ = 246). What is clear from the chromatogram is that the hydrate or equivalent ring opened structure observed for methylated adduct **366** is not detected. The *ortho*-methoxy substituent on the aryl aldehyde portion of the adduct clearly plays a role in protecting the substrate to hydrolysis either by sterics or electronics, or a combination of the two effects.

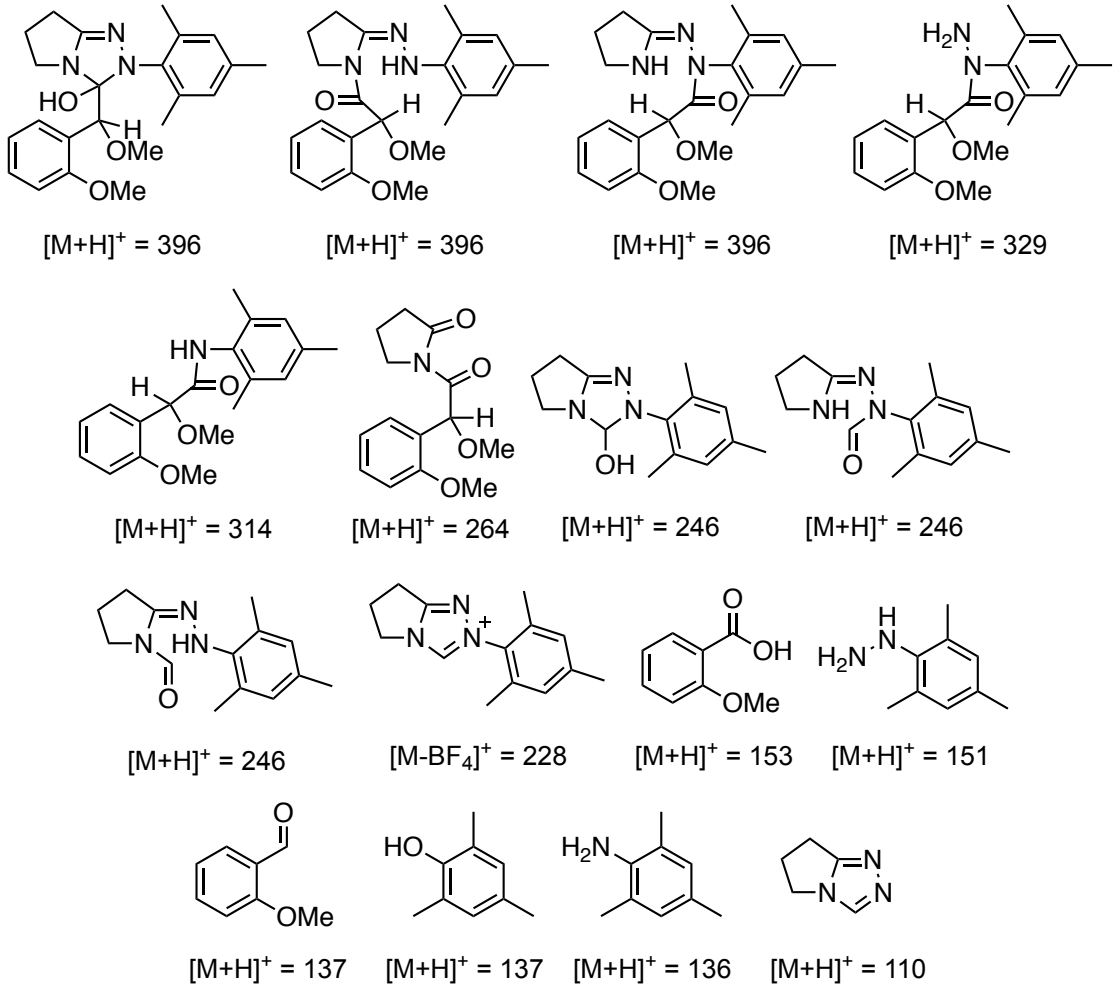

Figure 84: Possible decomposition products with masses that may be expected by electrospray mass spectrometry in order of decreasing *m*/*z*.

These results obtained by ^{1}H NMR spectroscopy and LCMS are significant in the context of the UV-vis stopped flow spectrophotometric data (Figure 72). It demonstrates that on the timescale of the experiment (200 s), there is very little (< 5%) decomposition as shown by ^{1}H NMR spectroscopy (Figure 82). The absorbance of any of the decomposition products shown in Figure 84 are unlikely to appear at a significantly longer wavelength than that of adduct **367**.

4.2.2.3.3 *Ortho*-bromobenzaldehyde adduct (368)

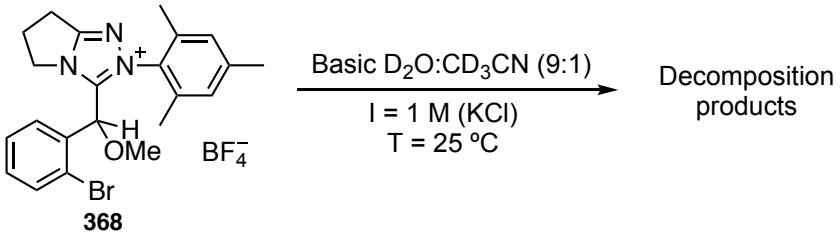

368

Methylated adduct **368** appeared to be the most susceptible to decomposition (Figure 85). An attempt was made to follow decomposition by ^{1}H NMR spectroscopy. Within ~

12 mins, significant decomposition was observable (Figure 85) but precipitation also occurred within < 28 mins, giving an opaque white suspension, and the products were not characterised. No electrospray mass spectrum was obtained for this compound due to the precipitation.

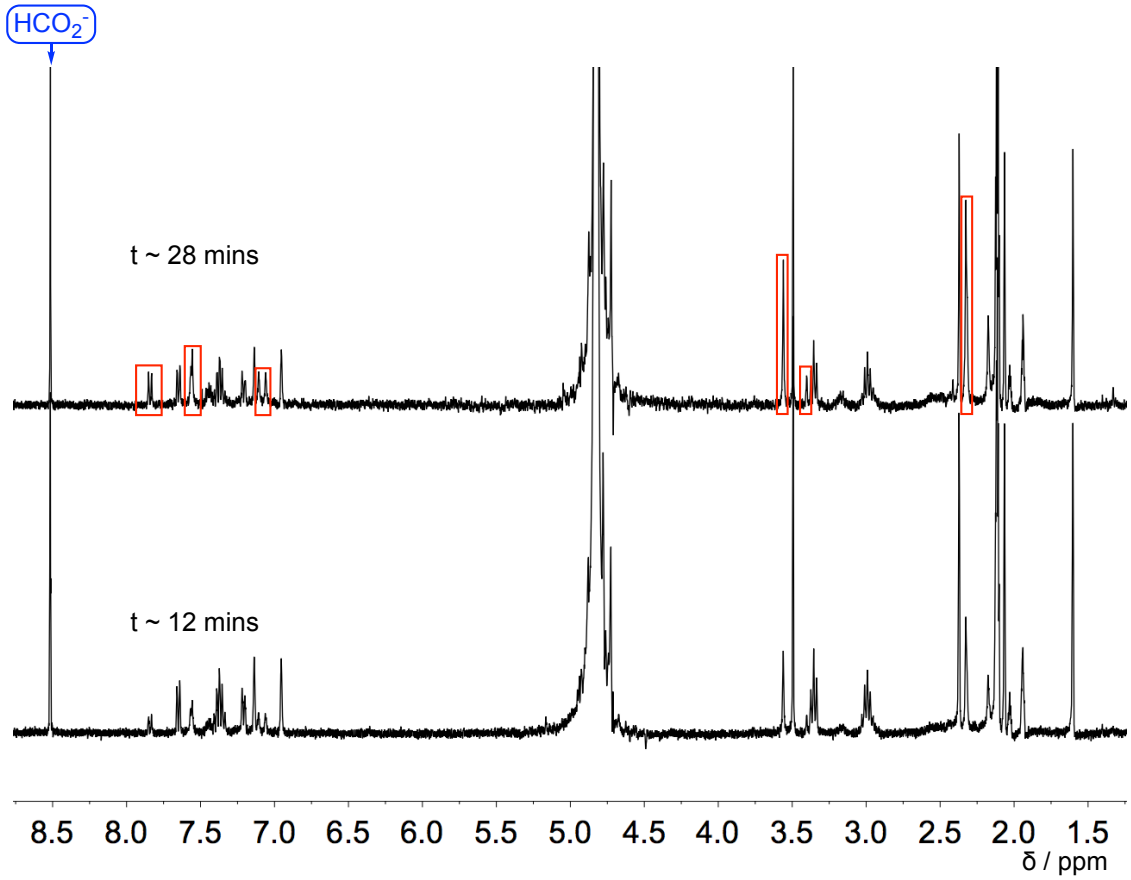

Figure 85: Representative ^{1}H NMR spectra at 400 MHz of O-methylated adduct 368 (5 mM) obtained in 0.5 M KOD in D_2O:CD_3CN (9:1) at 25 °C and I = 1.0 M (KCl) after ~ 12 and 28 mins. Some of the decomposition signals are highlighted by red boxes

There is no shift, or the appearance of, new signals at lower δ values that would be consistent with deprotonation and therefore shielding of the ^{1}H signals of the methylated adduct. Some of the new signals are highlighted in Figure 85 and may be attributed to unknown decomposition products.

4.2.2.4 Kinetics – Reprotonation: UV/vis spectrophotometric studies

The BI derived from adduct **367** was chosen for reprotonation studies as it was the most stable adduct with respect to decomposition and so represented a best case scenario for generating the BI. Initially, attempts were made to quantitatively deprotonate the adduct using potassium dimsylate in DMSO. Generating a stock solution of O-methylated BI would aid the study of the reprotonation kinetics. However, attempts to quantitatively deprotonate adduct **367** were unsuccessful. Next, a small proportion of BI was

generated by premixing methylated adduct **367** in aqueous hydroxide solution and then adding in aqueous acid solutions to observe the decay in absorbance.

4.2.2.4.1 Attempts to quantitatively deprotonate O-methylated adduct 367 using potassium dimsylate

Given the apparent stability of adduct **367** under basic conditions, attempts were made to quantitatively deprotonate the adduct using potassium dimsylate. Potassium dimsylate was generated by stirring KH in anhydrous DMSO under argon. The concentration of potassium dimsylate was found by titration with HCl using phenolphthalein as an indicator. The pK_a of DMSO in DMSO is 35.1[139] and is likely to be at least 15 orders of magnitude more basic than the methylated adduct **367**.

Using a conventional UV-vis spectrophotometer with a 10 mm path length cuvette, methylated adduct **367** was dissolved in anhydrous DMSO and a 10-fold excess of potassium dimsylate was added to make a final substrate concentration of 0.1 mM and potassium dimsylate concentration of 1 mM. The largest change in absorbance occurs at 384 nm (Figure 86). After an initial increase, the absorbance decreases with first order exponential behaviour. This behaviour is may be due to (1) the instability of potassium dimsylate, which is susceptible to decomposition by water, O_2 and CO_2, (2) nucleophilic attack of the dimsylate anion on the methylated adduct or (3) initial deprotonation of adduct **367** by dimsylate anion, followed by a slower reprotonation of solvent water.

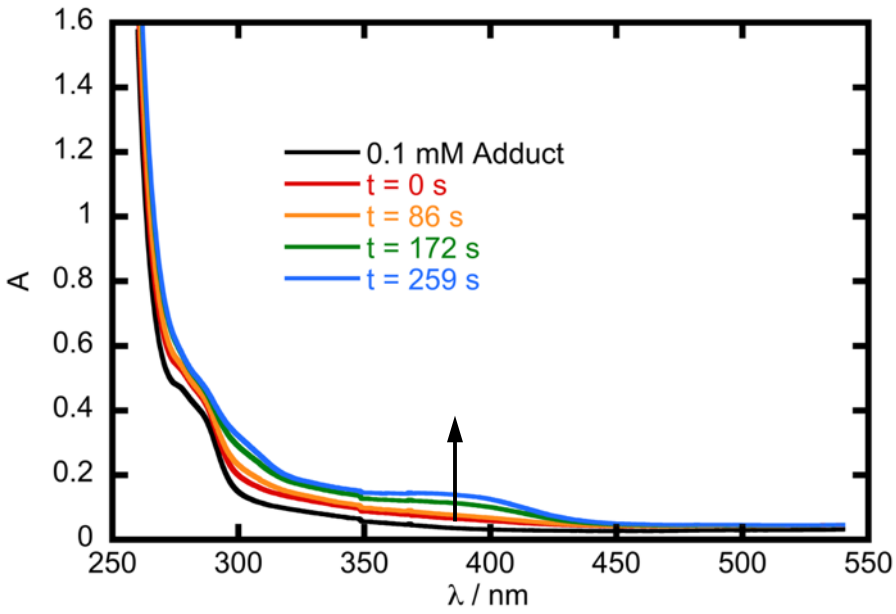

Figure 86: UV-vis spectra of starting adduct 367 in anhydrous DMSO and at four time points after the addition of potassium dimsylate solution at 25 °C.

To test whether reprotonation by water was occurring, five additions of potassium dimsylate were made, and the reaction was followed at 384 nm. If there was any water present in either the starting dimsylate or adduct solution, it would be expected to be completely deprotonated to give hydroxide and therefore not reprotonate the O-methylated BI. Figure 87 shows the UV-vis absorbance traces at 384 nm of the five additions of potassium dimsylate. On addition, there is a relatively sharp increase in absorbance followed by an exponential decay. Based on these results, it was concluded that it was not possible to quantitatively deprotonate the methylated adduct **367**, and the next set of experiments would involve generation of a small quantity of O-methylated BI in aqueous solution (next section).

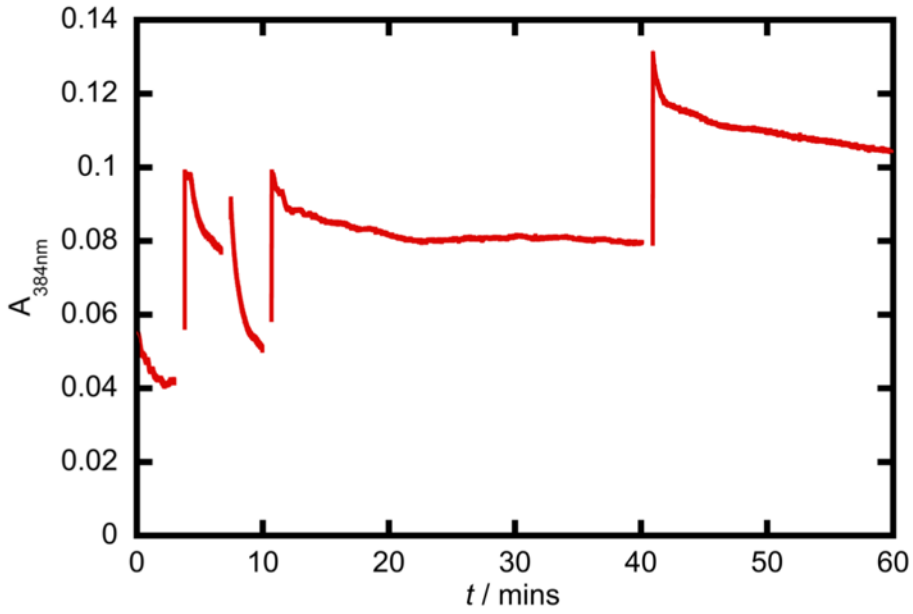

Figure 87: Five additions of potassium dimsylate to methylated adduct 367 over the course of 60 minutes at 384 nm and 25 ºC.

4.2.2.4.2 Attempts to reprotonate *ortho*-methoxyphenyl adduct 367 in aqueous solution

The next experiment involved generating a small proportion of the apparent BI using aqueous KOH. Based on deprotonation and stability studies, methylated adduct **367** was mixed with KOH to give an adduct concentration of 1.25 mM and KOH concentration of 0.500 M and left in a water bath at 25 ºC for 10 minutes. This time was chosen as there is good evidence from C(α)-H/D exchange kinetics and stopped flow spectrophotometric traces that O-methylated BI should form on this timescale, albeit with a small amount of parallel decomposition.

Stopped flow UV-vis spectrophotometry was then used to follow the absorbance change at 330 nm when the aqueous hydroxide solution of methylated adduct **367** is quenched with aqueous acid solutions at constant ionic strength I = 0.5 M (KCl). A representative set of absorbance traces are shown in Figure 88. Since the absorbance changes were small and relatively fast, rate constants were obtained by averaging the fitting of first order exponential decays to at least three runs.

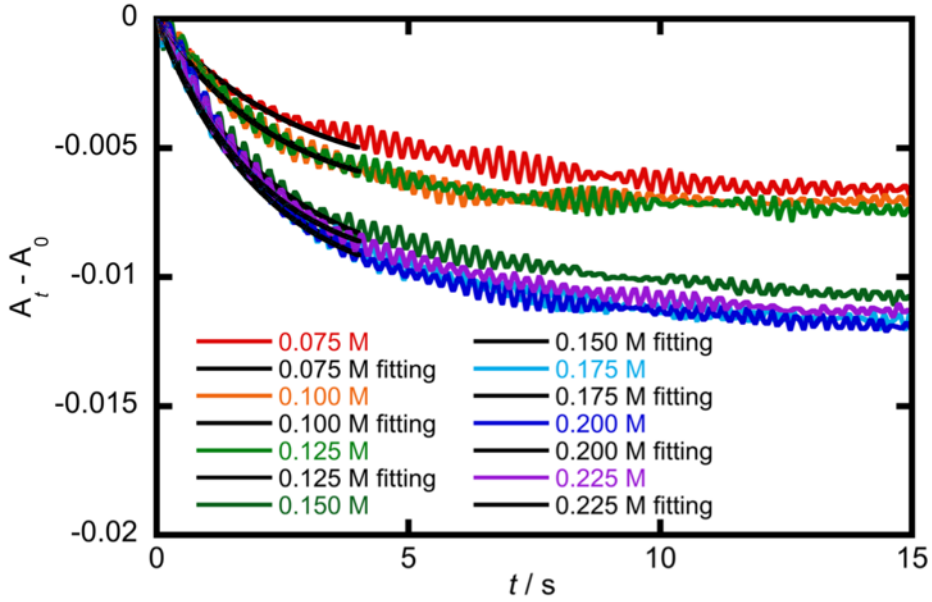

Figure 88: Representative absorbance traces obtained at various concentrations of added HCl to alkali solutions of 367 at 25 °C in H_2O:MeCN (9:1) and I = 0.5 M (KCl). Also shown are the first order exponential fittings for approximately three half-lives, obtained using the Pro-Data SX data associated with the stopped flow spectrometer. Rate constants obtained are given in Appendix 3.

The absorbance traces are noisy but the changes over the 15 seconds are outside the noise limit of the instrument (± 0.005). The rate constants were plotted against concentration of added H_3O^+ in the mixing chamber to extract apparent rate constants for acid and pH-independent reprotonation. Figure 89 shows the second order plot where the second order rate constant for acid mediated reprotonation, k_{H3O} (M^{-1} s^{-1}), and pseudo first order pH-independent reprotonation, k_{HOH} (s^{-1}), are obtained from the gradient and intercept, respectively. These values were k_{H3O} = 0.76 ± 0.07 M^{-1} s^{-1} and k_{HOH} = 0.319 ± 0.011 s^{-1}.

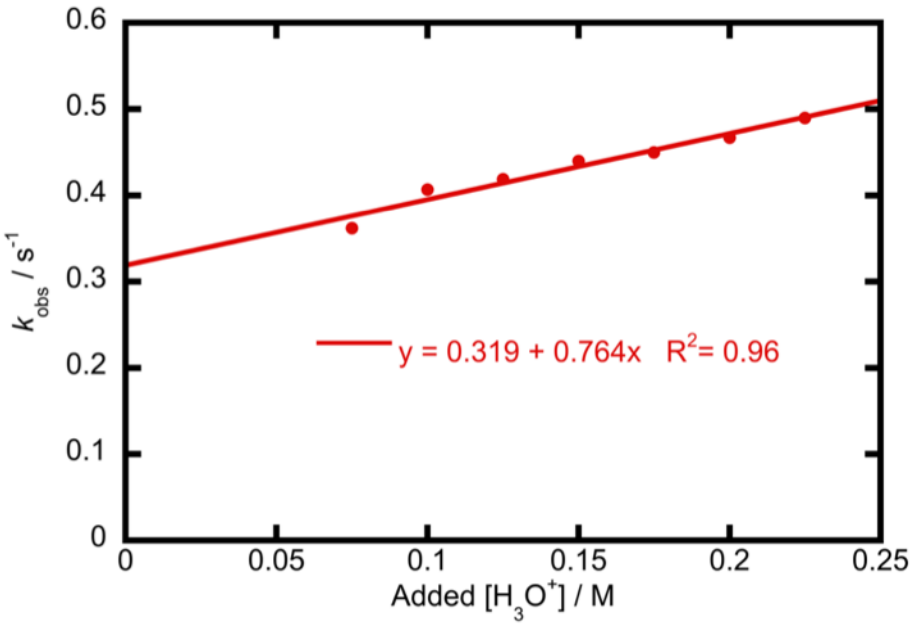

Figure 89: Dependence of the pseudo first order rate constant for the decay of the aborbance signal as a function of [H_3O^+] added to a solution of methylated adduct 367 (1.25 mM) in 0.500 M KOH at 25 °C in H_2O:MeCN (9:1) and I = 0.5 M (KCl).

Unlike the deprotonation step, there was no other method available to us which could be used to determine the rate constant for reprotonation or a reliable concentration of the adduct in solution. To determine whether a reprotonation was being observed, and the validity of the resulting rate constant for pH-independent reprotonation, k_{HOH} (s^{-1}), the rate constants for deprotonation (k_{HO} = 0.40 M^{-1} s^{-1}) and reprotonation (k_{HOH} = 0.319 s^{-1}) obtained under stopped flow UV-vis conditions were used to estimate a pK_a of the adduct. The absorbance changes in the deprotonation step were then used to determine approximate molar extinction coefficients, ε (M^{-1} cm^{-1}), and compared to values of a similar chromophore (Figure 90). Eqn. (18) was used to estimate a pK_a for adduct **367**, where pK_w = 13.96 is the ionic product of water:acetonitrile (9:1).[140]

$$pK_a = pK_w + log\left(\frac{k_{HOH}}{k_{HO}}\right) \quad (18)$$

A pK_a = 14.1 was estimated based on rate constants for deprotonation and reprotonation. Reviewing the absorbance change observed after 200 seconds for deprotonation of adduct **367** with 0.500 M KOH of ΔA ~ 0.065 (Figure 72) gives an estimate of the molar absorption coefficient ε ~ 520 M^{-1} cm^{-1}.[††] Jordan and co-workers reported the absorption coefficient of adduct **375** in DMSO to be ε = 17 000 M^{-1} cm^{-1} at

[††] At [HO^-] = 0.500 M, and γ_{HO} = 0.72 is the activity coefficient for hydroxide ion under our experimental conditions,[78] the pH = pK_w + log(γ_{HO}[HO^-]) = 13.5 and with an apparent pK_a = 14.1, the [BI] = 0.125 mM. From the Beer Lambert law, ε = A / cl, = 520 M^{-1} cm^{-1}.

380 nm (Figure 90). Without *ortho*-substituents, adduct **375** may become fully planar leading to a relatively large absorption coefficient. In the case of methylated adduct **367**, the presence of an *ortho* substituent on the aldehyde portion and a sterically bulky N-mesityl substituent on the triazolium portion may mean that a fully delocalised BI is not possible (**376**, Figure 90), therefore reducing both the λ_{max} and ε, relative to adduct **375**.

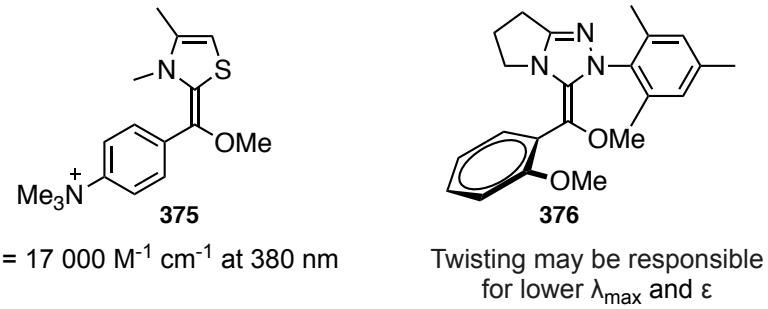

Figure 90: Molar absorption coefficient determined in DMSO by Jordan and co-workers.[86]

If the pK_a = 14.1, there should be an observable quantity of the BI by ^{1}H NMR spectroscopy in 1.00 M KOD. In 0.500 M KOH, the ratio of methylated adduct **367**: O-methylated BI **376** would be 4 : 1. Figure 81 showed that there is no shift, or the appearance of, new signals at lower δ values that would be consistent with deprotonation and therefore shielding of ^{1}H signals of the methylated adduct in ~ 10 mins. But integrals of the substrate signals show a relatively slow decrease, with a pseudo first order rate constant $k = (1.661 \pm 0.011) \times 10^{-4}$ s^{-1}, corresponding to a half-life of ~ 70 mins. The pseudo first order rate constants for deprotonation that would be predicted from C(α)-H/D and UV-vis deprotonation studies in 1.0 M KOD would be k = 0.291 and 0.40 s^{-1}, respectively. This decay in the ^{1}H NMR substrate signals may therefore be attributed to a decomposition reaction rather than a deprotonation. Formation of the O-methylated BI would be expected to result in (1) either the appearance of relatively shielded proton signals or a shift in the proton signals to lower δ values and (2) a rate constant in agreement with C(α)-H/D exchange and stopped flow deprotonation studies. If there is any O-methylated BI in solution, it is present in a lower concentration than can be detected by ^{1}H NMR spectroscopy. A pK_a of 14.1 is therefore a lower limit for O-methylated adduct **367** and this is most likely due to an underestimation of k_{HOH}.

4.3 Implications for catalysis

The results described in this chapter indicated that (1) the absorbance traces observed by mixing phenyl and *ortho*-methoxyphenyl adducts in aqueous hydroxide solutions are

consistent with the formation of the O-methylated BI, but the pK_a estimated for *ortho*-methoxyphenyl adduct **367** is likely to be at least 1 unit higher than that predicted from the kinetics of reprotonation (k_{HOH}, s^{-1}) and (2) proton transfer is faster from phenyl adduct **366** than *ortho*-methoxyphenyl **367** and *ortho*-bromophenyl **368** adducts which may be attributed to reduced steric hindrance of either the approach of the base or formation of the O-methylated BI.

The rate constants obtained by C(α)-H/D exchange and UV-vis spectrophotometry, combined with chemical shifts (chapter 3) of the three adducts show that there is a higher concentration and/or more nucleophilic BI derived from the phenyl adduct **366**. Despite the larger rate constants and equilibrium constants for hydroxyaryl adduct formation for *ortho*-methoxybenzaldehyde than benzaldehyde (chapter 3), the formation and onwards reaction of the BI is key to determining the product outcome. The *ortho*-bromophenyl adduct may be expected to have a more labile C(α)-H based on electronics (σ_p = 0.696). Sterics therefore plays a key role in the formation and potentially onwards reaction of the BI.

Crossover experiments would be informative and is a suggestion for future work (chapter 5). However, it has been shown that the retro-benzoin reaction of homo-coupled *ortho*-substituted benzoins is typically very slow[17] and that of unsubstituted benzoin is signifinicant even with a sterically bulky N-mesityl substituted thiazolium precatalyst.[18] These findings would suggest that attack of the BI based on the *ortho*-substituted aldehyde adduct is dictated mostly by kinetics of the formation and onward reaction of the BI, which has been shown to be typically slower than non-*ortho*-substituted aldehyde adducts in this and the previous chapter. The reaction of the non-*ortho*-substituted aldehyde adduct is therefore dictated by a mixture of kinetics and equilibria. Finding rate constants for the reaction of a range of BIs with a range of aldehydes would give clues as to whether the *ortho*-methoxybenzaldehyde is more electrophilic than benzaldehyde in the reaction of the BI.

4.4 Conclusions and future work

Five methylated adducts were prepared, but only three (based on the N-mesityl substituted triazolium ion) were purified successfully. Stability in hydroxide solutions decreases in the order *ortho*-methoxyphenyl **367** > phenyl **366** > *ortho*-bromo **368**. An increase in absorbance at 330 nm as a function of time is apparent with all three compounds studied.

It was not possible to both sufficiently suppress parallel hydrolysis and access sufficiently acidic adducts to determine (1) the pK_a and (2) relative nucleophilicites of the resulting BI of these adducts.

Further work should be focussed on studying a range of methylated adducts to investigate the effect of both the N-aryl ring of the catalyst and substituents on the aryl aldehyde. The issues with the synthesis discussed in section 4.2.1.2 are (1) the TMSDAM reagent is expensive and (2) the methylation reaction is extremely inefficient with ~ 100 equivalents required for quantitative conversion from hydroxyaryl adduct.

Chapter 5: Conclusions and future work

This thesis has described the effects of *ortho*-substituents on both the triazolium precatalyst and aryl aldehyde substrate on rate constants and equilibrium constants of key steps in the benzoin condensation. These steps of interest were the initial deprotonation of the triazolium precatalyst to give NHC (chapter 2), addition of the NHC to aryl aldehydes to give hydroxyaryl adduct (chapter 3) and formation of the BI (chapters 3 and 4).

Chapter 2 detailed the work carried out to investigate the mechanism of C(3)-H/D exchange of *ortho*-heteroatom substituted triazolium salts. It was previously found[58,59] that *ortho*-halo, *ortho*-pyrimidinyl and *ortho*-pyridyl triazolium salts display additional mechanisms of C(3)-H/D exchange in addition to the SBC mechanism at pD < 1. It had previously been proposed that N1 protonation was likely to be responsible, although the implications of this on NHC catalysis were not evident. The formation of a dicationic species would be expected to make C(3)-H more labile and therefore increase the rate of C(3)-H/D exchange. The N1 protonation was proposed to reduce electrostatic interactions between *ortho*-heteroatom and N1 lone pairs. *Ortho*-pyridyl triazolium salts displayed a region of acid catalysed C(3)-H/D exchange, proposed to be due to N1 protonation in conjunction with intramolecular GBC by the pyridyl substituent.

To investigate these mechanisms further, two *ortho*-alkoxy and one *ortho*-pyridyl triazolium salt were prepared. The original *ortho*-pyridyl triazolium salt that showed acid catalysis was also re-evaluated, with additional data points obtained in the SBC region between pD 3 – 4. *Ortho*-alkoxy triazolium salts show an upward bend in the pD – log rate profile but no observable downward bend. A downward bend, which would occur at the pK_a of the titratable group (the previously proposed N1 protonation), would be predicted to occur at a higher pD than *ortho*-halo substituted triaozlium salts based on electronic arguments. No evidence for N1 protonation was found by investigating the effect of pD on the C(3)-H chemical shifts of the two *ortho*-alkoxy triazolium salts, nor of the N-pentafluorophenyl and N-pyridmidinyl triazolium salts which displayed the unusual pD – log rate profile behaviour. As a control, the N-phenyl triazolium salt also did not show any evidence for a substrate titration. These findings suggest that N1 protonation is not occurring in the pD region and may not be responsible for the upward bends seen in the pD – log rate profiles.

New data for an *ortho*-pyridyl triazolium salt bearing an electron donating substituent relative to the pyridyl nitrogen also displays a region of acid catalysis, which occurs up to a higher pD than the unsubstituted *ortho*-pyridyl triazolium salt. The effect of pD on

the C(3)-H chemical shifts suggests that a substrate titration is occurring, but not on N1. The electron donating pyridyl substituent would not be expected to have a dramatic effect on the pK_a of N1, yet the acid catalysed H/D exchange appears at a higher pD than the unsubstituted *ortho*-pyridyl triazolium salt.

To investigate how structure affects the second order rate constants for C(3)-H/D exchange, k_{DO} (M^{-1} s^{-1}), X-ray crystal structures were obtained for a wide range of triazolium salts and show the following trends: (1) non-*ortho*-substituted triazolium salts adopt relatively coplanar conformations with the triazolium ring; (2) *ortho*-substituted triazolium salts adopt relatively orthogonal conformations with the triazolium ring and (3) *ortho*-pyridyl triazolium salts adopt the most coplanar conformations of all the triazolium salts, with the pyridyl nitrogen pointing towards C(3)-H rather than N1 to reduce steric and electrostatic repulsions. DFT calculations were run on these structures at the B3LYP level of theory to investigate the effect of the dihedral angle between the N-aryl and triazolium ring and clearly demonstrate that it is energetically unfavourable for the (1) non-*ortho*-substituted N-aryl rings to become orthogonal with the triazolium ring; (2) *ortho*-substituted rings to become coplanar with the triazolium ring and (3) *ortho*-pyridyl rings to become orthogonal or rotate so that the pyridyl nitrogen points towards N1. Based on these results, it is difficult to rationalise the kinetic behaviour in terms of an N1 protonation. Since the *ortho*-pyridyl triazolium salts adopt conformations that cause the pyridyl nitrogen to point towards C(3)-H, it appears unlikely that N1 protonation would be apparent for these systems, as N1 would be in a similar environment as in the N-phenyl triazolium salt.

A Hammett analysis was carried out and show that non-*ortho*- and *ortho*-substituted triazolium salts do not fit on the same correlation. For a given σ, *ortho*-substituted triazolium salts display larger second order rate constants for C(3)-H/D exchange, k_{DO} (M^{-1} s^{-1}). The reaction constants obtained for non-*ortho*- and *ortho*-substituted triazolium salts were ρ = + 0.96 and + 0.79, respectively. These findings, along with X-ray cystal structures and DFT calcualtions are interpreted as follows: (1) non-*ortho*-substituted triazolium salts benefit from resonance with the triazolium salt which stabilises the cationic charge and therefore causes reduced C(3)-H lability and (2) *ortho*-substituted triazolium salts cannot benefit from this resonance stabilisation, and based on kinetic rate constants and DFT calculations, is likely due to ground state destabilisation rather than transition state stabilisation of *ortho*-substituted triazolium compared to non-*ortho*-subsituted triazolium salts.

Chapter 3 detailed the work carried out to investigate the effects of *ortho*-substituted N-aryl triazolium salts and aryl aldehyde on the rate constants and equilibrium constants for hydroxyaryl adduct formation/dissociation. It was previously found that *ortho*-heteroatom substituted aryl aldehydes give larger rate constants and equilibrium constants for hydroxyaryl adduct formation with N-phenyl triazolium salt.[25,79] The mechanistic reason for this was not clear. To investigate the reason for this behaviour, and also the effects of *ortho*-substituted N-aryl triazolium salts on the hydroxyaryl adduct forming step, the rate constants and therefore the equilibrium constants were obtained for seven triazolium salts and three aryl aldehydes,[‡‡] using conditions adopted previously.[25,73] In addition to the kinetic work, an X-ray crystal structure and DFT calculations were obtained for *ortho*-methoxybenzaldehyde, and the ^{1}H and ^{13}C NMR chemical shifts of all three aryl aldehydes were studied. This was to investigate whether the enhanced reactivity of *ortho*-methoxybenzaldehyde is a ground state destabilisation or transition state stabilisation effect and what the mechanistic reason for such behaviour is.

The X-ray crystal structure of *ortho*-methoxybenzaldehyde shows that the carbonyl group is not rotated out of the plane of the aryl ring by the *ortho*-methoxy substituent. DFT calculations were carried out on these structures at the B3LYP level of theory to investigate the effect of the dihedral angle between the carbonyl group and the aryl ring and suggests that any meaningful rotation which would lead to a more reactive aldehyde requires a relatively large energetic penalty (greater than thermal energy) which cannot therefore explain the enhanced rate constants for hydroxyaryl adduct formation compared to benzaldehyde. ^{1}H and ^{13}C NMR chemical shifts suggest that the carbonyl carbon of *ortho*-methoxybenzladehyde is less electrophilic than benzaldehyde. But the clue to the enhanced reactivity lies in the ^{1}H NMR chemical shift of the aldehydic proton for *ortho*-methoxybenzladhyde – it is deshielded relative to benzaldehyde which suggests that intramolecular H-bonding is present. This does not lead to a more electrophilic aldehyde, but its benefit is realised in the transition state for hydroxyaryl adduct formation. The conformation of the *ortho*-methoxy substituent in the X-ray crystal structure would suggest that the intramolecular H-bond is less than optimal. However, as the NHC adds to the carbonyl, a hyrbidisation change occurs from sp^2 to sp^3 and the aldehydic proton moves out of plane of the aryl ring, which increases the overlap with the sp^3 hybridised lone pair of electrons on the *ortho*-methoxy substituent.

[‡‡] Jiayun Zhu, a member of the research group, obtained data for one of these triazolium salts.

It may be predicted that any *ortho*-substituted aldehyde that has the ability to H-bond (has lone pairs available) could benefit from this interaction. It is not, as previously suggested, due to intramolecular H-bonding between C(α)-OH and the *ortho*-methoxy substituent. This is because in the TS for hydroxyaryl adduct formation, a partial negative charge will develop on C(α)-O^- which would lead to transition state destabilisation and lower the rate constant for addition. Future work may include studying a range of *ortho*-substituted aryl aldehydes to investigate whether this intramolecular H-bonding is possible with other *ortho*-heteroatom substituted benzaldehydes.

The rate constants for formation of the hydroxyaryl adduct, k_1 (M^{-1} s^{-1}), from the seven triazolium salts with benzaldehyde and *para*-methoxybenzaldehyde shows similar Hammett relationships as observed for second order rate constants for C(3)-H/D exchange, k_{DO} (M^{-1} s^{-1}), described in chapter 2. For a given σ, *ortho*-substituted triazolium salts display larger second order rate constants for hydroxyaryl adduct formation than non-*ortho*-substituted triazolium salts. The reverse is true for the reverse rate constants for hydroxyaryl adduct dissociation - for a given σ, *ortho*-substituted triazolium salts display lower first order rate constants for hydroxyaryl adduct dissociation than non-*ortho*-substituted triazolium salts. These findings are interpreted as (1) a greater concentration of NHCs from *ortho*-substituted triazolium salts for a given σ and (2) an energetic penalty which non-*ortho*-substituted triazolium salts must pay (cf. DFT calculations in chapter 2) to rotate the N-aryl ring out of plane of the triazolium ring. As discussed in chapter 3, X-ray crystal structures were obtained previously[79] for three hydroxyaryl adducts based on the N-phenyl triazolium precatalyst. Comparing the dihedral angle between the N-aryl ring and triazolium ring in the catalyst (19.45º)[126] and in the three hydroxyaryl adducts (65 – 68º) demonstrates a requirement of the N-aryl ring to rotate to accommodate the approach of the aryl aldehyde. Future work may include expanding the Hammett analysis to include a wide range of non-*ortho*- and *ortho*-substituted triazolium salts.

The rate constants for addition for *ortho*-methoxybenzaldehyde are generally larger than for benzaldehyde and is due to the previously described intramolecular H-bonding TS stabilisation effect. Equilibrium constants for hydroxyaryl adduct formation are larger for *ortho*-methoxybenzaldehyde than benzaldehyde because of the electron donating effect of the methoxy substituent which makes C(α)-OH less acidic. The reverse is true for *ortho*-alkoxy-substituted triazolium salts and this is interpreted as an electrostatic

repulsion between *ortho*-heteroatom substituted N-aryl triazolium ion and aryl aldehyde, which outweighs the stabilising intramolecular H-bond which forms in the TS and hydroxyaryl adduct. Attempts were made to study two other *ortho*-heteroatom-substituted N-aryl triazolium salts: N-pentafluorophenyl and N-2,4,6-trichlorophenyl. However, these triazolium salts were unstable under these reaction conditions and so relaiable data could not be obtained. It is perhaps not unreasonable to extrapolate from the data obtained for *ortho*-alkoxy triazolium salts to all *ortho*-heteroatom-substituted triazolium salts bearing lone pairs of electrons. Future work may include the study of *ortho*-halo-substituted triazolium salts with electron donating substituents attached to reduce decomposition (Figure 91).

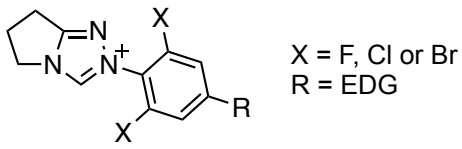

Figure 91: Potential *ortho*-heteroatom-substituted triazolium salts for future work, which may mitigate decomposition reactions observed in chapter 3.

The ^{1}H NMR chemical shifts of C(α)-H of the hydroxyaryl adducts and the kinetics of C(α)-H/D exchange were briefly explored. The findings show that the C(α)-H of the *ortho*-methoxybenzaldehyde adduct is deshielded relative to benzaldehyde and this is due to intramolecular H-bonding. It is proposed that the rate constants for C(α)-H/D are slower for the *ortho*-methoxybenzaldehyde adducts than the benzaldehyde adducts due to a combination of (1) steric hindrance of the approach of the base and/or formation of the BI and (2) electron donating resonance effect of the *ortho*-methoxy substituent.

Chapter 4 detailed the work carried out to investigate (1) whether it was possible to obtain rate constants for deprotonation of analogues of three hydroxyaryl adducts and reprotonation of the resulting BI and (2) the effect of *ortho*-substituents on the aldehyde portion of the adduct on the rate constants of BI formation. Methylated hydroxyaryl adducts were prepared using TMSDAM under acidic conditions.

The kinetics of C(α)-H/D exchange followed by ^{1}H NMR spectroscopy showed that the phenyl adduct displays SBC of exchange, whereas *ortho*-methoxy and *ortho*-bromobenzaldehyde adducts displayed GBC of exchange. These findings show the dominance of steric hindrance in the approach of the base and/or formation of the BI. The second order rate constants for exchange, k_{DO} (M^{-1} s^{-1}) follow the order phenyl > *ortho*-methoxyphenyl > *ortho*-bromophenyl.

Absorbance traces consistent with formation of the BI based on the phenyl and *ortho*-methoxyphenyl were observed by conventional and stopped flow UV-vis spectrophotometry. The second order rate constants obtained[§§] were ~ 1.4-fold larger than that obtained by C(α)-H/D exchange. This would be expected for these reactions which were carried out at a lower ionic strength. The *ortho*-bromophenyl adduct gave absorbance traces which did not correlate well with hydroxide ion concentration.

Decomposition was observed in hydroxide solutions in conventional and stopped flow UV-vis spectrophotometry for all three adducts. The order of stability was *ortho*-methoxyphenyl > phenyl > *ortho*-bromophenyl.

Attempts to quantitatively deprotonate the *ortho*-methoxyphenyl using potassium dimsylate in anyhydrous DMSO were unsuccessful most likely due to protonation by trace water, reaction with air or nucleophilic attack of the dimsylate anion. A small proportion of the *ortho*-methoxyphenyl BI was generated using 0.500 M KOH and attempts to follow reprotonation using various concentrations of HCl by stopped flow UV-vis spectrophotometry were made. Pseudo first order exponential decays were observed which showed a correlation with $[H_3O^+]$. By extrapolating the rate constants for reprotonation back to $[H_3O^+] = 0$, an estimate of the pseudo first order rate constant for reprotonation by water, k_{HOH} (s^{-1}), was made. A pK_a = 14.1 was estimated based on the ratio of rate constants for deprotonation and reprotonation, however it is likely that this has been underestimated by at least 1 unit based on (1) a very low molar extinction coefficient obtained based on this pK_a and (2) attempts to generate an observable amount of BI in 1.00 M KOD only led to decomposition.

Future work may include running the following crossover experiments (Figure 92) to determine the extent of reversibility of the cross-benzoin condensation with these triazolium precatalysts and may give additional insight into the observed product outcome observed in cross benzoin condensations.[25] A particularly informative experiment would be (2), which would show the reversibility of the major product.[25]

[§§] Only two first order rate constants could be obtained for the phenyl adduct, however agreement between ^{1}H NMR and UV-vis for phenyl and *ortho*-methoxyphenyl adducts would suggest that these are reliable data.

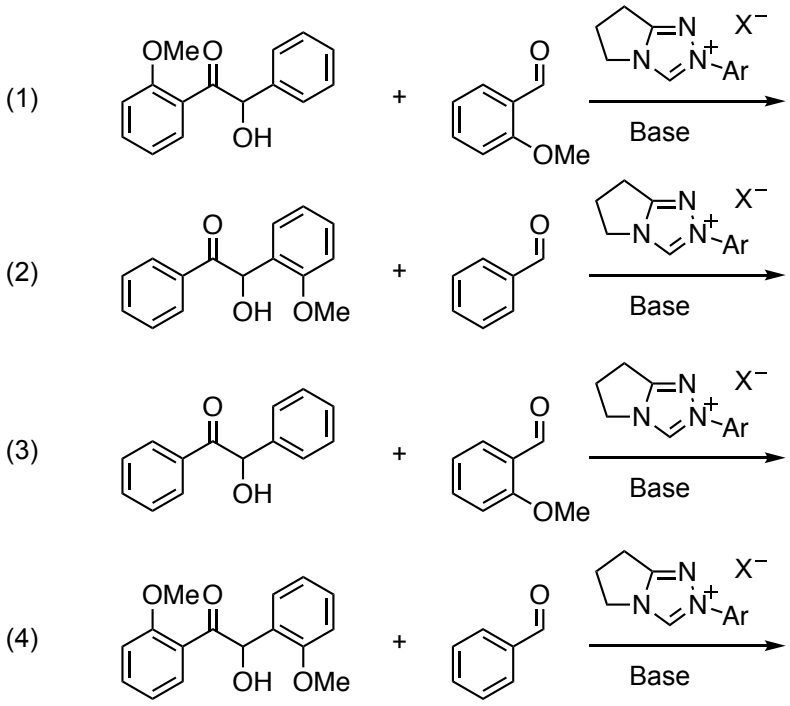

Figure 92: Potential crossover experiments for future work.

Overall, a summary of the key findings from this thesis are as follows:

(1) *Ortho*-substituted triazolium salt precatalysts are beneficial in catalysis due to steric hindrance which prevents the N-aryl and triazolium rings becoming coplanar therefore increasing the rate constant of deprotonation to give NHC and aiding the approach of the electrophile to the NHC compared to non-*ortho*-substituted triazolium salt precatalysts (Figure 93).

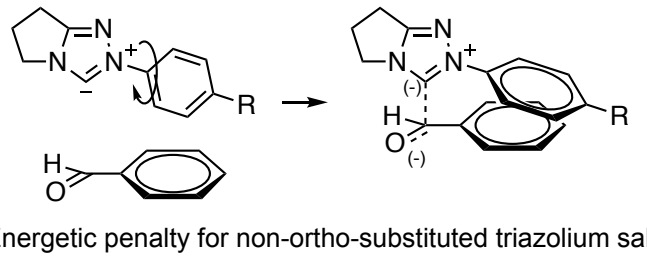

Figure 93: Non-*ortho*-substituted N-aryl triazoliums show slower k_1 values because of an energetic penalty that must be paid by rotating the N-aryl ring to accommodate the approach of the incoming aryl aldehyde.

(2) *Ortho*-heteroatom-substituted aldehydes with lone pairs of electrons have the potential to form intramolecular H-bonds which assist in the formation of the hydroxyaryl adduct (Figure 94), but steric hindrance of the approach of the base in the deprotonation of C(α)-H (Figure 95) and/or formation of the BI and/or onwards reaction of the BI (Figure 96) means that the product based on this hydroxyaryl adduct is less favoured.

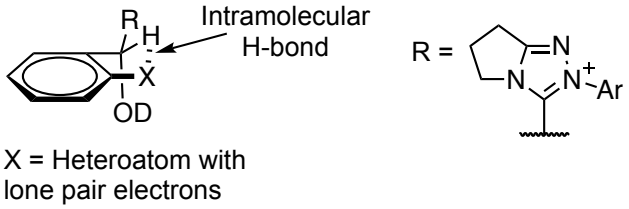

Figure 94: Potential for intramolecular H-bonding which increases rate of addition to *ortho*-heteroatom substituted aryl aldehydes.

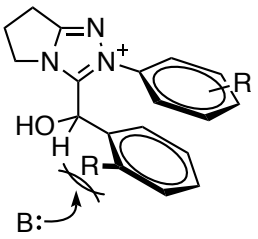

Figure 95: Steric hindrance of the approach of the base to deprotonate C(α)-H

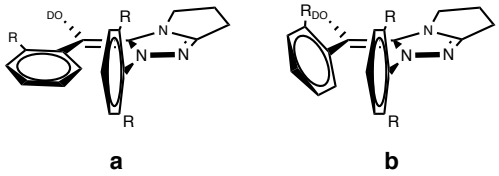

Figure 96: Steric hindrance of the BI (most likely to be in conformation b) as a nucleophile means onwards reaction of the BI based on the favoured hydroxyaryl adduct is slower than the less sterically hindered by less favoured hydroxyaryl adduct.

Chapter 6: Experimental

6.1 Materials

Chemicals were purchased from Sigma-Aldrich, Alfa Aesar, Fluorochem and Manchester Organics. NMR solvents were purchased from Cambridge Isotopes Inc., supplied by Goss Scientific and Sigma-Aldrich. These chemicals were used without further purification and stored under appropriate conditions, as detailed in the manufacturer's instructions. Benzaldehyde, *ortho*-bromobenzaldehyde and triethylamine were purified by vacuum distillation prior to use.

A 50 mM solution of tetramethylammonium deuteriosulphate in D_2O (I = 1.0 M) was prepared and used as a non-exchanging internal standard in the H/D exchange experiments. All glassware for dry reactions were dried at 100 ˚C overnight in an oven and cooled in a desiccator with $CaCl_2$, or under a stream of argon prior to use. Volumetric flasks were placed in Schlenk tube and placed on a high vacuum to dry.

Thin layer chromatography was performed using silica-backed Machery-Nagel Polygram SILG/UV_{254} plates and visualised under UV irradiation at 254 nm. Column chromatography was performed using silica gel.

6.2 Instrumentation

NMR spectra at 400, 500, 600 and 700 MHz were recorded on Varian Mercury-400, Bruker Avance-400, Varian Inova-500, Varian VNMRS-600 and Varian VNMRS-700 instruments. NMR samples were prepared in CD_3CN, acetone-d_6, $CDCl_3$, D_2O, DCM-d_2, DMSO-d_6 and methanol-d_4. ^1H and ^{13}C NMR chemical shifts are reported relative to the residual solvent signals as shown in Table 18.[141]

Table 18: ^1H and ^{13}C NMR residual solvent signals used to reference NMR spectra.

Solvent	δ_H	δ_C
CD_3CN	1.94	1.32, 118.26
Acetone-d_6	2.05	29.84, 206.26
$CDCl_3$	7.26	77.16
D_2O	4.79	-
DCM-d_2	5.32	53.84
DMSO-d_6	2.50	39.52
Methanol-d_4	3.31	49.00

Electrospray mass spectra data were obtained on a Waters TQD mass spectrometer interfaced with an Acquity UPLC system.

Infrared spectra were obtained as neat samples on a Perkin Elmer Spectrum *RX I* FT-IR spectrometer fitted with an ATR attachment.

UV-vis measurements were carried out on a Cary-100 UV-VIS spectrophotometer, using a 1 mL quartz cuvette and a 10 mm path length at a temperature of 25.0 ± 0.1 °C.

Stopped-flow spectrophotometry was performed on an Applied Photophysics SX-17MV instrument using a 2 mm path length at a temperature of 25.0 ± 0.1 °C.

Melting points were measured on a Gallenkamp melting point apparatus, and are uncorrected.

6.3 Synthetic details

6.3.1 Di-*tert*-butyl 1-(2,6-dimethoxyphenyl) hydrazine-1,2-dicarboxylate (278a)

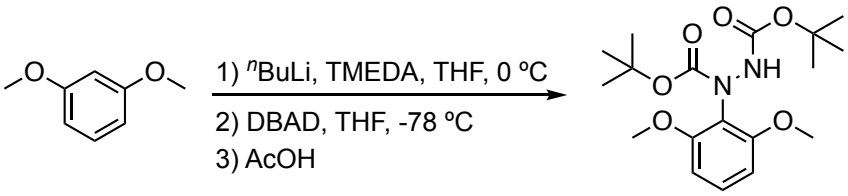

278a

1,3-Dimethoxybenzene (1.31 mL, 10.0 mmol) was dissolved in anhydrous THF (80 mL). Tetramethylethylenediamine (1.64 mL, 11.0 mmol) was added and the mixture was cooled to 0 °C. *n*-BuLi (1.6 M in hexanes, 6.9 mL, 11.0 mmol) was added dropwise and the reaction stirred at 0 °C for 1 h. A solution of di-*tert*-butyl diazo-1,2-dicarboxylate (2.30 g, 10.0 mmol) in anhydrous THF (20 mL) was added dropwise via cannula. After 20 min, the reaction mixture was quenched at – 78 °C with addition of AcOH (575 μL, 10 mmol). The reaction mixture was allowed to warm to room temperature, diluted with EtOAc (200 mL) and poured into distilled water (300 mL). The organic layer was separated and the aqueous phase was extracted with EtOAc (3 × 200 mL). The organic layers were combined, washed with brine (200 mL), dried over Na_2SO_4, filtered and concentrated under reduced pressure to give a yellow oil. The resulting oil was purified by flash column chromatography (hexane:EtOAc 3:1) to give a yellow, sticky, foamy residue. The residue was dissolved in a small amount of eluent, transferred to a glass vial and placed inside a Schlenk tube. Rotary evaporation gave a white powder (2.27 g, 62%), where the product exists as a ~ 1.8:1 mixture of carbamate rotamers; mp 97 – 99 °C (No lit. value)[***]; ν_{max} / cm^{-1} 3295w (C-H stretch), 2976m, 1723m, 1709m (C=O carbamate), 1706m (C=O carbamate), 1704m, 1591m, 1481m

[***] No literature value exists for the melting point as this product was obtained as a sticky yellow foam in the literature procedure.

(C-H stretch); δ_H (400MHz, $(CD_3)_2SO$) Major rotamer: 1.30 (9H, s, C(CH_3)$_3$), 1.37 (9H, s, C(CH_3)$_3$, 3.75 (6H, s, (CH_3)$_2$), 6.62 (2H, d, *J* 8.4, Ar*H*), 7.18 (1H, t, *J* 8.4, Ar*H*), 8.80 (1H, br s, N*H*). Minor rotamer: 1.41 (9H, s, C(CH_3)$_3$), 1.43 (9H, s, C(CH_3)$_3$, 3.72 (6H, s, (CH_3)$_2$), 6.63 (2H, d, *J* 8.4, Ar*H*), 7.21 (1H, t, *J* 8.4, Ar*H*), 8.46 (1H, br s, N*H*); δ_C (100 MHz, $(CD_3)_2SO$) Major rotamer: 28.2, 28.5, 56.0, 79.2, 80.2, 104.7, 119.8, 128.7, 154.2, 156.6. Minor rotamer: 28.3, 28.5, 56.3, 79.4, 80.2, 105.2, 119.8, 129.0, 153.7, 155.7.

6.3.2 2-(2,6-Dimethoxyphenyl)-6,7-dihydro-5*H*-pyrrolo[2,1-c][1,2,4]triazol-2-ium tetrafluoroborate (255)

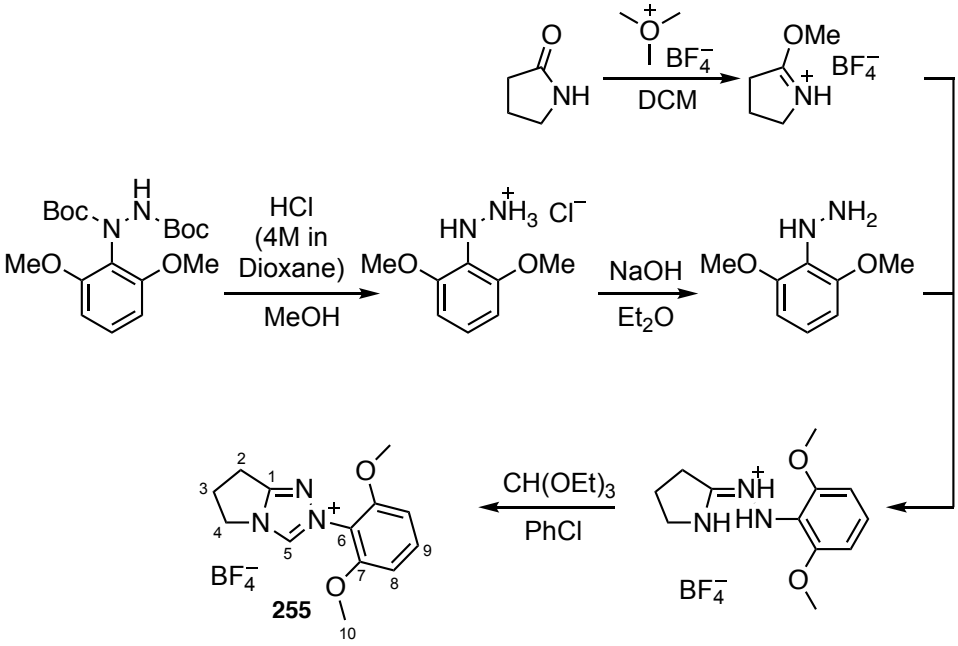

2-Pyrrolidinone (321 μL, 4.23 mmol) was dissolved in anhydrous DCM (20 mL) under argon. Trimethyloxonium tetrafluoroborate (646 mg, 4.37 mmol) was added in one portion and the reaction mixture stirred at room temperature under argon overnight. Di-*tert*-butyl 1-(2,6-dimethoxyphenyl)hydrazine-1,2-dicarboxylate (1.5573 g, 4.23 mmol) was dissolved in anhydrous methanol (10 mL) and HCl (4 M in 1,4-dioxane, 10.46 mL, 41.8 mmol) was added slowly to the solution. The mixture was stirred for 4 h at room temperature. All volatiles were then removed *in vacuo* to give hydrazine hydrochloride as an orange solid which was used in the next step without purification (LCMS (ESI+) *m*/*z* 169 $[M\text{-}Cl]^+$). Diethyl ether (20 mL) and 1 M NaOH (20 mL) were cooled in an ice bath. 2,6-Dimethoxphenyl hydrazinium chloride was added to this cooled mixture and stirred for ~ 10 minutes. The ether layer was separated and the aqueous phase was washed with diethyl ether (3 × 20 mL). The combined organics were washed with brine (20 mL), dried over Na_2SO_4, filtered and concentrated to give an orange residue. This

orange residue was dissolved in anhydrous DCM (10 mL) and transferred to the amidate. The mixture was stirred at room temperature under argon overnight. The solvent was removed to give a brown oil which was then dissolved in chlorobenzene (4 mL). Triethyl orthoformate (5.63 mL, 33.8 mmol) was added and the mixture heated at 80 °C overnight. The reaction was allowed to cool and the solvent was removed *in vacuo* to give a brown oil. Flash column chromatography (DCM:MeOH 95:5) gave the desired compound as a brown oil (151 mg, 11% from 2-pyrrolidinone). The product could be crystallised by slow evaporation from MeOH; δ_H (600 MHz, $CDCl_3$) 2.89 (2H, app quin, C*H*$_2$, H^3), 3.24 (2H, t, *J* 7.8, C*H*$_2$, H^2), 3.83 (6H, s, 2 × C*H*$_3$, H^{10}), 4.70 (2H, t, *J* 7.8, C*H*$_2$, H^4), 6.69 (2H, d, *J* 8.4, 2 × Ar*H*, H^8), 7.48 (1H, t, *J* 8.4, Ar*H*, H^9), 9.60 (1H, s, NC*H*N, H^5); δ_C (151 MHz, $CDCl_3$) 22.0 (C^2), 26.7 (C^3), 48.0 (C^4), 56.4 (C^{10}), 104.3 (C^8), 113.2 (ArC), 133.5 (C^9), 142.6 (C^5), 155.5 (ArC), 161.9 (C^1); LCMS (ESI+) *m*/*z* 246 [M-BF_4]$^+$; HRMS (ESI+) *m*/*z* 246.1249 [M-BF_4]$^+$ ($C_{13}H_{16}N_3O_2^+$ requires 246.1243).

6.3.3 Di-*tert*-butyl 1-(2,6-diisopropoxyphenyl)hydrazine-1,2-dicarboxylate (278b)

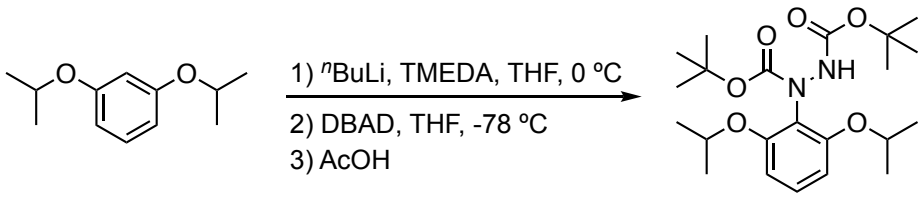

278b

1,3-Diisopropoxybenzene (1.21 mL, 6 mmol) was dissolved in anhydrous THF (50 mL). Tetramethylethylenediamine (0.99 mL, 6.6 mmol) was added and the mixture was cooled to 0 °C. *n*-BuLi (2.5 M in hexanes, 2.64 mL, 6.6 mmol) was added dropwise and the reaction stirred at 0 °C for 1 h. A solution of di-*tert*-butyl diazo-1,2-dicarboxylate (1.39g, 6 mmol) in anhydrous THF (12 mL) was added dropwise via cannula. After 20 min, the reaction mixture was quenched at – 78 °C with addition of AcOH (360 µL, 6 mmol). The reaction mixture was allowed to warm to room temperature, diluted with EtOAc (100 mL) and poured into distilled water (150 mL). The organic layer was separated and the aqueous phase was extracted with EtOAc (3 × 100 mL). The organic layers were combined, washed with brine (100 mL), dried over Na_2SO_4, filtered and concentrated under reduced pressure to give a yellow oil. The resulting oil was purified by flash column chromatography (hexane:EtOAc 9:1 R_f = 0.16) to give a yellow oil with spectroscopic details in accordance with the literature (982 mg, 39%); ν_{max} / cm^{-1}

2978m, 2933w, 1759m, 1718m (C=O carbamate), 1590m, 1472m (C-H stretch); δ_H (600MHz, $CDCl_3$) 1.27 – 1.54 (30H, m, 10 × CH_3), 4.52 – 4.62 (2H, m, CH, H^3), 6.48 – 6.54 (2H, m, ArH, H^2), 6.72 (1H, br s, NH), 7.11 (1H, t, *J* 8.4, ArH, H^1); δ_C (151MHz, $CDCl_3$) 22.2, 22.3, 28.06, 28.14, 28.18, 28.3, 28.4, 70.9, 71.2 (C^3), 80.6, 80.8, 128.2 (C^1), 128.5, 155.2, 154.8.

6.3.4 2-(2,6-Diisopropoxyphenyl)-6,7-dihydro-5*H*-pyrrolo[2,1-c][1,2,4]triazol-2-ium tetrafluoroborate (256)

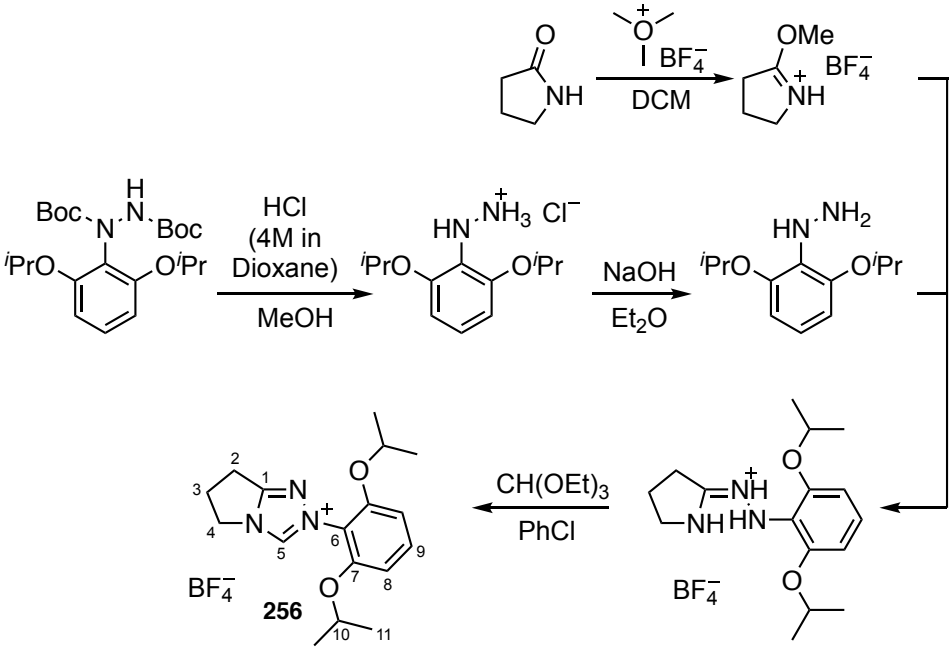

2-Pyrrolidinone (479 μL, 6.31 mmol) was dissolved in anhydrous DCM (30 mL) under argon. Trimethyloxonium tetrafluoroborate (948 mg, 6.41 mmol) was added in one portion and the reaction mixture stirred at room temperature under argon overnight. Di-*tert*-butyl 1-(2,6-diisopropoxyphenyl)hydrazine-1,2-dicarboxylate (2.68 g, 6.31 mmol) was dissolved in anhydrous methanol (16 mL) and HCl (4 M in 1,4-dioxane, 15.8 mL, 63.1 mmol) was added slowly to the solution. The mixture was stirred for 4 h at room temperature. All volatiles were then removed *in vacuo* to give hydrazine hydrochloride which was used in the next step without purification (LCMS (ESI+) *m*/*z* 247 $[M+Na]^+$). Diethyl ether (30 mL) and 1 M NaOH (30 mL) were cooled in an ice bath. 2,6-Diisopropoxyphenyl hydrazinium chloride was added to this cooled mixture and stirred for ~ 10 minutes. The ether layer was separated and the aqueous phase was washed with diethyl ether (3 × 30 mL). The combined organics were washed with brine (30 mL), dried over Na_2SO_4, filtered and concentrated to give a yellow oil. This yellow oil was dissolved in anhydrous DCM (15 mL) and transferred to the amidate. The mixture was stirred at room temperature under argon overnight. The solvent was removed to give a

brown oil (LCMS (ESI+) *m/z* 292 $[M+H-BF_4]^+$) which was then dissolved in chlorobenzene (6 mL). Triethyl orthoformate (8.40 mL, 50.5 mmol, 8 equiv) was added and the mixture heated at 80 °C overnight. The reaction was allowed to cool and the solvent was removed *in vacuo* to give a brown oil (LCMS (ESI+) *m/z* 302 $[M-BF_4]^+$). Flash column chromatography (DCM:MeOH 95:5) gave the desired compound as a brown oil (312 mg, 13% from 2-pyrrolidinone); δ_H (700 MHz, $CDCl_3$) 1.24 (12H, d, *J* 6.3, CH_3, H^{11}), 2.87 (2H, app quin, CH_2, H^3) 3.22 (2H, t, *J* 7.7, H^2), 4.56 (2H, sept, *J* 6.3, C*H*$(CH_3)_2$, H^{10}), 4.67 (2H, t, *J* 7.7, CH_2, H^4), 6.59 (2H, d, *J* 8.4, ArH, H^8), 7.37 (1H, t, *J* 8.4, ArH, H^9), 9.48 (1H, s, NCHN, H^5); δ_C (176 MHz, $CDCl_3$) 21.6 (C^{11}), 21.8 (C^2), 26.6 (C^3), 47.9 (C^4), 72.1 (C^{10}), 105.5 (C^8), 114.7 (C^6), 132.9 (C^9), 142.2 (C^5), 154.1 (C^7), 161.7 (C^1); LCMS (ESI+) *m/z* 302 $[M-BF_4]^+$; HRMS (ESI+) *m/z* 302.1862 $[M-BF_4]^+$ ($C_{17}H_{24}N_3O_2^+$ requires 302.1869).

6.3.5 2-[2-(Diphenylmethylidene)hydrazine]-4-methoxypyridine (293)

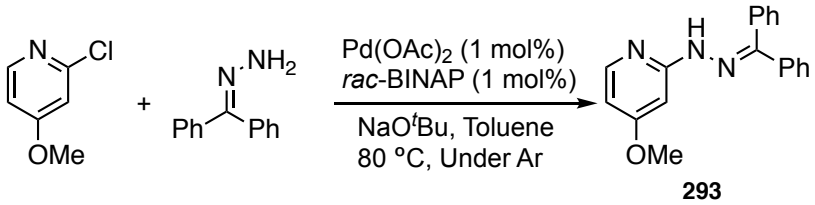

293

2-Chloro-4-methoxypyridine (397.5 μL, 3.483 mmol) and benzophenone hydrazine (719.3 mg, 3.665 mmol) were dissolved in anhydrous toluene (7 mL). $Pd(OAc)_2$ (10.9 mg, 0.0486 mmol) and *rac*-BINAP (22.5 mg, 0.0361 mmol) were added. NaO*t*Bu (4.90 mmol) and another portion of anhydrous toluene (7 mL) were added. The mixture was stirred at 80 °C overnight. The reaction mixture was cooled, diluted with Et_2O (35 mL) and filter through a celite pad. The celite pad was rinsed with Et_2O (70 mL), concentrated under reduced pressure and purified by flash column chromatography (Hex:EtOAc 8:2) to give a white solid (1.0483 g, 99%); mp 117.0 – 118.6 °C (No literature mp); δ_H (700MHz, $CDCl_3$) 3.91 (3H, s, OMe), 6.34 (1H, dd, *J* 5.8, 2.4, ArH), 7.00 (1H, d, *J* 2.4, ArH) 7.29 – 7.35 (5H, m, Ph), 7.48 (1H, t, *J* 8.4, 0.7, Ph), 7.52-7.60 (4H, m, Ph), 7.87 (1H, d, *J* 5.8, ArH), 8.14 (1H, br s, NH); δ_C (176 MHz, $CDCl_3$) 55.2, 91.5, 104.2, 126.8, 128.2, 128.5, 128.9, 129.4, 129.7, 132.5, 138.0, 146.3, 148.6, 158.4, 167.6; LCMS (ESI+) *m/z* 304 $[M+H]^+$; HRMS (ESI+) *m/z* 304.1454 $[M+H]^+$ ($C_{19}H_{18}N_3O$ requires 304.1454); Anal. Calc. for $C_{19}H_{18}N_3O$: C, 75.23; H, 5.65; N, 13.85, found C, 74.98; H, 5.63; N, 13.09.

6.3.6 2-(5-Methoxypyrid-2-yl)-6,7-dihydro-5*H*-pyrrolo[2,1-c][1,2,4]triazol-2-ium tetrafluoroborate (257)

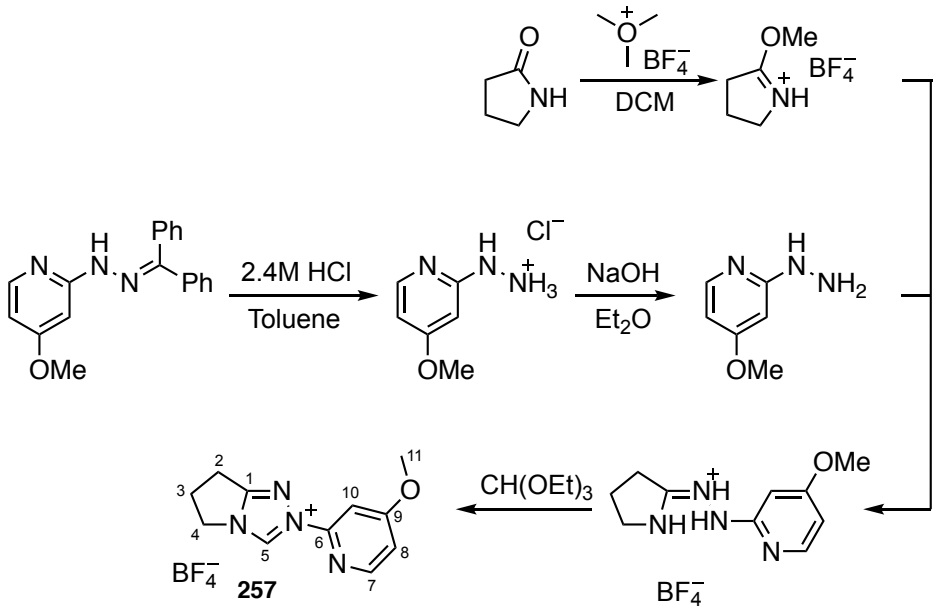

2-Pyrrolidinone (233.7 μL, 3.076 mmol) was dissolved in anhydrous DCM (15 mL) under argon. Trimethyloxonium tetrafluoroborate (466.8 mg, 3.156 mmol) was added in one portion and the reaction mixture stirred at room temperature under argon overnight. In a separate flask, 2-[2-(Diphenylmethylidene)hydrazine]-4-methoxypyridine **293** (933.3 mg, 3.076 mmol) was suspended in toluene (6.2 mL) and 2.400 M HCl (15.5438 mL) and heated to 90 °C overnight. The reaction mixture was cooled and toluene (10 mL) was added. The aqueous phase was separated and added to diethyl ether (100 mL). 1.000 M NaOH (62.1937 mL) was added slowly with stirring. The ether layer was separated and the aqueous phase was extracted with diethyl ether (3 × 90 mL). The organic layers were combined, washed with brine (100 mL) and concentrated under reduced pressure to give a yellow oil which was added directly to the flask containing the imidate. The mixture was stirred at room temperature under argon over the weekend. The solvent was evaporated and $CH(OEt)_3$ (10.23 mL, 61.52 mmol) was added. The mixture was heated at 120 °C overnight. The reaction mixture was cooled and the solvent was evaporated under reduced pressure. Flash column chromatography (DCM:MeOH 9:1 $R_f = 0.23$) gave the title compound as a yellow solid (51.8 mg, 6 %) which could be crystallised by slow evaporation of methanol; δ_H (700 MHz, CD_3CN) 2.83 (2H, app quin, C*H*$_2$, H^3), 3.21 (2H, t, *J* 7.7, C*H*$_2$, H^2), 3.99 (3H, s, OMe, H^{11}), 4.44 (2H, t, *J* 7.4, C*H*$_2$, H^4), 7.14 (1H, dd, *J* 5.6, 2.3, ArH, H^8), 7.47 (1H, d, *J* 2.3, ArH, H^{10}), 8.39 (1H, d, *J* 5.6, ArH, H^7), 10.00 (1H, s, NC*H*N, H^5); δ_C (176 MHz, CD_3CN) 21.5 (C^2), 26.6 (C^3), 47.5 (C^4), 56.3 (C^{11}), 99.7 (C^{10}), 112.1 (C^8), 137.0 (C^5), 149.1 (C^6),

150.3 (C^7), 164.0 (C^1), 168.8 (C^9); LCMS (ESI+) *m/z* 217 $[M\text{-}BF_4]^+$; HRMS (ESI+) *m/z* 217.1096 $[M\text{-}BF_4]^+$ ($C_{11}H_{13}N_4O$ requires 217.1089).

6.3.7 2-(Phenyl)-6,7-dihydro-5*H*-pyrrolo[2,1-c][1,2,4]triazol-2-ium tetrafluoroborate (259)

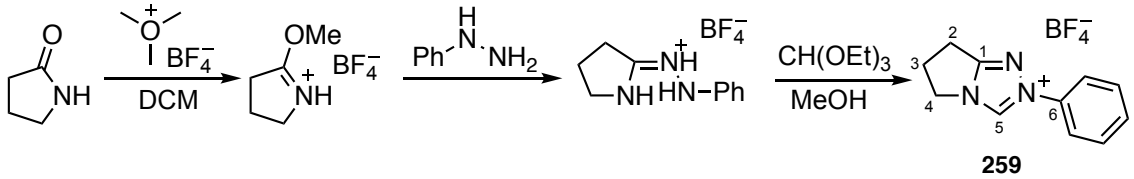

2-Pyrrolidinone (2.28 mL, 30.0 mmol) was dissolved in anhydrous DCM (150 mL) under argon. Trimethyloxonium tetrafluoroborate (4.45 g, 30.1 mmol) was added in one portion and the reaction mixture stirred at room temperature under argon overnight. Phenyl hydrazine (2.74 mL, 27.8 mmol) was added in one portion and the mixture stirred for 72 h at room temperature. The solvent was evaporated under reduced pressure. Methanol (12 mL) and triethyl orthoformate (24 mL, 144 mmol) were added and the mixture stirred at 120 °C overnight. The mixture was cooled and the solvent was evaporated under reduced pressure. Trituration with ethyl acetate gave the product as a tan solid with spectroscopic details in accordance with the literature (4.18 g, 55%). The product could be crystallised by slow evaporation of CH_3CN; mp 152 – 153 °C (lit.[142] 154 – 156 °C); ν_{max} / cm^{-1} 3140w, 1590m, 1502w, 1434m, 1385m, 1291w, 1226m, 1026m; δ_H (700 MHz, $(CD_3)_2CO$) 2.97 (2H, app quin, CH_2, H^3), 3.36 (2H, t, J7.7, CH_2, H^2), 4.66 (2H, t, J 7.4, CH_3, H^4), 7.63 – 7.71 (3H, m, ArH), 7.91 (2H, m, ArH), 10.32 (1H, s, NCHN, H^5); δ_C (176 MHz, $(CD_3)_2CO$) 21.5 (C^2), 26.8 (C^3), 47.6 (C^4), 121.1 (ArCH), 130.2 (ArCH), 130.6 (ArCH), 136.1 (C^6), 137.9 (C^5), 163.7 (C^1); LCMS (ESI+) *m/z* 186 $[M\text{-}BF_4]^+$; HRMS (ESI+) *m/z* 186.1000 $[M\text{-}BF_4]^+$ ($C_{11}H_{12}N_3$ requires 186.1031).

6.3.8 2-(4-Methoxyphenyl)-6,7-dihydro-5*H*-pyrrolo[2,1-c][1,2,4]triazol-2-ium tetrafluoroborate (260)

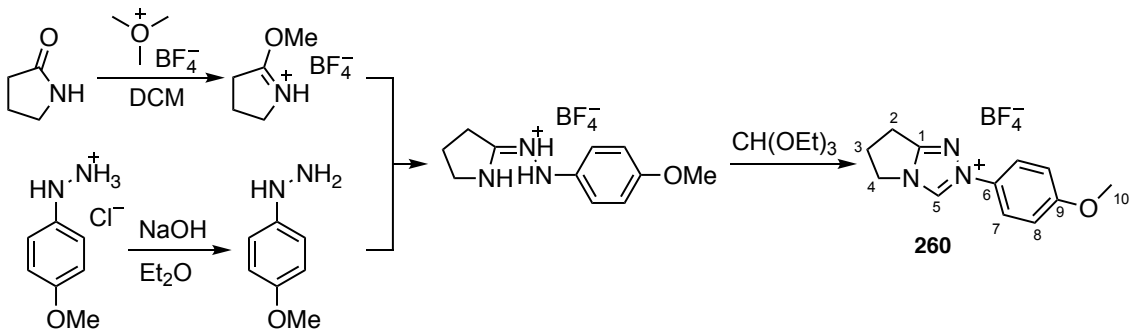

2-Pyrrolidinone (462 μL, 6.08 mmol) was dissolved in anhydrous DCM (25 mL) under argon. Trimethyloxonium tetrafluoroborate (0.916 g, 6.19 mmol) was added in one portion and the reaction mixture stirred at room temperature under argon overnight. Diethyl ether (25 mL) and 0.5 M NaOH (25 mL) were cooled in an ice bath. 4-Methoxyphenyl hydrazine hydrochloride (1.06g, 6.08 mmol) was added to this cooled mixture and stirred for ~ 10 minutes. The ether layer was separated and the aqueous phase was washed with diethyl ether (3 × 25 mL). The combined organics were washed with brine (25 mL), dried over Na_2SO_4, filtered and concentrated to give a yellow residue. This yellow residue was dissolved in anhydrous DCM (10 mL) and transferred to the amidate and the mixture stirred overnight at room temperature. The solvent was evaporated under reduced pressure. Triethyl orthoformate (20 mL, 120 mmol) was added and the mixture heated at 140 °C for 4 hours. The mixture was cooled and the solvent was evaporated under reduced pressure. Trituration with ethyl acetate and diethyl ether gave the product as a white solid with spectroscopic details in accordance with the literature (0.89 g, 48%). The product could be crystallised by slow evaporation of MeOH; mp 155 – 156 °C (lit.[143] 155 – 157 °C); ν_{max} / cm^{-1} 3146w, 1591m, 1517m, 1461m, 1396m, 1262m, 1217m, 1178m, 1038m; δ_H (700 MHz, CD_3CN) 2.81 (2H, app quin, CH_2, H^3), 3.18 (2H, t, *J* 7.7, CH_2, H^2), 3.89 (3H, s, OCH_3, H^{10}), 4.40 (2H, t, *J* 7.4, CH_2, H^4), 7.16 (2H, d, *J* 9.1, ArH), 7.68 (2H, d, *J* 9.1, ArH), 9.51 (1H, s, NCHN, H^5); δ_C (176 MHz, CD_3CN) 22.5 (C^2), 27.5 (C^3), 48.4 (C^4), 56.6 (C^{10}), 116.1 (ArCH), 124.1 (ArCH), 129.8 (C^6), 137.7 (C^5), 162.4 (C^9), 164.3 (C^1); LCMS (ESI+) *m/z* 216 [M-BF_4]$^+$; HRMS (ESI+) *m/z* 216.1112 [M-BF_4]$^+$ ($C_{12}H_{14}N_3O$ requires 216.1137).

6.3.9 2-(4-Fluorophenyl)-6,7-dihydro-5*H*-pyrrolo[2,1-c][1,2,4]triazol-2-ium tetrafluoroborate (261)

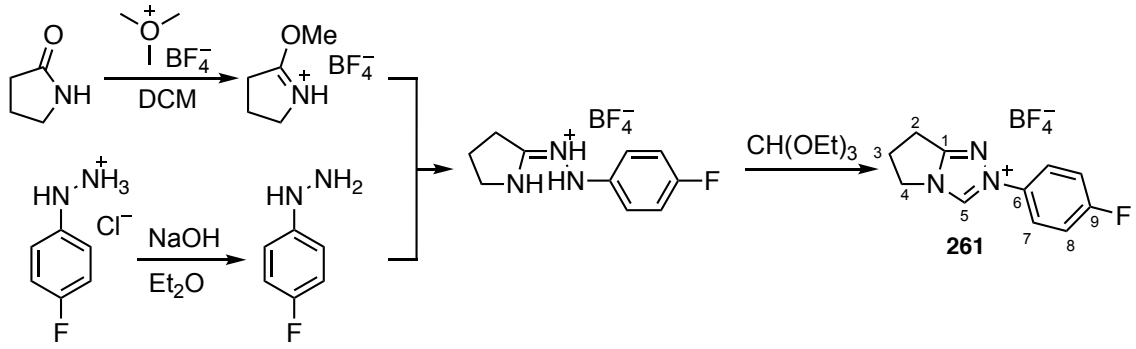

2-Pyrrolidinone (462 μL, 6.08 mmol) was dissolved in anhydrous DCM (25 mL) under argon. Trimethyloxonium tetrafluoroborate (0.910 g, 6.15 mmol) was added in one portion and the reaction mixture stirred at room temperature under argon overnight.

Diethyl ether (25 mL) and 1M NaOH (25 mL) were cooled in an ice bath. 4-Fluorophenyl hydrazine hydrochloride (0.989 g, 6.08 mmol) was added to this cooled mixture and stirred for ~ 5 minutes. The ether layer was separated and the aqueous phase was washed with diethyl ether (3 × 25 mL). The combined organics were washed with brine (25 mL), dried over Na_2SO_4, filtered and concentrated to give a yellow residue. This yellow residue was dissolved in anhydrous DCM (25 mL) and transferred to the amidate and the mixture stirred overnight at room temperature. The solvent was evaporated under reduced pressure. Triethyl orthoformate (20 mL, 120 mmol) was added and the mixture heated at 140 °C for 3 hours. The mixture was cooled and the solvent was evaporated under reduced pressure. Trituration with ethyl acetate and diethyl ether gave the product as an off-white solid with spectroscopic details in accordance with the literature (0.742 g, 42%). The product could be crystallised by slow evaporation of MeOH; mp 115 – 116 ºC (lit.[58] 109 – 111 ºC); ν_{max} / cm^{-1} 3133w, 1593m, 1520m, 1446w, 1293w, 1228m, 1033m; δ_H (700 MHz, CD_3CN) 2.82 (2H, app quin, CH_2, H^3), 3.20 (2H, t, *J* 7.7, CH_2, H^2), 4.42 (2H, t, *J* 7.4, CH_2, H^4), 7.39 – 7.42 (2H, m, ArH), 7.79 – 7.82 (2H, m, ArH), 9.59 (1H, s, NCHN, H^5); δ_C (176 MHz, CD_3CN) 22.5 (C^2), 27.6 (C^3), 48.6 (C^4), 118.1 (d, *J* 24.6, ArCH), 125.0 (d, *J* 8.8, ArCH), 133.1 (ArC), 138.4 (C^5), 164.5 (d, J 246, ArC), 164.6 (C^1); LCMS (ESI+) *m/z* 204 $[M\text{-}BF_4]^+$; HRMS (ESI+) *m/z* 204.0912 $[M\text{-}BF_4]^+$ ($C_{11}H_{11}N_3F$ requires 204.0937).

6.3.10 2-(2,4,6-Trichlorophenyl)-6,7-dihydro-5*H*-pyrrolo[2,1-c][1,2,4]triazol-2-ium tetrafluoroborate (264)

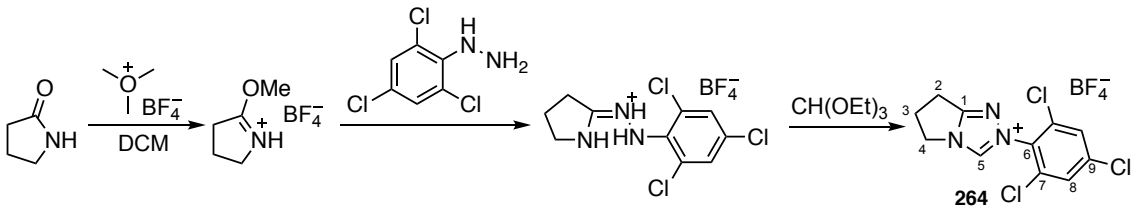

2-Pyrrolidinone (313 μL, 4.12 mmol) was dissolved in anhydrous DCM (20 mL) under argon. Trimethyloxonium tetrafluoroborate (0.618 g, 4.18 mmol) was added in one portion and the reaction mixture stirred at room temperature under argon overnight. 2,4,6-Trichlorophenyl hydrazine (0.870 g, 4.12 mmol) was added in one portion and the mixture stirred overnight at room temperature. The solvent was evaporated under reduced pressure. Triethyl orthoformate (10 mL, 60 mmol) was added and the mixture stirred at 140 °C for 3 days. The mixture was cooled and the solvent was evaporated under reduced pressure. Trituration with ethyl acetate gave the product as a tan solid with spectroscopic details in accordance with the literature[77] (0.34g, 22%). The product

could be crystallised by slow evaporation of MeOH; mp 196 – 197 ºC (no lit. mp); ν_{max} / cm^{-1} 3089w, 1598m, 1568m, 1521w, 1415w, 1386w, 1289w, 1204w, 1030m; δ_H (700 MHz, CD_3CN) 2.85 (2H, app quin, CH_2, H^3), 3.23 (2H, t, *J* 7.7, CH_2, H^2), 4.49 (2H, t, *J* 7.4, CH_3, H^4), 7.82 (2H, s, ArH, H^8), 9.51 (1H, s, NCHN, H^5); δ_C (176 MHz, CD_3CN) 21.7 (C^2), 26.4 (C^3), 48.3 (C^4), 129.5 (C^8), 130.2 (ArC), 134.2 (ArC), 138.9 (ArC), 142.0 (C^5), 164.6 (C^1); LCMS (ESI+) *m*/*z* 288 $[M\text{-}BF_4]^+$; HRMS (ESI+) *m*/*z* 287.9857 $[M\text{-}BF_4]^+$ ($C_{11}H_9N_3Cl_3$ requires 287.9862).

6.3.11 2-(Pentafluorophenyl)-6,7-dihydro-5*H*-pyrrolo[2,1-c][1,2,4]triazol-2-ium tetrafluoroborate (266)

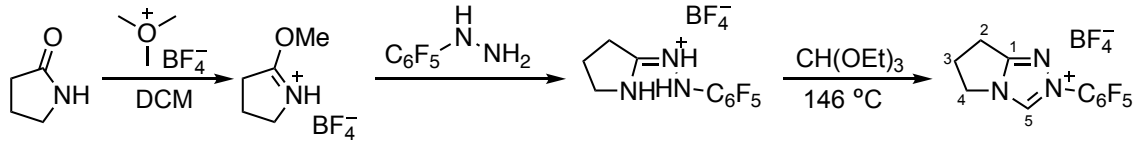

266

2-Pyrrolidinone (760 µL, 10.0 mmol) was dissolved in anhydrous DCM (50 mL) under argon. Trimethyloxonium tetrafluoroborate (1.4889 g, 10.1 mmol) was added in one portion and the reaction mixture stirred at room temperature under argon overnight. Pentafluorophenyl hydrazine (1.9784 g, 9.99 mmol) was added in one portion and the mixture stirred for 72 h at room temperature. The solvent was evaporated under reduced pressure. Triethyl orthoformate (25 mL, 150 mmol) was added and the mixture stirred at 140 °C overnight. The mixture was cooled and the solvent was evaporated under reduced pressure to give a brown gum. Trituration with ethyl acetate and diethyl ether gave the product as a pale brown solid with spectroscopic details in accordance with the literature (1.7844 g, 49%). The product could be crystallised by slow evaporation of CD_3CN; mp 245 – 247 °C (lit.[144] 248–253 °C); ν_{max} / cm^{-1} 3146w, 1604m, 1521m, 1380w, 1294w, 1029m, 992m; δ_H (700 MHz, CD_3CN) 2.83 (2H, app quin, C*H*$_2$, H^3), 3.22 (2H, t, *J* 7.7, C*H*$_2$, H^2), 4.49 (2H, t, *J* 7.4, C*H*$_2$, H^4), 9.66 (1H, s, NC*H*N, H^5); δ_C (176 MHz, CD_3CN) 21.7 (C^2), 26.5 (C^3), 48.4 (C^4), 142.7 (C^5), 164.8 (C^1); δ_F (376 MHz, CD_3CN) −161.6 - −161.5 (2F, m, ArF), −152.1 (s, BF_4^-), −149.7 (1F, tt, *J* 20.8, 4.1, ArF), −146.9 - −147.0 (2F, m, ArF); LCMS (ESI+) *m*/*z* 276 $[M\text{-}BF_4]^+$; HRMS (ESI+) *m*/*z* 276.0570 $[M\text{-}BF_4]^+$ ($C_{11}H_7N_3F_5$ requires 276.0560).

6.3.12 2-(2,4,6-Trimethylphenyl)-6,7-dihydro-5*H*-pyrrolo[2,1-c][1,2,4]triazol-2-ium tetrafluoroborate (267)

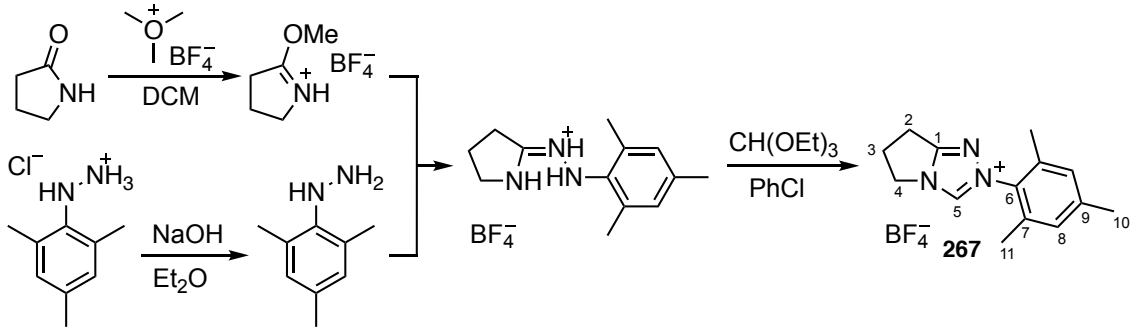

2-Pyrrolidinone (407 μL, 5.36 mmol) was dissolved in anhydrous DCM (25 mL) under argon. Trimethyloxonium tetrafluoroborate (795 mg, 5.37 mmol) was added in one portion and the reaction mixture stirred at room temperature under argon overnight. Diethyl ether (25 mL) and 1 M NaOH (25 mL) were cooled in an ice bath. 2,4,6-Trimethylphenyl hydrazinium chloride was added to this cooled mixture and stirred for ~ 15 minutes. The ether layer was separated and the aqueous phase was washed with diethyl ether (2 × 25 mL). The combined organics were washed with brine (25 mL), dried over Na_2SO_4, filtered and concentrated to give a yellow oil. This yellow oil was dissolved in anhydrous DCM (12 mL) and transferred to the amidate. The mixture was stirred at room temperature under argon for 48 h. The solvent was removed to give a red oil which was then dissolved in chlorobenzene (10 mL). Triethyl orthoformate (5 mL, 30.1 mmol) was added and the mixture heated at 125 °C for 72 hours. The reaction was allowed to cool and the solvent was removed *in vacuo* to give a brown oil. Either precipitation of the product using ethyl acetate, or failing that, flash column chromatography (DCM:MeOH 95:5) gave the desired compound as a brown solid (596 mg, 35% from 2-pyrrolidinone) with spectroscopic details in accordance with the literature.[78] The product could be crystallised by slow evaporation from chloroform; δ_H (600 MHz, $CDCl_3$) 2.05 (6H, s, 2 × C*H*$_3$, H^{11}), 2.35 (3H, s, C*H*$_3$, H^{10}), 2.87 (2H, app quin, C*H*$_2$, H^3), 3.23 (2H, t, *J* 7.8, C*H*$_2$, H^2), 4.67 (2H, t, *J* 7.8, C*H*$_2$, H^4), 6.98 (2H, s, Ar*H*, H^8), 9.47 (1H, s, NC*H*N, H^5); δ_C (151 MHz, $CDCl_3$) 17.2 (C^{11}), 21.2 (C^{10}), 21.9 (C^2), 26.6 (C^3), 47.8 (C^4), 129.6 (C^8), 131.8 (C^7), 135.2 (C^6), 141.3 (C^5), 141.8 (C^9), 162.8 (C^1); LCMS (ESI+) *m*/*z* 228 $[M\text{-}BF_4]^+$; HRMS (ESI+) *m*/*z* 228.1505 $[M\text{-}BF_4]^+$ ($C_{14}H_{18}N_3^+$ requires 228.1501).

6.3.13 2-(2,6-Dimethoxyphenyl)-6,7-dihydro-5*H*-pyrrolo[2,1-c][1,2,4]triazol-2-ium chloride (283)

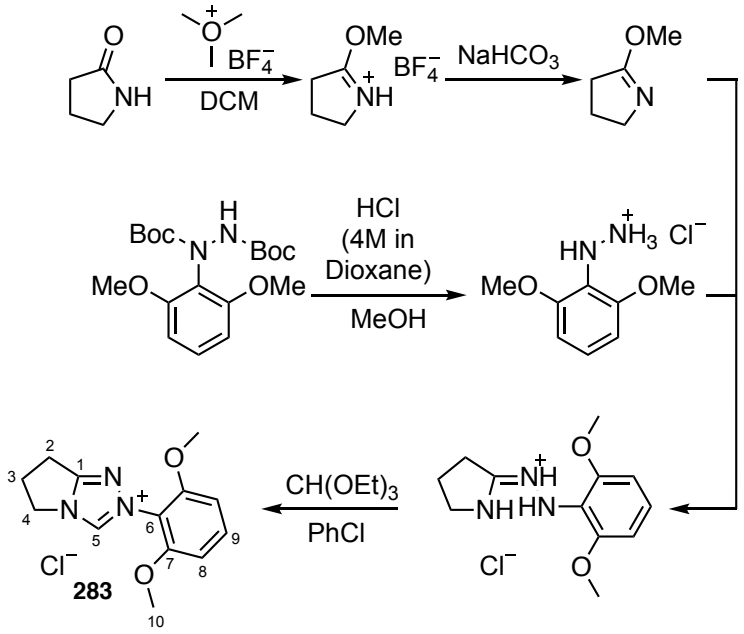

According to a literature procedure,[36] 2-pyrrolidone (0.78 mL, 10.1 mmol) was dissolved in anhydrous DCM (50 mL) and Me_3OBF_4 (1.789 g, 12.1 mmol) was added and the mixture stirred under an inert atmosphere overnight. Saturated $NaHCO_3$ (50 mL) was added slowly over 20 minutes. The organic phase was separated and the aqueous phase was extracted with DCM (3 × 50 mL). The combined organic layers were dried with Na_2SO_4 and filtered. Most of the DCM was removed on a rotary evaporator at ≥200 mbar (the imino ether is volatile) to give the title compound which was used directly without further purification; δ_H (400MHz, $(CD_3)_2SO$) 1.90 – 2.00 (2H, m, C*H*$_2$), 2.36 – 2.42 (2H, m, C*H*$_2$), 3.50 – 3.55 (2H, m, C*H*$_2$), 3.70 (3H, s, C*H*$_3$).

Di-*tert*-butyl 1-(2,6-dimethoxyphenyl)hydrazine-1,2-dicarboxylate **278a** (3.72 g, 10.1 mmol) was dissolved in anhydrous methanol (25 mL) and HCl (4 M in 1,4-dioxane, 25 mL, 101 mmol) was added slowly to the solution. The mixture was stirred for 4 h at room temperature. All volatiles were then removed *in vacuo* to give the hydrazine hydrochloride as an orange solid which was used in the next step without purification; δ_H (400MHz, CD_3OD) 3.94 (6H, s, (C*H*$_3$)$_2$), 6.76 (2H, d, *J* 8.4, Ar*H*), 7.18 (1H, t, *J* 8.4, Ar*H*); δ_C (100 MHz, CD_3OD) 55.2, 104.2, 125.9, 151.9; LCMS (ESI+) *m*/*z* 169 [M-Cl]$^+$.

The imino ether was dissolved in MeOH (40 mL) and added to the hydrazine hydrochloride. A HCl solution (4 M in 1,4-dioxane, 2.5 mL, 1.01 mmol) was added slowly to the solution resulting the evolution of a white gas. The mixture was stirred at

room temperature overnight. All volatiles were removed *in vacuo* to give the amidrazone as a brown oil which was used in the next step without further purification. R_f (DCM:MeOH 9:1) = 0.28; LCMS (ESI+) *m/z* 236 $[M\text{-}Cl]^+$.

The amidrazone was dissolved in anhydrous chlorobenzene (10 mL) and activated 4 Å molecular sieves were added to the solution. Triethyl orthoformate (13.3 mL, 80 mmol) and HCl (4 M in 1,4-dioxane, 10 mmol) were added to the reaction mixture. A reflux condenser with a drying tube filled with $CaCl_2$ was fitted and the mixture was heated to 80 °C overnight. The mixture was cooled and the molecular sieves were filtered and washed with DCM. The filtrate was concentrated *in vacuo* and the crude product was triturated with diethyl ether as a sticky brown solid (1.50 g). Flash column chromatography (DCM:MeOH 95:5 to 90:10) gave the title compound as a brown oil (212 mg, 8% from 2-pyrrolidinone); ν_{max} / cm^{-1} 3327m, 2942m (C-H stretch), 1603m, 1589m, 1485m, 1436m, 1266m (C-O stretch), 1109s, 1025, 971; δ_H (700 MHz, $CDCl_3$) 2.85 (2H, app quin, *J* 7.7, C*H*$_2$), 3.20 (2H, t, *J* 7.7, C*H*$_2$), 3.78 (6H, s, (C*H*$_3$)$_2$), 4.85 (2H, t, *J* 7.7, C*H*$_2$), 6.64 (2H, d, *J* 8.4, Ar*H*), 7.45 (1H, t, *J* 8.4, Ar*H*), 11.14 (1H, s, NC*H*N); δ_C (176 MHz, $CDCl_3$) 22.0, 26.9, 48.5, 56.4, 104.2, 113.2, 133.4, 144.1, 155.5, 161.4;); LCMS (ESI+) *m/z* 246 $[M\text{-}Cl]^+$; HRMS (ESI+) *m/z* 246.1242 $[M\text{-}Cl]^+$ ($C_{13}H_{16}N_3O_2$ requires 246.1243).

6.3.14 2-(2,4,6-Trimethylphenyl)-3-(α-methoxybenzyl)-6,7-dihydro-5*H*-pyrrolo[2,1-c][1,2,4]triazol-2-ium tetrafluoroborate (366)

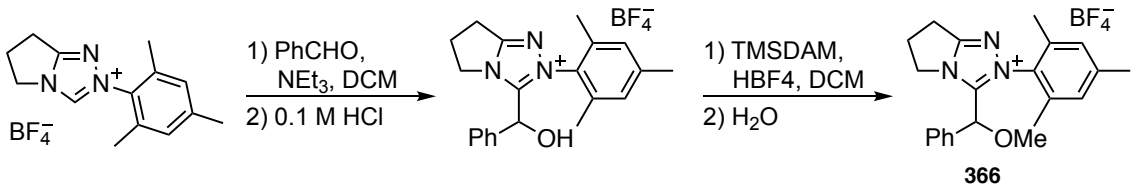

366

N-mesityl substituted triazolium salt (207.4 mg, 0.658 mmol) was dissolved in anhydrous DCM (9 mL). Triethylamine (183 µL, 1.32 mmol) was added and mixture was stirred at room temperature for 15 mins. Benzaldehyde (669 µL, 0.658 mmol) was added and the mixture stirred at room temperature for 3 h. The reaction was quenched with 0.1 M HCl (3 mL) and the organic layer was extracted and evaporated to give a pale yellow oil; LCMS (ESI+) *m/z* (ES+) 334 $[M\text{-}BF_4]^+$. The conversion was determined by ^{1}H NMR spectroscopy to be 96%.

The crude hydroxyaryl adduct was dissolved in DCM (2.5 mL). HBF_4 (48 wt. % in H_2O, 7.65 M, 610 µL, 4.75 mmol) was added and the mixture cooled in an ice bath.

Trimethylsilyldiazomethane (2M in hexanes, 2.30 mL, 4.67 mmol) was added slowly below the surface of the DCM layer. The mixture was stirred for 20 minutes. Trimethylsilyldiazomethane (2M in hexanes, 2.30 mL, 4.67 mmol) was added slowly below the surface of the DCM layer and the mixture stirred for 20 minutes. This process of adding HBF_4 followed by TMSDAM was repeated until a total of 100 equivalents had been added. The mixture was stirred for 30 minutes in the ice bath and quenched with distilled water (10 mL). The hexane and DCM were evaporated and the aqueous layer extracted with DCM (5 × 10 mL). The combined organic layers were dried over Na_2SO_4, filtered and concentrated to give an orange residue. Flash column chromatography (DCM:MeOH 95:5, R_f = 0.27) gave a yellow oil (60.3 mg, 30%); δ_H (700 MHz, CD_2Cl_2) 1.38 (3H, s, C*H*$_3$), 2.13 (3H, s, C*H*$_3$), 2.37 (3H, s, C*H*$_3$), 2.89 – 2.99 (2H, m, C*H*$_2$), 3.22 – 3.32 (2H, m, C*H*$_2$), 3.36 (3H, s, OC*H*$_3$), 4.58 – 4.72 (2H, m, C*H*$_2$), 5.30 (1H, s, C*H*(OMe)), 6.84 (1H, s, Mes*H*), 6.99 – 7.02 (2H, m, Ar*H*), 7.08 (1H, s, Mes*H*), 7.30 – 7.34 (2H, m, Ar*H*), 7.38 – 7.42 (1H, m, Ar*H*); δ_C (175 MHz, CD_2Cl_2) 17.1 (Mes*C*H$_3$), 17.6 (Mes*C*H$_3$), 21.5 (Mes*C*H$_3$), 22.4 (CH_2), 27.3 (CH_2), 50.1 (CH_2), 58.3 (CH(O*C*H$_3$)), 77.8 (*C*H(OMe)), 128.2 (ArCH), 129.9 (ArCH), 130.2 (MesCH), 130.3 (MesCH), 131.1 (ArCH), 131.2 (MesC), 132.7 (MesC), 135.2 (MesC), 136.7 (MesC), 143.2 (MesC), 151.4 (NCN), 163.8 (NCN); LCMS (ESI+) *m*/*z* 348 $[M\text{-}BF_4]^+$; HRMS (ESI+) *m*/*z* 348.2058 $[M\text{-}BF_4]^+$ ($C_{22}H_{26}N_3O$ requires 348.2076).

6.3.15 2-(2,4,6-Trimethylphenyl)-3-(methoxy(2-methoxyphenyl)methyl)-6,7-dihydro-5*H*-pyrrolo[2,1-c][1,2,4]triazol-2-ium tetrafluoroborate (367)

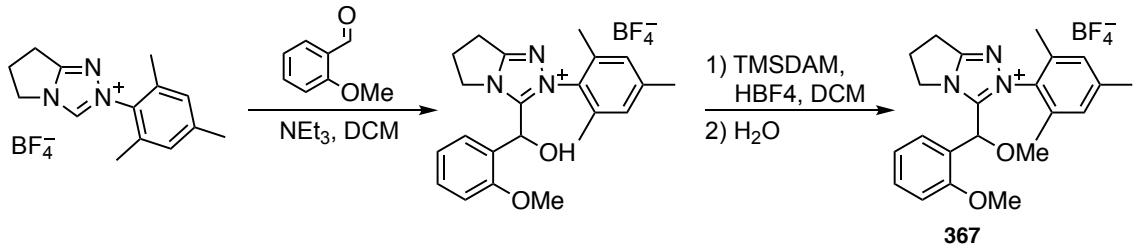

367

N-mesityl substituted triazolium salt (199.4 mg, 0.633 mmol) was dissolved in anhydrous DCM (20 mL). Triethylamine (176 µL, 1.27 mmol) was added and mixture was stirred at room temperature for 15 mins. 2-Methoxybenzaldehyde (86.1 mg, 0.633 mmol) was added and the mixture stirred at room temperature for 30 mins. The solvent was evaporated *in vacuo* to give an orange oil. The conversion was determined by ^{1}H NMR spectroscopy to be 100%.

The crude hydroxyaryl adduct (0.633 mmol) was dissolved in DCM (25 mL). HBF_4 (48 wt. % in H_2O, 7.65 M, 827 µL, 6.33 mmol) was added and the mixture cooled in an ice

bath. Trimethylsilyldiazomethane (2M in hexanes, 3.17 mL, 6.33 mmol) was added slowly below the surface of the DCM layer. The mixture was stirred for 20 minutes. HBF_4 (48 wt. % in H_2O, 7.65 M, 827 µL, 6.33 mmol) was added followed by trimethylsilyldiazomethane (2M in hexanes, 3.17 mL, 6.33 mmol) which was added slowly below the surface of the DCM layer and the mixture stirred for 20 minutes. This process of adding HBF_4 followed by TMSDAM was repeated until 70 equivalents had been added. The mixture was stirred for 30 minutes in the ice bath and quenched with distilled water (10 mL). The organic layer was separated and the aqueous layer extracted with DCM (3 × 10 mL). The combined organic layers were dried over Na_2SO_4, filtered and concentrated to give a yellow oil. Flash column chromatography (DCM:MeOH 95:5, R_f = 0.27) gave a yellow oil (71.2 mg, 0.188 mmol, 30 %); δ_H (700 MHz, CD_2Cl_2) 1.56 (3H, s, MesC*H*$_3$), 2.03 (3H, s, MesC*H*$_3$), 2.35 (3H, s, MesC*H*$_3$), 2.88 – 2.94 (2H, m, C*H*$_2$, H^3), 3.27 (2H, t, *J* 7.7, C*H*$_2$, H^2), 3.31 (3H, s, C(H)OC*H*$_3$, H^7), 3.63 (3H, s, ArOC*H*$_3$, H^{10}), 4.39 – 4.56 (2H, m, C*H*$_2$, H^4), 5.60 (1H, s, C(*H*)OMe, H^6), 6.85 (1H, s, Mes*H*), 6.85 (1H, d, *J* 10.0, Ar*H*), 6.93 (1H, td, *J* 7.7, 1.4, Ar*H*), 7.03 (1H, s, Mes*H*), 7.04 (2H, dd, *J* 7.7, 1.8, Ar*H*), 7.39 (1H, ddd, *J* 8.3, 7.4, 1.7, Ar*H*); δ_C (176 MHz, CD_2Cl_2) 16.3, 16.8, 20.9, 21.8, 26.8, 49.1, 55.6, 57.9, 71.8, 110.9, 119.8, 121.1, 128.8, 129.3, 130.6, 131.9, 135.1, 135.9, 142.2, 150.9, 156.9, 162.7; LCMS (ESI+) *m*/*z* 378 $[M\text{-}BF_4]^+$; HRMS (ESI+) *m*/*z* 378.2177 $[M\text{-}BF_4]^+$ ($C_{23}H_{28}N_3O_2$ requires 378.2182).

6.3.16 2-(2,4,6-Trimethylphenyl)-3-(methoxy(2-bromophenyl)methyl)-6,7-dihydro-5*H*-pyrrolo[2,1-c][1,2,4]triazol-2-ium tetrafluoroborate (368)

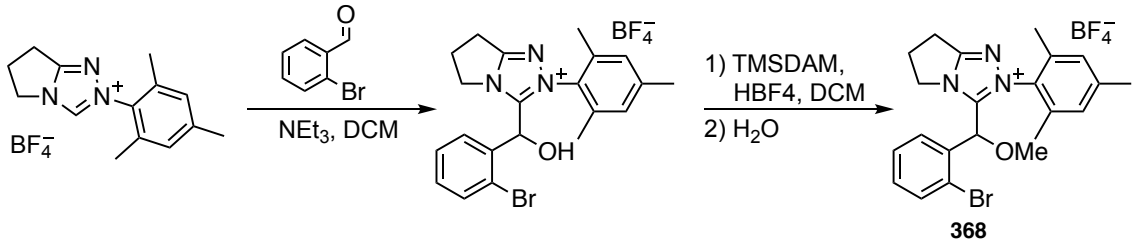

368

N-mesityl substituted triazolium salt (98.8 mg, 0.314 mmol) was dissolved in anhydrous DCM (10 mL). Triethylamine (87.4 µL, 0.627 mmol) was added and mixture was stirred at room temperature for 15 mins. 2-Bromobenzaldehyde (36.7 µL, 0.314 mmol) was added and the mixture stirred at room temperature for 15 mins. The solvent was evaporated to give an orange/brown oil; LCMS (ESI+) *m*/*z* 412 $[M(^{79}Br)\text{-}BF_4]^+$. The conversion was determined by ^{1}H NMR spectroscopy to be 68%.

The crude hydroxyaryl adduct (0.226 mmol) was dissolved in DCM (5 mL). HBF_4 (48 wt. % in H_2O, 7.65 M, 29.5 µL, 0.226 mmol) was added and the mixture cooled in an

ice bath. Trimethylsilyldiazomethane (2M in hexanes, 0.11 mL, 0.226 mmol) was added slowly below the surface of the DCM layer. The mixture was stirred for 20 minutes. HBF_4 (48 wt. % in H_2O, 7.65 M, 29.5 μL, 0.226 mmol) was added followed by trimethylsilyldiazomethane (2M in hexanes, 0.11 mL, 0.226 mmol) which was added slowly below the surface of the DCM layer and the mixture stirred for 20 minutes. This process of adding HBF_4 followed by TMSDAM was repeated until 130 equivalents had been added. The mixture was stirred for 30 minutes in the ice bath and quenched with distilled water (10 mL). The organic layer was separated and the aqueous layer extracted with DCM (3 × 10 mL). The combined organic layers were dried over Na_2SO_4, filtered and concentrated to give an orange residue. Flash column chromatography (DCM:MeOH 95:5, R_f = 0.35) gave a yellow oil (42.6 mg, 0.0983 mmol, 31 %); δ_H (600 MHz, CD_2Cl_2) 1.57 (3H, s, C*H*$_3$), 2.06 (3H, s, C*H*$_3$), 2.32 (3H, s, C*H*$_3$), 2.91 – 3.00 (2H, m, C*H*$_2$), 3.26 – 3.33 (2H, m, C*H*$_2$), 3.36 (3H, s, CH(OC*H*$_3$)), 4.62 – 4.72 (2H, m, C*H*$_2$), 5.80 (1H, s, C*H*(OMe)), 6.79 (1H, s, Mes*H*), 6.99 (1H, s, Mes*H*), 7.17 (1H, dd, *J* 7.6, 1.9, Ar*H*), 7.25 – 7.32 (2H, m, Ar*H*), 7.50 (1H, dd, *J* 7.8, 1.4, Ar*H*); δ_C (150 MHz, CD_2Cl_2) 16.5 (MesCH_3), 17.0 (MesCH_3), 20.8 (MesCH_3), 21.9 (CH_2), 26.7 (CH_2), 49.8 (CH_2), 57.6 (CH(O*C*H$_3$)), 76.2 (*C*H(OMe)), 123.6, 128.7 (Ar*C*H), 129.5 (Mes*C*H), 129.7 (Mes*C*H), 130.4 (Mes*C*), 130.7 (Ar*C*H), 131.6 (Ar*C*), 131.9 (Ar*C*), 133.3 (Ar*C*H), 135.1 (Mes*C*), 135.9 (Mes*C*), 142.4 (Mes*C*), 150.3, 163.2; LCMS (ESI+) *m*/*z* 426 $[M(^{79}Br)\text{-}BF_4]^+$; HRMS (ESI+) *m*/*z* 426.1187 $[M(^{79}Br)\text{-}BF_4]^+$ ($C_{22}H_{25}N_3O^{79}Br$ requires 426.1181).

6.3.17 Potassium dimsylate

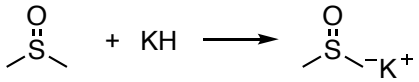

Potassium hydride (30 wt% dispersion in mineral oil, 0.75 mL) was washed with anhydrous hexane (6 × 5 mL) and dried for 16 h under a high vacuum. Under an argon atmosphere, anhydrous DMSO (25 mL) was added slowly and the solution stirred for 3.5 h. The solution was filtered through a filter stick and the resulting green solution was stored under argon in the fridge. The concentration was determined to be 0.205 M by withdrawing 500 μL and making it up to 2 mL with distilled water, and titration with 1.000 M HCl with phenolphthalein indicator.

6.4 Kinetic details

6.4.1 Preparations of solutions for kinetic experiments

Solutions of DCl in D_2O were prepared by dilution of the commercially available stock solution (35 wt. %), followed by titration against standard solutions of KOH to determine concentration. A range of dilutions was made and KCl was added to the stock solutions to make the ionic strength up to 1.0 M.

Formate and DMAP buffers were prepared by mixing stock solutions of potassium formate or DMAP with DCl to give buffer solutions with varying free base ratios and made up to I = 1.0 M using KCl. Carbonate buffers were made by initially preparing DCO_3^- from HCO_3^- and then mixing stock solutions of each to give buffer solutions with varying free base ratios and made up to I = 1.0 M using KCl.

Hydroxide solutions were prepared using titrimetrically-known solutions of NaOH and KOH and ultra-high purity water. Solutions run at constant ionic strength were made up to I = 1.0 M using KCl.

6.4.2 Measurement of pH and determination of pD

The pH values of reaction solutions were determined at 25 ºC using a MeterLab^{TM} PHM 290 p*H*-Stat Controller equipped with a radiometer combination electrode filled with saturated KCl solution. The apparatus was calibrated between pH 1.68 – 4, pH 4 – 7, pH 7 – 10 or pH 10 – 12.46 to encompass the pH of the reaction solution. The pD in D_2O was calculated by adding 0.40 to the reading on the pH meter.[145] The pD in D_2O:CD_3CN (9:1) was calculated by adding 0.44 to the reading on the pH meter.[145,146]

The activity coefficient for hydroxide ion was determined previously by a member of our laboratory[78] from the slope of $10^{pH - pK_w}$ vs hydroxide ion concentration of a series of titrimetrically-known solutions of KOH at 25 °C and ionic strength I = 1.0 M (KCl) . A value of $\gamma_{HO} = 0.72$ was found.

6.4.3 Kinetics of C(3)-H/D exchange (chapter 2)

Kinetics of C(3)-H/D exchange of the 1,2,4-triazolium ion were followed by monitoring the disappearance of this signal in the ^1H NMR spectrum relative to the signal due to the twelve equivalent, non-exchanging protons of the tetramethylammonium deuteriosulphate internal standard as a function of time. The time was measured as the endpoint of the ^1H NMR experiments. These reactions were carried out in D_2O solutions of varying acidity and were kept at constant ionic strength of 1.0 M with KCl.

Reactions were initiated by the addition of DCl or buffer solution (0.75 mL), which had been previously equilibrated at 25 °C, containing internal standard to the rigorously dried triazolium salt, making the final substrate concentration up to 10 mM. Reactions were initiated and monitored directly in the NMR tube. For reactions with $t_{1/2} < 4$ hours, reactions were monitored directly in a thermostatted NMR spectrometer.

6.4.4 Kinetics of hydroxyaryl adduct formation (chapter 3)

Kinetics of hydroxyaryl adduct formation were followed by monitoring the the ^{1}H signals corresponding to non-exchanging protons on triazolium salt, aryl aldehyde, hydroxyaryl adduct and exchangeable protons on aryl aldehyde (aldehydic proton), hydroxyaryl adduct and benzoin (where addition of the hydroxyaryl adduct may occur either to exchanged or unexchanged aldehyde). Concentrations of all species were made relative to the starting concentration of triazolium salt (0.08 M). The reactions were carried out in buffered methanol-d_4.

Reactions were initiated by dissolving rigorously dried triazolium salt in triethylamine buffered methanol-d_4 (0.75 mL) which had been previously equilibrated at 25 °C and adding this directly to the aryl aldehyde in a glass vial. The mixture was shaken briefly before being transferred to an NMR tube. Reactions were monitored directly in a thermostatted NMR spectrometer.

6.4.5 Kinetics of C(α)-H/D exchange (chapter 4)

Kinetics of C(α)-H/D exchange of the methylated adducts were followed by monitoring the disappearance of this signal in the ^{1}H NMR spectrum relative to the signal due to the non-exchanging protons of the potassium formate or tetramethylammonium deuteriosulphate internal standard as a function of time. The time was measured as the endpoint of the ^{1}H NMR experiments. These reactions were carried out in D_2O:CD_3CN (9:1) solutions of varying acidity and were kept at constant ionic strength of 1.0 M with KCl.

Reactions were initiated by the addition of buffer solution (0.75 mL), which had been previously equilibrated at 25 °C, containing internal standard to the triazolium salt, making the final substrate concentration up to 5 mM. Reactions were initiated and monitored directly in the NMR tube. For reactions with $t_{1/2} < 4$ hours, reactions were monitored directly in a thermostatted NMR spectrometer.

6.4.6 ^{1}H NMR Conditions

6.4.6.1 H/D Exchange kinetics (chapters 2 and 4)

For H/D exchange reactions, ^{1}H NMR spectra were recorded on a Varian 400 or Varian Inova-500 spectrometer with a relaxation delay of 20 s, sweep width of 8298.8 Hz, acquisition time of 4 s and a 90° pulse angle. Spectra were run with 32 transients. ^{1}H NMR spectral baselines were subject to a first-order drift correction followed by a 6th order Bernstein polynomial baseline correction, before integration of the signal areas. Substrate signal areas were compared with the signal of the internal standard (tetramethylammonium deuteriosulphate or potassium formate).

Exchange kinetics for N-5-methoxypyrid-2-yl triazolium salt were particularly fast and the above parameters were altered slightly to allow data acquisition. Kinetics were run recorded with a relaxation delay of 2 s, a 45º pulse angle and 16 transients.

6.4.6.2 Hydroxyaryl adduct formation (chapter 3)

For hydroxyaryl adduct formation reactions, ^{1}H NMR spectra were recorded on a Varian Inova-500 spectrometer with a relaxation delay of 5 s, sweep width of 8298.8 Hz, acquisition time of 2 s and a 45° pulse angle. Spectra were run with 32 transients. ^{1}H NMR spectral baselines were subject to a first-order drift correction followed by a 6th order Bernstein polynomial baseline correction, before integration of the signal areas.

6.5 DFT Calculations

DFT calculations were carried out using Gaussian 09[127] using the Durham University Hamilton HPC.[128] The level of theory used was B3LYP/6-31(g), using redundant internal coordinates and with solvent methanol modelled using an implicit polarisable continuum model (PCM). Calculations were run using 5º steps starting from a dihedral angle of 0º. Coordinates were obtained from crystal structures obtained in this thesis and from the literature for N-phenyl triazolium salt.[126] Energies were converted from Hartree to kJ mol^{-1}.

Appendix 1

Conditions used in attempted diazotisation of 2,6-dimethoxyaniline

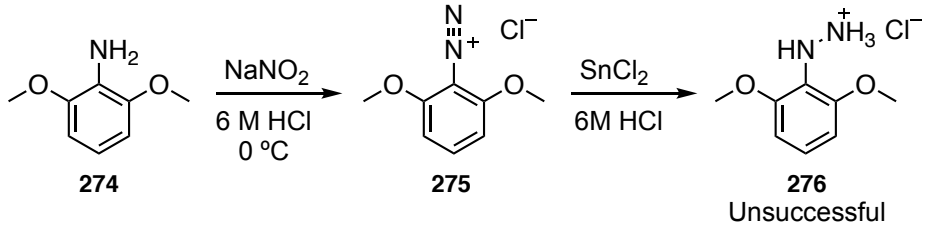

Scheme 66: Attempted synthesis of 2,6-dimethoxypheyl hydrazinium hydrochloride.

In general, 2,6-dimethoxyaniline **274** was dissolved in twenty equivalents of HCl and cooled in an ice bath. Sodium nitrite was dissolved in distilled water. The sodium nitrite solution was added dropwise to the cooled solution of **274**. Reaction times in the literature for the two anilines were 1 h for 2,4-dimethylaniline and 20 mins for 2,6-dimethylaniline. As methoxy substituents are more electron releasing than methyl substituents, the dimethoxyaniline should be more susceptible to electrophilic attack by the nitrosating species, however, reactions were still stirred for 1 h. $SnCl_2$ dihydrate was dissolved in aqueous HCl, and added dropwise to the reaction mixture. The changes in conditions employed from entry 1 – 5 (Table 19) reflected the idea that the two methoxy substituents would stabilise the diazonium salt to a greater extent than two methyl substituents, meaning that the reduction step with $SnCl_2$ would be slower. ^{1}H NMR spectroscopy and ESI-MS showed no evidence for the formation of the hydrazine or the hydrazinium chloride. This may have been due to decomposition back the aniline.

Table 19: Conditions used in the attempted synthesis of the hydrazinium hydrochloride by diazotisation of 2,6-dimethoxyaniline.

Entry	Conditions	Observations
1	Step 1: $NaNO_2$ (1.2 equiv.), HCl (20 equiv.) Step 2: $SnCl_2$ (1.4 equiv.), HCl (10 equiv.) Basified (pH 14) and extracted with EtOAc.	No *m/z* corresponding to $[M+H]^+$, inconclusive ^1H NMR.
2	Step 1: $NaNO_2$ (1.2 equiv.), HCl (20 equiv.) Step 2: $SnCl_2$ (1.4 equiv.), HCl (10 equiv.) Filtered black solid, evaporated filtrate and column chromatography of resulting residue.	Black solid: no evidence for product. Red residue from filtrate: *m/z* corresponding to $[M+H]^+$ but inconclusive ^1H NMR.
3	Step 1: $NaNO_2$ (1.2 equiv.), HCl (20 equiv.) Step 2: $SnCl_2$ (1.4 equiv.), HCl (10 equiv.) Filtered solid, basified filtrate (pH 11). Extract into EtOAc.	Solid: Product not observed by ESI-MS and inconclusive ^1H NMR spectrum Residue from filtrate: ^1H NMR showed starting aniline.
4	Step 1: $NaNO_2$ (1.2 equiv.), HCl (20 equiv.) Step 2: $SnCl_2$ (1.4 equiv.), HCl (10 equiv.) Filtered solid, basified solid and extracted into EtOAc.	Product not observed by ESI-MS
5	Step 1: $NaNO_2$ (1.1 equiv.), HCl (20 equiv.) Step 2: $SnCl_2$ (3 equiv.), HCl (20 equiv.) Filtered solid, basified filtrate (pH 14).	^1H NMR showed starting aniline.

C(3)-H/D Exchange kinetics

2-(2,6-Dimethoxyphenyl)-6,7-dihydro-5*H*-pyrrolo[2,1-c][1,2,4]triazol-2-ium tetrafluoroborate (255)

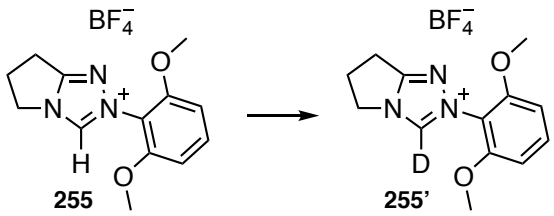

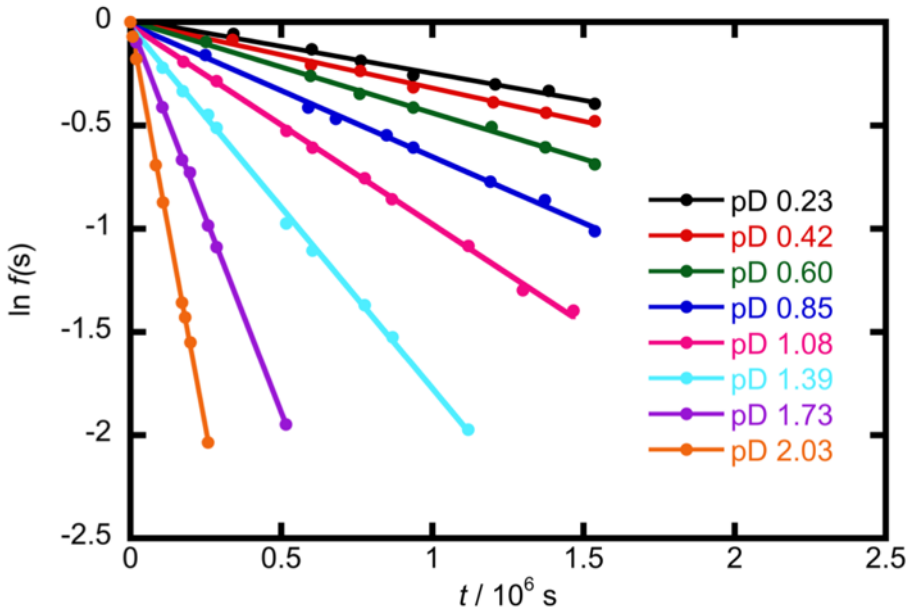

Figure 97: Semi-logarithmic plot of the fraction of unexchanged substrate against time for C(3)-H/D exchange reaction of N-2,6-dimethoxyphenyl triazolium salt 255 at 25 °C in D_2O between pD 0.23 – 2.03, and I = 1.0 M (KCl).

Table 20: Pseudo first order rate constants, k_{ex} (s^{-1}), for C(3)-H/D exchange of N-2,6-dimethoxyphenyl triazolium salt 255 at 25 °C in D_2O and I = 1.0 M (KCl) as a function of pD.

pD	$10^6\ k_{ex}$ / s^{-1}	*log* (k_{ex} / s^{-1})	pD	$10^6\ k_{ex}$ / s^{-1}	*log* (k_{ex} / s^{-1})
0.23	0.261 ± 0.012	-6.58	1.08	0.962 ± 0.013	-6.02
0.42	0.321 ± 0.010	-6.49	1.39	1.75 ± 0.02	-5.76
0.60	0.445 ± 0.008	-6.35	1.73	3.76 ± 0.03	-5.42
0.85	0.641 ± 0.013	-6.19	2.03	7.80 ± 0.05	-5.11

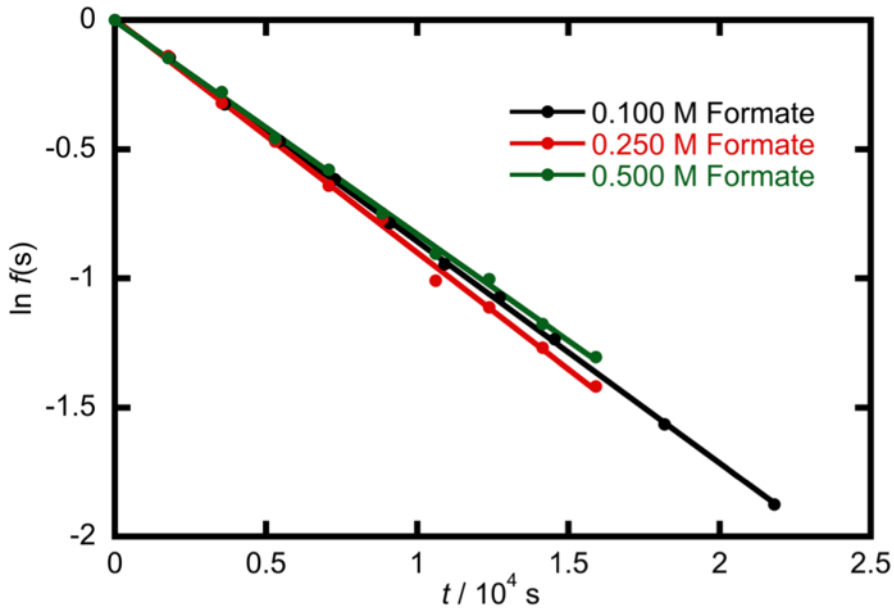

Figure 98: Semi-logarithmic plot of the fraction of unexchanged substrate against time for C(3)-H/D exchange reaction of N-2,6-dimethoxyphenyl triazolium salt 255 at 25 °C in D_2O in a range of buffers at pD 3.07, and I = 1.0 M (KCl).

Table 21: Pseudo first order rate constants, k_{ex} (s^{-1}), for C(3)-H/D exchange of N-2,6-dimethoxyphenyl triazolium salt 255 at 25 °C in D_2O and I = 1.0 M (KCl) as a function of buffer concentration at pD 3.07.

pD	[HCO_2^- + HCO_2D] / M	$10^5\ k_{ex}$ / s^{-1}	$10^5\ k_{ex}$ / s^{-1} *(Averaged)*	*log* (k_{ex} / s^{-1})
3.07	0.100	8.58 ± 0.05		
(Formate	0.250	9.04 ± 0.14	8.62	-4.06
buffer)	0.500	8.25 ± 0.10		

2-(2,6-Diisopropoxyphenyl)-6,7-dihydro-5*H*-pyrrolo[2,1-c][1,2,4]triazol-2-ium tetrafluoroborate (256)

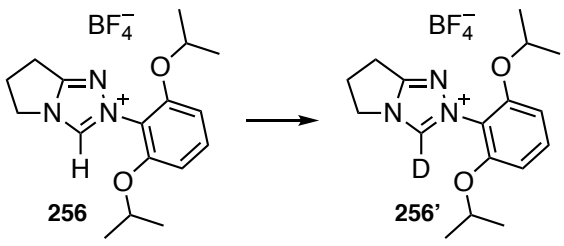

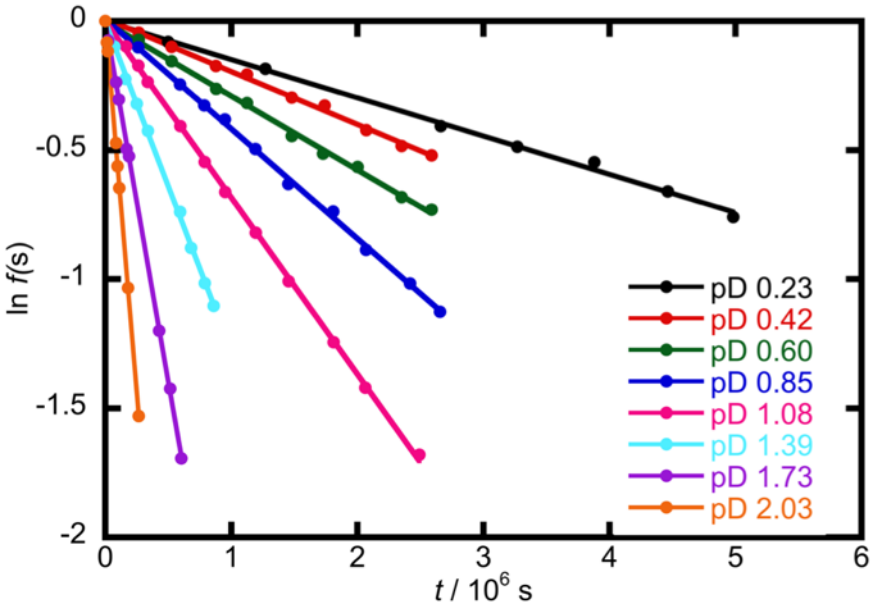

Figure 99: Semi-logarithmic plot of the fraction of unexchanged substrate against time for C(3)-H/D exchange reaction of N-2,6-diisopropoxyphenyl triazolium salt 256 at 25 ºC in D_2O between pD 0.23 – 2.03, and I = 1.0 M (KCl).

Table 22: Pseudo first order rate constants, k_{ex} (s^{-1}), for C(3)-H/D exchange of N-2,6-diisopropoxyphenyl triazolium salt 256 at 25 °C in D_2O and I = 1.0 M (KCl) as a function of pD.

pD	$10^6\ k_{ex}$ / s^{-1}	*log* (k_{ex} / s^{-1})	pD	$10^6\ k_{ex}$ / s^{-1}	*log* (k_{ex} / s^{-1})
0.23	0.148 ± 0.003	-6.83	1.08	0.684 ± 0.004	-6.16
0.42	0.205 ± 0.004	-6.69	1.39	1.275 ± 0.013	-5.90
0.60	0.286 ± 0.004	-6.54	1.73	2.782 ± 0.019	-5.56
0.85	0.425 ± 0.005	-6.37	2.03	5.72 ± 0.04	-5.24

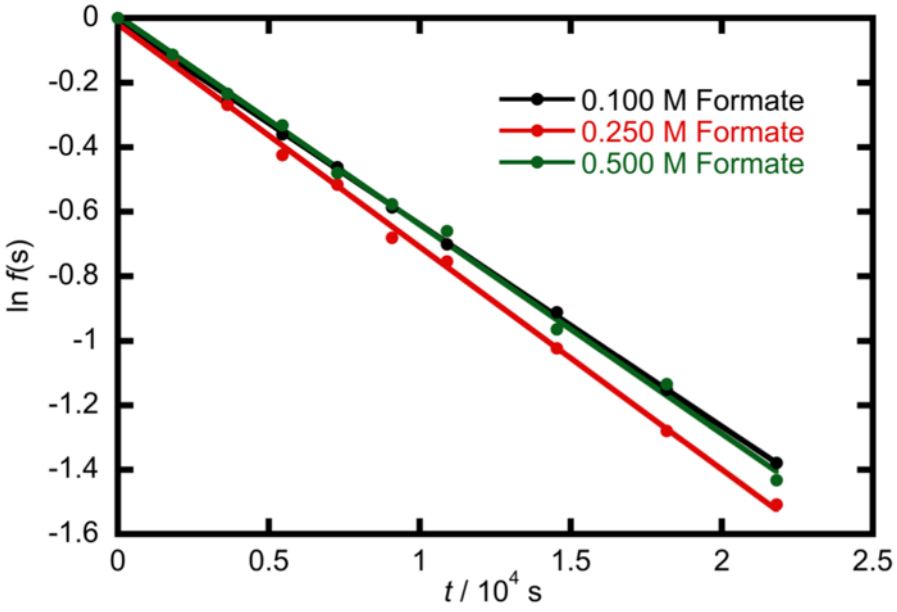

Figure 100: Semi-logarithmic plot of the fraction of unexchanged substrate against time for C(3)-H/D exchange reaction of N-2,6-diisopropoxyphenyl triazolium salt 256 at 25 ºC in D_2O in a range of buffers at pD 3.07, and I = 1.0 M (KCl).

Table 23: Pseudo first order rate constants, k_{ex} (s^{-1}), for C(3)-H/D exchange of N-2,6-diisopropoxyphenyl triazolium salt 256 at 25 °C in D_2O and I = 1.0 M (KCl) as a function of buffer concentration at pD 3.07.

pD	$[HCO_2^- + HCO_2D]$ / M	$10^5\ k_{ex}$ / s^{-1}	$10^5\ k_{ex}$ / s^{-1} *(Averaged)*	*log* (k_{ex} / s^{-1})
3.07 (Formate buffer)	0.100	6.26 ± 0.05	6.55	-4.18
	0.250	6.90 ± 0.09		
	0.500	6.48 ± 0.12		

2-(5-Methoxypyrid-2-yl)-6,7-dihydro-5*H*-pyrrolo[2,1-c][1,2,4]triazol-2-ium tetrafluoroborate (257)

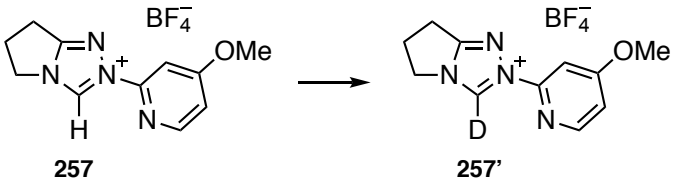

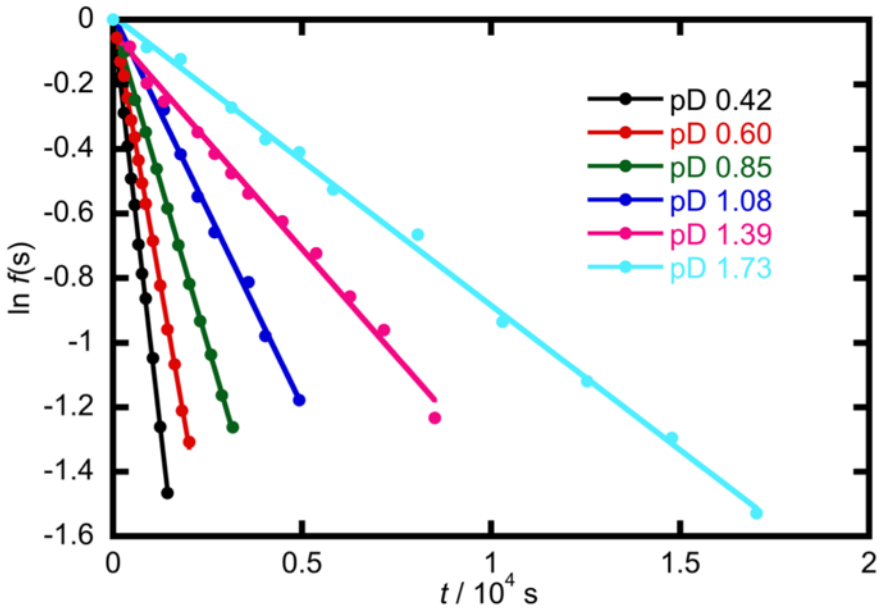

Figure 101: Semi-logarithmic plot of the fraction of unexchanged substrate against time for C(3)-H/D exchange reaction of N-5-methoxypyrid-2-yl triazolium salt 257 at 25 °C in D_2O between pD 0.42 – 1.73, and I = 1.0 M (KCl).

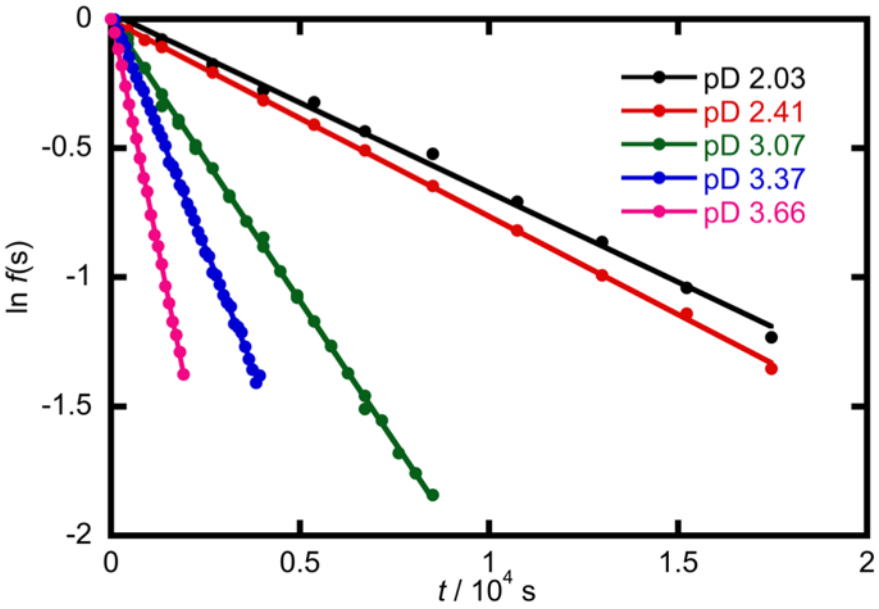

Figure 102: Semi-logarithmic plot of the fraction of unexchanged substrate against time for C(3)-H/D exchange reaction of N-5-methoxypyrid-2-yl triazolium salt 257 at 25 °C in D_2O between pD 2.03 – 3.66, and I = 1.0 M (KCl).

Table 24: Pseudo first order rate constants, k_{ex} (s^{-1}), for C(3)-H/D exchange of N-5-methoxypyrid-2-yl triazolium salt 257 at 25 °C in D_2O and I = 1.0 M (KCl) as a function of pD.

pD	$10^4\ k_{ex}$ / s^{-1}	*log* (k_{ex} / s^{-1})	pD	$10^4\ k_{ex}$ / s^{-1}	*log* (k_{ex} / s^{-1})
0.42	10.10 ± 0.08	-3.00	2.03	0.677 ± 0.007	-4.17
0.60	6.60 ± 0.04	-3.18	2.41	0.760 ± 0.005	-4.12
0.85	4.02 ± 0.03	-3.40	3.07	2.181 ± 0.006	-3.66
1.08	2.42 ± 0.05	-3.62	3.37	3.657 ± 0.017	-3.44
1.39	1.34 ± 0.04	-3.87	3.66	7.23 ± 0.04	-3.14
1.73	0.896 ± 0.013	-4.05			

2-(Pyrid-2-yl)-6,7-dihydro-5*H*-pyrrolo[2,1-c][1,2,4]triazol-2-ium tetrafluoroborate (258)

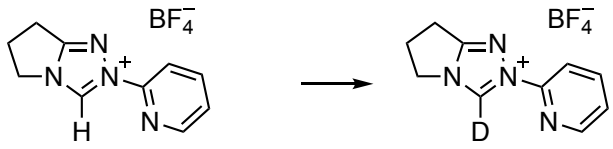

258 **258'**

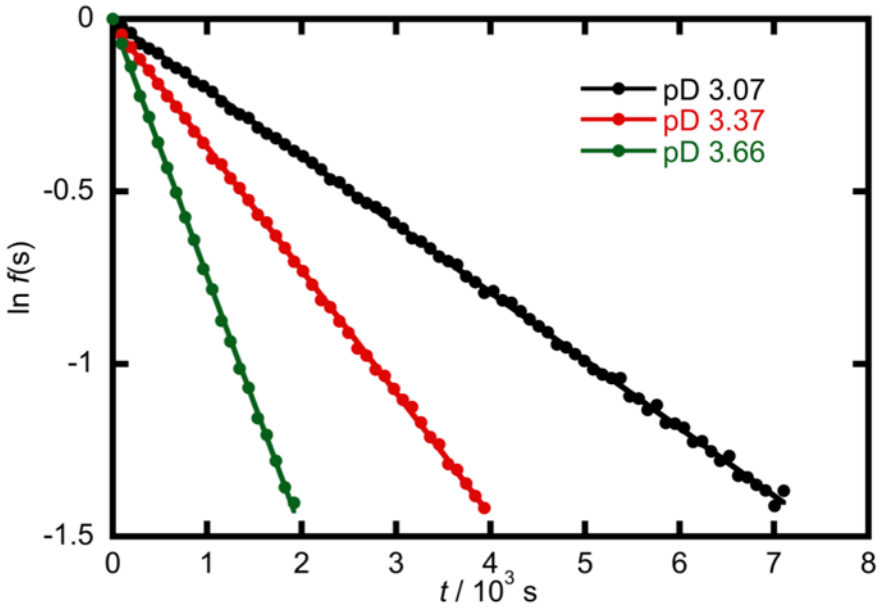

Figure 103: Semi-logarithmic plot of the fraction of unexchanged substrate against time for C(3)-H/D exchange reaction of N-pyrid-2-yl triazolium salt 258 at 25 ºC in D_2O between pD 3.07 – 3.66, and I = 1.0 M (KCl).

Table 25: Pseudo first order rate constants, k_{ex} (s^{-1}), for C(3)-H/D exchange of N-pyrid-2-yl triazolium salt 258 at 25 °C in D_2O and I = 1.0 M (KCl) as a function of pD.

pD	$10^4\ k_{ex}$ / s^{-1}	$log\ (k_{ex}$ / $s^{-1})$
3.07	1.963 ± 0.005	-3.71
3.37	3.559 ± 0.009	-3.45
3.66	7.41 ± 0.04	-3.13

Table 26: Pseudo first order rate constants, k_{ex} (s^{-1}), for C(3)-H/D exchange of N-pyrid-2-yl triazolium salt 258 at 25 °C in D_2O and I = 1.0 M (KCl) as a function of pD obtained by O'Donoghue and co-workers.[59]

pD	$10^4\ k_{ex}$ / s^{-1}	$log\ (k_{ex}$ / $s^{-1})$	pD	$10^4\ k_{ex}$ / s^{-1}	$log\ (k_{ex}$ / $s^{-1})$
0.08	6.92	-4.16	1.66	1.39	-4.86
0.37	4.27	-4.37	1.75	1.57	-4.80
0.76	2.22	-4.65	1.88	1.83	-4.74
1.03	1.40	-4.85	2.05	2.47	-4.61
1.34	1.11	-4.95	2.31	4.20	-4.38

Attempted Fitting to two Mechanisms of C(3)-H/D Exchange

Attempts were made to fit the data for *ortho*-alkoxy-substituted triazolium salts **255** and **256** to the kinetically indistinguishable equations used previously.[59] The absence of a downward bend in the data led to large errors in K_a^{N1}, and so this fitting was not used to extract the final k_{DO} values.

$$\log(k_{ex}) = log\left[\frac{K_a^{N1}\left(\left(\frac{k_{DO}K_W}{\gamma_{DO}}\right)10^{pD}\right)+(K_a^{N1}k_{D_2O})}{K_a^{N1}+10^{-pD}}\right] \quad \text{(A1)}$$

$$\log(k_{ex}) = log\left[\frac{K_a^{N1}\left(\left(\frac{k_{DO}K_W}{\gamma_{DO}}\right)10^{pD}\right)+\left(\frac{k'_{DO}K_W}{\gamma_{DO}}\right)}{K_a^{N1}+10^{-pD}}\right] \quad \text{(A2)}$$

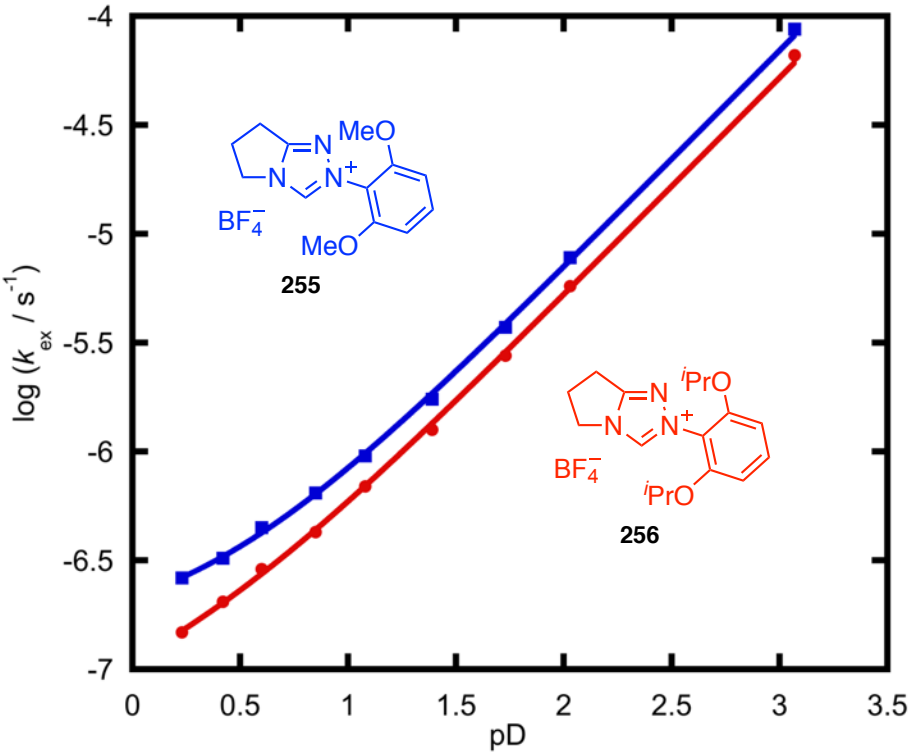

Figure 104: pD – log k_{ex} profile for C(3)-H/D exchange for N-2,6-dimethoxyphenyl 255 (■) and N-2,6-diisopropoxyphenyl 256 (●) triazolium salts, which allows for additional pathways for C(3)-H/D exchange according to kinetically indistinguishable Eqn. (A1) and (A2).

DFT dihedral calculations

Calculations on ylides/carbenes

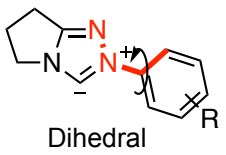

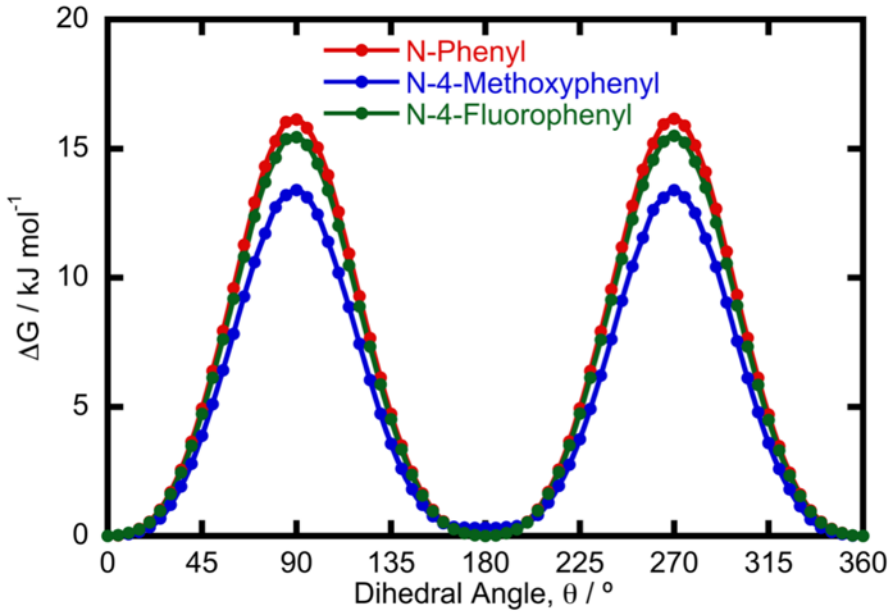

Figure 105: Effect of dihedral angle between N-aryl and triazolium rings on the calculated energy of non-*ortho*-substituted N-aryl ylides/carbenes using B3LYP/6-31(g) and PCM solvent methanol. Points are calculated energies; solid curve is an interpolation between data points.

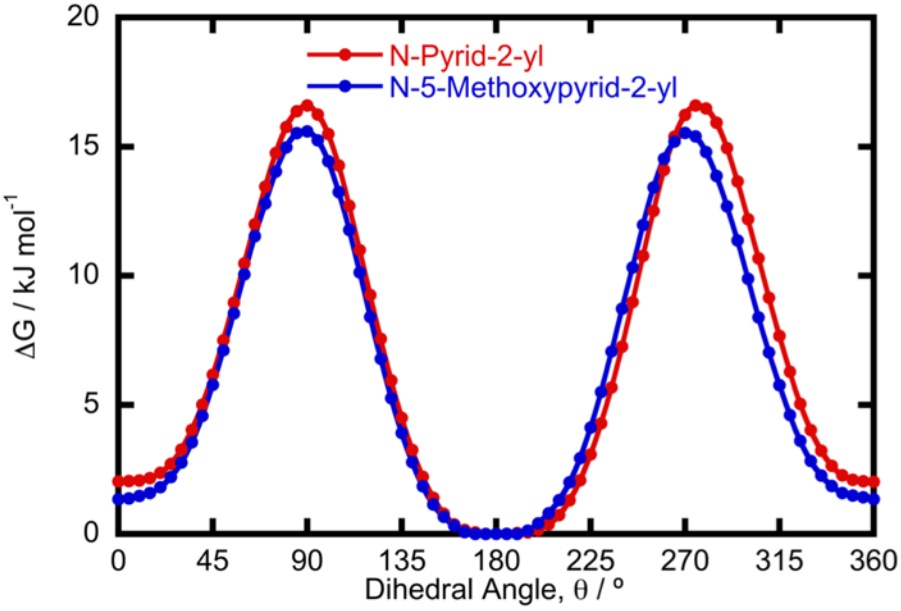

Figure 106: Effect of dihedral angle between N-aryl and triazolium rings on the calculated energy of *ortho*-pyridyl-substituted ylides/carbenes using B3LYP/6-31(g) and PCM solvent methanol. Points are calculated energies; solid curve is an interpolation between data points.

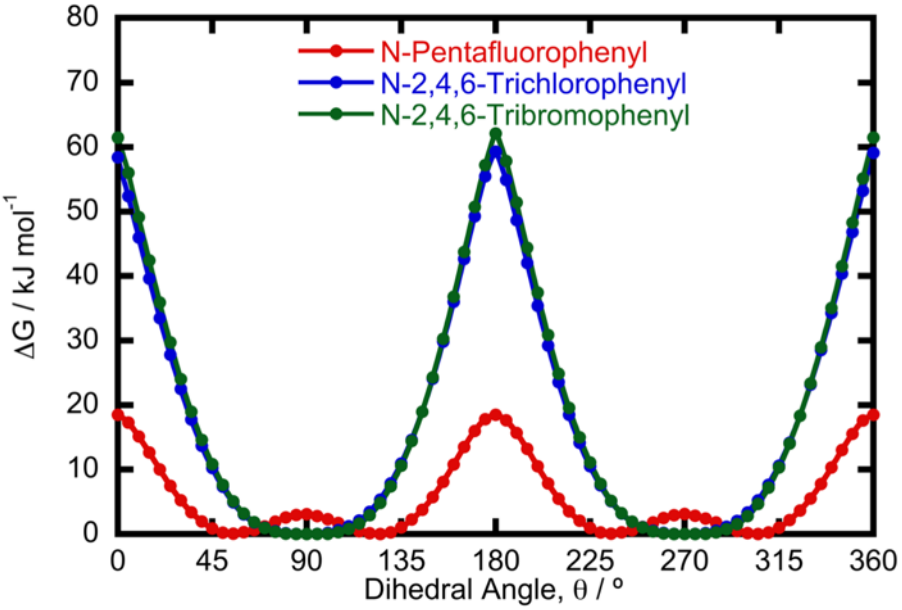

Figure 107: Effect of dihedral angle between N-aryl and triazolium rings on the calculated energy of *ortho*-halo-substituted ylides/carbenes using B3LYP/6-31(g) and PCM solvent methanol. Points are calculated energies; solid curve is an interpolation between data points.

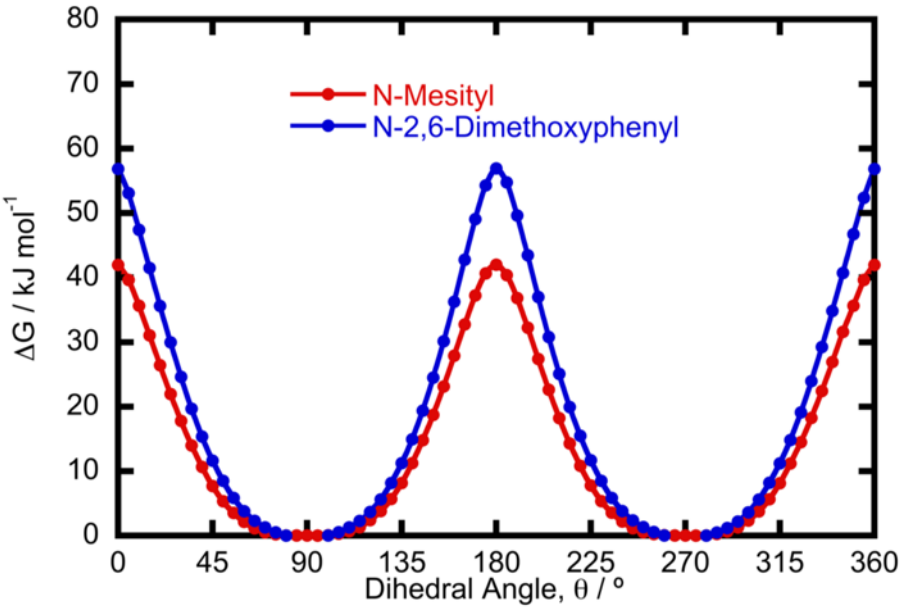

Figure 108: Effect of dihedral angle between N-aryl and triazolium rings on the calculated energy of *ortho*-alkyl and *ortho*-alkoxy-substituted N-aryl triazolium ions using B3LYP/6-31(g) and PCM solvent methanol. Points are calculated energies; solid curve is an interpolation between data points.

Calculations on dications

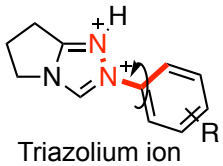

Triazolium ion dication

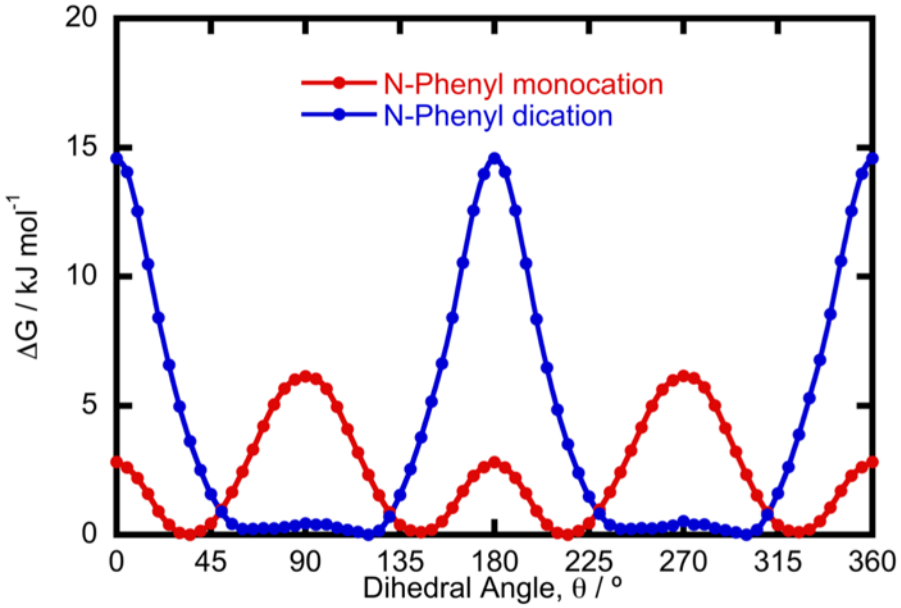

Figure 109: Effect of dihedral angle between N-aryl and triazolium rings on the calculated energy of N-phenyl mono and dicationic triazolium ions using B3LYP/6-31(g) and PCM solvent methanol. Points are calculated energies; solid curve is an interpolation between data points.

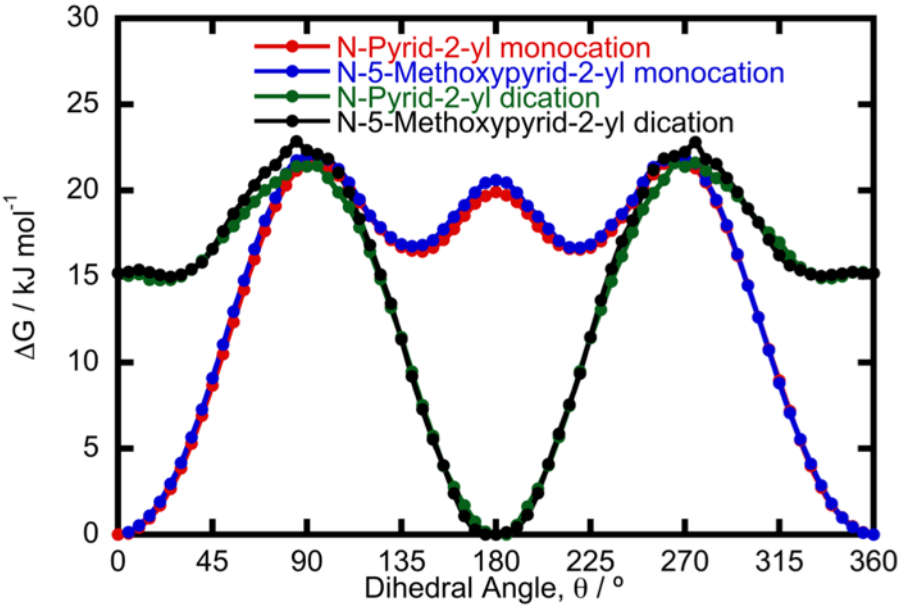

Figure 110: Effect of dihedral angle between N-aryl and triazolium rings on the calculated energy of *ortho*-pyridyl-substituted mono and dicationic N-aryl triazolium ions using B3LYP/6-31(g) and PCM solvent methanol. Points are calculated energies; solid curve is an interpolation between data points.

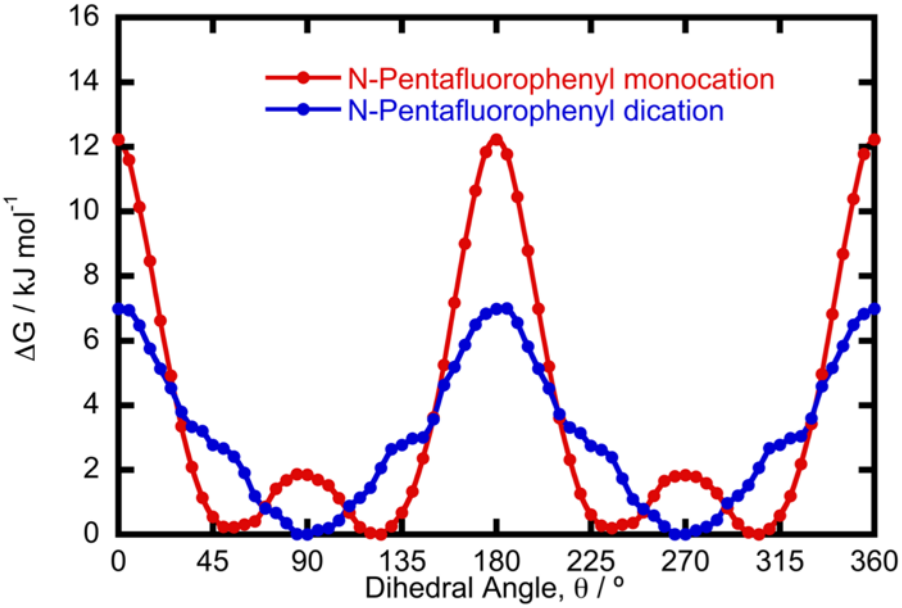

Figure 111: Effect of dihedral angle between N-aryl and triazolium rings on the calculated energy of N-pentafluorphenyl mono and dicationic triazolium ions using B3LYP/6-31(g) and PCM solvent methanol. Points are calculated energies; solid curve is an interpolation between data points.

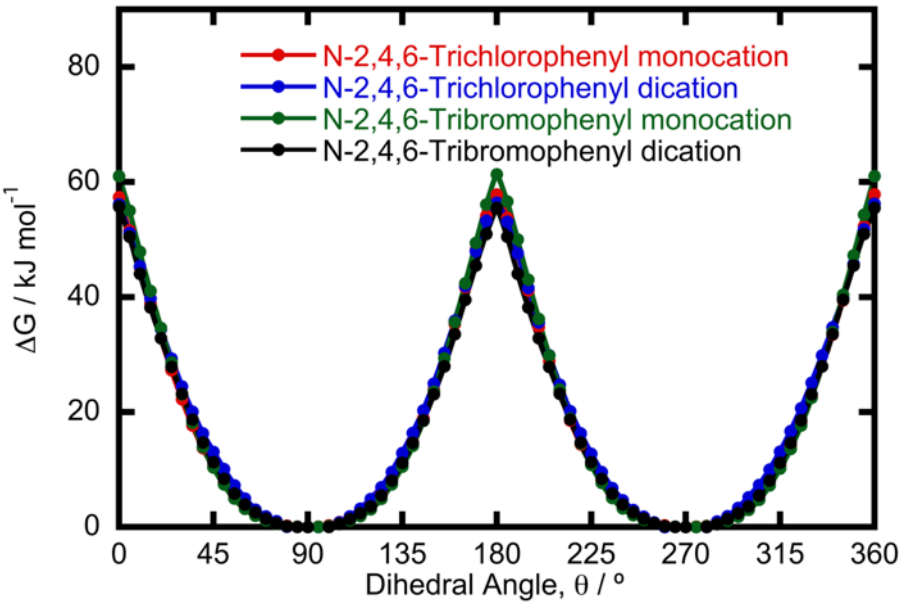

Figure 112: Effect of dihedral angle between N-aryl and triazolium rings on the calculated energy of *ortho*-halo-substituted mono and dicationic N-aryl triazolium ions using B3LYP/6-31(g) and PCM solvent methanol. Points are calculated energies; solid curve is an interpolation between data points.

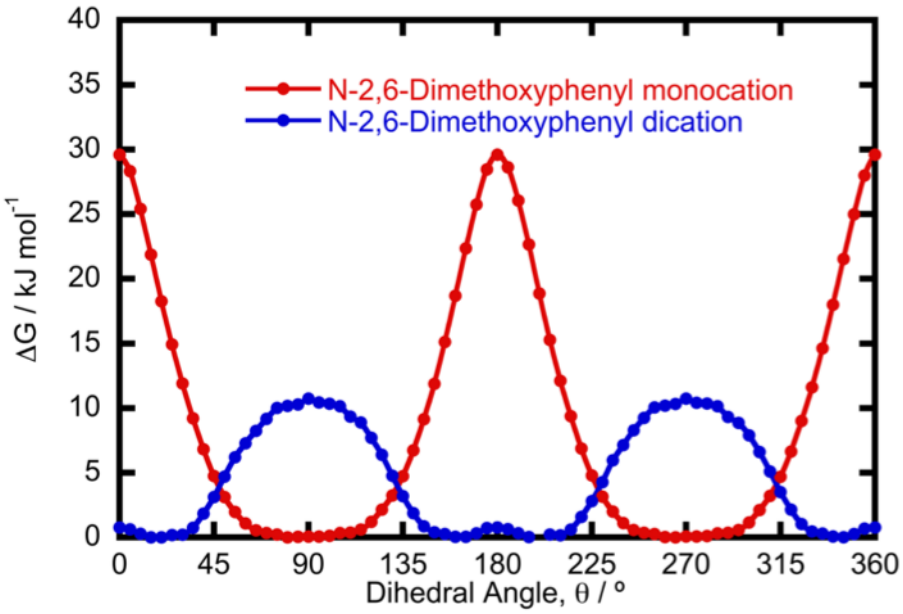

Figure 113: Effect of dihedral angle between N-aryl and triazolium rings on the calculated energy of N-2,6-dimethoxyphenyl mono and dicationic triazolium ions using B3LYP/6-31(g) and PCM solvent methanol. Points are calculated energies; solid curve is an interpolation between data points.

Appendix 2

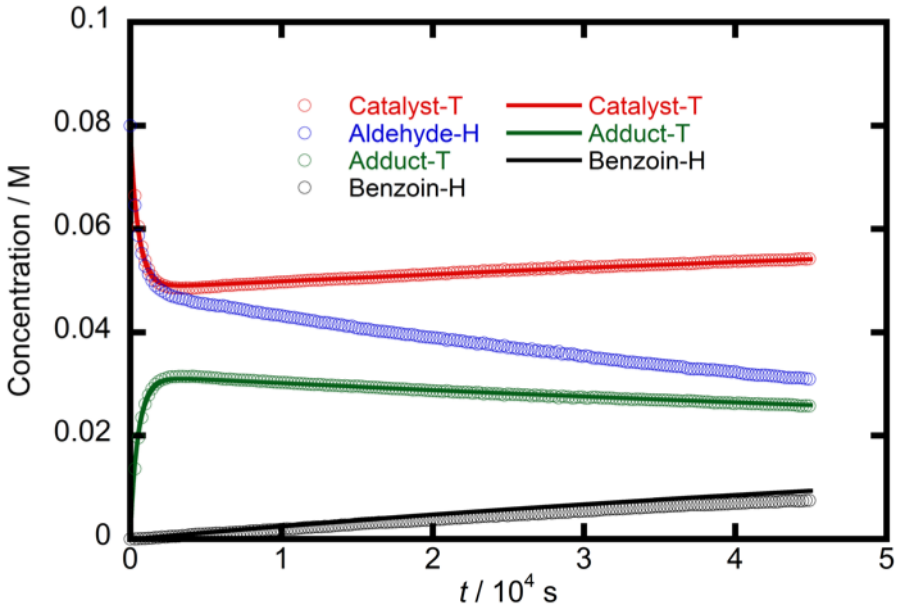

Figure 114: Concentration profile for the reaction between N-phenyl triazolium salt 259 and benzaldehyde 338 at 25 °C in CD_3OD. Open circles represent the total concentrations of triazolium salt (Catalyst-T), aryl aldehyde (Aldehyde-T) and hydroxyaryl adduct (Adduct-T), and the concentration of benzoin with H at the 2-position (Benzoin-H). The solid line is the fitting obtained using Berkeley Madonna.

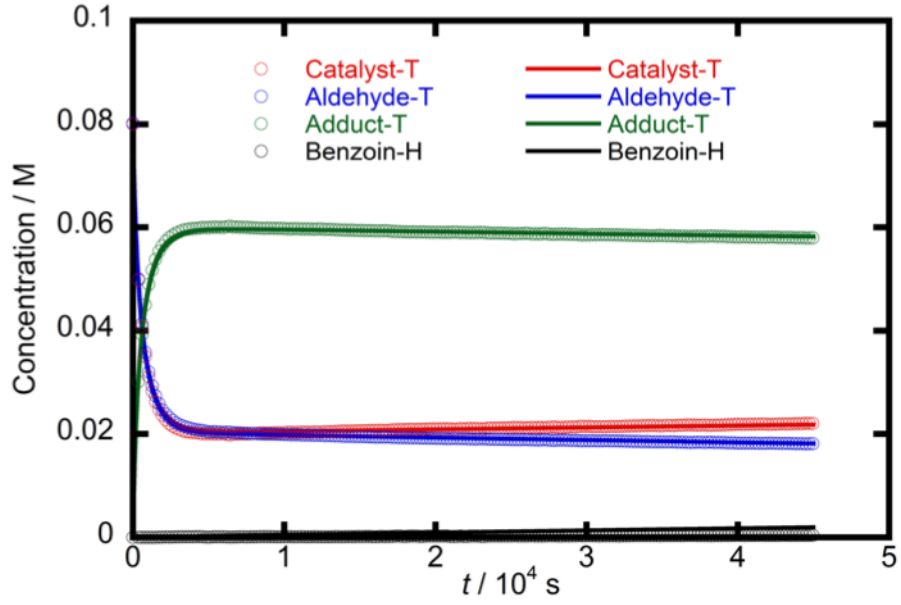

Figure 115: Concentration profile for the reaction between N-phenyl triazolium salt 259 and *ortho*-methoxybenzaldehyde 339 at 25 °C in CD_3OD. Open circles represent the total concentrations of triazolium salt (Catalyst-T), aryl aldehyde (Aldehyde-T) and hydroxyaryl adduct (Adduct-T), and the concentration of benzoin with H at the 2-position (Benzoin-H). The solid line is the fitting obtained using Berkeley Madonna.

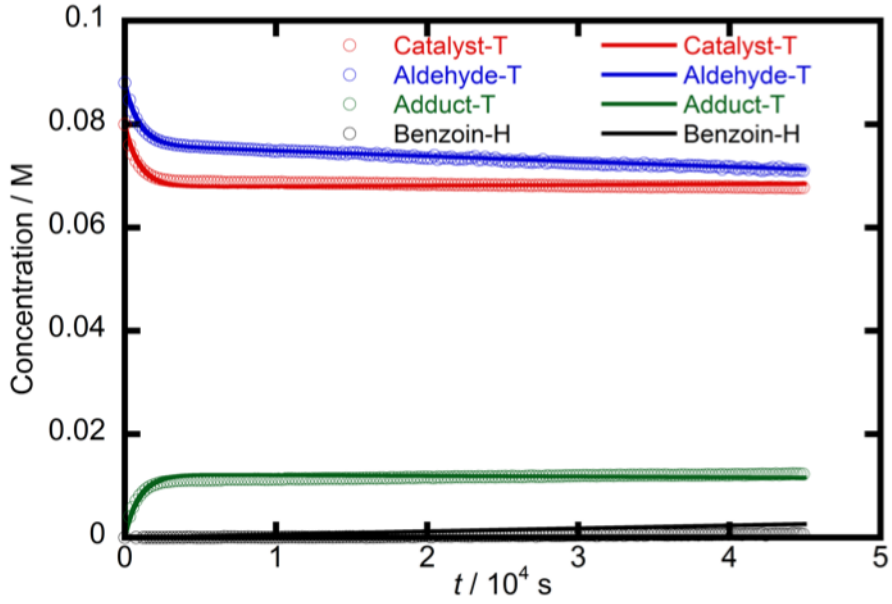

Figure 116: Concentration profile for the reaction between N-phenyl triazolium salt 259 and *para*-methoxybenzaldehyde 340 at 25 °C in CD_3OD. Open circles represent the total concentrations of triazolium salt (Catalyst-T), aryl aldehyde (Aldehyde-T) and hydroxyaryl adduct (Adduct-T), and the concentration of benzoin with H at the 2-position (Benzoin-H). The solid line is the fitting obtained using Berkeley Madonna.

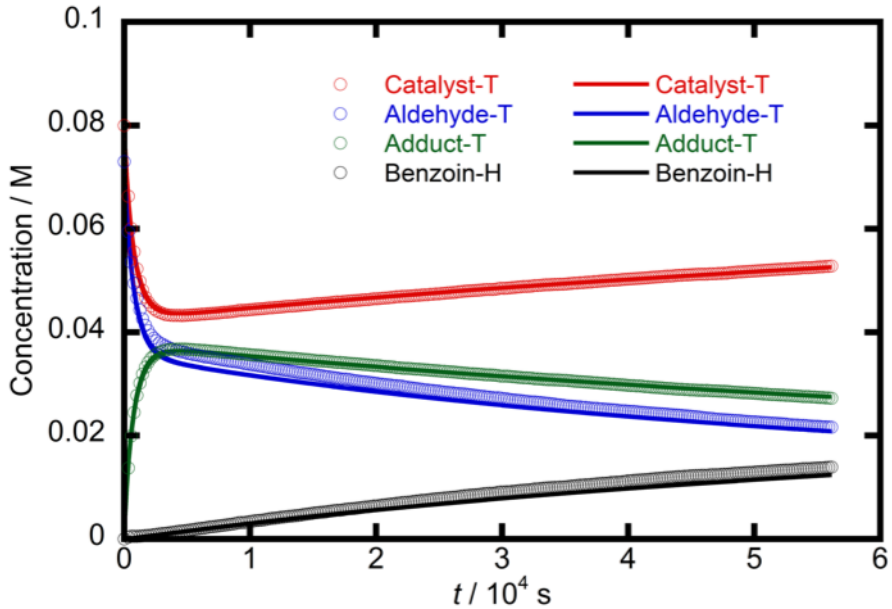

Figure 117: Concentration profile for the reaction between N-4-methoxyphenyl triazolium salt 260 and benzaldehyde 338 at 25 °C in CD_3OD. Open circles represent the total concentrations of triazolium salt (Catalyst-T), aryl aldehyde (Aldehyde-T) and hydroxyaryl adduct (Adduct-T), and the concentration of benzoin with H at the 2-position (Benzoin-H). The solid line is the fitting obtained using Berkeley Madonna.

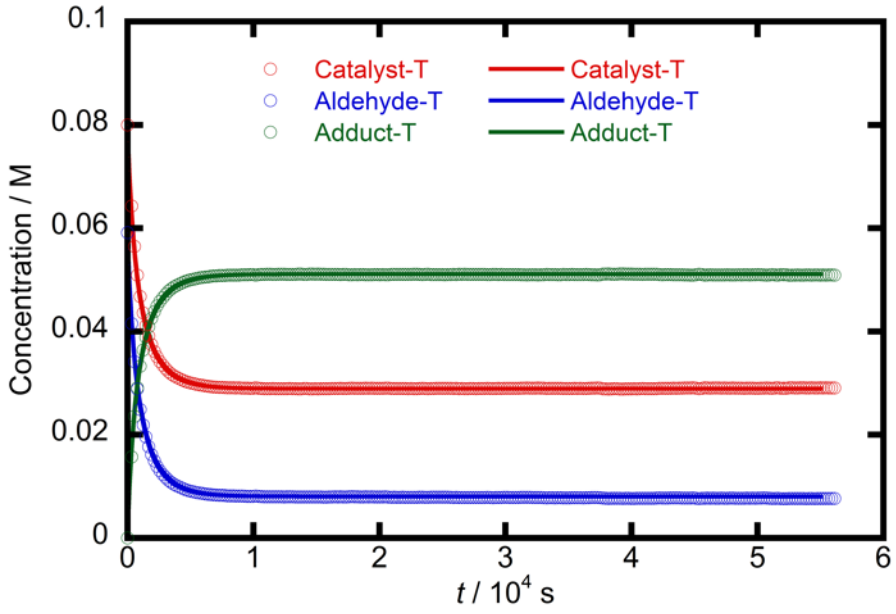

Figure 118: Concentration profile for the reaction between N-4-methoxyphenyl triazolium salt 260 and *ortho*-methoxybenzaldehyde 339 at 25 °C in CD_3OD. Open circles represent the total concentrations of triazolium salt (Catalyst-T), aryl aldehyde (Aldehyde-T) and hydroxyaryl adduct (Adduct-T), and the concentration of benzoin with H at the 2-position (Benzoin-H). The solid line is the fitting obtained using Berkeley Madonna.

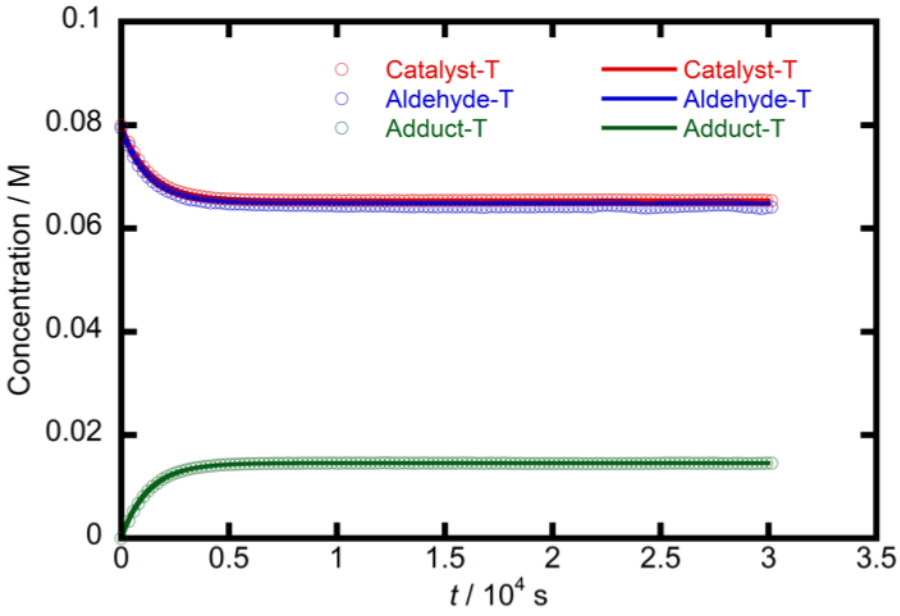

Figure 119: Concentration profile for the reaction between N-4-methoxyphenyl triazolium salt 260 and *para*-methoxybenzaldehyde 340 at 25 °C in CD_3OD. Open circles represent the total concentrations of triazolium salt (Catalyst-T), aryl aldehyde (Aldehyde-T) and hydroxyaryl adduct (Adduct-T), and the concentration of benzoin with H at the 2-position (Benzoin-H). The solid line is the fitting obtained using Berkeley Madonna.

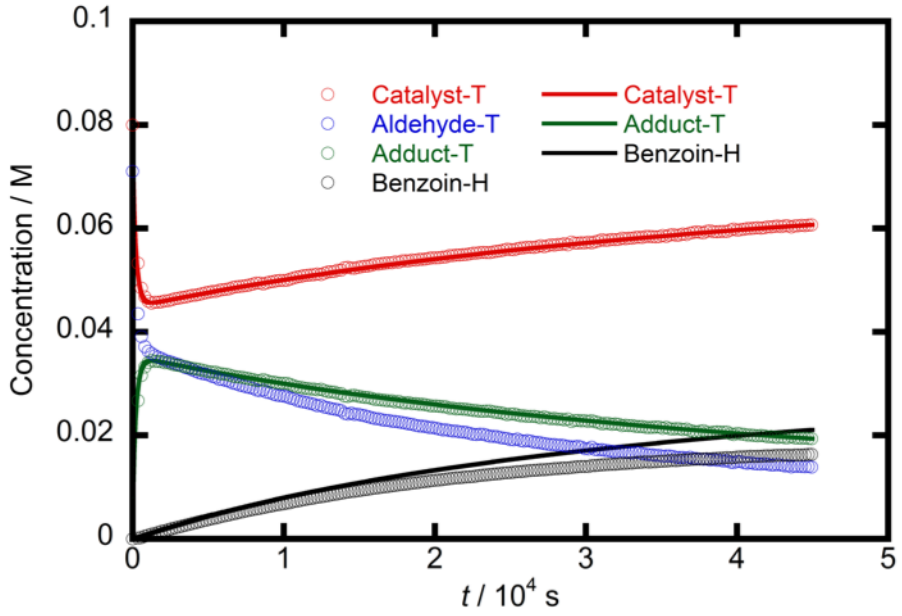

Figure 120: Concentration profile for the reaction between N-4-fluorophenyl triazolium salt 261 and benzaldehyde 338 at 25 °C in CD_3OD. Open circles represent the total concentrations of triazolium salt (Catalyst-T), aryl aldehyde (Aldehyde-T) and hydroxyaryl adduct (Adduct-T), and the concentration of benzoin with H at the 2-position (Benzoin-H). The solid line is the fitting obtained using Berkeley Madonna.

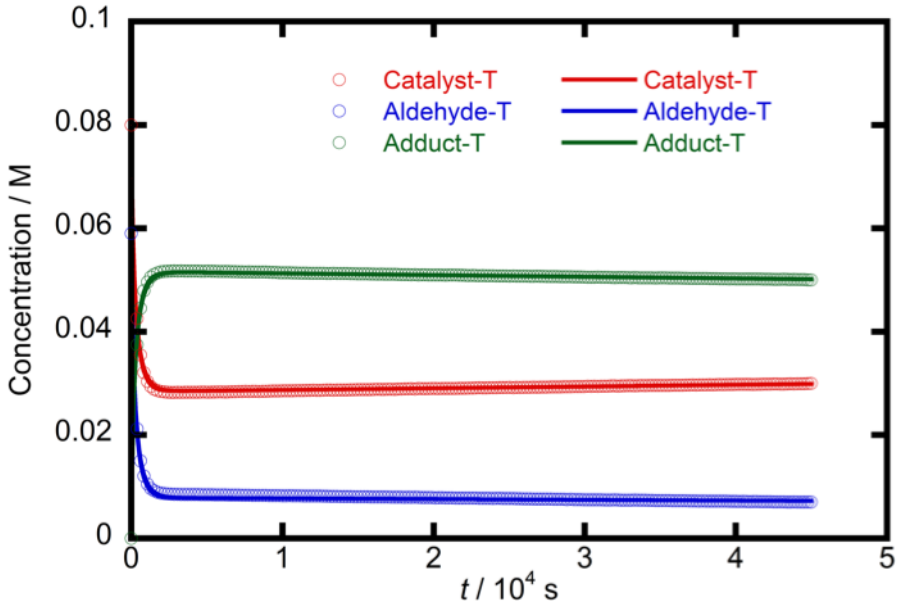

Figure 121: Concentration profile for the reaction between N-4-fluorophenyl triazolium salt 261 and *ortho*-methoxybenzaldehyde 339 at 25 °C in CD_3OD. Open circles represent the total concentrations of triazolium salt (Catalyst-T), aryl aldehyde (Aldehyde-T) and hydroxyaryl adduct (Adduct-T), and the concentration of benzoin with H at the 2-position (Benzoin-H). The solid line is the fitting obtained using Berkeley Madonna.

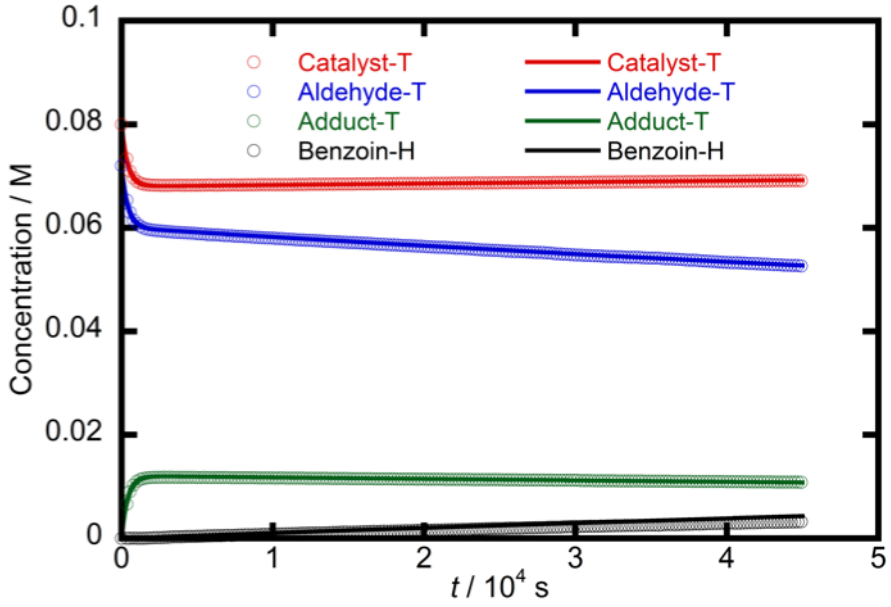

Figure 122: Concentration profile for the reaction between N-4-fluorophenyl triazolium salt 261 and *para*-methoxybenzaldehyde 340 at 25 °C in CD_3OD. Open circles represent the total concentrations of triazolium salt (Catalyst-T), aryl aldehyde (Aldehyde-T) and hydroxyaryl adduct (Adduct-T), and the concentration of benzoin with H at the 2-position (Benzoin-H). The solid line is the fitting obtained using Berkeley Madonna.

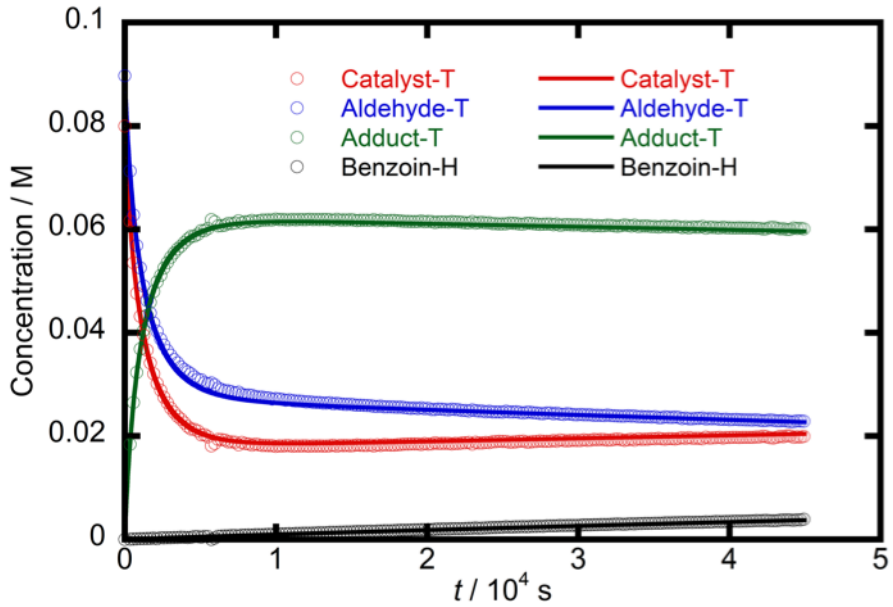

Figure 123: Concentration profile for the reaction between N-mesityl triazolium salt 267 and benzaldehyde 338 at 25 °C in CD_3OD. Open circles represent the total concentrations of triazolium salt (Catalyst-T), aryl aldehyde (Aldehyde-T) and hydroxyaryl adduct (Adduct-T), and the concentration of benzoin with H at the 2-position (Benzoin-H). The solid line is the fitting obtained using Berkeley Madonna.

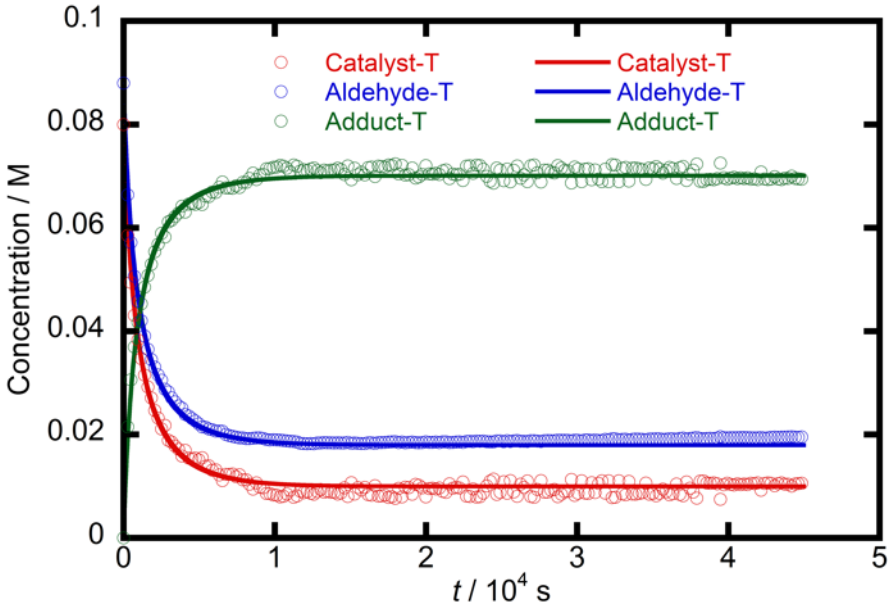

Figure 124: Concentration profile for the reaction between N-mesityl triazolium salt 267 and *ortho*-methoxybenzaldehyde 339 at 25 °C in CD_3OD. Open circles represent the total concentrations of triazolium salt (Catalyst-T), aryl aldehyde (Aldehyde-T) and hydroxyaryl adduct (Adduct-T), and the concentration of benzoin with H at the 2-position (Benzoin-H). The solid line is the fitting obtained using Berkeley Madonna.

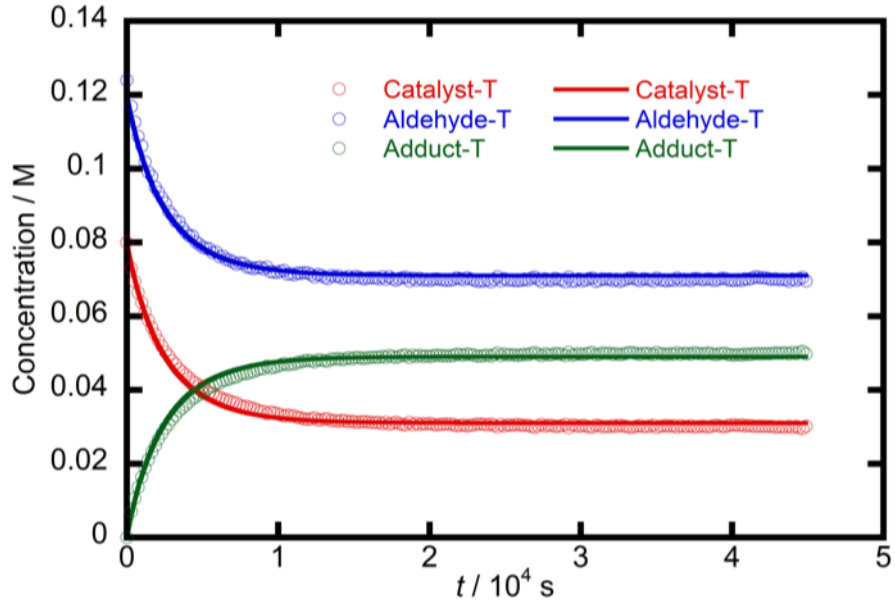

Figure 125: Concentration profile for the reaction between N-mesityl triazolium salt 267 and *para*-methoxybenzaldehyde 340 at 25 °C in CD_3OD. Open circles represent the total concentrations of triazolium salt (Catalyst-T), aryl aldehyde (Aldehyde-T) and hydroxyaryl adduct (Adduct-T), and the concentration of benzoin with H at the 2-position (Benzoin-H). The solid line is the fitting obtained using Berkeley Madonna.

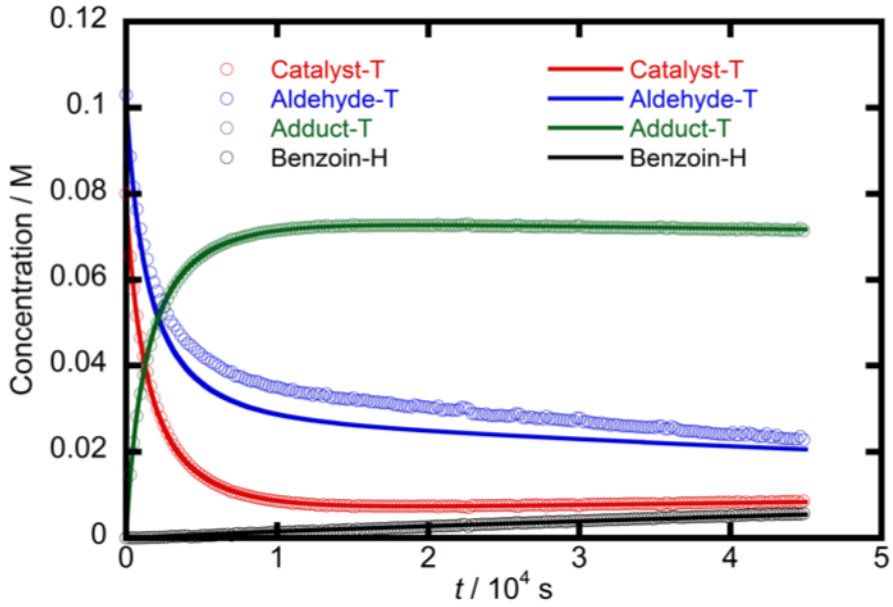

Figure 126: Concentration profile for the reaction between N-2,6-dimethoxyphenyl triazolium salt 255 and benzaldehyde 338 at 25 °C in CD_3OD. Open circles represent the total concentrations of triazolium salt (Catalyst-T), aryl aldehyde (Aldehyde-T) and hydroxyaryl adduct (Adduct-T), and the concentration of benzoin with H at the 2-position (Benzoin-H). The solid line is the fitting obtained using Berkeley Madonna.

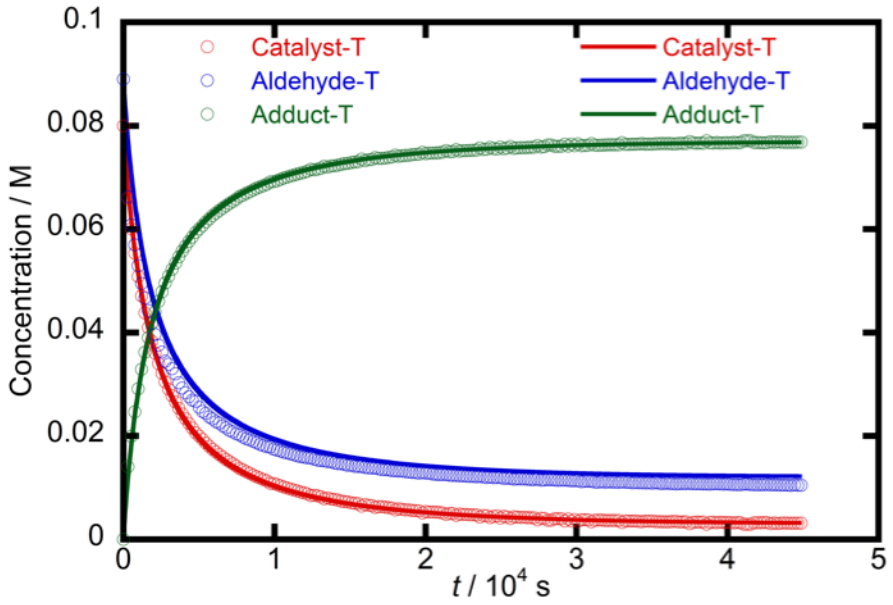

Figure 127: Concentration profile for the reaction between N-2,6-dimethoxyphenyl triazolium salt 255 and *ortho*-methoxybenzaldehyde 339 at 25 °C in CD_3OD. Open circles represent the total concentrations of triazolium salt (Catalyst-T), aryl aldehyde (Aldehyde-T) and hydroxyaryl adduct (Adduct-T), and the concentration of benzoin with H at the 2-position (Benzoin-H). The solid line is the fitting obtained using Berkeley Madonna.

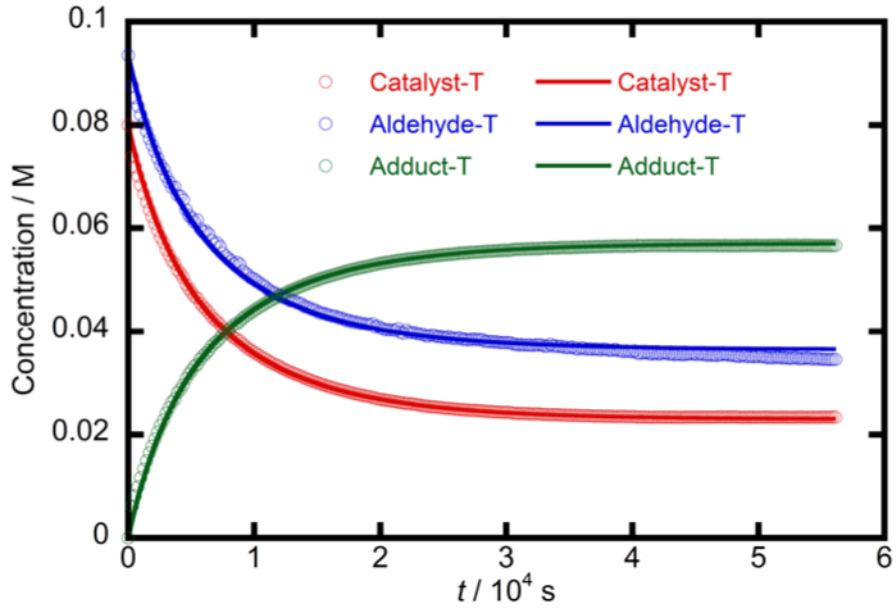

Figure 128: Concentration profile for the reaction between N-2,6-dimethoxyphenyl triazolium salt 255 and *para*-methoxybenzaldehyde 340 at 25 °C in CD_3OD. Open circles represent the total concentrations of triazolium salt (Catalyst-T), aryl aldehyde (Aldehyde-T) and hydroxyaryl adduct (Adduct-T), and the concentration of benzoin with H at the 2-position (Benzoin-H). The solid line is the fitting obtained using Berkeley Madonna.

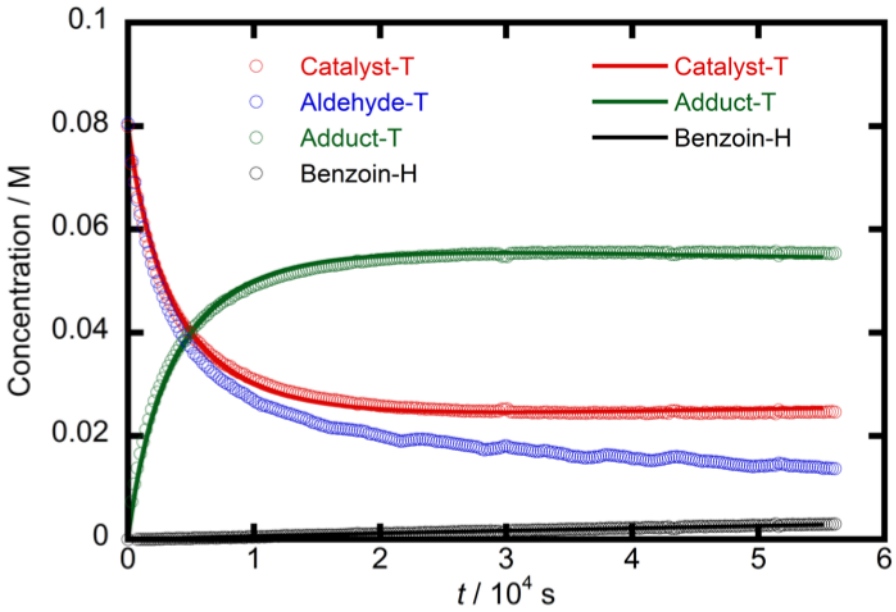

Figure 129: Concentration profile for the reaction between N-2,6-diisopropoxyphenyl triazolium salt 256 and benzaldehyde 338 at 25 °C in CD_3OD. Open circles represent the total concentrations of triazolium salt (Catalyst-T), aryl aldehyde (Aldehyde-T) and hydroxyaryl adduct (Adduct-T), and the concentration of benzoin with H at the 2-position (Benzoin-H). The solid line is the fitting obtained using Berkeley Madonna.

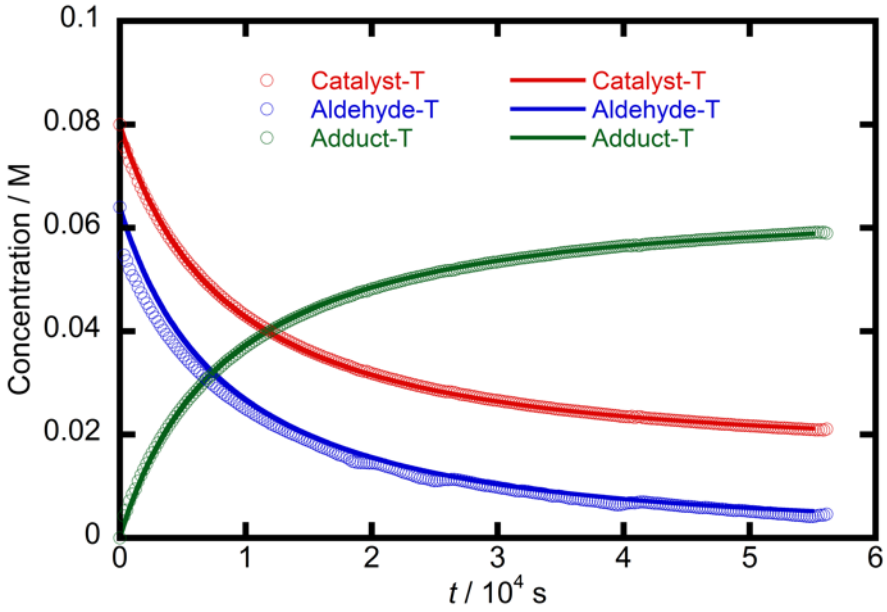

Figure 130: Concentration profile for the reaction between N-2,6-diisopropoxyphenyl triazolium salt 256 and *ortho*-methoxybenzaldehyde 339 at 25 °C in CD_3OD. Open circles represent the total concentrations of triazolium salt (Catalyst-T), aryl aldehyde (Aldehyde-T) and hydroxyaryl adduct (Adduct-T), and the concentration of benzoin with H at the 2-position (Benzoin-H). The solid line is the fitting obtained using Berkeley Madonna.

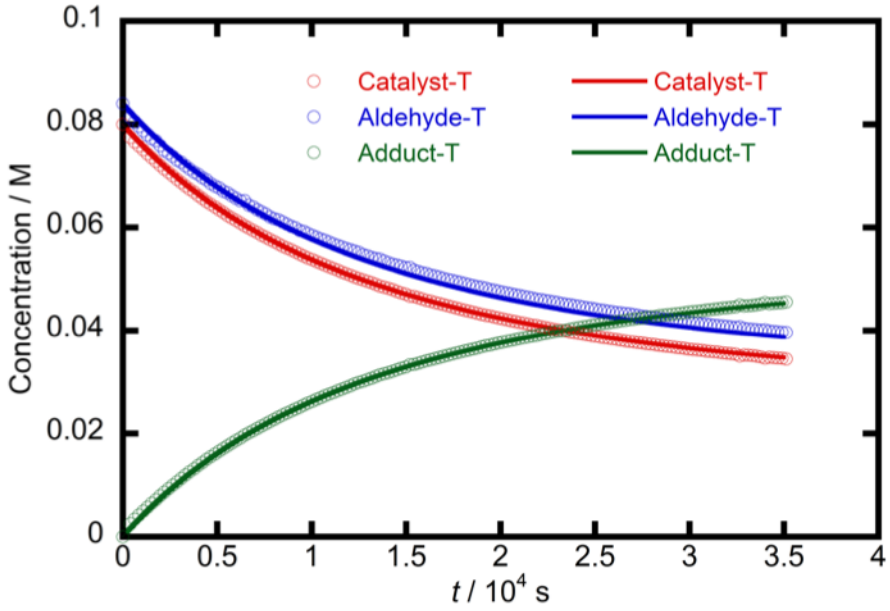

Figure 131: Concentration profile for the reaction between N-2,6-diisopropoxyphenyl triazolium salt 256 and *para*-methoxybenzaldehyde 340 at 25 °C in CD_3OD. Open circles represent the total concentrations of triazolium salt (Catalyst-T), aryl aldehyde (Aldehyde-T) and hydroxyaryl adduct (Adduct-T), and the concentration of benzoin with H at the 2-position (Benzoin-H). The solid line is the fitting obtained using Berkeley Madonna.

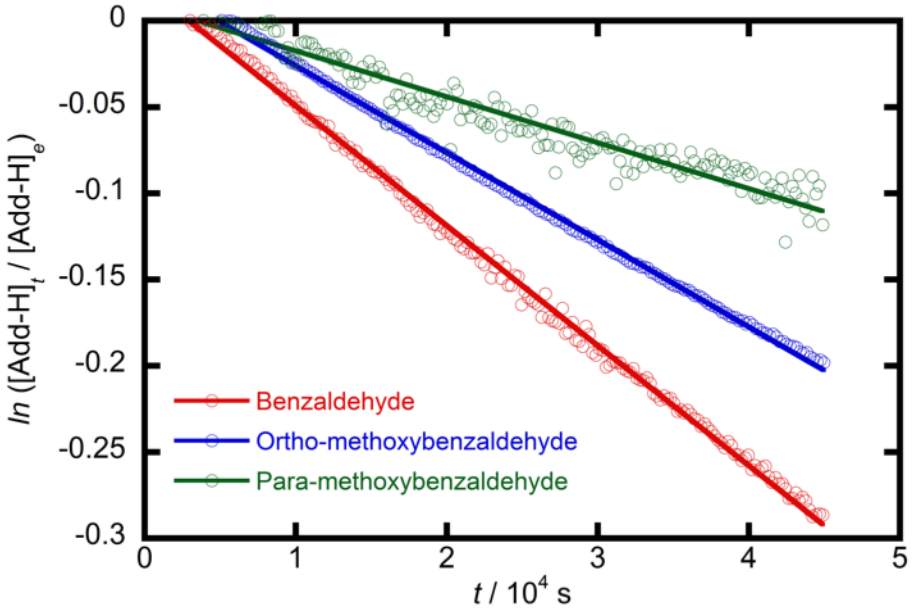

Figure 132: Determination of k_2 values for N-phenyl triazolium 259 from the slope of a semi-logarithmic plot of the concentration of the C(α)-H signal at time *t*, relative to the integral of this signal at its largest value, at or near to equilibrium.

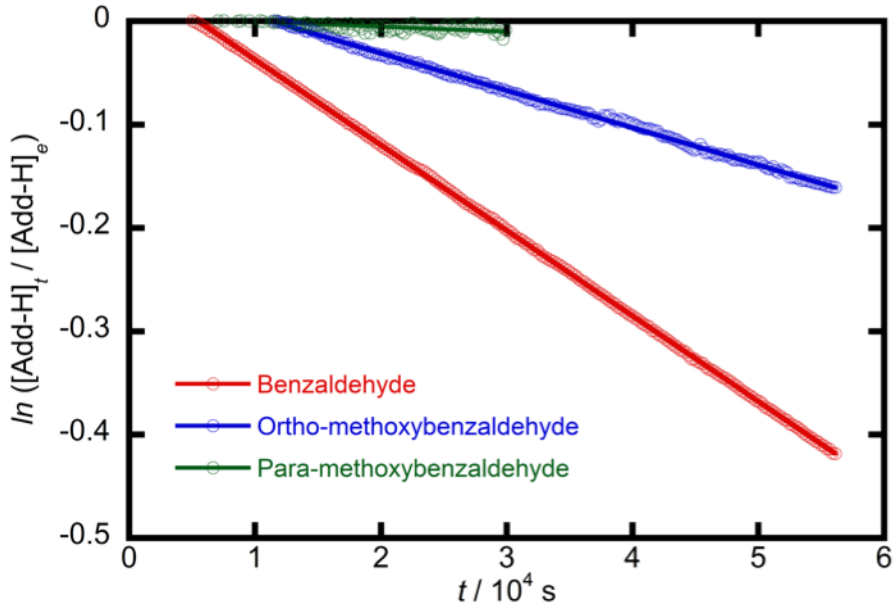

Figure 133: Determination of k_2 values for N-4-methoxyphenyl triazolium 260 from the slope of a semi-logarithmic plot of the concentration of the C(α)-H signal at time *t*, relative to the integral of this signal at its largest value, at or near to equilibrium.

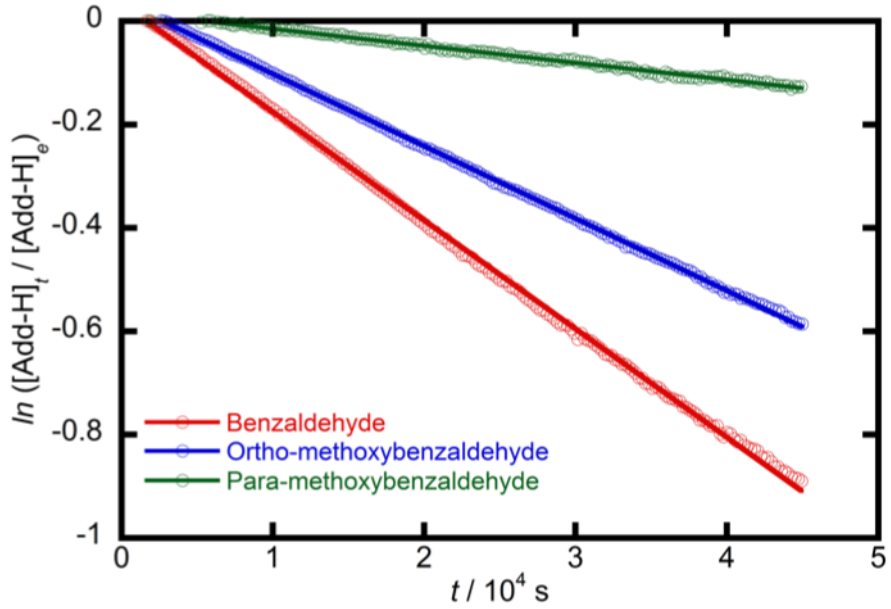

Figure 134: Determination of k_2 values for N-4-fluorophenyl triazolium 261 from the slope of a semi-logarithmic plot of the concentration of the C(α)-H signal at time *t*, relative to the integral of this signal at its largest value, at or near to equilibrium.

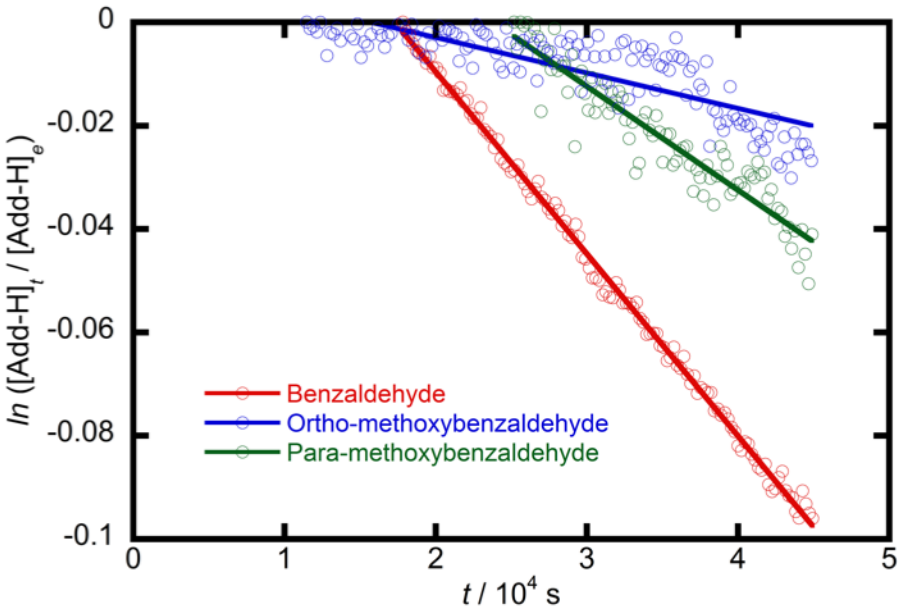

Figure 135: Determination of k_2 values for N-mesityl triazolium 267 from the slope of a semi-logarithmic plot of the concentration of the C(α)-H signal at time *t*, relative to the integral of this signal at its largest value, at or near to equilibrium.

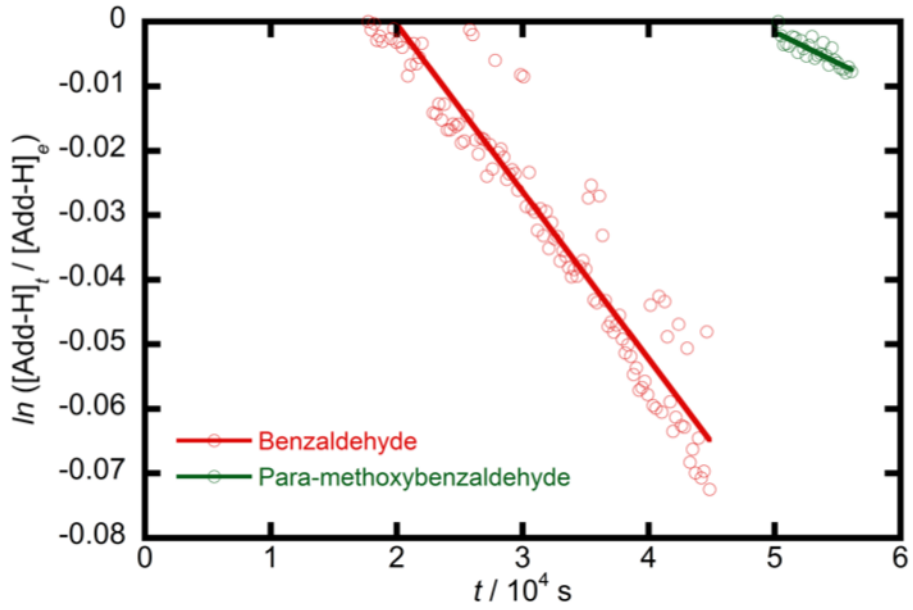

Figure 136: Determination of k_2 values for N-2,6-dimethoxyphenyl triazolium 255 from the slope of a semi-logarithmic plot of the concentration of the C(α)-H signal at time *t*, relative to the integral of this signal at its largest value, at or near to equilibrium.

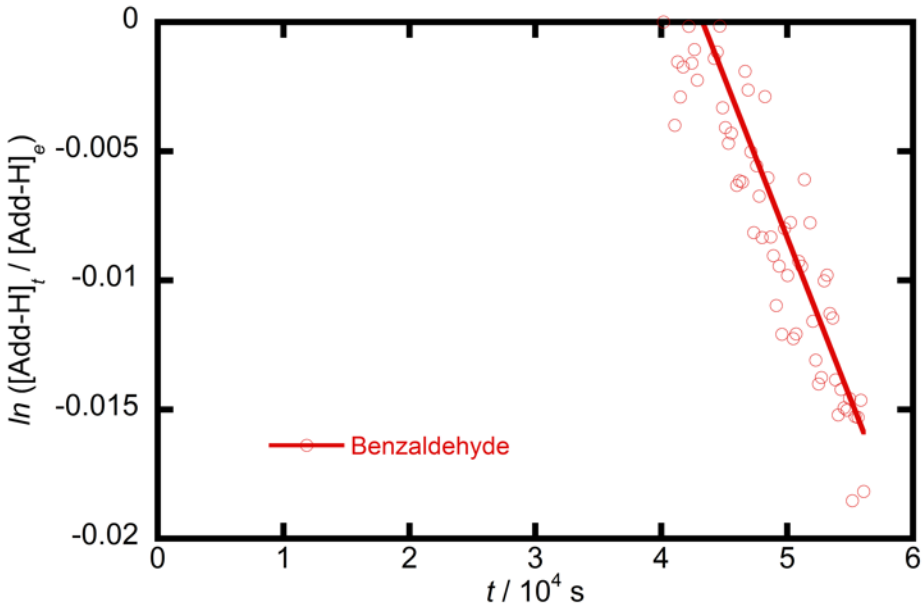

Figure 137: Determination of k_2 values for N-2,6-diisopropoxyphenyl triazolium 256 from the slope of a semi-logarithmic plot of the concentration of the C(α)-H signal at time *t*, relative to the integral of this signal at its largest value, at or near to equilibrium.

Appendix 3

C(α)-H/D Exchange rate constants

2-Mesityl-3-(α-methoxy-benzyl)-6,7-dihydro-5H-pyrrolo [2,1-c][1,2,4]triazol-2-ium tetrafluoroborate (366)

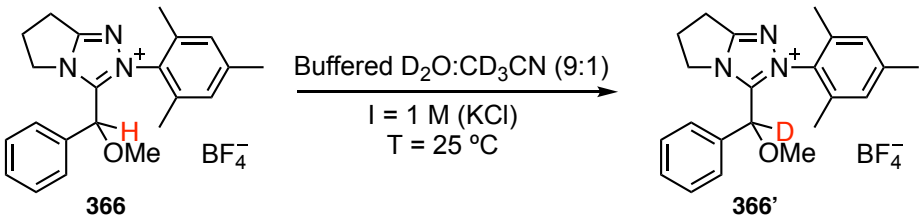

366 366'

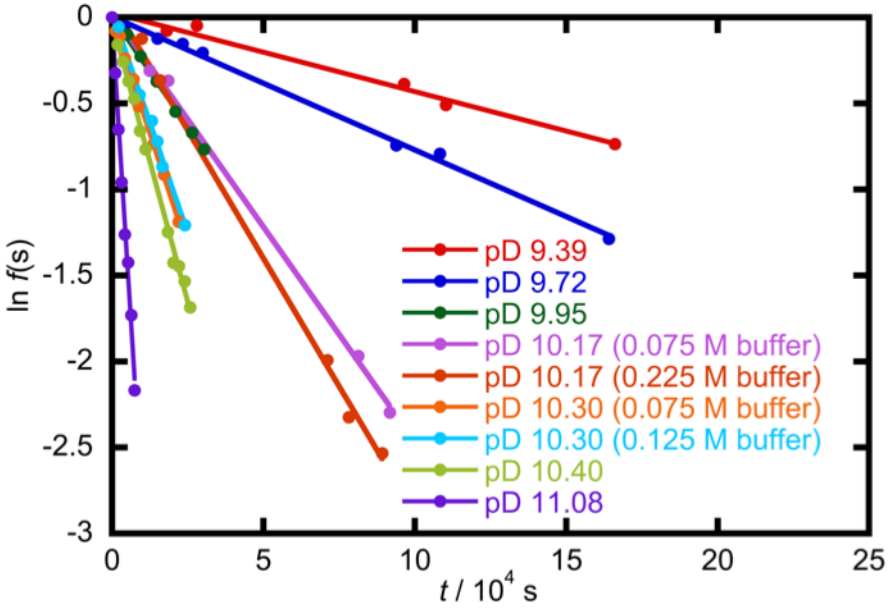

Figure 138: Semi-logarithmic plot of the fraction of unexchanged substrate against time for C(α)-H/D exchange reaction of adduct 366 in at 25 °C in D_2O:CD_3CN (9:1) and I = 1.0 M (KCl) at a range of pDs and buffer concentrations.

Table 27: Reaction data and observed pseudo first-order rate constants for exchange, k_{ex} (s^{-1}), of C(α)-H/D exchange of methylated adduct 366 at a range of pD and buffer concentrations in D_2O:CD_3CN (9:1) at 25 °C and I = 1 M (KCl). General base catalysis of exchange is shown to be weak or insignificant at two pD values.

pD	10^4 [DO] / M	$10^4 k_{ex}$ / s^{-1}
9.39	0.0460	0.046 ± 0.003
9.72	0.0983	0.0774 ± 0.0017
9.95	0.167	0.258 ± 0.005
10.17 (0.075 M buffer)	0.277	0.250 ± 0.006
10.17 (0.225 M buffer)	0.277	0.297 ± 0.009
10.30 (0.075 M buffer)	0.374	0.537 ± 0.010
10.30 (0.125 M buffer)	0.374	0.512 ± 0.016
10.40	0.471	0.651 ± 0.012
11.08	2.25	2.75 ± 0.09

2-Mesityl-3-(α-methoxy-orthomethoxybenzyl)-6,7-dihydro-5H-pyrrolo [2,1-c][1,2,4]triazol-2-ium tetrafluoroborate (367)

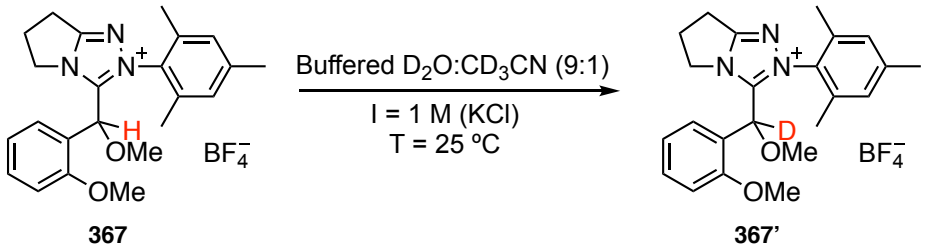

367 **367'**

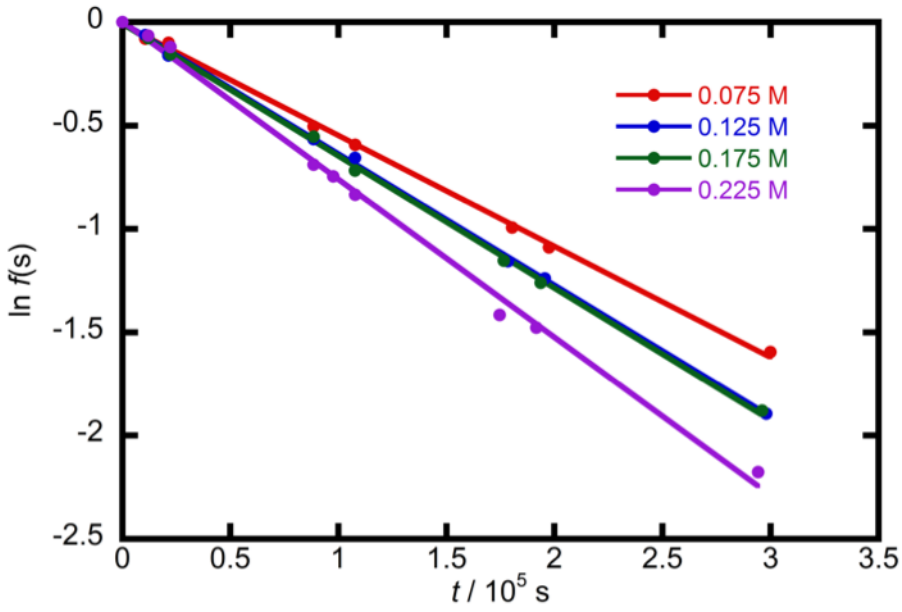

Figure 139: Semi-logarithmic plot of the fraction of unexchanged adduct 367 against time for C(α)-H/D exchange at 25 °C in D_2O:CD_3CN (9:1) at pD 9.95 and I = 1.0 M (KCl).

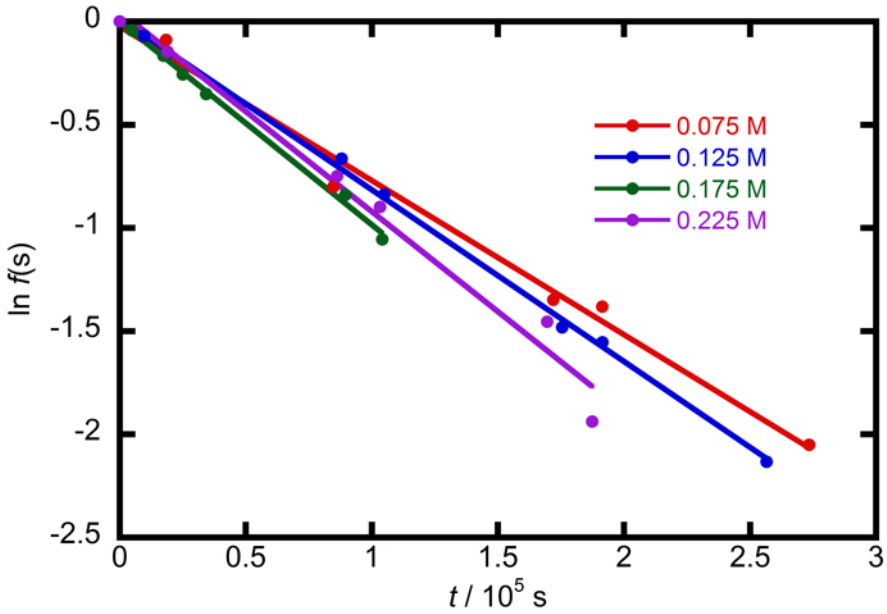

Figure 140: Semi-logarithmic plot of the fraction of unexchanged adduct 367 against time for C(α)-H/D exchange at 25 °C in D_2O:CD_3CN (9:1) at pD 10.17 and I = 1.0 M (KCl).

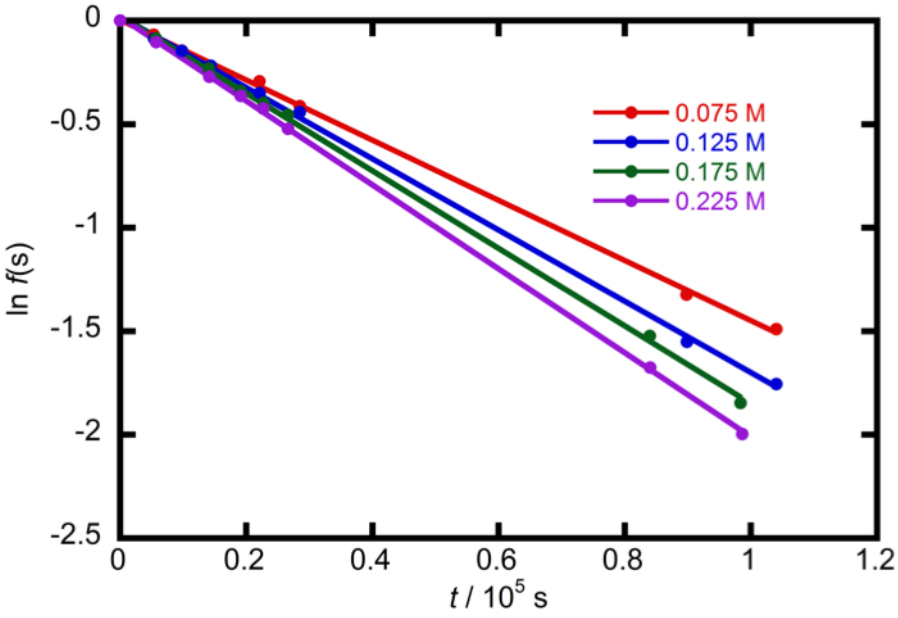

Figure 141: Semi-logarithmic plot of the fraction of unexchanged adduct 367 against time for C(α)-H/D exchange at 25 °C in D_2O:CD_3CN (9:1) at pD 10.40 and I = 1.0 M (KCl).

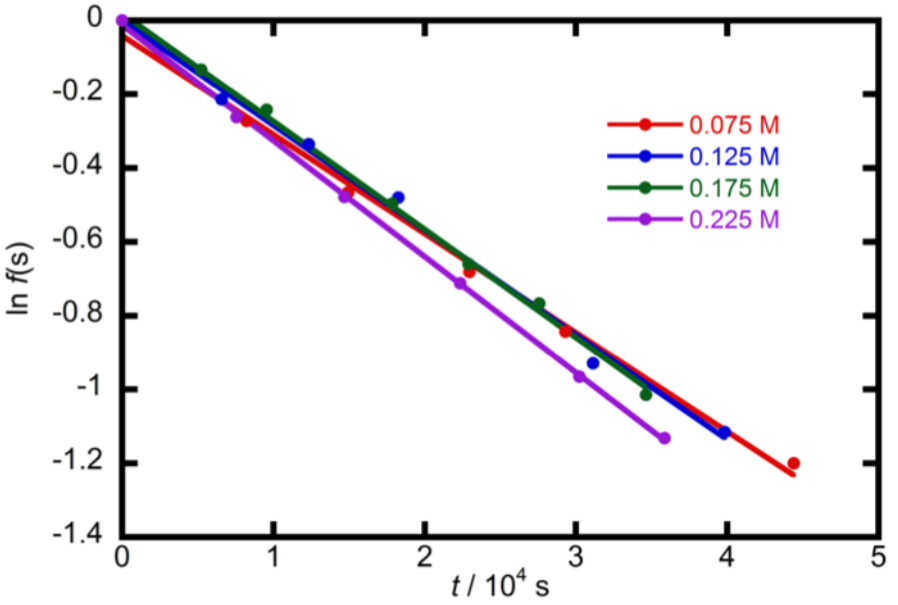

Figure 142: Semi-logarithmic plot of the fraction of unexchanged adduct 367 against time for C(α)-H/D exchange at 25 °C in D_2O:CD_3CN (9:1) at pD 10.68 and I = 1.0 M (KCl).

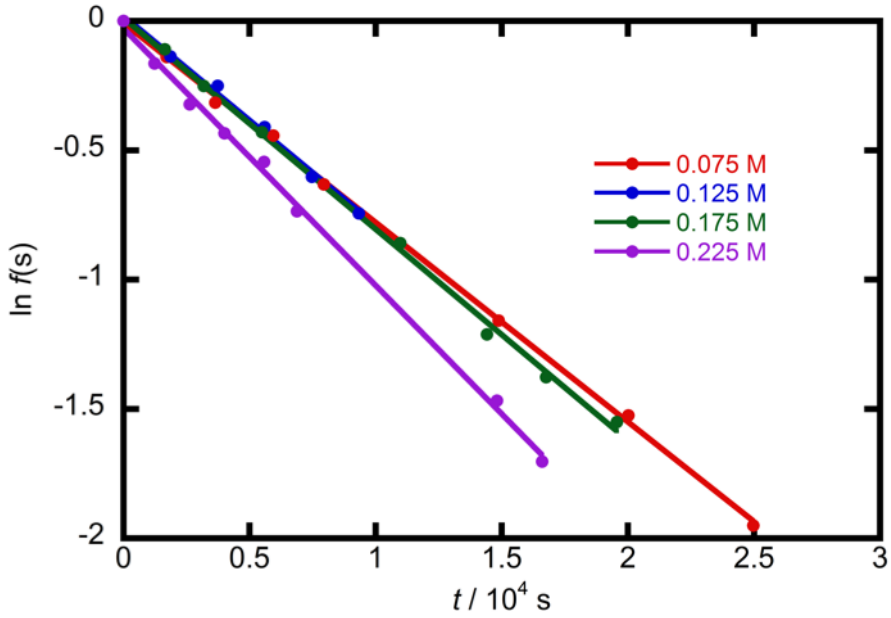

Figure 143: Semi-logarithmic plot of the fraction of unexchanged adduct 367 against time for C(α)-H/D exchange at 25 °C in D_2O:CD_3CN (9:1) at pD 11.08 and I = 1.0 M (KCl).

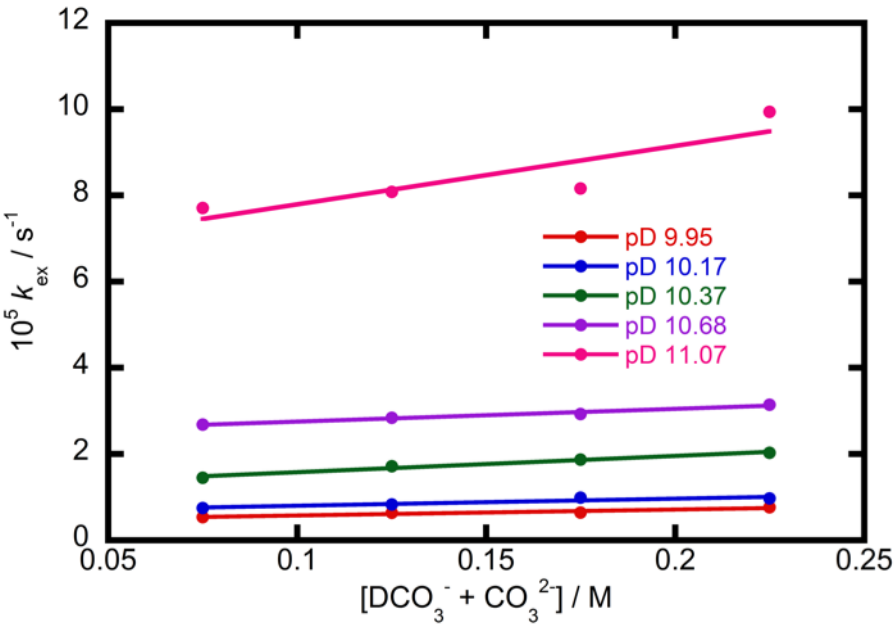

Figure 144: Buffer plot for methylated adduct 367 demonstrating weak GBC of C(α)-H/D exchange at 25 °C in D_2O:CD_3CN (9:1) and I = 1.0 M (KCl).

Table 28: Reaction data and observed pseudo first-order rate constants for exchange, k_{ex} (s^{-1}), of C(α)-H/D exchange of methylated adduct 367 at a range of pD and buffer concentrations in D_2O:CD_3CN (9:1) at 25 °C and I = 1.0 M (KCl).

pD	10^4 [DO] / M	[DCO_3^- + CO_3^{2-}] / M	10^5 k_{ex} / s^{-1}	10^4 (k_0 + k_{DO}[DO])
9.95	0.167	0.075	0.536 ± 0.007	0.044 ± 0.005
		0.125	0.635 ± 0.007	
		0.175	0.639 ± 0.007	
		0.225	0.764 ± 0.017	
10.17	0.277	0.075	0.75 ± 0.04	0.064 ± 0.007
		0.125	0.832 ± 0.012	
		0.175	0.985 ± 0.02	
		0.225	0.97 ± 0.07	
10.40	0.471	0.075	1.452 ± 0.016	0.120 ± 0.006
		0.125	1.720 ± 0.019	
		0.175	1.87 ± 0.02	
		0.225	2.027 ± 0.014	
10.68	0.897	0.075	2.68 ± 0.09	0.246 ± 0.005
		0.125	2.84 ± 0.10	
		0.175	2.93 ± 0.06	
		0.225	3.14 ± 0.03	
11.08	2.25	0.075	7.71 ± 0.08	0.64 ± 0.08
		0.125	8.1 ± 0.3	
		0.175	8.16 ± 0.14	
		0.225	9.94 ± 0.19	

2-Mesityl-3-(α-methoxy-orthobromobenzyl)-6,7-dihydro-5H-pyrrolo [2,1-c][1,2,4]triazol-2-ium tetrafluoroborate (368)

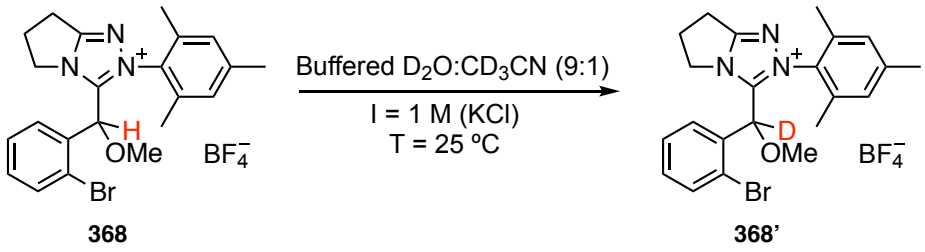

368 **368'**

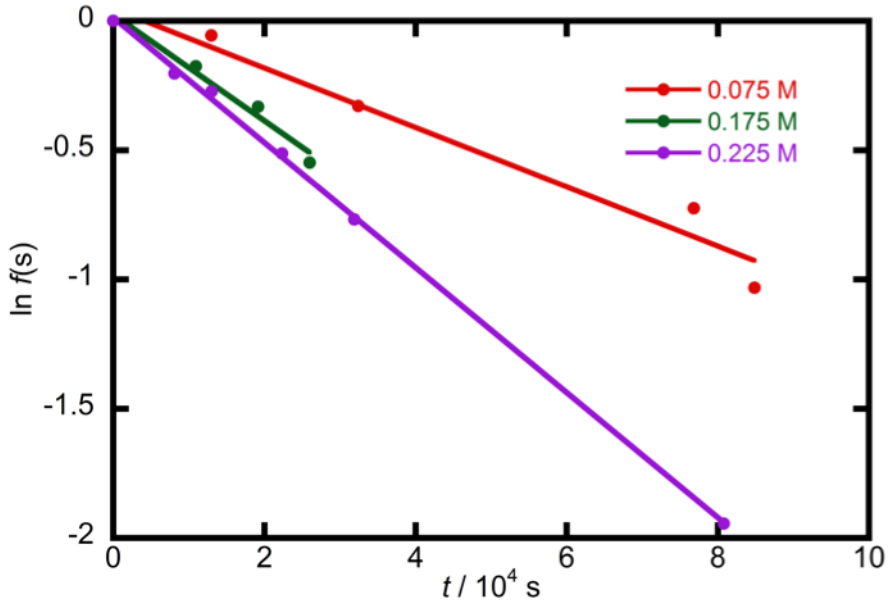

Figure 145: Semi-logarithmic plot of the fraction of unexchanged adduct 368 against time for C(α)-H/D exchange at 25 °C in D_2O:CD_3CN (9:1) at pD 10.17 and I = 1.0 M (KCl).

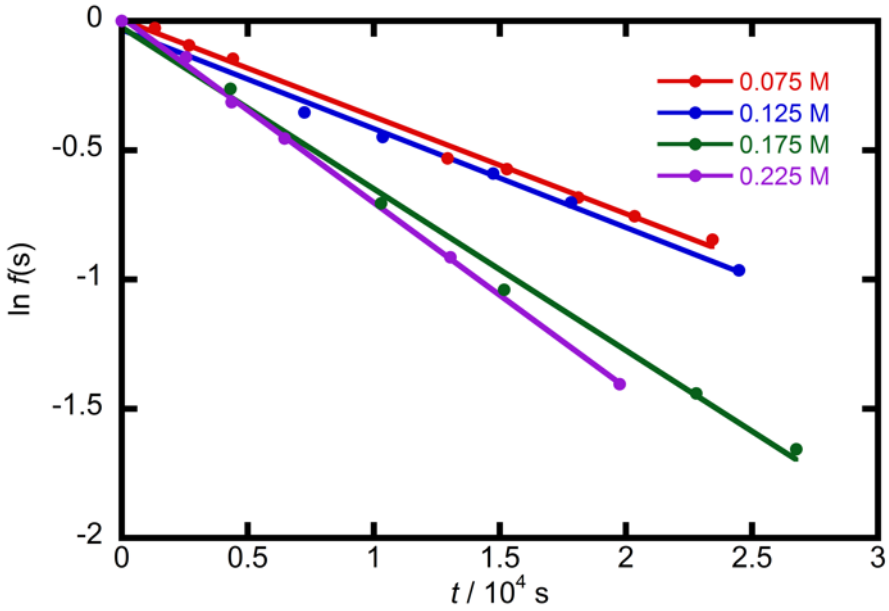

Figure 146: Semi-logarithmic plot of the fraction of unexchanged adduct 368 against time for C(α)-H/D exchange at 25 °C in D_2O:CD_3CN (9:1) at pD 10.68 and I = 1.0 M (KCl).

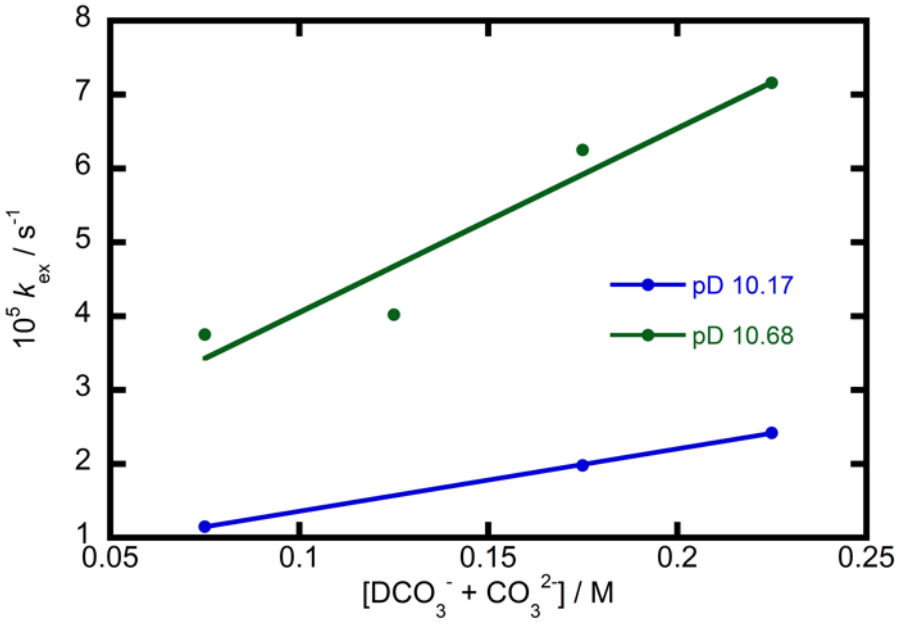

Figure 147: Buffer plot for methylated adduct 368 demonstrating weak GBC of C(α)-H/D exchange at 25 °C in D_2O:CD_3CN (9:1) and I = 1.0 M (KCl).

Table 29: Reaction data and observed pseudo first-order rate constants for exchange, k_{ex} (s^{-1}), of C(α)-H/D exchange of methylated adduct 368 at a range of pD and buffer concentrations in D_2O:CD_3CN (9:1) at 25 °C and I = 1.0 M (KCl).

pD	10^4 [DO] / M	$[DCO_3^- + CO_3^{2-}]$ / M	$10^5\ k_{ex}$ / s^{-1}	$10^4\ (k_0 + k_{DO}[DO])$
10.17	0.277	0.075	1.15 ± 0.13	0.053 ± 0.013
		0.175	2.10 ± 0.2	
		0.225	2.42 ± 0.03	
10.68	0.897	0.075	3.75 ± 0.10	0.16 ± 0.08
		0.125	4.02 ± 0.16	
		0.175	6.3 ± 0.2	
		0.225	7.16 ± 0.11	

Stopped flow deprotonation rate constants

2-Mesityl-3-(α-methoxy-benzyl)-6,7-dihydro-5H-pyrrolo [2,1-c][1,2,4]triazol-2-ium tetrafluoroborate (366)

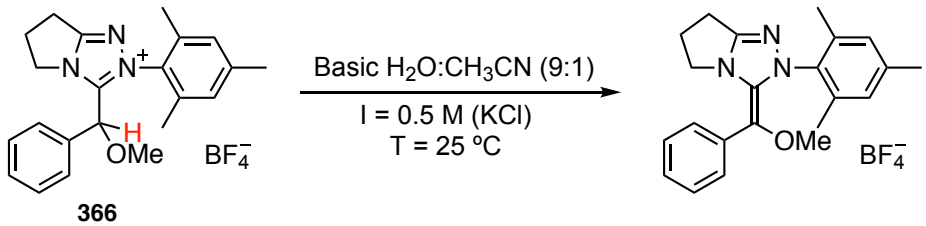

366

Table 30: Reaction data and observed pseudo first-order rate constants for deprotonation of methylated adduct 366 at two hydroxide concentrations in H_2O:CH_3CN (9:1) at 25 °C and I = 0.5 M (KCl).

$[HO^-]$ / M	k_{obs} / s^{-1}
0.050	0.088 ± 0.004
0.375	0.651 ± 0.005

2-Mesityl-3-(α-methoxy-orthomethoxybenzyl)-6,7-dihydro-5H-pyrrolo [2,1-c][1,2,4]triazol-2-ium tetrafluoroborate (367)

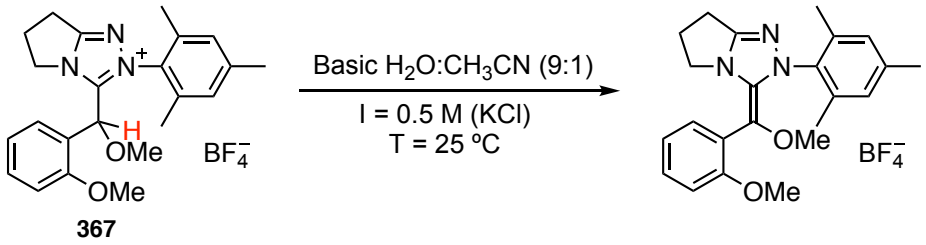

367

Table 31: Reaction data and observed pseudo first-order rate constants for deprotonation of methylated adduct 367 at a range of hydroxide concentrations in H_2O:CH_3CN (9:1) at 25 °C and I = 0.5 M (KCl).

$[HO^-]$ / M	k_{obs} / s^{-1}
0.050	0.01339 ± 0.00008
0.125	0.0558 ± 0.0015
0.250	0.107 ± 0.005
0.500	0.198 ± 0.003

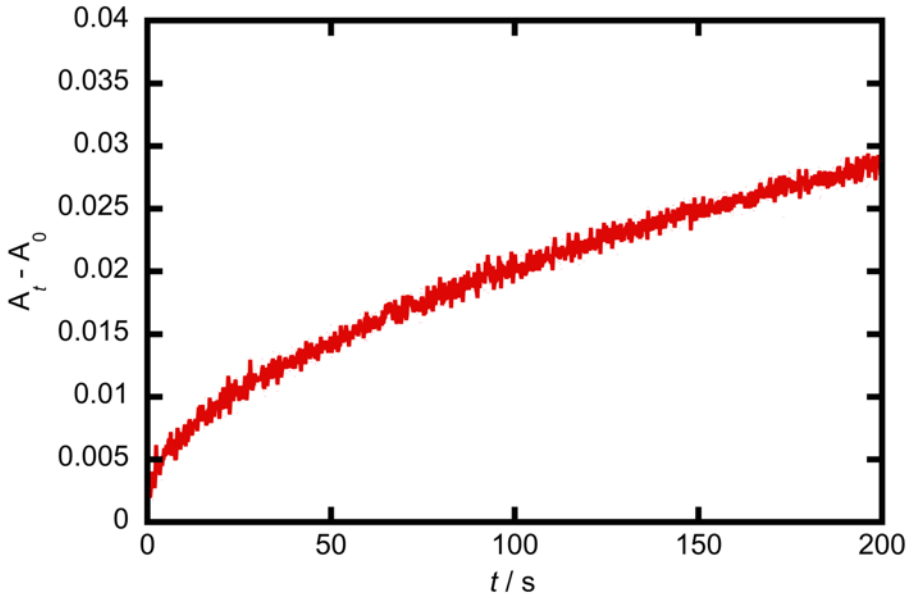

Figure 148: Conventional UV-vis spectrophotometry trace for adduct 366 obtained on a conventional UV-vis spectrophotometer to demonstrate that data obtained by stopped flow spectrophotometry are not instrument artefacts.

Reprotonation kinetics

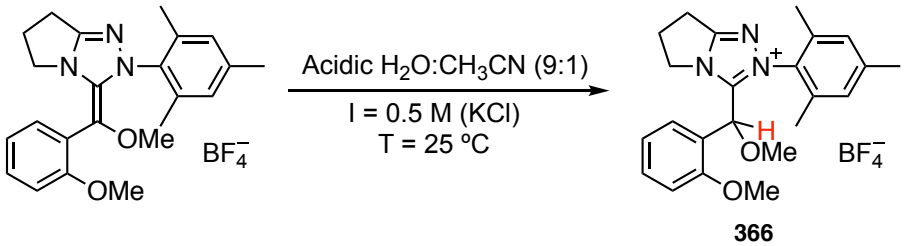

366

Table 32: Reaction data and observed pseudo first-order rate constants for reprotonation of the BI derived from methylated adduct 365 at a range of added hydronium ion concentrations in H_2O:CH_3CN (9:1) at 25 °C and I = 0.5 M (KCl).

$[H_3O^+]$ / M	k_{obs} / s^{-1}
0.075	0.362 ± 0.016
0.100	0.407 ± 0.011
0.125	0.419 ± 0.015
0.150	0.440 ± 0.011
0.175	0.45 ± 0.04
0.200	0.47 ± 0.03
0.225	0.49 ± 0.03

References

1 A. Iglau, H. Grutzmache, A. Baceiredo and G. Bertrand, *J. Am. Chem. Soc.*, 1988, **110**, 6463.
2 A. J. Arduengo, R. L. Harlow and M. Kline, *J. Am. Chem. Soc*., 1991, **113**, 361.
3 D. Bourissou, O. Guerret, F. P. Gabbai and G. Bertrand, *Chem. Rev*., 2000, **100**, 39.
4 (a) D. M. Flanigan, F. Romanov-Michailidis, N. A. White and T. Rovis, *Chem. Rev*., 2015, **115**, 9307; (b) D. J. Nelson and S. P. Nolan, *Chem. Soc. Rev*., 2013, **42**, 6723; (c) D. Enders, O. Niemeier and A. Henseler, *Chem. Rev.,* 2007, **107**, 5606
5 F. Wöhler and J. Liebig, *Ann. Pharm*., 1832, **3**, 249.
6 A. Lapworth, *J. Chem. Soc., Trans*., 1903, **83**, 995.
7 T. Ukai, R. Tanaka and T. Dokawa*, J. Pharm. Soc. Jpn*., 1943, **63**, 296.
8 R. Breslow, *J. Am. Chem. Soc.*, 1958, **80**, 3719.
9 J. Sheehan and D. H. Hunneman, *J. Am. Chem. Soc*., 1966, **88**, 3666.
10 J. C. Sheehan and T. Hara, *J. Org. Chem*., 1974, **39**, 1196.
11 D. Enders, K. Breuer, J. H. Teles, *Helv. Chim. Acta*., 1996, **79**, 1217.
12 R. L. Knight and F. J. Leeper, *Tetrahedron. Lett*., 1997, **38**, 3611.
13 R. L. Knight and F. J. Leeper, *J. Chem. Soc., Perkin Trans.*, 1998, 1891.
14 D. Enders and U. Kallfass, *Angew. Chem. Int. Ed*., 2002, **41**, 1743.
15 L. Baragwanath, C. A. Rose, K. Zeitler and S. J. Connon, *J. Org. Chem*., 2009, **74**, 9214.
16 T. Soeta, Y. Tabatake, K. Inomata and Y. Ukaji, *Tetrahedron*, 2012, **68**, 894.
17 S. E. O'Toole, C. A. Rose, S. Gundala, K. Zeitler and S. J. Connon, *J. Org. Chem.*, 2011, **76**, 347.
18 I. Piel, M. D. Pawelczyk, K. Hirano, R. Fröhlich and F. Glorius, *Eur. J. Org. Chem.*, 2011, 5475.
19 M. Y. Jin, S. M. Kim, H. Han, D. H. Ryu and J. W. Yang, *Org. Lett*., 2011, **13**, 880.
20 M. Y. Jin, S. M. Kim, H. Mao, D. H. Ryu, C. E. Song and J. W. Yang, *Org. Biomol. Chem*., 2014, **12**, 1547.
21 S. M. Langdon, M. M. D. Wilde, K. Thai and M. Gravel, *J. Am. Chem. Soc*., 2014, **136**, 7539.
22 Jiayun Zhu, Unpublished Results.
23 M. Beigi, E. Gauchenova, L. Walter, S. Waltzer, F. Bonina, T. Stillger, D. Rother, M. Pohl and M. Müller, *Chem. Eur. J*., 2016, **22**, 13999.
24 E. G. Delany and S. J. Connon, *Org. Biomol. Chem*., 2018, **16**, 780.
25 C. J. Collett, R. S. Massey, J. E. Taylor, O. R. Maguire, A. C. O'Donoghue and A. D. Smith, *Angew. Chem. Int. Ed.*, 2015, **54**, 6887.
26 H. Stetter, *Angew. Chem., Int. Ed*., 1976, **15**, 639.
27 E. Ciganek, *Synthesis*, 1995, 1311.
28 D. Enders, K. Breuer, J. Runsink, J. H. Teles, *Helv. Chim. Acta*, 1996, **79**, 1899.
29 M. S. Kerr, J. Read de Alaniz and T. Rovis, *J. Am. Chem. Soc*., 2002, **124**, 10298.
30 K. R. Law and C. S. P. McErlean, *Chem. Eur. J*., 2013, **19**, 15852.
31 K. Hirano, A. T. Biju, I. Piel and F. Glorius, *J. Am. Chem. Soc*., 2009, **131**, 14190.
32 M. C. Willis, *Chem. Rev*., 2010, **110**, 725.

33 I. Piel, M. Steinmetz, K. Hirano, R. Fröhlich, S. Grimme and F. Glorius, *Angew. Chem. Int. Ed.*, 2011, **50**, 4983.
34 A. T. Biju, N. E. Wurz and F. Glorius, *J. Am. Chem. Soc*., 2010, **132**, 5970.
35 X. Bugaut, F. Liu and F. Glorius, *J. Am. Chem. Soc*., 2011, **133**, 8130.
36 F. Liu, X. Bugaut, M. Schedler, R. Fröhlich and F. Glorius, *Angew. Chem. Int. Ed.*, 2011, **50**, 12626.
37 M. Schedler, R. Fröhlich, C.-G. Daniliuc and F. Glorius, *Eur. J. Org. Chem*., 2012, 4164.
38 M. Schedler, D.-S. Wang and F. Glorius, *Angew. Chem. Int. Ed*., 2013, **52**, 2585.
39 S. S. Sohn, E. L. Rosen and J. W. Bode, *J. Am. Chem. Soc*., 2004, **126**, 14370.
40 C. Burstein and F. Glorius, *Angew. Chem. Int. Ed*., 2004, **43**, 6205.
41 V. Nair, S. Vellalath, M. Poonoth, R. Mohan and E. Suresh, *Org. Lett*., 2006, **8**, 507.
42 M. He and J. W. Bode, *Org. Lett*., 2005, **7**, 3131.
43 V. Nair, S. Vellalath, M. Poonoth and E. Suresh, *J. Am. Chem. Soc*., 2006, **128**, 8736.
44 Z. Fu, J. Xu, T. Zhu, W. W. Leong and Y. R. Chi, *Nature Chem*., 2013, **8**, 835.
45 A. Chan and K. A. Scheidt, *Org. Lett*., 2005, **7**, 905.
46 M. He, J. R. Struble and J. W. Bode*, J. Am. Chem. Soc*., 2006, **128**, 8418.
47 N. T. Reynolds, J. Read de Alaniz and T. Rovis, *J. Am. Chem. Soc.*, 2004, **126**, 9518.
48 Y.-J. Kim and A. Streitwieser, *J. Am. Chem. Soc*., 2002, **124**, 5757.
49 F. G. Bordwell and A. V. Satish, *J. Am. Chem. Soc*., 1991, **113**, 985.
50 R. W. Alder, P. R. Allen and S. J. Williams, *J. Chem. Soc., Chem. Commun*., 1995, **12**, 1267.
51 Y. Chu, H. Deng and J.-P. Cheng, *J. Org. Chem*., 2007, **72**, 7790.
52 M. H. Dunn, N. Konstandaras, M. L. Cole and J. B. Harper, *J. Org. Chem*., 2017, **82**, 7324.
53 Z. Li, X. Li and J.-P. Cheng, *J. Org. Chem*., 2017, **82**, 9675.
54 (a) J. M. Dubois and P. Haake, Biochemistry, 1974, **13**, 5358; (b) J.-M. El Hage Chahine and J. E. Dubois, *J. Am. Chem. Soc*., 1983, **105**, 2335.
55 M. W. Washabaugh and W. P. Jencks, *Biochemistry*, 1988, **27**, 5044.
56 E. M. Higgins, J. A. Sherwood, A. G. Lindsay, J. Armstrong, R. S. Massey, R. W. Alder and A. C. O'Donoghue, *Chem. Commun*., 2011, **47**, 1559.
57 T. L. Amyes, S. T. Diver, J. P. Richard, F. M. Rivas and K. Toth, *J. Am. Chem. Soc*., 2004,**126**, 4366.
58 R. S. Massey, C. J. Collett, A. G. Lindsay, A. D. Smith, *J. Am. Chem. Soc*., 2012, **134**, 20421.
59 D. E. Tucker, P. Quinn, R. S. Massey, C. J. Collett, D. J. Jasiewicz, C. R. Bramley, A. D. Smith and A. C. O'Donoghue, *J. Phys. Org. Chem*., 2015, **28**, 108.
60 (a) B. Maji, M.Breugst and H. Mayr, *Angew. Chem. Int. Ed.*, 2011, **50**, 6919; (b) A. Levens, F. An, M. Breugst, H. Mayr and D. W. Lupton, *Org. Lett*., 2016, **18**, 3566.
61 M. W. Washabaugh and W. P. Jencks, *J. Am. Chem. Soc*., 1989, **111**, 674.
62 M. W. Washabaugh and W. P. Jencks, *J. Am. Chem. Soc*., 1989, **111**, 683.
63 H.-W. Wanzlick and H. J. Kleiner, *Angew. Chem.*, 1963, **75**, 1204.
64 D. M. Lemal, R. R. Lovald and K. I. Kawano, *J. Am. Chem. Soc*., 1964, **86**, 2518.
65 J. Castells, F. López-Calahorra and L. Domingo, *J. Org. Chem*., 1988, **53**, 4433.

66 J. Martí, J. Castells and F. López-Calahorra, *Tet. Lett*., 1993, **34**, 521.
67 F. López-Calahorra and R. Rubires, *Tetrahedron*, 1995, **51**, 9713.
68 F. López-Calahorra, E. Castro, A. Ochoa and J. Martí, *Tet. Lett*., 1996, **37**, 5019.
69 R. Breslow and R. Kim, *Tet. Lett*., 1994, **35**, 699.
70 H. J. van den Berg, G. Challa and U. K. Pandit, *J. Mol. Cat*., 1989, **51**, 1.
71 R. Breslow and C. Schmuck, *Tet. Lett*., 1996, **37**, 8241.
72 F. Diederich and H.-D. Lutter, *J. Am. Chem. Soc*., 1989, **111**, 8438.
73 M. J. White and F. J. Leeper, *J. Org. Chem*., 2001, **66**, 5124.
74 Y. Yano, Y. Tamura and W. Tagaki, *Bull. Chem. Soc. Jpn*., 1980, **53**, 740.
75 R. Breslow and E. T. Kool, *Tet. Lett*., 1988, **29**, 1635.
76 J. R. Struble, J. Kaeobamrung and J. W. Bode, *Org. Lett*., 2008, **10**, 957.
77 J. Mahatthananchai and J. W. Bode, *Chem. Sci*., 2012, **3**, 192.
78 R. S. Massey, Ph.D. Thesis, University of Durham, 2013.
79 C. J. Collett, R. S. Massey, O. R. Maguire, A. S. Batsanov, A. C. O'Donoghue and A. D. Smith, *Chem. Sci*., 2013, **4**, 1514.
80 J. T. Stivers and M. W. Washabaugh, *Bioorg. Chem*., 1991, **19**, 369.
81 J. T. Stivers and M. W. Washabaugh, *Bioorg. Chem*., 1992, **20**, 155.
82 A. J. Kresge amd M. F. Powell, *J. Org. Chem*., 1986, **51**, 819.
83 R. Bednar and W. P. Jencks, *J. Am. Chem. Soc*., 1985, **107**, 7117.
84 M. W. Washabaugh, J. T. Stivers and K. A. Hickey, *J. Am. Chem. Soc.*, 1994, **116**, 7094.
85 C. G. Swain, E. C. Stivers, J. F. Reuwer Jr. and L. J. Schaad, *J. Am. Chem. Soc.*, 1958, **80**, 5885.
86 G. B. Barletta, Y. Zou, W. P. Huskey and F. Jordan, *J. Am. Chem. Soc*., 1997, **119**, 2356.
87 M. W. Washabaugh, C. C. Yang, A. D. Hollenbach and P. Chen*, Bioorg. Chem.*, 1993, **21**, 170.
88 M. W. Washabaugh, C. C. Yang, A. D. Hollenbach and P. Chen*, Bioorg. Chem.*, 1993, **21**, 170.
89 A. Berkessel, S. Elfert, K. Etzenbach-Effers and J. H. Teles, *Angew. Chem. Int. Ed*., 2010, **49**, 7120.
90 D. A. DiRocco, K. M. Oberg and T. Rovis, *J. Am. Chem. Soc*., 2012, **134**, 6143.
91 A. Berkessel, S. Elfert, V. R. Yatham, J. M. Neudörfl, N. E. Schlörer and J. E. Teles, *Angew. Chem. Int. Ed*., 2012, **51**, 12370.
92 O. R. Maguire, M.Chem. Thesis, University of Durham, 2012.
93 A. Kotschy, G. Hajós, A. Messmer and G. Jones, *Tetrahedron*, 1996, **52**, 1399.
94 B. Maji and H. Mayr, *Angew. Chem. Int. Ed*., 2012, **51**, 10408.
95 A. Berkessel, V. R. Yatham, S. Elfert and J.-M. Neudörfl, *Angew. Chem. Int. Ed*., 2013, **52**, 11158.
96 V. R. Yatham, J.-M. Neudörfl, N. E. Schlörer and A. Berkessel, *Chem. Sci*., 2015, **6**, 3706.
97 V. R. Yatham, W. Harnying, D. Kootz, J.-M. Neudörfl, N. Schlörer and A. Berkessel, *J. Am. Chem. Soc*., 2016, **138**, 2670.
98 M. Paul, M. Breugst, J.-M. Neudörfl, R. B. Sunoj and A. Berkessel, *J. Am. Chem. Soc.*, 2016, **138**, 5044.
99 M. Paul, P. Sudkaow, A. Wessels, N. Schlörer, J.-M. Neudörfl and A. Berkessel, *Angew. Chem. Int. Ed*., 2018, **57**, 8310.
100 R. B. Carlin and D. P. Carlson, *J. Am. Chem. Soc.,* 1959, **81**, 4673.
101 *US Pat*., WO2004/50650 A1, 2004.
102 J. P. Demers and D. H. Klaubert, *Tet. Lett*., 1987, **28**, 4933.

103 V. S. Padalkar, V. S. Patil, K. R. Phatangare, P. G. Umape and N. Sekar, *Synth. Commun*., 2011, **41**, 925.

104 K. Sirakawa, S. Ban and M. Yoneda, *Yakugaku Zasshi*, 1953, **73**, 598.

105 M. F. Reich, P. F. Fabio, V. J. Lee, N. A. Kuck and R. T. Testa, *J. Med. Chem.*, 1989, **32**, 2474.

106 A. Lewis and R. G. Shepherd, *J. Heterocycl. Chem*., 1971, **8**, 41.

107 J. Easmon, G. Heinisch, G. Pürstinger, T. Langer and J. K. Österreicher, *J. Med. Chem.*, 1997, **40**, 4420.

108 (a) J. F. Hartwig, *Angew. Chem. Int. Ed*., 1998, **37**, 2090; (b) S. Wagaw, B. H. Yrang and S. L. Buchwald, *J. Am. Chem. Soc*., 1998, **120**, 6621; (c) S. Wagaw, B. H. Yang and S. L. Buchwald, *J. Am. Chem. Soc.*, 1999, **121**, 10251.

109 It has been shown that no H/D exchange is observed in 1 M KOD in D_2O at 25 ºC after 16 days; A. G. Lindsay, PhD thesis, University of Durham, 2010.

110 A. K. Covington, R. A. Robinson and R. G. Bates, *J. Phys. Chem*., 1966, **70**, 3820.

111 Determined previously by R. S. Massey, a former member of this research group.

112 A. Streitweiser Jr., W. B. Hollyhead, G. Sonnichsen, A. H. Pudjaatmaka, C. J. Chang and T. L. Kruger, *J. Am. Chem. Soc*., 1971, **93**, 5096.

113 C. G. Swain, E. C. Stivers, J. F. Reuwer Jr. and L. J. Schaad, *J. Am. Chem. Soc*., 1958, **80**, 5885.

114 A. J. Kresge, R. A. More-O'Ferrall and M. F. Powell, in *Isotopes in Organic Chemistry*, E. Buncel, C. C. Lee, Eds., Elsevier, New York, 1987, Vol. 7

115 V. Gold and S. Christ, *J. Chem. Soc., Perkin Trans. 2*, 1972, 89.

116 J. Peon, D. Polshakov and B. Kohler, *J. Am. Chem. Soc*., 2002, **124**, 6428.

117 U. Kaatze, R. Pottel and A. Schumacher, *J. Phys. Chem*., 1992, **96**, 6017.

118 K. Giese, U. Kaatze and R. Pottel, *J. Phys. Chem*., 1970, **74**, 3718.

119 G. H. Haggis, J. B. Hasted and T. J. Buchanan, *J. Chem. Phys*., 1952, **20**, 1452

120 W. P. Jencks, *Catalysis in Chemistry and Enzymology*, Dover, New York, 1987.

121 U. Kaatze, *J. Chem. Eng. Data*, 1989, **34**, 371.

122 J. P. Richard, T. L. Amyes and M. M. Toteva, *Acc. Chem. Res.*, 2001, **34**, 981.

123 M. Eigen, *Angew. Chem., Int. Ed*., 1964, **3**, 1.

124 E. V. Anslyn and D. A. Dougherty, *Modern Physical Organic Chemistry*, University Science Books, 2006.

125 C Reichardt, *Solvents and Solvent Effects in Organic Chemistry*, Wiley-VCH, Weinheim, 2003.

126 C. D. Campbell, C. J. Collett, J. E. Thomson, A. M. Z. Slawin and A. D. Smith, *Org. Biomol. Chem*., 2011, **9**, 4205.

127 Gaussian 09, Revision A.02, M. J. Frisch, G. W. Trucks, H. B. Schlegel, G. E. Scuseria, M. A. Robb, J. R. Cheeseman, G. Scalmani, V. Barone, B. Mennucci, G. A. Petersson, H. Nakatsuji, M. Caricato, X. Li, H. P. Hratchian, A. F. Izmaylov, J. Bloino, G. Zheng, J. L. Sonnenberg, M. Hada, M. Ehara, K. Toyota, R. Fukuda, J. Hasegawa, M. Ishida, T. Nakajima, Y. Honda, O. Kitao, H. Nakai, T. Vreven, J. A. Montgomery, Jr., J. E. Peralta, F. Ogliaro, M. Bearpark, J. J. Heyd, E. Brothers, K. N. Kudin, V. N. Staroverov, R. Kobayashi, J. Normand, K. Raghavachari, A. Rendell, J. C. Burant, S. S. Iyengar, J. Tomasi, M. Cossi, N. Rega, J. M. Millam, M. Klene, J. E. Knox, J. B. Cross, V. Bakken, C. Adamo, J. Jaramillo, R. Gomperts, R. E. Stratmann, O. Yazyev, A. J. Austin, R. Cammi, C. Pomelli, J. W. Ochterski, R. L. Martin, K. Morokuma, V. G. Zakrzewski, G. A. Voth, P. Salvador, J. J. Dannenberg, S. Dapprich, A. D.

Daniels, O. Farkas, J. B. Foresman, J. V. Ortiz, J. Cioslowski and D. J. Fox, Gaussian, Inc., Wallingford CT, 2009.
128 This work made use of the facilities of the Hamilton HPC Service of Durham University.
129 H. H. Jaffé, *Chem. Rev.*, **1953**, *53*, 191.
130 R. Fuchs, C. A. Kaplan, J. J. Bloomfield and L. F. Hatch, *J. Org. Chem*., 1962, **27**, 733.
131 The N-2,4,6-Triisopropylphenyl triazolium salt was prepared by a member of the research group, Jiayun Zhu
132 F. Rived, M. Rosés and E. Bosch, *Anal. Chim. Acta*, 1998, **374**, 309.
133 Z. G. Szabó in *Comprehensive Chemical Kinetics*, ed. C. H. Bamford and C. F. H. Tipper, Elsevier, Amsterdam, 1969, vol. 2, ch. 1, pp. 35-37
134 T. Aoyama and T. Shioiri, *Tet. Lett*., 1990, **31**, 5507.
135 N. Hashimoto, T. Aoyama and T. Shioiri, *Chem. Pharm. Bull*., 1981, **29**, 1475.
136 E. Kühnel, D. P. Laffan, G. C. Lloyd-Jones, T. Martínez del Campo, I. R. Shepperson and J. L. Slaughter, *Angew. Chem. Int. Ed*., 2007, **46**, 7075.
137 It has been shown that no H/D exchange is observed in 1 M KOD in D_2O at 25 ºC after 16 days; A. G. Lindsay, PhD thesis, University of Durham, 2010.
138 (a) A. J. Kresge, *Acc. Chem. Res*., 1975, **8**, 354; (b) C. F. Bernasconi, *Pure Appl. Chem*., 1982, **54**, 2335; (c) R. P. Bell, *The Proton in Chemistry*, 2nd ed, Cornell University Press, Ithaca, NY, 1973, p 194; (d) A. C. Lin, D. B. Dahlberg and A. J. Kresge, *J. Am. Chem. Soc*., 1983, **105**, 5380; (e) A. J. Kresge and M. F. Powell, *J. Org. Chem*., 1986, **51**, 819; (f) A. J. Kresge and M. F. Powell, *J. Org. Chem*., 1986, **51**, 822; (g) T. Aroella, C. H. Arrowsmith, M. Hojatti, A. J. Kresge, M. F. Powell, Y. S. Tang and W. –H. Wang, *J. Am. Chem. Soc*., 1987, **109**, 7198; (h) R. A. Bednar and W. P. Jencks, *J. Am. Chem. Soc*., 1985, **107**, 7177.
139 W. S. Matthews, J. E. Bares, J. E. Bartmess, F. G. Bordwell, F. J. Cornforth, G. E. Drucker, Z. Margolin, R. J. McCallum, G. J. McCollum and N. R. Vanier, *J. Am. Chem. Soc*., 1975, **97**, 7006.
140 E. Kiliç and N. Aslan, *Microchim. Acta*, 2005, **151**, 89.
141 G. R. Fulmer, A. J. M. Miller, N. H. Sherden, H. E. Gottlieb, A. Nudelman, B. M. Stoltz, J. E. Bercaw and K. I. Goldberg, *Organometallics*, 2010, **29**, 2176.
142 J. E. Thomson, K. Rix and A. D. Smith, *Org. Lett*., 2006, **7**, 3785.
143 J. E. Thomson, C. D. Campbell, C. Concellón, N. Duguet, K. Rix, A. M. Z. Slawin and A. D. Smith, *J. Org. Chem*., 2008, **73**, 2784.
144 M. S. Kerr, J. Read de Alaniz and T. Rovis, *J. Org. Chem*., 2005, **70**, 5725.
145 P. K. Glasoe and F. A. Long, *J. Phys. Chem.*, 1960, **64**, 188.
146 L. G. Gagliardi, C. B. Castells, C. Ràfols, M. Rosés and E. Bosch, *Anal. Chem*., 2007, **79**, 3180.